

**OPTIMIZATION OF
NORMAL-INCIDENCE
GaAs-AlGaAs MULTIPLE
QUANTUM WELL OPTICAL
MODULATORS**

A thesis by

Mark Whitehead

Submitted to the University of London for the degree of Ph.D.

*Department of Electronic and Electrical Engineering
University College London
January 1990*

ProQuest Number: 10797807

All rights reserved

INFORMATION TO ALL USERS

The quality of this reproduction is dependent upon the quality of the copy submitted.

In the unlikely event that the author did not send a complete manuscript and there are missing pages, these will be noted. Also, if material had to be removed, a note will indicate the deletion.



ProQuest 10797807

Published by ProQuest LLC (2018). Copyright of the Dissertation is held by the Author.

All rights reserved.

This work is protected against unauthorized copying under Title 17, United States Code
Microform Edition © ProQuest LLC.

ProQuest LLC.
789 East Eisenhower Parkway
P.O. Box 1346
Ann Arbor, MI 48106 – 1346

ABSTRACT

This thesis concerns the experimental and theoretical optimization of electric field-induced optical modulation in GaAs–AlGaAs multiple quantum well (MQW) structures with light incident normal to the quantum well layers. The basic modulator device consists of an epitaxially-grown *p-i-n* diode, which contains the quantum wells in the intrinsic region and allows the absorption and the refractive index of the MQWs to be modified by the application of small reverse bias voltages.

Room temperature photocurrent and transmission spectroscopy have been used to determine electric field effects on the absorption in GaAs–AlGaAs MQWs, and also to assess the possible improvements to be made in MQW modulator performance by optimum choice of well and barrier thicknesses. The devices investigated have been fabricated from material grown by both high-resolution epitaxial techniques, namely metal-organic vapour phase epitaxy (MOVPE) and molecular beam epitaxy (MBE). The details of device fabrication and measurement are discussed briefly.

From the measurements of absorption changes in various MQW devices for a range of applied bias voltages, calculations of the corresponding changes in refractive index have been carried out by the Kramers-Krönig transformation. With the information on electro-absorption and electro-refraction the potential for improved modulator performance by incorporating the MQWs within a Fabry-Perot cavity structure has been assessed, where the incident light makes multiple passes through the MQW structure, resulting in destructive or constructive interference depending on the wavelength and bias voltage.

The general modelling of MQW Fabry-Perot modulators has ultimately led to the experimental investigation of an asymmetric cavity device (low front and high back surface reflectivity). This type of structure operates solely in reflection, thus avoiding the need for substrate removal, and offers large, broadband reflection changes and very high on:off ratios with low operating voltages.

for Patricia, Catherine, Jack and Michael

CONTENTS

	Page Number
Acknowledgements	6
List Of Abbreviations	8
Preface	9
Chapter 1 THE BASIS FOR MULTIPLE QUANTUM WELL OPTICAL MODULATORS	
1.1 Introduction	16
1.2 From LPE to QCSE	17
1.3 Optical Properties of Quantum Wells	25
1.4 The Multiple Quantum Well <i>p-i-n</i> Diode	35
Chapter 2 FABRICATION AND ASSESSMENT OF GaAs MQW <i>p-i-n</i> DIODE STRUCTURES	
2.1 Introduction	53
2.2 Growth of GaAs MQW <i>p-i-n</i> Diode Structures	54
2.3 Fabrication and Assessment of MQW Mesa Diodes	59
2.4 Photocurrent and Absorption	65
2.5 Photocurrent Studies of MOVPE-Grown Devices	67
2.6 Photocurrent Studies of MBE-Grown Devices	87
2.7 Summary	95
Chapter 3 ABSORPTION, ELECTRO-ABSORPTION AND ELECTRO- REFRACTION IN GaAs MULTIPLE QUANTUM WELLS	
3.1 Introduction	100
3.2 Limits to the Accurate Measurement of Absorption	102
3.3 Calculation of Absorption from Transmission Measurements ..	113
3.4 Calculation of Absorption Spectra from Photocurrent Measurements	119
3.5 Calculation of Electro-Refraction	128
3.6 Summary	136

Chapter 4	GaAs MULTIPLE QUANTUM WELL TRANSMISSION MODULATORS	
4.1	Introduction	141
4.2	Fabrication and Characterization of MQW Transmission Modulators	143
4.3	The CPM7 (100Å well) Transmission Modulator	153
4.4	The CPM405 (87Å well) Transmission Modulator	156
4.5	The MV245 (145Å well) Transmission Modulator	162
4.6	The MV246 (47Å well) Transmission Modulator	166
4.7	The CPM405 (87Å well) Reflection Modulator	173
4.8	Limits to Modulation at Normal Incidence in GaAs MQW Devices	176
4.9	Summary	181
Chapter 5	THE USE OF FABRY-PEROT EFFECTS TO ENHANCE THE PERFORMANCE OF MQW OPTICAL MODULATORS	
5.1	Introduction	189
5.2	Simulation of MQW Fabry-Perot Cavity Modulators	192
5.3	Low-Finesse MQW Transmission Modulators	203
5.4	Low-Finesse MQW Reflection Modulators	212
5.5	High-Finesse MQW Reflection Modulators	219
5.6	Sensitivity of FP Cavity Modulators	225
5.7	Summary	228
Chapter 6	MQW ASYMMETRIC FABRY-PEROT CAVITY MODULATORS (AFPMs)	
6.1	Introduction	234
6.2	Theory of Operation of the AFPM	236
6.3	Modelling of AFPM Performance	242
6.4	Initial Demonstration of an AFPM	252
6.5	Multilayer Stack Reflectors for an Integrated AFPM	258
6.6	The Integrated AFPM	268
6.7	Summary	279
Conclusions	285
Appendix	Fabry-Perot Cavity Equations	287
List Of Publications	291

ACKNOWLEDGEMENTS

Since the male of the species is, for the present, incapable of bearing children, perhaps the closest traumatic experience he can suffer is producing a Ph.D. thesis. As with a real child you spend sleepless nights wondering "*What will it look like? Will it have all the right parts?*" As with a real child it has features belonging to previous generations, but taken as a whole it is unique. Anyway, here's my "baby" – the result of a protracted labour. Some of my colleagues may express surprise that I haven't "given birth" to a baby elephant, considering the gestation period. I can forgive them for that. I would also like to take the opportunity to express my gratitude to those who have helped me through a difficult "confinement".

First and foremost I would like to thank Prof. Gareth Parry for having confidence in me and, more importantly, giving *me* the confidence to see the whole thing through. Rather than a supervisor, I have come to regard him more as a colleague and a friend. For providing the framework within which the Digital Optics Group (DOG) at UCL exists and *thrives*, Gareth and Prof. John Midwinter are to be congratulated.

Over the years (count 'em!) that I've been at UCL members of the DOG have always provided a superb safety net, by allowing me to bounce ideas off them before subjecting myself to a more public critique. To Drs. Paul Wheatley, John Halley, Piero Bradley, Drs-elect Peter Stevens and Craig Tombling and present DOG Drs-in-waiting I am indebted for many hours spent discussing both academic and non-academic subjects. It is also fair to say that without the constant interest, concern, cajoling, attempts at embarrassment and threats from certain "DOGs", I would probably still be floundering in mid-thesis!

Two colleagues who deserve a special mention are Tony Rivers and Mark Abbott; Tony for his toil in the clean-room on my behalf, and Mark for his invaluable computing efforts, particularly with "Goober" and "Tropical" (also for being the only person who shares my irrational love for Manchester United F. C.).

MQW materials do not grow on trees, nor, unfortunately, do they exist in the Ealing catalogue. Thus our collaborators at the University of Sheffield and Philips Research Labs. fall into the "*those without whom....*" category. Thanks go to Dr. John Roberts, Chris Button,

Prakesh Mistry and Dr. Karl Woodbridge for essential growth, and to Malcolm Pate, Dr. Patrick Li Kam Wa, Dr. Geoff Hill, Prof. Peter Robson, Dr. Pete Dobson and Dr. Geoff Duggan for help and support in many forms. Thanks also to Dr. David Guy (RSRE) and Dr. Phil Klipstein (ICSTM) for enlightening discussions.

I am grateful to the SERC and Philips Research Labs for financially supporting me during the course of my studentship, and to British Telecom for funding my current position.

Lastly I would like to thank my fellow occupants of Room 1111, numerous other members of the department, my friends outside UCL (particularly Sally and Nev) and my family for patiently listening to the phrase "*It's nearly finished*" for so long.

LIST OF ABBREVIATIONS

A number of abbreviations appear frequently throughout this thesis. They are listed here, with their meanings, for convenience.

AFPM	Asymmetric Fabry-Perot (cavity) modulator.
AR	Anti-reflection (coating, layer).
BA	Bias-absorbing (modulation).
BT	Bias-transmitting (modulation).
$\Delta\alpha$	Change in absorption coefficient.
Δn	Change in refractive index.
ΔR	Change in reflection coefficient.
ΔT	Change in transmission coefficient.
en-hhm	Exciton formed between n^{th} electron and m^{th} heavy hole sub-band.
en-lhm	Exciton formed between n^{th} electron and m^{th} light hole sub-band.
FP	Fabry-Perot (cavity, resonance, modulator).
KK	Kramers-Krönig (equations, integral)
MBE	Molecular beam epitaxy.
MLS	Multi-layer (reflector) stack.
MOVPE	Metal-organic vapour phase epitaxy.
MQW	Multiple quantum well.
QCSE	Quantum-confined Stark effect.
QW	Quantum well.
SFPM	Symmetric (high-finesse) Fabry-Perot (cavity) modulator.

PREFACE

The observation of strongly enhanced electro-absorption in GaAs-AlGaAs multiple quantum well (MQW) structures in 1983 [1] and the subsequent demonstration of the MQW optical modulator [2] were significant developments in optoelectronic device physics and technology. For the first time it was possible to achieve substantial optical modulation ($\approx 2:1$ on:off ratio) at low bias voltages ($<10\text{V}$) with a non-waveguiding modulator compatible with semiconductor laser/LED sources and existing III-V fabrication/processing.

The improved performance arises from the confinement of electrons and holes in very thin ($\approx 100\text{\AA}$) GaAs layers, which form potential wells with quantized carrier energy states when bounded by wider band-gap AlGaAs layers. This radically alters the optical properties of the quantum well GaAs compared to those of the bulk material. Briefly, the absorption strength at the band edge is increased, along with the red-shift induced in the edge by an electric field applied perpendicular to the plane of the MQW layers – termed the quantum-confined Stark effect (QCSE) [3]. The resultant electro-absorptive changes near the absorption edge are up to ten times greater than in bulk GaAs [4], so the thickness of the MQW region in the modulator need only be $\approx 1\mu\text{m}$ to achieve strong modulation of light incident normal to the plane of the MQWs. Operating in this normal-incidence configuration means that coupling and background absorption losses can be low.

The standard modulator structure has the MQWs embedded in the undoped region of a *p-i-n* diode. Thus the necessary modulating field ($\approx 50\text{-}100\text{ kV}\cdot\text{cm}^{-1}$) can be applied with low bias voltages. The *p-i-n* structure is also compatible with high frequency operation [5], and efficient photodetection [6]. The ability to modulate and detect in the same device has led to optical switching applications of quantum well modulators such as the diode- and transistor-biased self electro-optic effect devices (known generally as SEEDs [6-8]). They also appear to be promising optical:electronic interface devices for the proposed optical interconnection of electronics in large processors [9,10].

The purpose of this thesis is to investigate ways of maximizing the modulation which may be achieved in a normal-incidence MQW modulator. We consider the following parameters: the absolute change in transmission or reflection (ΔT or ΔR), contrast (on:off ratio), insertion loss and operating voltage, with the aim of maximizing ΔT or ΔR and contrast, whilst minimizing insertion loss and voltage.

The original intention from the outset of this project was to investigate the possibility of enhancing the optical modulation in a GaAs-AlGaAs MQW *p-i-n* diode by incorporating it within a Fabry-Perot (FP) cavity. The proposal was that the electro-refractive effects, which occur simultaneously with changes in absorption, would be strong enough in MQWs to detune a high-finesse FP étalon from resonance at low bias voltages. The narrow resonances of the high-finesse structure containing the MQWs should then permit on:off ratios much greater than $\approx 2:1$ which had been observed in the single-pass transmission modulator.

Before any form of resonant MQW modulator could even be contemplated, let alone fabricated and tested, there were a number of developmental stages necessary. The first stage was to establish a supply of device quality MQW material and instigate the means of processing and optically assessing this material. The second stage was the optimization of the design of the MQW structure itself (well and barrier widths) for the most efficient electric field response. A third stage involved the computer modelling of the performance of resonant MQW modulators in general, in order to determine the optimum cavity structure, along with the design and growth of semiconductor quarter-wave stack high reflectors as the integrated mirrors for resonant modulators.

The structure of this thesis is as follows:

In Chapter 1 the developments which made possible the demonstration of the MQW optical modulator are reviewed. We outline the basic optical and electronic properties of semiconductor MQW structures which set them apart from normal bulk semiconductors and permit much stronger electro-optic modulation. We discuss also the requirements for the *p-i-n* device structure.

The early work which is contained in Chapter 2 is concerned principally with the optical assessment of MQW *p-i-n* diode devices. Samples of MQW material were obtained in collaboration with the SERC Central Facility for III-V Semiconductors at the University of Sheffield, and through an SERC CASE studentship with Philips Research Laboratories, Redhill. It was soon realised that useful qualitative information about the optical and electrical properties of the device structures could be deduced from room temperature photocurrent spectroscopy. This was at a time when it was not yet possible for us to produce MQW transmission modulators because device fabrication techniques were not sufficiently developed. The results of photocurrent measurements on a range of MQW structures are described in Chapter 2, with emphasis on the effects of non-optimized growth and the width of well (GaAs) and barrier (AlGaAs) layers on the electro-absorptive properties. It is shown for the first time that high quality MQW *p-i-n* diodes may be grown by metal-organic vapour phase epitaxy (MOVPE).

In Chapter 3 the problems associated with deducing absorption data from MQW transmission spectra are addressed, particularly the ever-present effect of FP resonance. We assess the accuracy of estimating absorption given a particular degree of FP effect and level of absorption. As a convenient way around the problem of measuring transmission spectra in order to obtain absorption data, we also show how, with certain approximations, photocurrent spectra may be rescaled to represent absorption. The calculated electro-absorption spectra are then used to generate the corresponding electro-refraction spectra.

In Chapter 4 we examine how the width of the quantum wells affects the modulation obtainable in MQW transmission modulators [11]. To limit the operating voltage to a maximum of $\approx 16\text{V}$, the total MQW thickness for a range of devices is kept to $\approx 1\mu\text{m}$. The data presented in this section include the first for wells which are substantially wider (145\AA) or narrower (47\AA) than the standard $\approx 100\text{\AA}$. The results are found to be in good agreement with subsequent experimental electro-absorption data and projected optimum performance figures from other authors. An initial attempt is made here to improve modulation by operating a device in reflection mode [12] – effectively a double-pass transmission modulator.

Having determined in Chapter 4 the scope for improving modulation simply by altering the MQW structure, in Chapter 5 we move on to consider how much improvement can be made by deliberately introducing FP resonance into the transmission or reflection response. Using electro-absorption and electro-refraction data from Chapter 3 with the standard absorptive FP cavity equations, we model the performance of both low and high finesse devices in transmission and reflection [13]. The principal result from this modelling is a new device concept – a resonant MQW modulator which operates in reflection within an *asymmetric* FP cavity, i.e. one with low reflectivity at the front surface and high reflectivity at the back. This device makes optimum use of MQW electro-absorption, rather than the electro-refractive effect which was the original intended mechanism, and, despite the fact that it is resonant, has an operating linewidth comparable with non-resonant MQW modulators

We end this thesis in Chapter 6 with a full investigation of the asymmetric FP cavity modulator (AFPM), showing the advantages of this type of structure over a high-finesse FP modulator. The characteristics of the device are described in detail and we calculate the limits to contrast and operating voltage. An initial demonstration of the device is made using an adapted MQW transmission modulator. We proceed with the design of the complete epitaxial structure of the AFPM, which incorporates a quarter-wave stack mirror. In initial experiments this device shows what we believe to be the highest contrast ever reported for a normal-incidence electro-absorptive modulator [14] – approximately 20dB (100:1) with <4dB insertion loss and 9V bias.

REFERENCES (Preface)

- [1] D. S. CHEMLA, T. C. DAMEN, D. A. B. MILLER, A. C. GOSSARD and W. WIEGMANN, "Electroabsorption by Stark effect on room-temperature excitons in GaAs/GaAlAs multiple quantum well structures", *Appl. Phys. Lett.* (1983), **42**, pp. 864-6.
- [2] T. H. WOOD, C. A. BURRUS, D. A. B. MILLER, D. S. CHEMLA, T. C. DAMEN, A. C. GOSSARD and W. WIEGMANN, "High speed optical modulation with GaAs/GaAlAs quantum in a *p-i-n* diode structure", *Appl. Phys. Lett.* (1984), **44**, pp. 16-18.
- [3] D. A. B. MILLER, D. S. CHEMLA, T. C. DAMEN, A. C. GOSSARD, W. WIEGMANN, T. H. WOOD and C. A. BURRUS, "Band-edge electroabsorption in quantum well structures: The quantum-confined Stark effect", *Phys. Rev. Lett.* (1984), **53**, pp. 2173-6.
- [4] G. E. STILLMAN, C. M. WOLFE, C. O. BOZLER and J. A. ROSSI, "Electroabsorption in GaAs and its application to waveguide detectors and modulators", *Appl. Phys. Lett.* (1976), **28**, pp. 544-6.
- [5] T. H. WOOD, C. A. BURRUS, D. A. B. MILLER, D. S. CHEMLA, T. C. DAMEN, A. C. GOSSARD and W. WIEGMANN, "131ps optical modulation in semiconductor multiple quantum wells (MQW's)", *IEEE J. Quantum Electron.* (1985), **QE-21**, pp. 117-8.
- [6] D. A. B. MILLER, D. S. CHEMLA, T. C. DAMEN, A. C. GOSSARD, W. WIEGMANN, T. H. WOOD and C. A. BURRUS, "Novel hybrid optically bistable switch: The quantum well self-electro-optic effect device", *Appl. Phys. Lett.* (1984), **45**, pp. 13-15.
- [7] A. L. LENTINE, H. S. HINTON, D. A. B. MILLER, J. E. HENRY, J. E. CUNNINGHAM and L. M. F. CHIROVSKY, "Symmetric self-electro-optic effect device: Optical set-reset latch", *Appl. Phys. Lett.* (1988), **52**, pp. 1419-21.
- [8] P. WHEATLEY, P. J. BRADLEY, M. WHITEHEAD, J. E. MIDWINTER, G. PARRY, P. MISTRY, M. A. PATE and J. S. ROBERTS, "Novel nonresonant optoelectronic logic device", *Electron. Lett.*, **23**, pp. 92-3.
- [9] J. E. MIDWINTER, "Photonic switching technology: Component characteristics versus network requirements", *J. Lightwave Tech.* (1988), **LT-6**, pp.1512-19.
- [10] H. S. HINTON, "Architectural considerations for photonic switching networks", *IEEE Journal on Selected Areas in Communications* (1988), **6**, pp.1209-26.
and "Relationship between the hardware required for photonic switching and optical computing based on free-space digital optics", *OSA Proc. Photonic Switching* (1989), **3**, pp. 184-91.
- [11] M. WHITEHEAD, P. STEVENS, A. RIVERS, G. PARRY, J. S. ROBERTS, P. MISTRY, M. A. PATE and G. HILL, "The effects of well width on the characteristics of GaAs/AlGaAs multiple quantum well modulators", *Appl. Phys. Lett.* (1988), **53**, pp. 956-8.

- [12] G. D. BOYD, D. A. B. MILLER, D. S. CHEMLA, S. L. McCALL, A. C. GOSSARD and J. H. ENGLISH, "Multiple quantum well reflection modulator", Appl. Phys. Lett. (1987), 50, pp. 1119-21.

- [13] M. WHITEHEAD, G. PARRY and P. WHEATLEY, "Investigation of étalon effects in GaAs-AlGaAs multiple quantum well optical modulators", IEE Proceedings Pt. J (1988), 136, pp. 52-58.

- [14] M. WHITEHEAD, A. RIVERS, G. PARRY, J. S. ROBERTS and C. BUTTON, "Low-voltage multiple quantum well reflection modulator with on:off ratio > 100:1", Electron. Lett. (1989), 25, pp. 984-5.

CHAPTER ONE

THE BASIS FOR MULTIPLE QUANTUM WELL OPTICAL MODULATORS

1.1 Introduction

1.2 From LPE to QCSE

- 1.2.1 Initial Development of Low-Dimensional Semiconductor Structures and Devices
- 1.2.2 The Origins of the GaAs-AlGaAs QCSE Modulator
- 1.2.3 GaAs MQW Device Developments
- 1.2.4 Other Quantum Well Materials

1.3 Optical Properties of Quantum Wells

- 1.3.1 Zero-field Properties
- 1.3.2 Electro-Absorption in Quantum Wells – The Quantum-Confined Stark Effect

1.4 The Multiple Quantum Well *p-i-n* Diode

- 1.4.1 General Design Considerations
- 1.4.2 Effect of Background Doping on Field Uniformity
- 1.4.3 Effect of Field Non-Uniformity on Electro-Absorption

1.1 INTRODUCTION

The work which will be described in the rest of this thesis requires some background knowledge of the optical properties of quantum wells and the basic design of the modulator which exploits them. It is the purpose of this first chapter to introduce the relevant properties which make the use of GaAs MQW structures attractive for optical modulation, and to discuss the factors which affect device quality.

We begin with a summary of the developments of the last two decades which have led to the enormous present-day interest in quasi-2D semiconductor structures, and, in particular, the demonstration of the MQW optical modulator. This is followed by a brief discussion of the optical properties of quantum wells which set them apart from bulk semiconductors. The important feature is the existence of strong peaks at the absorption edge at room temperature, due to bound states of electrons and holes called "excitons". These may be strongly red-shifted by an electric field applied perpendicular to the plane of the quantum well to give absorption changes of more than 10 times those observed in bulk III-V semiconductors, and at smaller fields.

Having set out the principles on which enhanced electro-absorption in MQWs is based, we end with a look at how the MQW *p-i-n* diode device is constructed, which allows the necessary modulating field to be applied to the MQW structure in an efficient manner. We outline the importance of achieving low background doping in the undoped MQW material, so as to avoid spectral broadening of the electro-absorption.

1.2 FROM LPE TO QCSE

1.2.1 INITIAL DEVELOPMENT OF LOW-DIMENSIONAL SEMICONDUCTOR STRUCTURES AND DEVICES

For quantum well devices to be realised required two essential ingredients, one being the physical insight to predict the novel properties of such structures, the other being a material growth technology capable of achieving the layer thickness and doping control necessary.

In the late 1960s Esaki and Tsu [1] at IBM Yorktown proposed the first device based on quantum confinement effects. Their prediction was that by introducing a periodic variation in the direct band gap of a single-crystal semiconductor, if the structural period were $\approx 100\text{-}200\text{\AA}$, a "superlattice" could be made in which the energy of carriers would be restricted to narrow minibands, according to the well-known model of Krönig and Penney [2]. Such a structure would exhibit negative differential resistance (NDR) when a small voltage was applied to it. Furthermore, the authors prompted, or perhaps foresaw, developments in crystal growth by outlining possible methods of achieving the necessary band gap "engineering"; one option being the alternate growth of layers of lattice-matched semiconductors having different energy gaps, the other the periodic incorporation of donors and acceptors generating a spatially oscillating internal potential in a homogeneous crystal – what has since become known as the doping superlattice.

At the time the superlattice was proposed, the chief epitaxial growth technology was liquid phase epitaxy (LPE), which had been successfully used to produce GaAs-AlGaAs single heterostructure lasers [3], but this technique is incapable of producing layers much thinner than 1000\AA . However, suitable methods for the growth of ultrathin layers were at hand in the rapidly developing techniques of molecular beam epitaxy (MBE) [4] and metal-organic vapour phase epitaxy (MOVPE) [5]. By 1971 Cho at Bell Labs. had already succeeded in growing a periodic GaAs-AlGaAs structure by MBE [6] with individual layer thicknesses of $\approx 1700\text{\AA}$, although still too large to produce quantum effects.

While this progress was being achieved at Bell, Esaki and co-workers were at the same time attempting to obtain experimental evidence for their NDR predictions. In 1974, with improvements in layer thickness control to $\pm 50\text{\AA}$, they were able to report the observation of oscillatory

conductance in an MBE-grown GaAs-AlAs superlattice [7].

The first fruits of the new epitaxial methods, in terms of optical properties, also came in 1974, when Dingle and co-workers at Bell Laboratories observed strong quantization effects in GaAs-AlGaAs multiple quantum well (MQW) structures at liquid helium temperatures [8]. The main features were the modification of the shape of the absorption spectrum from the roughly parabolic 3D (bulk) form to the stepped form expected of a system with quasi-2D character, and the appearance of sharp excitonic peaks at the edge of the absorption steps. Both these effects were ascribed to the confinement of carriers in the quantum well (GaAs) layers; the first due to the formation of discrete allowed energy levels, the second due to the increase in the spatial overlap of electron and hole wavefunctions. This is discussed in more detail in the next section.

The early investigations of Dingle et al. quickly led to work on quantum well lasers, which offered such benefits as reduced threshold currents and temperature sensitivity compared to bulk semiconductor lasers. The first demonstration with an optically pumped structure was made by van der Ziel et al. [9] in 1975. However, it was not until 1978 that Dupuis et al. [10] demonstrated the first room-temperature, current injection laser with a QW active region. The device was grown by MOVPE, somewhat surprisingly in view of the respective achievements in material quality by the MBE and MOVPE methods in the preceding years. This was the first evidence that the control of doping and layer thicknesses had begun to reach the levels which would subsequently be needed for the MQW modulator. Further improvements in doping control and the smoothness of the GaAs-AlGaAs heterointerface allowed Dingle et al. to demonstrate increased mobilities with modulation-doped heterojunctions [11], where the spatial separation of electrons from their donor sites in the AlGaAs from causes the formation of a narrow conduction channel (2D electron gas) close to the interface. This principle was then utilised in the high electron mobility transistor (HEMT) [12] demonstrated by Mimura et al. in 1980.

Up until the early 1980's the two main areas of research into devices employing quantum confinement effects remained the QW laser and the HEMT. The effect of an electric field on the optical properties of MQWs had not been considered up to this time.

1.2.2 THE ORIGINS OF THE GaAs-AlGaAs QCSE MODULATOR

It is not obvious when the idea of using high electric fields on MQWs to achieve strong optical intensity modulation was first considered. It may well be that material quality, although sufficient for QW lasers, prevented the investigation of MQW Stark effect devices before the first normal-incidence modulator [13] was demonstrated by Wood et al. in 1984. Certainly it was not until 1981 that clear excitonic features were observed at *room temperature* in a GaAs-AlAs superlattice by Ishibashi et al. [14]. The same year saw a resurgence of theoretical interest with calculations of the confinement energy levels of superlattices/MQWs by Bastard [15]. This was followed up in 1982 by an analysis of the exciton binding energy as a function of well width [16].

Mendez et al., working in conjunction with Bastard made the first observations of the effect of a transverse electric field (perpendicular to the plane of the wells) on low temperature photoluminescence from 30Å GaAs QWs [17]. They noted the shift to lower energies and quenching of the exciton-associated photoluminescence (PL) intensity peak at fields of a few tens of kV.cm^{-1} , which was attributed to field-induced separation of electrons and holes, along with modification of their confinement energies due to distortion of the quantum well potential profile. Preliminary variational calculations of the shift of the PL peak [18] by Bastard later showed a discrepancy between experiment and theory, believed to be mostly due to interwell coupling. Around the same time, this enhanced field effect was proposed as a means of tuning the output of a QW laser by Yamanishi and Suemune [19].

During this period considerable interest arose in the nonlinear optical properties of quantum wells with a view to their application in all-optical switching devices. Initial measurements of the nonlinearities associated with the strongly-bound room-temperature exciton in GaAs-AlGaAs MQWs were made by D. A. B. Miller and co-workers, who observed enhanced exciton saturation [20] and degenerate four-wave mixing [21] with wells of $\approx 100\text{\AA}$, much wider than had been used previously. Low-power optical bistability in a high finesse Fabry-Perot étalon containing GaAs quantum wells was reported by Tarng et al shortly afterwards [22].

Within the same research group as Miller at AT&T Bell Labs., Chemla et al. then made the first measurements of the effect of an electric field on the absorption spectrum of an MQW structure [23]. Although the orientation of the applied field with respect to the quantum wells was

rather ambiguous, a marked red shift of heavy and light hole excitons in the transmitted spectrum was observed.

Having achieved some success with a fairly crude device, the next step was to produce an efficient MQW device structure for electro-absorptive optical modulation. This was duly done by Wood et al. with the incorporation of undoped QWs into the i-region of an epitaxial p-i-n diode [13]. The basic structure of this device, which is the starting point for the original work in this thesis, can be seen in Figs. 1.4.1 and 4.2.1.1. A reduction in transmission by a factor of 2 was achieved with only 8V reverse bias; an encouraging figure considering that the absorbing (MQW) region of the device was only $1\mu\text{m}$ thick. The modulator was shown to work with rise times down to less than 3ns, this being almost totally attributable to the RC time constant. With a reduction in the diameter of the device to $\approx 95\mu\text{m}$, Wood et al. [24] then managed to achieve a switching time of 131ps, thus confirming the inherent speed of the modulation mechanism.

1.2.3 GaAs MQW DEVICE DEVELOPMENTS

Since the initial demonstration of the MQW transmission modulator a considerable amount of interest has arisen in the possibility of using these compact, efficient devices as components in optoelectronic processing systems, which, it is envisaged, may overcome some of the fundamental limitations of purely electronic systems. Many authors have considered device requirements and system architectures. Examples can be found in Refs. 25-32.

Two schools of thought now exist as to the best way to incorporate optics into the framework of information processing: one suggests using optics solely as the interconnection medium [27-31], with modulators acting as optoelectronic input/output between electronic processor "islands", exploiting both the modulation and photodetection properties of the MQW *p-i-n* diode [33]; the other brings some logic operations into the optical domain [27-29, 32], and thus the need for suitable optical logic devices. The bistable optical switch known as the SEED (Self Electro-optic Effect Device), invented by D. A. B. Miller [34], has received most attention from this point of view. The device in its most simple form consists of an MQW modulator in series with a resistor. Under certain

biasing conditions, with incident light at the wavelength of the unbiased exciton peak at the MQW absorption edge, the output intensity of the modulator is switched nonlinearly from high to low as input intensity is linearly increased. This device uses the photocurrent generated in the modulator as the feedback to control its output state.

Variants on the basic SEED have been developed, notably the D-SEED [35], which integrates a photodiode as the resistive load with the MQW modulator; the T-SEED [36], which uses a phototransistor load to achieve gain; and the S(ymmetric)-SEED [37], where two reverse-biased MQW modulators are linked in series, one acting as the load of the other, and vice versa. In this latter configuration, it is possible to achieve "time-sequential" gain and immunity from input intensity fluctuations. The SEED approach has now been developed to a relatively high degree of sophistication, with the group at AT&T Bell recently reporting 16×8 arrays of reflective S-SEEDs with very uniform operating characteristics [38], and an all-optical shift register based on the same device array [39].

As well as the development of the MQW SEED arrays, there have been proposals to use MQWs in spatial light modulator applications [40, 41], and a CCD-addressed, linear array of MQW transmission modulators has been demonstrated [42]. Wood et al. have used a GaAs MQW device with a metallic back reflector to operate as a modulator/detector in a bi-directional optical fibre link at up to 600Mbit/s [43].

Considerable thought has also been given to improving the depth of modulation achievable with the normal incidence MQW modulator itself. Incorporating a quarter-wave multilayer stack (MLS) reflector within the epitaxial *p-i-n* diode structure in order to effectively double the interaction length, Boyd et al. succeeded in increasing the on:off ratio in reflection to $\approx 8:1$ [44], compared to the usual $\approx 2:1$ observed in transmission. With refinements in device fabrication, this reflective structure has been operated at up to 5.5 GHz [45].

Attempts to improve performance by simply increasing the thickness of the MQW region in the transmission modulator have met with limited success. An on:off ratio of 10:1 was achieved by Hsu et al., using a 4 μ m-thick structure [46]. However this was at the expense of a large insertion loss, the on-state transmission being only 5%.

The idea of using integrated mirrors to increase interaction of the incident light with the MQWs has been extended. Guy et al [47, 48] proposed using MLS high reflectors as the *p* and *n* regions of the MQW

diode. The high-finesse Fabry-Perot cavity thus formed could then be detuned from resonance using electro-absorptive or electro-refractive effects. Contrast ratios of 20:1 in transmission, and reflection changes of more than 60% were predicted. In reality, it has proved difficult to reproduce modelled performance. High-finesse MQW modulators have been demonstrated [49, 50], but with a maximum contrast of $\approx 8:1$. As a more viable alternative resonant MQW device, the low-finesse, asymmetric cavity has recently been proposed and demonstrated [51] and forms part of the original work described in this thesis.

Returning to the theme of optical interconnects in electronic systems, another goal has been the integration of III-V-based optical devices with Si-based electronics. There are significant problems in accommodating the large lattice mismatch between GaAs and silicon. However, despite high densities of dislocations, GaAs MQW reflection modulators have very recently been demonstrated grown on Si [52], with initially poorer performance compared to those grown on GaAs. The inclusion of MLS reflectors [53, 54] does seem to have beneficial effects on the diode leakage currents. It remains to be seen whether the technological problems can be overcome sufficiently to warrant the direct growth of III-V semiconductor devices on silicon. A second point concerns the drive voltages required for MQW modulators. Integrated with Si electronics, it will be desirable to reduce the required bias to 5V or less, and we shall address this question in later chapters for the standard MQW structure. One alternative suggestion for achieving this reduction, whilst retaining adequate modulation, is the use of a modified MQW structure with coupled pairs of wells [55, 56], where the Stark shift of the MQW absorption edge and the reduction in the peak absorption strength are in principle more sensitive to applied field. The coupled QW structures have, however, yet to show performance comparable to that of the standard uncoupled structures.

Finally, it is worth mentioning the work done on QW waveguide modulators. By guiding light in the plane of the MQW structure, interaction lengths are increased enormously and large on:off ratios can be achieved with few quantum wells, rather small changes in absorption and therefore small applied fields. First demonstrations of GaAs MQW waveguide modulators were by workers at NTT in Japan [57], closely followed by a group at AT&T Bell [58]. The polarization sensitivity of the modulation has been noted [59] and strong phase modulation has been reported [60, 61] due to the refractive index changes which accompany the

field-induced shift of the MQW absorption edge. Many applications have been demonstrated, among them a self-biased waveguide SEED [62], a segmented modulator structure as a wavelength demultiplexer [63], a crossing-channel switch [64], and an integrated laser and external modulator [65]. A comprehensive review of MQW waveguide modulators, covering both physics and devices, has been given by Wood [66].

1.2.4 OTHER QUANTUM WELL MATERIALS

The work on GaAs MQW devices aroused interest in other materials, particularly those with narrower band gaps corresponding to an absorption edge in the 1300-1550nm range, which is important for low-loss optical fibre transmission systems. Initial attention was focussed on the InGaAs (well):InAlAs (barrier) MQW system lattice-matched to transparent InP substrates [67, 68]. Normal-incidence and waveguide modulators [69, 70] were demonstrated with these materials, but showed generally poorer characteristics than GaAs-based devices. This was shown to be not solely dependent on the maturity of the growth technology, but due to strong alloy broadening effects [71] on the excitonic absorption edge.

As an alternative, the InGaAs:InP system has proved popular. Much clearer quantum-confined Stark shifts have been observed in this material system [72] and, again, both normal-incidence and waveguide transmission modulators [73, 74] have been shown to work. However, the exciton absorption edge for this material is fundamentally weaker, and the Stark shift smaller than for GaAs:AlGaAs. Consequently, thicker structures and larger bias voltages must be used to achieve comparable modulation at normal incidence [75]. Just as for GaAs MQWs, SEEDs have been produced in InGaAs: InP [76], as well as modulator arrays [77] and Fabry-Perot cavity devices [78].

Other less well established QW materials are GaSb:AlGaSb [79, 80], which is also compatible with the low-loss fibre window, and InGaAs: GaAs, where the wells are strained and the absorption edge occurs in the 900-1000nm region [81, 82].

More recently there have been moves towards using quaternary materials for long wavelength MQW modulators. By using InGaAsP:InP

[83-85, 87] and InGaAlAs:InAlAs [85-86], the band gap for the well material can be varied independently of the well width, by adjusting the individual group III and group V mole fractions. The absorption changes for a given electric field can thus be significantly increased compared to previous long-wavelength ternary material [85, 87].

1.3 OPTICAL PROPERTIES OF QUANTUM WELLS

In this section we introduce some basic concepts concerning the effects of carrier confinement on the optical properties of quantum wells which are relevant to the discussion in later chapters.

1.3.1 ZERO-FIELD PROPERTIES

If a layer of semiconductor material, with a direct band gap E_{g1} , is grown between layers of another semiconductor, with a larger direct gap E_{g2} , then the conduction and valence bands of the composite structure can appear as in Fig. 1.3.1.1 below. The direction of growth is from left to right, and the layer planes are in the vertical direction.

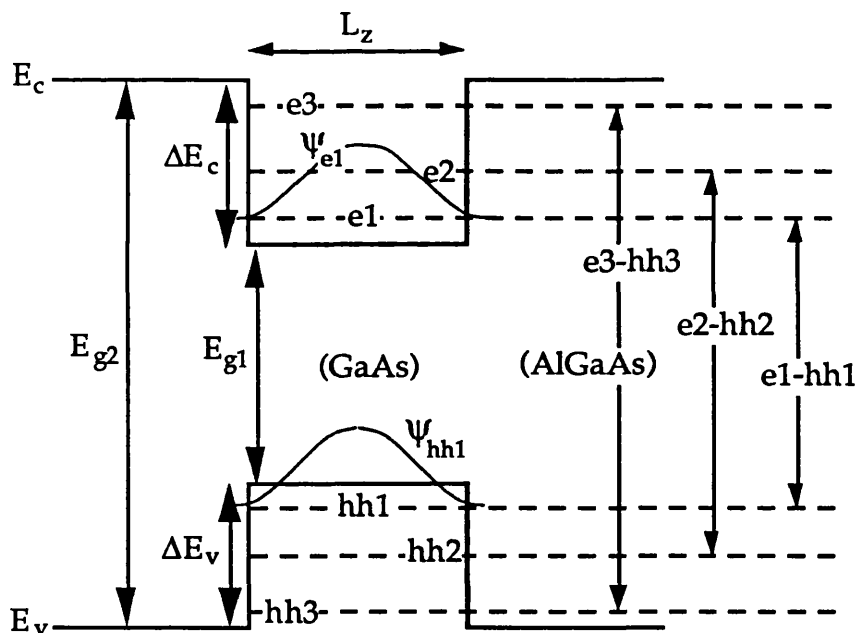


FIGURE 1.3.1.1:

A schematic of the quantized energy levels in a type I quantum well such as occurs in the GaAs-AlGaAs material system.

A potential well is formed in the direction of growth (z) for both electrons and holes in the material of smaller band gap. This configuration of the band offsets is called a Type I quantum well and is typical of the GaAs-AlGaAs material system, where at room temperature the values of E_{g1} and E_{g2} are 1.424eV and 1.798 eV (0.3 Al mole fraction) respectively [88]. The band offsets ΔE_c and ΔE_v have been the subject of much debate over

the last 10 years or so. It is now generally agreed that ΔE_c is $\approx 0.65 (E_{g2} - E_{g1})$ [89], giving a conduction band well depth of $\approx 243\text{meV}$ and a valence band well depth of $\approx 131\text{meV}$.

When the width of the well, L_z , is small ($\leq 200\text{\AA}$), two important effects arise from the confinement of carriers. The first is that electrons and holes are constrained to well-resolved discrete energy levels for motion in the direction normal to the plane of the well layer. These are marked as e1, 2, 3 and hh1, 2, 3 for electrons and heavy holes respectively. Here, for clarity, we have marked only the heavy hole energy levels in the valence band. Another set of levels exists for light holes. Motion in the plane of the layer still retains roughly the character of the bulk material, i.e. pseudo-parabolic continuous energy bands. The z-quantized states represent the lowest lying levels for quasi-2-dimensional sub-bands in a well of finite thickness.

To a first approximation the energy levels, E_{e_n}, E_{hh_n} , can be calculated by solving the Schrödinger equation for a 1-D finite potential well with the appropriate effective mass, $m_{e, hh}$, for electron and holes [8]. Carrier envelope wavefunctions, ψ_e, ψ_{hh} , are sinusoidal in nature inside the well and exponentially decreasing into the barriers. The free particle energy levels are approximately inversely dependent on $m_{e, hh}$ and the square of the well width, L_z^2 . More sophisticated calculations, accounting for effects such as energy-dependent effective masses and the non-parabolicity and intermixing of the valence band states have also been carried out [90].

The probability of absorption at a particular energy is related to the spatial overlap of wavefunctions in the corresponding conduction and valence band states. The *overlap integral* is defined as:

$$M_{e-h} = \left| \int_{-\infty}^{\infty} \psi_e(z) \cdot \psi_h^*(z) dz \right| \quad \dots(1.1)$$

A related quantity is the *oscillator strength* for the optical transition, which ultimately determines the absorption coefficient. This is proportional to the square of the overlap integral.

The important point here is that, unlike in the bulk material (GaAs), only certain direct transitions may be made between valence and conduction bands, such as those marked e1-hh1...en-hhn in Fig. 1.3.1.1, since only the wavefunctions for states of equal index, n, are non-orthogonal. This has a profound effect on the absorption spectrum. The

band gap is now larger than in the bulk, being defined by the e1-hh1 transition, the energy of which is in turn dependent on the well width. There are in fact a series of band edges with increasing energy, one for each of the en-hhn allowed transitions. In a well of finite depth, however small, there is always at least one quantized state in conduction and valence bands.

The effect of quantization is seen in the density of states (d.o.s) for the simple 2-D parabolic band model. In the 3D case the d.o.s is proportional to $\sqrt{(E - E_{g3D})}$, whereas in 2D it becomes constant for each individual sub-band [91]. This is shown below in Fig. 1.3.1.2.

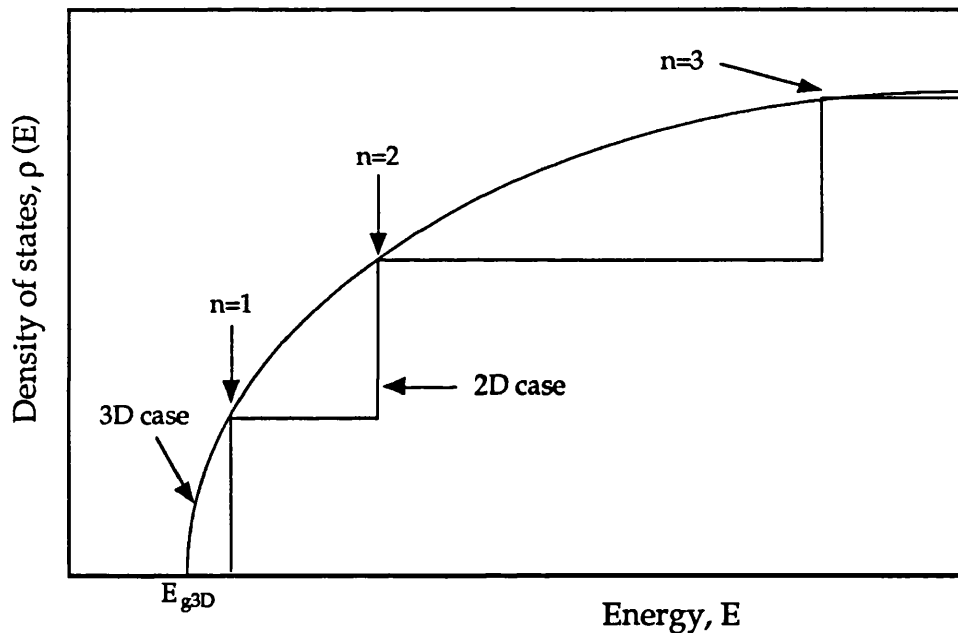


FIGURE 1.3.1.2:
Comparison of the density of states for the simple 2D and 3D models.

The second major effect of carrier confinement is the increase in the binding energy of excitonic states. An exciton is the result of an electron being promoted from the valence band to the conduction band but still remaining bound by Coulomb attraction to the hole left behind. The electron and hole orbit around each other as a hydrogen-like system with a diameter in the bulk of $\approx 300\text{\AA}$. The energy required to create an exciton is less than the en-hhn gap by an amount equal to the exciton binding energy, E_{exc} . Thus the lowest energy for absorption in the QW becomes (referring to Fig. 1.3.1.1):

$$E_{gQW} = E_{g1} + E_{e1} + E_{hh1} - E_{exc} \quad \dots(1.2)$$

In bulk materials excitons can be observed at low temperatures [92], but the effects are washed out by phonon ionization of the bound e-h pair as temperature is increased. In a quantum well of $\approx 100\text{\AA}$ width the spatial extent of the exciton is obviously reduced in the z-direction by the effect of the confining potential, but it also contracts in the plane of the layer [93]. The shrinking of the exciton volume compared to the bulk thus increases the binding energy and reduces the probability for phonon ionization. In the exact 2D limit the binding energy should be 4 times the 3D value [94]. Theoretical calculations by a number of authors predict values of $\approx 7\text{--}10\text{meV}$ for wells in the $50\text{--}150\text{\AA}$ thickness range [16, 95, 96]. The increased overlap of electron and hole wavefunctions produces a larger oscillator strength. Hence the observation of strong excitonic effects at room temperature. The reduced dimensionality also increases the exciton to continuum height ratio [94].

The combination of enhanced exciton oscillator strength and the step-like density of states results in an absorption spectrum as shown in Fig 1.3.1.3. The data were recorded at room temperature ($\approx 294\text{ K}$).

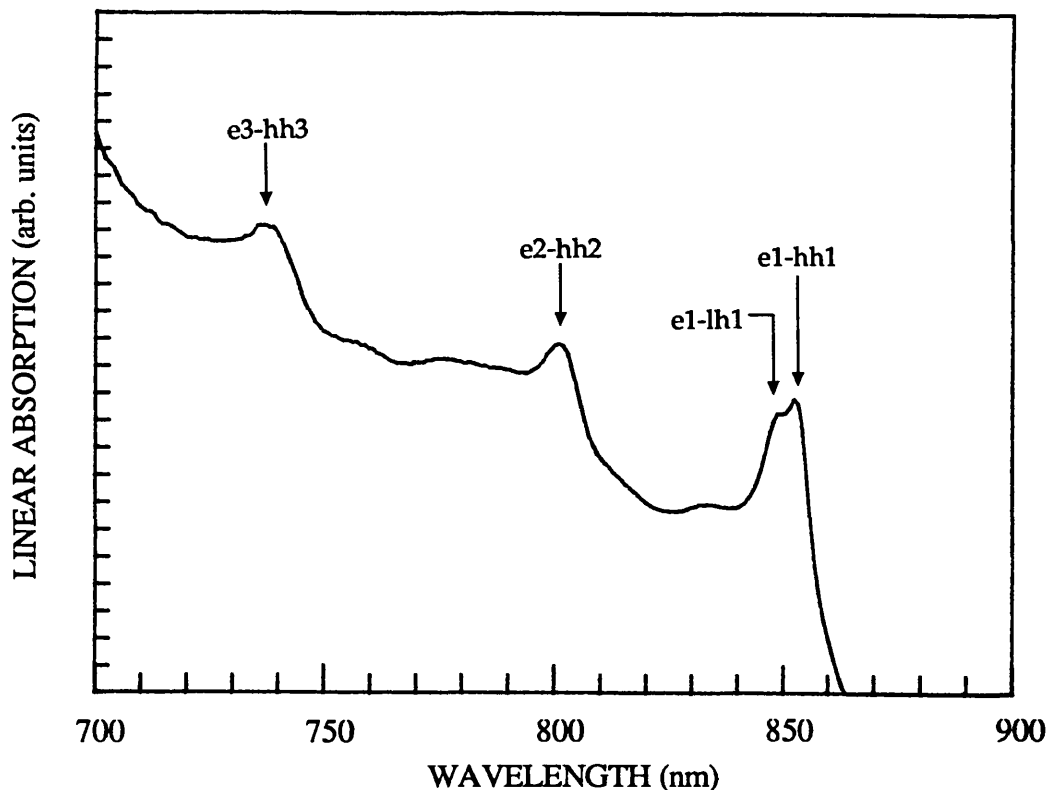


FIGURE 1.3.1.3:

Absorption spectrum for a MQW structure containing $\approx 100\text{\AA}$ wells. Sample grown by Dr. Karl Woodbridge at Philips Research Labs., Redhill.

Absorption for the $n=1, 2$ and 3 sub-bands can clearly be identified, with excitonic peaks at the edge of each. At the $n=1$ edge a double exciton peak is observed due to the splitting of the valence band into heavy and light hole levels. Note that the absorption edge occurs at $\approx 850\text{nm}$, compared to $\approx 870\text{nm}$ for the bulk material. Absorption coefficients and oscillator strengths have been experimentally determined at low temperatures by Masselink et al [97] for a range of well widths.

In the chapters which follow we shall generally identify well widths from the wavelength of the e1-hh1 exciton peak measured at room temperature. The theoretical curves, in Fig. 1.3.1.4 below, show how the e1-hh1 peak shifts with well width. The solid and dashed lines are for Al mole fractions of 0.3 and 0.4 respectively in the AlGaAs barriers. The calculation was carried out by Peter Stevens (UCL) using a tunnelling resonance numerical model [98] to determine confinement energies, and incorporating a fitted exciton binding energy variation [99].

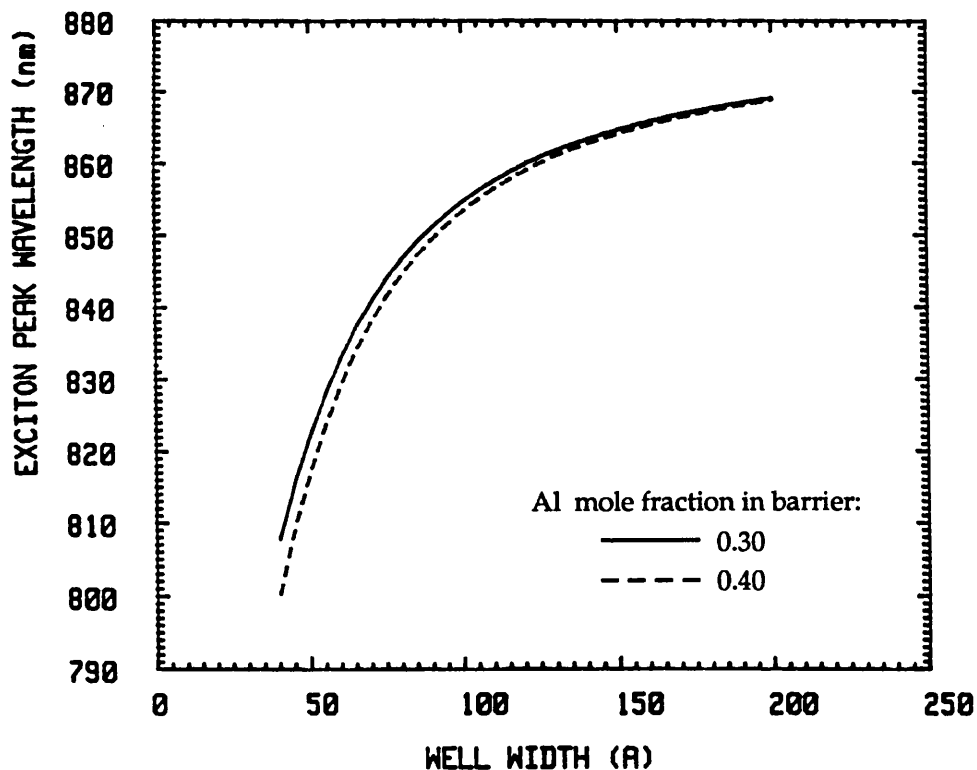


FIGURE 1.3.1.4:

Variation of the wavelength of the band-edge e1-hh1 exciton absorption peak at room temperature. Calculation carried out by Peter Stevens, UCL.

We note that the slope of the curve increases markedly as the well width is narrowed. Thus we should expect larger exciton linewidth broadening effects due to fluctuations in the well width for narrow wells. These

fluctuations cannot be completely eradicated in real QW samples, and generally are of the order of 1 monolayer or 2.8\AA (r.m.s) [100].

1.3.2 ELECTRO-ABSORPTION IN QUANTUM WELLS – THE QUANTUM-CONFINED STARK EFFECT

The effect of an electric field applied normal to the plane of a quantum well is shown schematically in Fig. 1.3.2.1. The potential profile of the well is skewed so that the carriers no longer see rectangular barriers on either side. Electron and hole wavefunctions are polarized in opposite directions. On the low energy side of the well the barrier becomes effectively triangular. As a result of this change in the shape of the potential, the energies of the lowest confined levels for electrons and holes decrease relative to the bottom of the well.

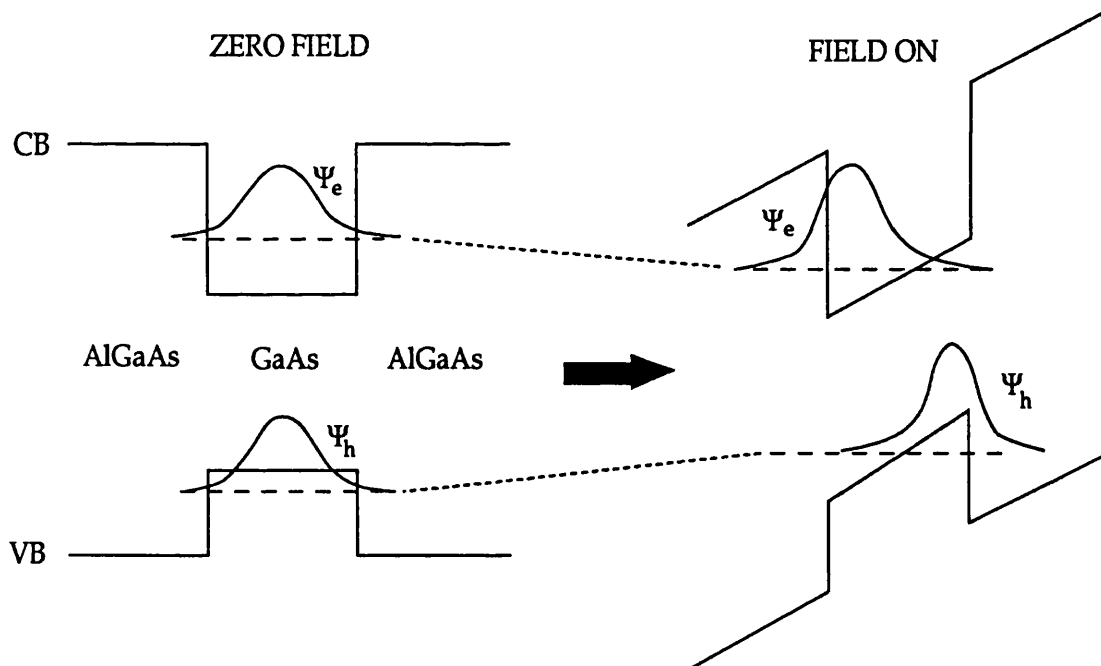


FIGURE 1.3.2.1:

The effect of an applied electric field on the lowest-lying energy levels in a quantum well.

The shift of the sub-band levels is a direct consequence of the quantum well structure and is qualitatively different from the Franz-Keldysh electro-absorption observed in bulk semiconductors [101], which is dominated by field-induced tunnelling broadening effects rather than an

actual shift of the edge.

Because there is still a barrier to free movement of carriers in the direction perpendicular to the well, the tunnelling time out of the well for electrons and holes still remains significantly longer than the characteristic exciton ionization time. This maintains the Coulomb interaction between electrons and holes, and thus the exciton binding energy and oscillator strength are retained to a large degree even at quite high fields ($\approx 2 \times 10^5$ V/cm). As the exciton peak largely maintains its position relative to the sub-band edge with increasing field, the net effect is a strong shift of the whole absorption edge, with maximum absorption changes of 10-50 times those seen in bulk GaAs for equivalent fields. A qualitative picture is given below in Fig. 1.3.2.2.

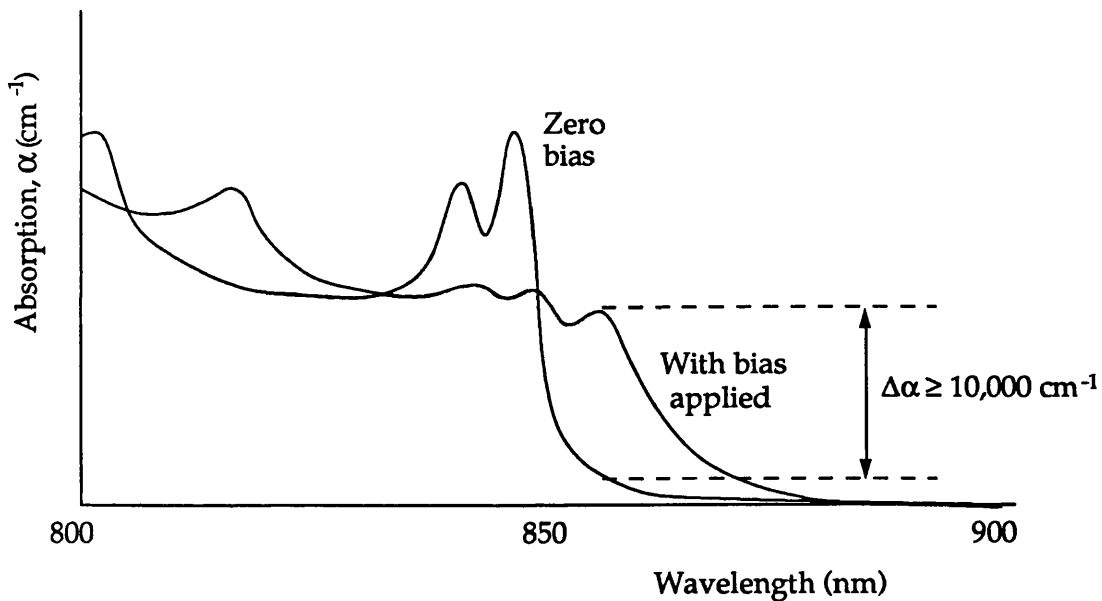


FIGURE 1.3.2.2:

The effect of an applied electric field on the absorption edge in a quantum well.

With light at a wavelength coincident with the foot of the unbiased absorption edge, *bias absorbing* modulation is achieved. If the input light is at the e1-hh1 exciton peak, then the modulation is *bias transmitting*. To achieve significant modulation it is necessary to use a multiple quantum well structure, consisting typically of 50-100 wells.

This enhanced electro-absorption was first observed by Chemla et al [23] and interpreted theoretically by D. A. B. Miller et al [102, 103], who named it the "quantum-confined Stark effect" (QCSE). Since the initial experimental observations, considerable theoretical and experimental

effort has been devoted to researching various aspects of the QCSE in greater detail. The Stark shift of energy levels has been calculated using, for example, the exact Airy function approach [104-106], tunnelling resonance [103, 107], and a Monte Carlo method [108]. Brum and Bastard [109] have analysed exciton dissociation in an applied field. It has also been shown that in the limit of very wide quantum wells the bulk Franz-Keldysh electro-absorption is recovered from a QCSE model [110]. Various attempts have been made to model the effects of an electric field on the absorption spectrum [111-114]. However, only the work of Stevens et al [98], which incorporates important exciton line broadening effects, bears comparison with experimental data. Due presumably to the difficulties in fabricating structures to measure electro-absorption directly in the GaAs-AlGaAs system, the majority of detailed experimental investigations of the QCSE have been via associated properties such as electro-reflectance [115, 116], photoluminescence [117-119] and photocurrent [120-122]. Electro-absorption and the associated electro-refraction have been determined from electro-reflectance spectra by Kan et al. [114]. Using a combination of biased transmission and photocurrent data, Wood has derived band-edge absorption spectra for MQW waveguides [123]. D. A. B Miller et al have obtained experimental evidence for electro-absorption sum rules [124] from waveguide transmission data. Our own photocurrent measurements (see Chapters 2 & 3) confirm the absorption conservation to a high degree of accuracy [125].

Important in the optimization of the QCSE for optical modulation is the width of the quantum wells used. In Chapter 4 we shall address this problem experimentally [126]. A simple second-order perturbation calculation for an infinitely deep well [18] shows that the energy shift of the lowest confined state is proportional to the fourth power of the well width (and also the square of the applied field). Figure 1.3.2.3 shows a numerical calculation of the field-induced shift of the $e1-hh1$ exciton peak for well widths in the range 50-150Å. At a field of 100 kV/cm the shift for a 50Å well is only ≈ 2 nm, whereas the corresponding shift for a 150Å well is more than 35nm. However, the size of the Stark shift is not the sole influence on the choice of well width. We must also consider how much of the exciton absorption is retained as it is shifted. Fig. 1.3.2.4 shows a calculation of the field effect on the exciton peak height for a 100Å quantum well. The absorption is proportional to the square of the

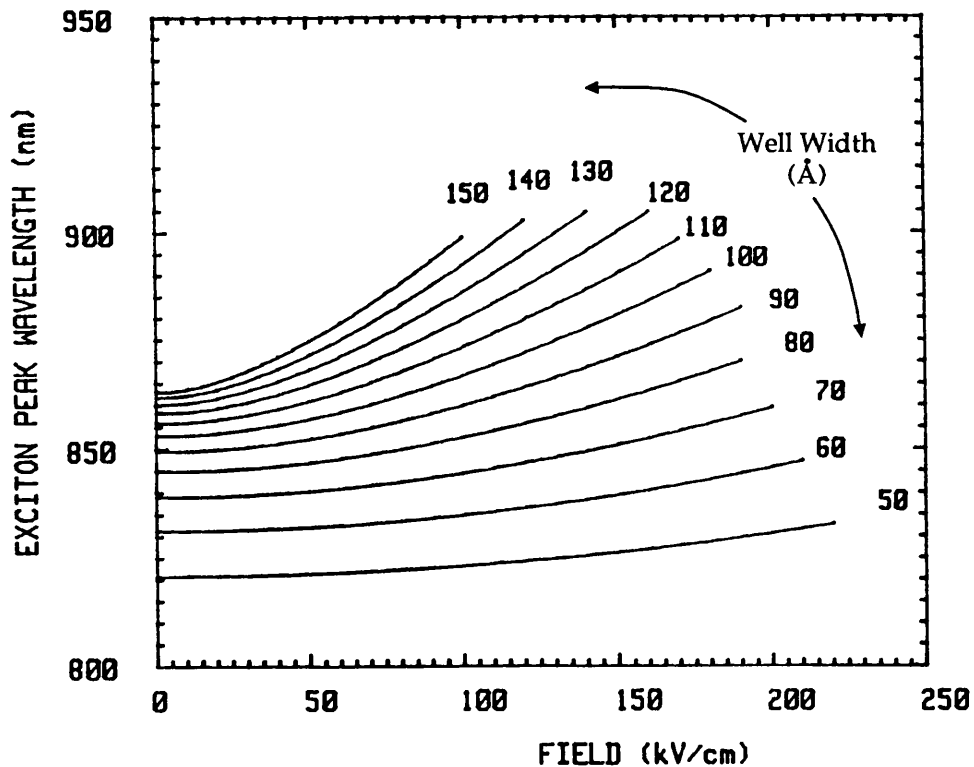


FIGURE 1.3.2.3: Illustrating how the sensitivity of the quantum-confined Stark shift to electric field increases with well width. Calculation carried out by Peter Stevens, UCL.

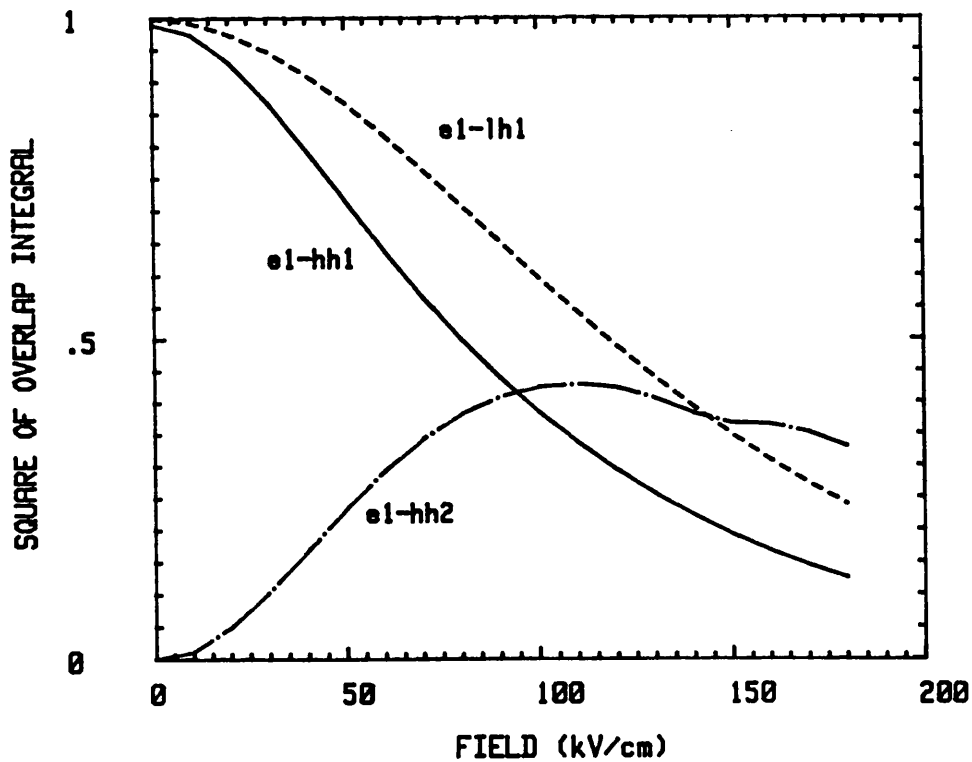


FIGURE 1.3.2.4: Reduction of the overlap integral for the band-edge e1-hh1, e1-lh1 excitons with increasing electric field for a well width of 100Å. This is reflected in the loss of absorption in the Stark-shifted edge. Calculation carried out by Peter Stevens, UCL.

overlap integral, and we see that this quantity falls significantly with field for the e1-hh1 and e1-lh1 excitons. These are the normally "allowed" zero-field transitions. Notice that as these transitions fall, the e1-hh2 exciton (which is the closest in energy) gains strength. At zero field, this transition is "forbidden" since the electron and hole wavefunctions are orthogonal. With the tilting of the well, as field is applied, there is a spatial redistribution of wavefunctions resulting in increased oscillator strength for these previously forbidden excitons. As well width increases, the unbiased e1-hh1 exciton peak absorption falls due to a reduced overlap integral. Furthermore, the wider the well the larger the possible spatial separation of electrons and holes when a field is applied. Thus the oscillator strength of the e1-hh1 exciton is lost more rapidly with field. A detailed assessment of MQW electro-absorption as a function of well width has recently been carried out by Jelley et al [127].

1.4 THE MULTIPLE QUANTUM WELL $p-i-n$ DIODE

1.4.1 GENERAL DESIGN CONSIDERATIONS

The most suitable method of applying high fields across MQW structures with a total thickness of $\approx 1\mu\text{m}$ is to embed the wells in the i -region of a $p-i-n$ diode. This is the method employed by Wood et al. [13] for the first demonstration of normal-incidence MQW transmission modulator. Prior to this, Schottky barrier diodes had been used to observe the effect of an electric field on photoluminescence from QWs [17]. However, that type of structure requires a semi-transparent metallic contact in order to apply the field to the area on which the light is incident, which would cause a significant insertion loss for a transmissive device. Fig. 1.4.1 shows the typical MQW $p-i-n$ layer structure, which is also discussed from a growth point of view in § 2.2.3.

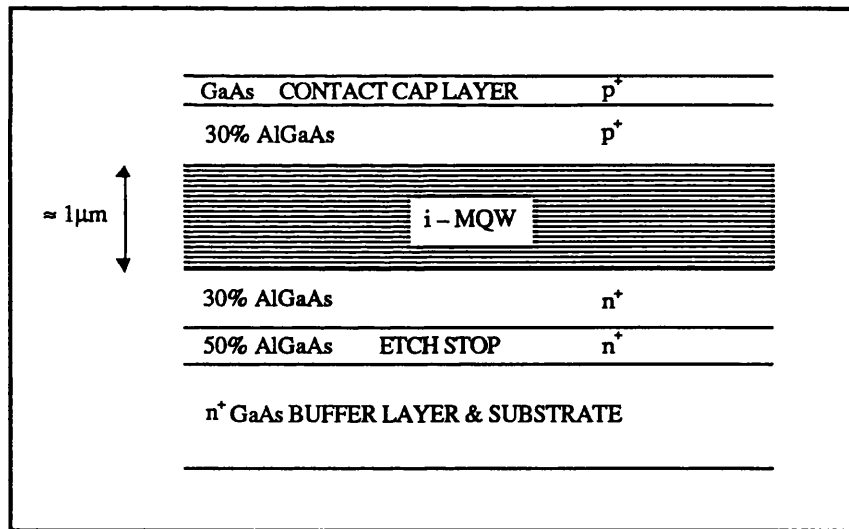


FIGURE 1.4.1: The MQW $p-i-n$ diode layer structure.

Alloyed ohmic contacts on exposed GaAs surfaces, top and bottom, allow low resistance electrical connection to the MQW region via the highly-doped, AlGaAs cladding layers either side of the MQWs. This means that the voltage applied to the whole $p-i-n$ diode is only dropped across the MQWs, so that if their total thickness is around $1\mu\text{m}$, the necessary field for a useful Stark shift ($\approx 50\text{-}100\text{ kV/cm}$) can be produced with only $5\text{-}10\text{V}$ bias. Leakage currents are typically reduced to sub-nanoamp levels by

etching the *p-i-n* structure away outside the contacted area, to leave a small mesa.

The etch stop layer is provided so that the GaAs substrate material, which is absorbing at the wavelengths where modulation occurs for quantum wells, can be selectively removed with a chemical etch (see § 4.2.1). Thus, modulated light, propagating normal to the MQW layers, can be detected on passing through the device, with little background attenuation in the unbiased state since the absorption edge for the 30% AlGaAs [88] is more than 250nm lower than that of the MQWs.

Doping levels in the contact regions should be made as high as possible (generally 10^{18} cm^{-3}), in order to reduce the depletion depth in the AlGaAs layers, which will lead to lowered fields for a given bias, and thus smaller Stark shifts. In addition, the doping in the MQW region must be low to achieve a uniform electric field and thus avoid broadening of the shifted MQW excitonic absorption edge, caused by each well seeing a different electric field.

Besides being a convenient way of applying the electric field, the *p-i-n* structure is compatible with high-frequency operation [24, 45] and offers the additional feature of high quantum efficiency photodetection [33, 34].

1.4.2 EFFECT OF BACKGROUND DOPING ON FIELD UNIFORMITY

Assuming that the *p* and *n* regions are highly doped, the average field across the undoped (MQW) region of the diode for a given bias, *V*, is simply $E_{av} = V/d$, where *d* is the thickness of the undoped region. However, with a finite background doping density, N_i , the field will fall off from a maximum value, with a slope proportional to N_i , the direction depending on whether the background is *p* or *n*-type. The higher the level of background doping, the higher the maximum field which occurs at the edge of the intrinsic region for a given bias voltage. This comes about simply because the integral of the electric field over the full depletion width must remain constant, and equal to the voltage, while at the same time the slope of the field is increasing. The effect is to reduce the voltage at which the breakdown field of the material is reached.

In Fig. 1.4.2 (over the page) the electric field profile has been modelled for a *p-i-n* structure with decreasing intrinsic doping, going from (a) to (c). The *i*-region is $1\mu\text{m}$ thick and the doping in the *p* and *n* regions is 10^{18} cm^{-3} . In each case the field is plotted for 0-8V bias in 2V steps.

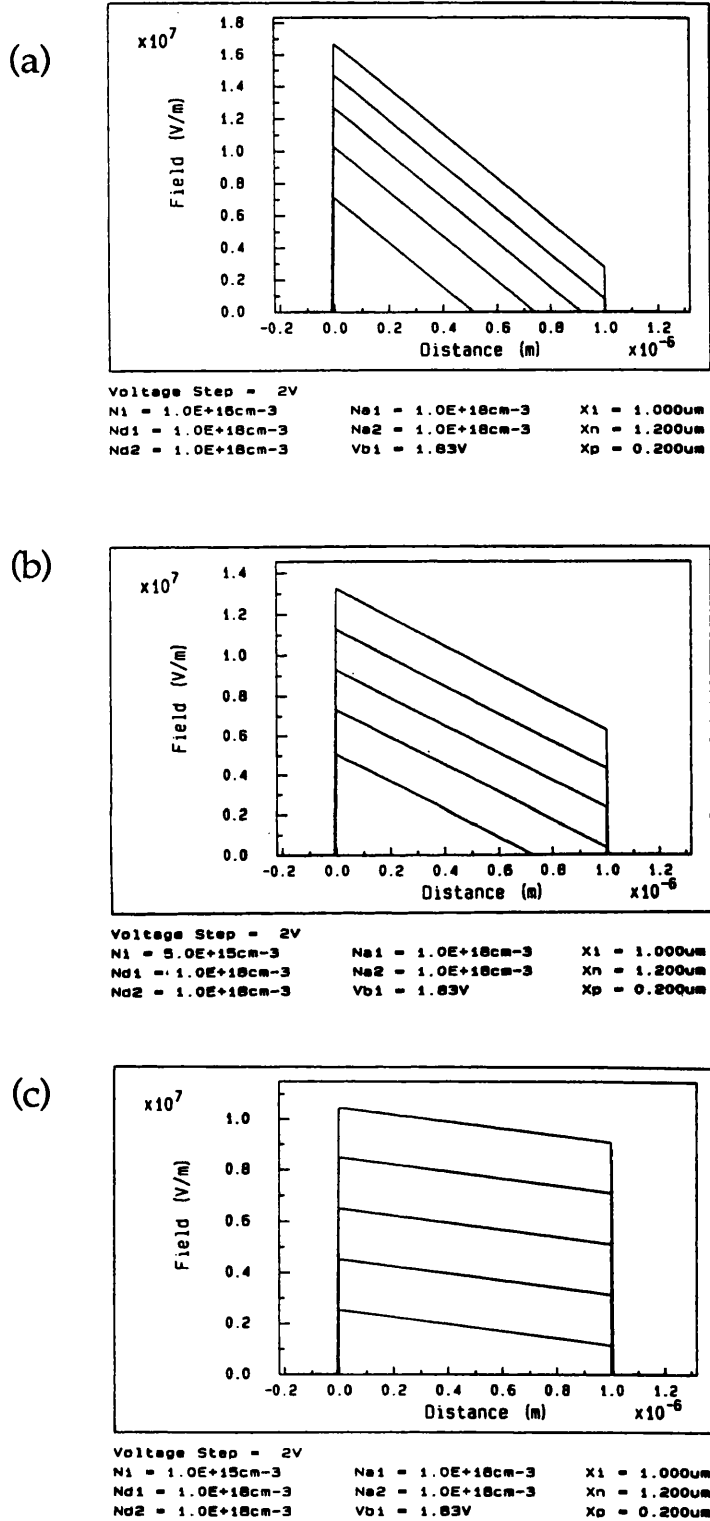


FIGURE 1.4.2:
 Calculated electric field profiles in a *p-i-n* diode with different background doping levels. (a) $1 \times 10^{16} cm^{-3}$, (b) $5 \times 10^{15} cm^{-3}$, (c) $1 \times 10^{15} cm^{-3}$. Figures by kind permission of Craig Tombling. Note the changes of scale on the field axis.

The calculation is carried out in the standard way [128], using Poisson's equation, matching fields at the $p-i$ and $i-n$ boundaries, and applying the conservation of space-charge.

These figures illustrate how the slope of the field remains fixed with increasing bias, so that as the peak field increases, the field variation as a fraction of E_{av} becomes smaller. Note that the variation in the field is down to only $\approx \pm 7\%$ of E_{av} for the highest biases at the lowest background doping level of $1 \times 10^{15} \text{ cm}^{-3}$, whereas at the higher doping levels the variations are $\approx \pm 50\%$ and $\approx \pm 72\%$ respectively. So we must obviously be looking for devices with a background doping level in the region of $1 \times 10^{15} \text{ cm}^{-3}$ for good performance.

1.4.3 EFFECT OF FIELD NON-UNIFORMITY ON ELECTRO-ABSORPTION

In this last section we consider just how the background doping affects the electro-absorption characteristics via the field-variation across the MQW structure. Figs. 1.4.3.1-4 below show calculated absorption spectra for a range of bias voltages and background doping levels. The model used is one mentioned previously [98], which incorporates the exciton broadening due to both well width fluctuations and field variation, and has been shown to give good agreement with experiment. The MQW structure is $\approx 1 \mu\text{m}$ thick in total, with 100 \AA GaAs wells and 60 \AA $\text{Al}_{0.3}\text{Ga}_{0.7}\text{As}$ barriers, which is typical of the devices which we shall investigate.

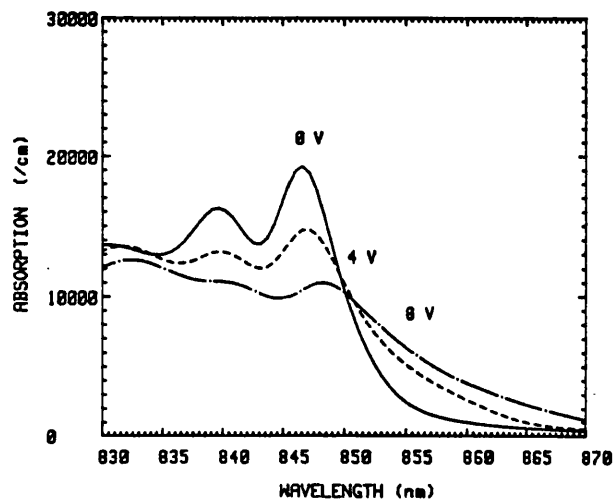


FIGURE 1.4.3.1: Modelled MQW absorption spectra for $1 \times 10^{16} \text{ cm}^{-3}$ background doping.

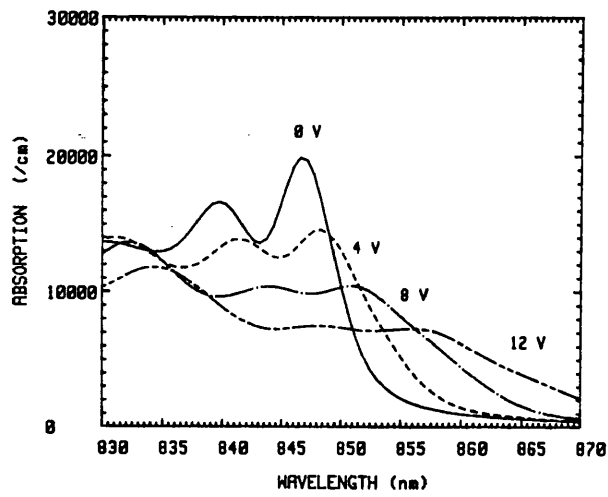


FIGURE 1.4.3.2: Modelled MQW absorption spectra for $5 \times 10^{15} \text{ cm}^{-3}$ background doping.

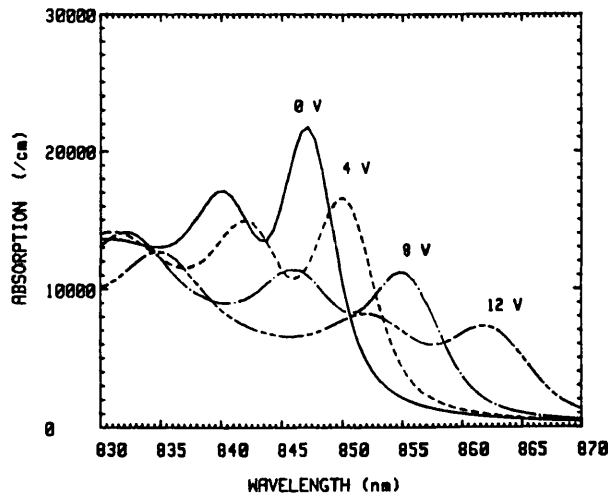


FIGURE 1.4.3.3: Modelled MQW absorption spectra for $1 \times 10^{15} \text{ cm}^{-3}$ background doping.

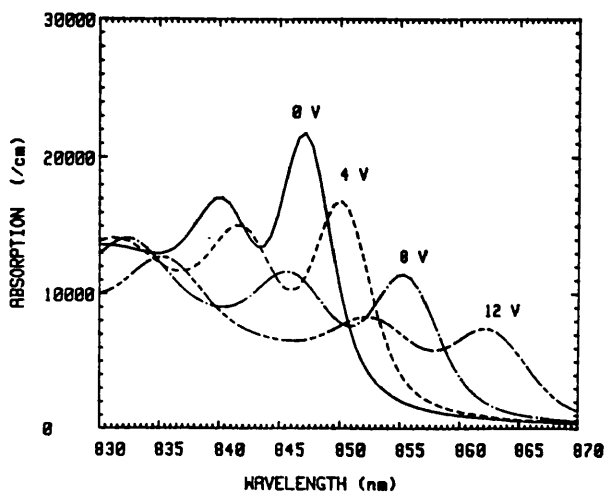


FIGURE 1.4.3.4: Modelled MQW absorption spectra for $1 \times 10^{14} \text{ cm}^{-3}$ background doping.

What can clearly be seen from these figures is that reducing the background doping from 10^{16} cm^{-3} to 10^{15} cm^{-3} has marked effect on the appearance of the shifted exciton peaks. The higher the doping the more quickly the peaks flatten and broaden, and the smaller the apparent shift since the strongest contribution to the sum of absorption from all the wells will come from those wells in the low field region of the intrinsic region, where the excitons retain their oscillator strength. This problem has been given some consideration by Newson and Kurobe [129], who assessed the doping broadening effect on the Stark shift, but stopped short of calculating the resultant spectra. Very recently, Little et al. have clearly observed field inhomogeneity effects in low temperature photocurrent spectra from MQW structures [130].

In Fig. 1.4.3.1, with 10^{16} cm^{-3} , the doping broadening is severely limiting the maximum absorption change off the edge, the largest changes occur at the wavelength of the unbiased e1-hh1 exciton peak. Reducing the doping by a factor of two begins to reveal the true QCSE. In Fig. 1.4.3.2. an exciton peak can still be seen, shifted to $\approx 857\text{nm}$, with 12V bias. Once the doping is as low as 10^{15} cm^{-3} , then the excitons remain clearly resolved even at the highest bias (equivalent to an average field of $\approx 120 \text{ kV/cm}$). This of course gives us the largest possible electro-absorptive changes. Comparing Figs. 1.4.3.3 and 1.4.3.4, it is interesting to note that reducing the doping by an order of magnitude further apparently has no effect on the quality of the electro-absorption spectra.

Thus for wells of $\approx 100\text{\AA}$ and $1\mu\text{m}$ total MQW thickness we have found the target background doping level of $\approx 10^{15} \text{ cm}^{-3}$ for optimum electro-absorption.

REFERENCES (Chapter 1)

- [1] L. ESAKI and R. TSU, "Superlattice and negative differential conductivity in semiconductors", IBM J. Res. Develop., Jan.1970, pp. 61-65.
- [2] R. de L. KRÖNIG and W. G. PENNEY, "Quantum mechanics of electrons in crystals", Proc. Roy. Soc. (1930), A130, pp. 499-513.
- [3] H. KRESSEL and H. NELSON, RCA Review (1969), 30, p. 106
- [4] A. Y. CHO, "Morphology of epitaxial growth of GaAs by a molecular beam method: the observation of surface structures", J. Appl. Phys. (1970), 41, p.2780.
- [5] H. MANASEVIT, "Single crystal GaAs on insulating substrates", Appl. Phys. Lett. (1968), 12, p.156.
- [6] A. Y. CHO, "Growth of periodic structures by the molecular beam method", Appl. Phys. Lett. (1971), 19, pp. 467-8.
- [7] L. ESAKI and L. L. CHANG, "New transport phenomenon in a semiconductor "superlattice"", Phys. Rev. Lett. (1974), 33, pp. 495-8.
- [8] R. DINGLE, W. WIEGMANN and C. H. HENRY, "Quantum states of confined carriers in very thin $\text{Al}_x\text{Ga}_{1-x}\text{As-GaAs-Al}_x\text{Ga}_{1-x}\text{As}$ heterostructures", Phys. Rev. Lett. (1974), 33, pp. 827-30.
- [9] J. P. VAN der ZIEL, R. DINGLE, R. C. MILLER, W. WIEGMANN and W. A. NORDLAND JR., "Laser oscillation from quantum states in very thin $\text{GaAs-Al}_{0.2}\text{Ga}_{0.8}\text{As}$ multilayer structures", Appl. Phys. Lett. (1975), 26, pp. 463-5.
- [10] R. D. DUPUIS, P. D. DAPKUS, N. HOLONYAK JR., E. A. REZEK and R. CHIN, "Room-temperature laser operation of quantum-well $\text{Ga}_{(1-x)}\text{Al}_x\text{As-GaAs}$ laser diodes grown by metalorganic chemical vapour deposition", Appl. Phys. Lett. (1978), 32, pp. 295-7.
- [11] R. DINGLE, H. L. STÖRMER, A. C. GOSSARD AND W. WIEGMANN, " Electron mobilities in modulation-doped semiconductor heterojunction superlattices", Appl. Phys. Lett. (1978), 33, pp. 665-7.
- [12] T. MIMURA, S. HIYAMIZU, T. FUJII, and K. NANBU, "A new field-effect transistor with selectively doped $\text{GaAs/n-Al}_x\text{Ga}_{1-x}\text{As}$ heterojunctions", Jpn. J. Appl. Phys. (1980), 19, L225-7.
- [13] T. H. WOOD, C. A. BURRUS, D. A. B. MILLER, D. S. CHEMLA, T. C. DAMEN, A. C. GOSSARD and W. WIEGMANN, "High speed optical modulation with GaAs/GaAlAs quantum in a *p-i-n* diode structure", Appl. Phys. Lett. (1984), 44, pp. 16-18.

- [14] T. ISHIBASHI, S. TARUCHA and H. OKAMOTO, "Exciton associated optical absorption spectra of AlAs/GaAs superlattices at 300K", *Int. Symp. GaAs and Related Compounds, Inst. Phys. Conf. Series No.63* (1981), pp. 587-8.
- [15] G. BASTARD, "Superlattice band structure in the envelope-function approximation", *Phys. Rev. B* (1981), **24**, pp. 5693-7.
- [16] G. BASTARD, E. E. MENDEZ, L. L. CHANG and L. ESAKI, "Exciton binding energy in quantum wells", *Phys. Rev. B* (1982), **26**, pp. 1974-9.
- [17] E. E. MENDEZ, G. BASTARD, L. L. CHANG and L. ESAKI, "Effect of an electric field on the luminescence of GaAs quantum wells", *Phys. Rev. B* (1982), **26**, pp. 7101-4.
- [18] G. BASTARD, E. E. MENDEZ, L.L. CHANG and L. ESAKI, "Variational calculations on a quantum well in an electric field", *Phys. Rev. B* (1983), **28**, pp. 3241-5.
- [19] M. YAMANISHI and I. SUEMUNE, "Quantum mechanical size effect modulation light sources – A new field effect semiconductor laser or light emitting device", *Jpn. J. Appl. Phys.* (1983), **22**, pp. L22-L24.
- [20] D. A. B. MILLER, D. S. CHEMLA, D. J. EILENBERGER, P. W. SMITH, A. C. GOSSARD and W. T. TSANG, "Large room-temperature optical nonlinearity in GaAs/Ga_xAl_{1-x}As multiple quantum well structures", *Appl. Phys. Lett.* (1982), **41**, pp. 679-81.
- [21] D. A. B. MILLER, D. S. CHEMLA, D. J. EILENBERGER, P. W. SMITH, A. C. GOSSARD and W. WIEGMANN, "Degenerate four-wave mixing in room temperature GaAs/GaAlAs multiple quantum well structures", *Appl. Phys. Lett.* (1983), **42**, pp. 925-7.
- [22] S. S. TARNG, H. M. GIBBS, J. L. JEWELL, N. PEYGHAMBARIAN, A.C. GOSSARD, T. VENKATESAN, W. WIEGMANN, "Use of a diode laser to observe room-temperature, low-power optical bistability in a GaAs-AlGaAs etalon", *Appl. Phys. Lett.* (1984), **44**, pp. 360-1.
- [23] D. S. CHEMLA, T. C. DAMEN, D. A. B. MILLER, A. C. GOSSARD and W. WIEGMANN, "Electroabsorption by Stark effect on room-temperature excitons in GaAs/GaAlAs multiple quantum well structures", *Appl. Phys. Lett.* (1983), **42**, pp. 864-6.
- [24] T. H. WOOD, C. A. BURRUS, D. A. B. MILLER, D. S. CHEMLA, T. C. DAMEN, A. C. GOSSARD and W. WIEGMANN, "131ps optical modulation in semiconductor multiple quantum wells (MQW's)", *IEEE J. Quantum Electron.* (1985), **QE-21**, pp. 117-8.
- [25] D. A. B. MILLER, "Quantum wells for optical information processing", *Opt. Eng.* (1987), **26**, pp. 368-72.
- [26] J. SINGH, S. HONG, P. K. BHATTACHARYA, R. SAHAI, C. LASTUFKA and H. R.

- SOBEL, "System requirements and feasibility studies for optical modulators based on GaAs/AlGaAs multiquantum well structures for optical processing", *J. Lightwave Technol.* (1988), **LT-6**, pp. 818-31.
- [27] J. E. MIDWINTER, "Digital optics, smart interconnect or optical logic?", *Phys. Technol.* (1988), **19**, pp 101-108, 153-165.
- [28] H. S. HINTON, "Architectural considerations for photonic switching networks", *IEEE J. Selected Areas in Communications* (1988), **6**, pp. 1209-26.
- [29] J. E. MIDWINTER, "Photonic switching technology: Component characteristics versus network requirements", *J. Lightwave Tech.* (1988), **6**, pp. 1512-19.
- [30] D. A. B. MILLER, "Optics for low-energy communication inside digital processors: quantum detectors, sources and modulators as efficient impedance converters", *Opt. Lett.* (1989), **14**, pp. 146-8.
- [31] J. W. GOODMAN, "Switching in an optical interconnect environment", *OSA Proceedings on Photonic Switching*, J. E. Midwinter and H. S. Hinton Eds. (Optical Soc. of America 1989), **3**, pp. 164-9.
- [32] H. S. HINTON, "Relationship between the hardware required for photonic switching and optical computing based on free-space digital optics", *ibid*, **3**, pp. 184-91.
- [33] T. H. WOOD, C. A. BURRUS, A. H. GNAUCK, J. M. WIESENFELD, D. A. B. MILLER, D. S. CHEMLA and T. C. DAMEN, "Wavelength-selective voltage-tunable photodetector made from multiple quantum wells", *Appl. Phys. Lett.* (1985), **47**, pp. 190-2.
- [34] D. A. B. MILLER, D. S. CHEMLA, T. C. DAMEN, A. C. GOSSARD, W. WIEGMANN, T. H. WOOD and C.A. BURRUS, "Novel hybrid optically bistable switch: The quantum well self-electro-optic effect device", *Appl. Phys. Lett.* (1984), **45**, pp. 13-15.
- [35] D. A. B. MILLER, J. E. HENRY, A. C. GOSSARD AND J. H. ENGLISH, "Integrated quantum well self-electro-optic effect device: 2x2 array of optically bistable switches", *Appl. Phys. Lett.* (1986), **49**, pp. 821-3.
- [36] P. WHEATLEY, P. J. BRADLEY, M. WHITEHEAD, J. E. MIDWINTER, G. PARRY, P. MISTRY, M. A. PATE and J. S. ROBERTS, "Novel nonresonant optoelectronic logic device", *Electron. Lett.*, **23**, pp. 92-3.
- [37] A. L. LENTINE, H. S. HINTON, D. A. B. MILLER, J. E. HENRY, J. E. CUNNINGHAM and L. M. F. CHIROVSKY, "Symmetric self-electro-optic effect device: Optical set-reset latch", *Appl. Phys. Lett.* (1988), **52**, pp. 1419-21.
- [38] L. M. F. CHIROVSKY, L. A. D'ASARO, C. W. TU, A. L. LENTINE, G. D. BOYD and D. A. B. MILLER, "Batch-fabricated symmetric self-electro-optic effect devices", *OSA*

Proceedings on Photonic Switching, J. E. Midwinter and H. S. Hinton Eds. (Optical Soc. of America 1989), 3, pp. 2-6.

- [39] F. B. McCORMICK, A. L. LENTINE, L. M. F. CHIROVSKY and L. A. D'ASARO, "All-optical shift register using symmetric self-electro-optic effect devices", *ibid*, 3, pp. 2-6.
- [40] W. D. GOODHUE, B. E. BURKE, K. B. NICHOLS, G. M. METZE and G. D. JOHNSON, "Quantum -well charge-coupled devices for charge-coupled device-addressed multiple-quantum-well spatial light modulators", *J. Vac. Sci. Technol.* (1986), B4, pp. 769-72.
- [41] U. EFRON, T. Y. HSU, J. N. SCHULMAN, W. Y. WU, I. ROUSE, I. J. D'HAENENS and Y.-C. CHANG, "Multiple quantum well -based spatial light modulators", *Proc. SPIE (Quantum well and superlattice physics, 1987)*, 792, pp. 197-207.
- [42] K. B. NICHOLS, B. E. BURKE, B. F. AULL, W. D. GOODHUE, B. F. GRAMSTORFF, C. D. HOYT and A. VERA, "Spatial light modulators using charge-coupled-device addressing and electroabsorption effects in GaAs/AlGaAs multiple quantum wells", *Appl. Phys. Lett.* (1988), 52, pp. 1116-8.
- [43] T. H. WOOD, E. C. CARR, B. L. KASPER, R. A. LINKE, C. A. BURRUS and K. L. WALKER, "Bidirectional fibre-optical transmission using a multiple-quantum-well (MQW) modulator/detector", *Electron. Lett.* (1986), 22, pp. 528-9.
- [44] G. D. BOYD, D. A. B. MILLER, D. S. CHEMLA, S. L. McCALL, A. C. GOSSARD and J. H. ENGLISH, "Multiple quantum well reflection modulator", *Appl. Phys. Lett.* (1987), 50, pp. 1119-21.
- [45] G. D. BOYD, J. E. BOWERS, C. E. SOCCOLICH, D. A. B. MILLER, D. S. CHEMLA, L. M. F. CHIROVSKY, A. C. GOSSARD and J. H. ENGLISH, "5.5 GHz multiple quantum well reflection modulator", *Electron. Lett.* (1989), 25, pp. 558-60.
- [46] T. Y. HSU, W. Y. WU and U. EFRON, "Amplitude and phase modulation in a 4 μ m-thick GaAs/AlGaAs multiple quantum well modulator", *Electron. Lett.* (1988), 24, pp. 603-4.
- [47] D. R. P. GUY, N. APSLEY, L. L. TAYLOR, S. J. BASS and P. C. KLIPSTEIN, "Theory of an electro-optic modulator based on quantum wells in a semiconductor étalon", *Proc. SPIE (Quantum well and superlattice physics, 1987)*, 792, pp. 189-196.
- [48] D. R. P. GUY and N. APSLEY, "Optical devices using III-V quantum wells and multilayers", *Proc. SPIE (Technologies for optoelectronics, 1987)*, 861, pp. 27-32.
- [49] R. J. SIMES, R. H. YAN, R. S. GEELS, L. A. COLDREN, J. H. ENGLISH, A. C. GOSSARD and D. G. LISHAN, "Electrically tunable Fabry-Perot mirror using multiple quantum well index modulation", *Appl. Phys. Lett.* (1988), 53, pp. 637-9.
- [50] Y. H. LEE, J. L. JEWELL, S. J. WALKER, C. W. TU, J. P. HARBISON and L. T. FLOREZ,

- "Electrodispersive multiple quantum well modulator", *Appl. Phys. Lett.* (1988), **53**, pp. 1684-6.
- [51] M. WHITEHEAD, G. PARRY, A. RIVERS and J. S. ROBERTS, "Multiple quantum well asymmetric Fabry-Perot etalons for high-contrast, low insertion loss optical modulation", Postdeadline paper PD4 at IEEE/OSA Topical Meeting on Photonic Switching, Salt Lake City, Utah, USA, March 1-3rd 1989.
- [52] W. DOBBELAERE, D. HUANG, M. S. UNLÜ and H. MORKOÇ, "AlGaAs/GaAs multiple quantum well reflection modulators grown on Si substrates", *Appl. Phys. Lett.* (1988), **53**, pp. 94-6.
- [53] P. BARNES, P. ZOUGANELI, A. RIVERS, M. WHITEHEAD, G. PARRY, K. WOODBRIDGE and C. ROBERTS, "GaAs/AlGaAs multiple quantum well optical modulator using multilayer reflector stacks grown on Si substrate", *Electron. Lett.* (1989), **25**, pp. 995-6.
- [54] K. W. GOOSEN, G. D. BOYD, J. E. CUNNINGHAM, W. Y. JAN, D. A. B. MILLER, D. S. CHEMLA and R. M. LUM, "GaAs multi-quantum well reflection modulators grown on GaAs and Si substrates", Postdeadline paper PD18, CLEO '89, Baltimore MD, 24-28th April 1989.
- [55] M. N. ISLAM, R. L. HILLMAN, D. A. B. MILLER, D. S. CHEMLA, A. C. GOSSARD and J. H. ENGLISH, "Electroabsorption in GaAs/AlGaAs coupled quantum well waveguides", *Appl. Phys. Lett.* (1987), **50**, pp. 1098-1100.
- [56] N. DEBBAR, S. HONG, J. SINGH, P. K. BHATTACHARYA and R. SAHAI, "Coupled GaAs/AlGaAs quantum-well electroabsorption modulators for low-electric-field optical modulation", *J. Appl. Phys.* (1989), **65**, pp. 383-5.
- [57] S. TARUCHA, H. IWAMURA, T. SAKU and H. OKAMOTO, "Waveguide-type optical modulator of GaAs quantum well double heterostructures using electric field effect on exciton absorption", *Jpn. J. Appl. Phys.* (1985), **24**, pp. L442-4.
- [58] T. H. WOOD, C. A. BURRUS, R. S. TUCKER, J. S. WEINER, D. A. B. MILLER, D. S. CHEMLA, T. C. DAMEN, A. C. GOSSARD and W. WIEGMANN, "100ps waveguide multiple quantum well (MQW) optical modulator with 10:1 on/off ratio", *Electron. Lett.* (1985), **21**, pp. 693-4.
- [59] J. S. WEINER, D. A. B. MILLER, D. S. CHEMLA, T. C. DAMEN, C. A. BURRUS, T. H. WOOD, A. C. GOSSARD and W. WIEGMANN, "Strong polarization-sensitive electroabsorption in GaAs/AlGaAs quantum well waveguides", *Appl. Phys. Lett.* (1985), **47**, pp. 1148-50.
- [60] M. GLICK, F. K. REINHART, G. WEIMANN and W. SCHLAPP "Quadratic electro-optic light modulation in a GaAs/AlGaAs multiquantum well heterostructure near the excitonic

- gap", Appl. Phys. Lett. (1986), 48, pp. 989-91.
- [61] J. E. ZUCKER, T. L. HENDRIKSON and C. A. BURRUS, "Electro-optic phase modulation in GaAs/AlGaAs quantum well waveguides", Appl. Phys. Lett. (1988), 52, pp. 945-7.
- [62] J. S. WEINER, A. C. GOSSARD, J. H. ENGLISH, D. A. B. MILLER, D. S. CHEMLA AND C. A. BURRUS, "Low-voltage modulator and self-biased self-electro-optic-effect device", Electron. Lett. (1987), 23, pp. 75-77.
- [63] A. LARSSON, P. A. ANDREKSON, P. ANDERSSON, S. T. ENG, J. SALZMAN and A. YARIV, "High-speed dual-wavelength demultiplexing and detection in a monolithic superlattice *p-i-n* waveguide detector array", Appl. Phys. Lett. (1986), 49, pp. 233-5.
- [64] H. YAMAMOTO, M. ASADA and Y. SUEMATSU, "Intersectional waveguide type optical switch with quantum well structure", Trans. IECE of Japan (1985), E68, pp. 737-9.
- [65] S. TARUCHA and H. OKAMOTO, "Monolithic integration of a laser diode and an optical waveguide modulator having a GaAs/AlGaAs quantum well double heterostructure", Appl. Phys. Lett. (1986), 48, pp. 1-3.
- [66] T. H. WOOD, "Multiple quantum well (MQW) waveguide modulators", IEEE J. Lightwave Technol. (1988), LT-6, pp. 743-757.
- [67] J. S. WEINER, D. S. CHEMLA, D. A. B. MILLER, T. H. WOOD, D. SIVCO and A. Y. CHO, "Room temperature excitons in 1.6 μ m band-gap GaInAs/AlInAs quantum wells", Appl. Phys. Lett. (1985), 46, pp. 619-21.
- [68] K. WAKITA, Y. KAWAMURA, Y. YOSHIKUNI AND H. ASAHI, "Electroabsorption on room-temperature excitons in InGaAs/InGaAlAs multiple quantum-well structures", Electron. Lett. (1985), 21, pp. 338-40.
- [69] K. WAKITA, Y. KAWAMURA, Y. YOSHIKUNI, H. ASAHI and S. UEHARA, "High-speed long-wavelength optical modulation in InGaAs/InAlAs multiple quantum wells", Electron. Lett. (1985), 21, pp. 951-2.
- [70] K. WAKITA, Y. KAWAMURA, Y. YOSHIKUNI and H. ASAHI, "Long-wavelength waveguide multiple-quantum-well (MQW) optical modulator with 30:1 on/off ratio", Electron. Lett. (1986), 22, pp. 907-8.
- [71] S. HONG and J. SINGH, "Excitonic energies and inhomogeneous line broadening effects in InAlAs/InGaAs modulator structures", J. Appl. Phys. (1987), 62, pp. 1994-1999.
- [72] I. BAR-JOSEPH, C. KLINGSHIRN, D. A. B. MILLER, D. S. CHEMLA, U. KOREN and B. I. MILLER, "Quantum-confined Stark effect in InGaAs/InP quantum wells grown by organometallic vapor phase epitaxy", Appl. Phys. Lett. (1987), 50, pp. 1010-12.

- [73] U. KOREN, B. I. MILLER, R. S. TUCKER, G. EISENSTEIN, I. BAR-JOSEPH, D. A. B. MILLER and D. S. CHEMLA, "High-frequency InGaAs/InP multiple-quantum-well buried-mesa electroabsorption optical modulator", *Electron. Lett.* (1987), **23**, 621-2.
- [74] U. KOREN, B. I. MILLER, T. L. KOCH, G. EISENSTEIN, R. S. TUCKER, I. BAR-JOSEPH and D. S. CHEMLA, "Low-loss InGaAs/InP multiple quantum well optical electroabsorption waveguide modulator", *Appl. Phys. Lett.* (1987), **51**, pp. 1132-4.
- [75] D. R. P. GUY, L. L. TAYLOR, D. D. BESGROVE, N. APSLEY AND S. J. BASS, "High contrast-ratio electroabsorptive GaInAs/InP quantum well modulator", *Electron. Lett.* (1988), **24**, pp. 1253-5.
- [76] I. BAR-JOSEPH, G. SUCHA, D. A. B. MILLER, D. S. CHEMLA, B. I. MILLER and U. KOREN, "Self-electro-optic effect device and modulation converter with InGaAs/InP multiple quantum wells", *Appl. Phys. Lett.* (1988), **52**, pp. 51-3.
- [77] M. A. Z. REJMAN-GREENE, E. G. SCOTT and E. MCGOLDRICK, "Planar 3 x 3 array of GaInAs/InP MQW surface optical modulators grown by gas-source MBE", *Electron. Lett.* (1988), **24**, pp. 1583-4.
- [78] A. TOMITA, Y. KOHGA, A. SUZUKI, T. TERAKADO and A. AJISAWA, "5:1 ON:OFF contrast InGaAs/InP multiple quantum well Fabry-Perot étalon modulator", *Appl. Phys. Lett.* (1989), **55**, pp. 1817-9.
- [79] T. MIYAZAWA, S. TARUCHA, Y. OHMORI, Y. SUZUKI and H. OKAMOTO, "Observation of room temperature excitons in GaSb-AlGaSb multi-quantum wells", *Jpn. J. Appl. Phys.* (1986), **25**, pp. L200-202.
- [80] T. H. WOOD, E. C. CARR, C. A. BURRUS, B. I. MILLER and U. KOREN, "Large electroabsorption effect in GaSb/AlGaSb multiple quantum well (MQW) optical modulator grown by OMVPE", *Electron. Lett.* (1988), **24**, pp. 840-1.
- [81] T. E. VAN ECK, P. CHU, W. S. C. CHANG and H. H. WIEDER, "Electroabsorption in an InGaAs/GaAs strained-layer multiple quantum well structure", *Appl. Phys. Lett.* (1986), **49**, pp. 135-6.
- [82] U. DAS, P. BERGER and P. BHATTACHARYA, "InGaAs/GaAs multiquantum-well electroabsorption modulator with integrated waveguide", *Opt. Lett.* (1987), **12**, pp. 820-22.
- [83] H. TEMKIN, D. GERSHONI and M. B. PANISH, "InGaAsP/InP quantum well modulators grown by gas source molecular beam epitaxy", *Appl. Phys. Lett.* (1987), **50**, pp. 1776-8.
- [84] M. SUGAWARA, T. FUJII, M. KONDO, K. KATO, K. DOMEN, S. YAMAZAKI and K. NAKAJIMA, "Evaluation of exciton absorption peak broadening factors in InGaAsP/InP multiple quantum wells", *Appl. Phys. Lett.* (1988), **53**, pp. 2290-2.

- [85] S. NOJIMA and K. WAKITA, "Optimization of quantum well materials and structures for excitonic electroabsorption effects", *Appl. Phys. Lett.* (1988), **53**, pp. 1958-60.
- [86] K. WAKITA, L. KOTAKA, H. ASAI, S. NOJIMA and O. MIKAMI, "High-efficiency electroabsorption in quaternary AlGaInAs quantum-well optical modulators", *Electron. Lett.* (1988), **24**, pp. 1324-5.
- [87] I. BAR-JOSEPH, J. E. ZUCKER, B. I. MILLER, U. KOREN and D. S. CHEMLA, "Compositional dependence of the quantum confined Stark effect in quaternary quantum wells", *IEEE/OSA Meeting on "Quantum Wells for Optics and Optoelectronics"*, Salt Lake City, UT, March 6-8th, 1989.
- [88] H. C. CASEY and M. B. PANISH, "Heterostructure Lasers: Part A Fundamental Principles", Academic Press NY (1978), p. 193.
- [89] G. DUGGAN, H. I. RALPH and K. J. MOORE "Reappraisal of the band-edge discontinuities at the $\text{Al}_x\text{Ga}_{1-x}\text{As-GaAs}$ heterojunction", *Phys. Rev. B* (1985), **32**, pp. 8395-7.
- [90] See G. BASTARD and J. A. BRUM, "Electronic states in semiconductor heterostructures", *IEEE J. Quantum Electron.* (1986), **QE-22**, pp. 1625-44, and references therein.
- [91] D. S. CHEMLA, "Quasi-two-dimensional excitons in GaAs/ $\text{Al}_x\text{Ga}_{1-x}\text{As}$ semiconductor multiple quantum well structures", *Helv. Phys. Acta* (1983), **56**, pp. 607-37.
- [92] D. D. SELL and H. C. CASEY Jr., "Optical absorption and photoluminescence studies of thin GaAs layers in GaAs- $\text{Al}_x\text{Ga}_{1-x}\text{As}$ double heterostructures", *J. Appl. Phys.* (1974), **45**, pp. 800-807.
- [93] Y. MASUMOTO, M. MATSUURA, S. TARUCHA and H. OKAMOTO, "Direct experimental observation of the two-dimensional shrinkage of the exciton wave function in quantum wells", *Phys. Rev. B* (1985), **32**, pp. 4275-8.
- [94] D. S. CHEMLA and D. A. B. MILLER, "Room-temperature excitonic nonlinear-optical effects in semiconductor quantum-well structures", *J. Opt. Soc. Am. B* (1985), **2**, pp. 1155-73.
- [95] R. L. GREENE, K. K. BAJAJ and D. E. PHELPS, "Energy levels of Wannier excitons in GaAs- $\text{Ga}_{1-x}\text{Al}_x\text{As}$ quantum-well structures", *Phys. Rev. B* (1984), **29**, pp. 1807-1812.
- [96] J. A. BRUM and G. BASTARD, "Excitons formed between excited sub-bands in GaAs- $\text{Ga}_{1-x}\text{Al}_x\text{As}$ quantum wells", *J. Phys. C* (1985), **18**, L789-94.
- [97] W. T. MASSELINK, P. J. PEARAH, J. KLEM, C. K. PENG, H. MORKOÇ, G. D. SANDERS and Y-C. CHANG, "Absorption coefficients and exciton oscillator strengths in AlGaAs-GaAs superlattices", *Phys. Rev. B* (1985), **32**, pp. 8027-34.

- [98] P. J. STEVENS, M. WHITEHEAD, G. PARRY and K. WOODBRIDGE, "Computer modeling of the electric field dependent absorption spectrum of multiple quantum well material", *IEEE J. Quantum. Electron.* (1988), QE-24, pp.2007-16.
- [99] U. EKENBERG and M. ALTARELLI, "Exciton binding energy in a quantum well with inclusion of valence band coupling and non-parabolicity", *Phys. Rev. B* (1987), 36, pp. 7585-7595.
- [100] B. DEVEAUD, J. Y. EMERY, A. CHOMETTE, B. LAMBERT and M. BAUDET, "Observation of one monolayer size fluctuations in a GaAs/GaAlAs superlattice", *Appl. Phys. Lett.* (1984), 45, pp. 1078-80.
- [101] J. D. DOW and D. REDFIELD, "Electroabsorption in semiconductors: The excitonic absorption edge", *Phys. Rev. B.* (1970), 1, pp. 3358-3371.
- [102] D. A. B. MILLER, D. S. CHEMLA, T. C. DAMEN, A. C. GOSSARD, W. WIEGMANN, T. H. WOOD and C. A. BURRUS, "Band-edge electroabsorption in quantum well structures: The quantum-confined Stark effect", *Phys. Rev. Lett.* (1984), 53, pp. 2173-6.
- [103] D. A. B. MILLER, D. S. CHEMLA, T. C. DAMEN, A. C. GOSSARD, W. WIEGMANN, T. H. WOOD and C.A. BURRUS, "Electric field dependence of optical absorption near the band gap of quantum well structures", *Phys. Rev. B* (1985), 32, pp. 1043-60.
- [104] E. J. AUSTIN and M. JAROS, "Electric field induced shifts and lifetimes in GaAs-GaAlAs quantum wells", *Appl. Phys. Lett.* (1985), 47, pp. 274-6.
- [105] M. MATSUURA and T. KAMIZATO, "Subbands and excitons in a quantum well in an electric field", *Phys. Rev. B* (1986), 33, pp. 8385-9.
- [106] D. AHN and S. L. CHUANG, "Exact calculations of quasibound states of an isolated quantum well with uniform electric field: Quantum well Stark resonance", *Phys. Rev. B* (1986), 34, pp. 9034-7.
- [107] A. HARWIT, J. S. HARRIS Jr. and A. KAPITULNIK, "Calculated quasi-eigenstates and quasi-eigenenergies of quantum well superlattices in an applied electric field", *J. Appl. Phys.* (1986), 60, pp. 3211-3.
- [108] J. SINGH and S. HONG, "Theory of electric field-induced optical modulation in single and multiple quantum well structures using a Monte Carlo approach", *IEEE J. Quantum Electron.* (1986), QE-22, pp. 2017-21.
- [109] J. A. BRUM and G. BASTARD, "Electric-field-induced dissociation of excitons in semiconductor quantum wells", *Phys. Rev. B* (1985), 31, pp. 3893-8.
- [110] D. A. B. MILLER, D. S. CHEMLA and S. SCHMITT-RINK, "Relation between electroabsorption in bulk semiconductors and in quantum wells: The quantum-confined

- Franz-Keldysh effect", Phys. Rev. B (1986), 33, pp. 6976-82.
- [111] P. C. KLIPSTEIN and N. APSLEY, "A theory for the electroreflectance spectra of quantum well structures", J. Phys. C (1986), 19, pp. 6461-78.
- [112] B. JOGAI and K. L. WANG, "Interband optical transitions in GaAs-Ga_{1-x}Al_xAs superlattices in an applied electric field", Phys. Rev. B (1987), 35, pp. 653-9.
- [113] Z. IKONIC, V. MILANOVIC and D. TJAPKIN, "Quantum well electro-absorption in a strong electric field: a continuum spectrum approach", J. Phys. C. (1987), 20, pp. 1147-60.
- [114] Y. KAN, H. NAGAI, M. YAMANISHI and I. SUEMUNE, "Field effects on the refractive index and absorption coefficient in AlGaAs quantum well structures and their feasibility for electrooptic device applications", IEEE J. Quantum Electron. (1987), QE-23, pp. 2167-79.
- [115] C. ALIBERT, S. GAILLARD, J. A. BRUM, G. BASTARD, P. FRIJLINK and M. ERMAN, "Measurements of electric-field-induced energy-level shifts in GaAs single-quantum wells using electroreflectance", Solid State Commun. (1985), 53, pp. 457-60.
- [116] P. C. KLIPSTEIN, P. R. TAPSTER, N. APSLEY, D. A. ANDERSON, M. S. SKOLNICK, T. M. KERR and K. WOODBRIDGE, "Electroreflectance spectroscopy from quantum well structures in an electric field", J. Phys. C (1986), 19, pp. 857-71.
- [117] Y. KAN, M. YAMANISHI, I. SUEMUNE, H. YAMAMOTO and T. YAO, "Electric field effect on subband state transition peaks in the photoluminescence from a GaAlAs quantum well structure", Jpn. J. Appl. Phys. (1985), 24, pp. L589-92.
- [118] F.-Y. JUANG, J. SINGH, P. K. BHATTARCHARYA, K. BAJEMA and R. MERLIN, "Field-dependent linewidths and photoluminescence energies in GaAs-AlGaAs multi-quantum well modulators", Appl. Phys. Lett. (1986), 48, pp. 1246-8.
- [119] L. VIÑA, E. E. MENDEZ, W. I. WANG, L. L. CHANG AND L. ESAKI, "Stark shifts in GaAs/GaAlAs quantum wells studied by photoluminescence spectroscopy", J. Phys. C (1987), 20, pp. 2803-15.
- [120] K. YAMANAKA, T. FUKUNAGA, N. TSUKADA, K. L. I. KOBAYASHI and M. ISHII, "Photocurrent spectroscopy in GaAs/AlGaAs multiple quantum wells under a high electric field perpendicular to the heterointerface", Appl. Phys. Lett. (1986), 48, pp. 840-2.
- [121] R. T. COLLINS, K. VON KLITZING and K. PLOOG, "Photocurrent spectroscopy of GaAs/Al_xGa_{1-x}As quantum wells in an electric field", Phys. Rev. B (1986), 33, 4378-81.
- [122] P. W. YU, G. D. SANDERS, D. C. REYNOLDS, K. K. BAJAJ, C. W. LITTON, J. KLEM, D. HUANG and H. MORKOÇ, "Determination of transition energies and oscillator strengths in GaAs-Al_xGa_{1-x}As multiple quantum wells using photovoltage-induced photocurrent spectroscopy", Phys. Rev. B (1987), 35, pp. 9250-8.

- [123] T. H. WOOD, "Direct measurement of the electric field dependent absorption coefficient in GaAs/AlGaAs multiple quantum wells", *Appl. Phys. Lett.* (1986), **48**, pp. 1413-5.
- [124] D. A. B. MILLER, J. S. WEINER and D. S. CHEMLA, "Electric-field dependence of linear optical properties in quantum well structures: Waveguide electroabsorption and sum rules", *IEEE J. Quantum Electron.* (1986), **QE-22**, pp. 1816-30.
- [125] M. WHITEHEAD, G. PARRY, K. WOODBRIDGE, P. J. DOBSON and G. DUGGAN, "Experimental confirmation of a sum rule for room temperature electroabsorption in GaAs-AlGaAs multiple quantum well structures", *Appl. Phys. Lett.* (1988), **52**, pp. 345-7.
- [126] M. WHITEHEAD, P. STEVENS, A. RIVERS, G. PARRY, J. S. ROBERTS, P. MISTRY, M. PATE and G. HILL, "Effects of well width on the characteristics of GaAs/AlGaAs multiple quantum well electroabsorption modulators", *Appl. Phys. Lett.* (1988), **53**, pp. 956-8.
- [127] K. W. JELLEY, R. W. H. ENGELMANN, K. ALAVI and H. LEE, "Well size related limitations on maximum electroabsorption in GaAs/AlGaAs multiple quantum well structures", *Appl. Phys. Lett.* (1989), **55**, pp. 70-72.
- [128] See for example S. M. SZE, "Physics of Semiconductor Devices", 2nd Edition, Wiley Interscience 1981.
- [129] D. J. NEWSON and A. KUROBE, "Effect of residual doping on optimum structure of multi-quantum-well optical modulators", *Electron. Lett.* (1987), **23**, pp. 439-440.
- [130] J. W. LITTLE, R. P. LEAVITT, S. OVADIA and C. H. LEE, "Optical characterization of nonuniform electric fields in multiple quantum well diodes", *Appl. Phys. Lett.* (1989), **55**, pp. 173-5.

FABRICATION AND ASSESSMENT OF GaAs MQW *p-i-n* DIODE STRUCTURES

2.1 Introduction

2.2 Growth of GaAs MQW *p-i-n* Diode Structures

2.2.1 Metal-Organic Vapour Phase Epitaxy (MOVPE)

2.2.2 Molecular Beam Epitaxy (MBE)

2.2.3 The Standard MQW *p-i-n* Structure

2.3 Fabrication and Assessment of MQW Mesa Photodiodes

2.3.1 Fabrication of the MQW *p-i-n* Photodiode

2.3.2 Electrical Assessment of Devices

2.3.3 Measurement of Photocurrent Spectra

2.4 Photocurrent and Absorption

2.5 Photocurrent Studies of MOVPE-Grown Devices

2.5.1 Sample CPM7 (55 x $\approx 97\text{\AA}$ well, $\approx 100\text{\AA}$ barrier)

2.5.2 Sample CPM147 (25 x $\approx 90\text{\AA}$ well, $\approx 100\text{\AA}$ barrier)

2.5.3 Sample CPM244 (100 x $\approx 51\text{\AA}$ well, $\approx 60\text{\AA}$ barrier)

2.5.4 Sample CPM363 (60 x $\approx 100\text{\AA}$ well, $\approx 60\text{\AA}$ barrier)

2.5.5 Samples CPM401 & CPM405 (50/60 x $\approx 85/87\text{\AA}$ well, $\approx 43\text{\AA}$ barrier)

2.5.6 Sample MV245 (45 x $\approx 145\text{\AA}$ well, $\approx 53\text{\AA}$ barrier)

2.5.7 Sample MV246 (75 x $\approx 47\text{\AA}$ well, $\approx 53\text{\AA}$ barrier)

2.5.8 Sample MV301 (Single $\approx 83\text{\AA}$ well)

2.5.9 Samples MV367 & MV370 (77/50 x $\approx 100/85\text{\AA}$ well, $\approx 35/67\text{\AA}$ barrier)

2.5.10 Sample CB93 (100 x $\approx 100\text{\AA}$ well, $\approx 60\text{\AA}$ barrier)

2.6 Photocurrent Studies of MBE-Grown Devices

2.6.1 Sample KLB461 (25 x $\approx 100\text{\AA}$ well, $\approx 100\text{\AA}$ barrier)

2.6.2 Sample M33 (20 x $\approx 100\text{\AA}$ well, $\approx 100\text{\AA}$ barrier)

2.7 Summary

2.1 INTRODUCTION

In Chapter 1 the basic optical and electronic properties of MQW structures were described. Here we discuss the practical aspects of producing MQW devices and some initial measurements of the quantum-confined Stark effect (QCSE) in a range of MQW structures. The intention is to provide a useful qualitative background for the chapters to follow.

First, a brief outline is given of the epitaxial growth techniques used to make MQW *p-i-n* diode structures. We have studied devices grown by both the major technologies – molecular beam epitaxy and metal-organic vapour phase epitaxy. We then describe the processing steps required to make the most simple device – the *p-i-n* photodiode, which is the basis of the MQW modulators of Chapters 4-6 – and the details of how the optoelectronic properties of the devices are assessed by photocurrent spectroscopy. Photocurrent spectroscopy offers a way of observing the absorption spectra indirectly, and can provide a wealth of information about the electrical quality of the *p-i-n* diode, and the structural integrity of the MQWs. In particular, we chart the development of the MOVPE material quality through the photocurrent spectra of a number of samples.

2.2 GROWTH OF GaAs MQW *p-i-n* DIODE STRUCTURES

It is not the intention here to critically compare epitaxial growth techniques for MQW *p-i-n* diodes; the relative merits of the two methods have previously been considered in some detail by Dapkus [1]. In our case, both MBE- and MOVPE-grown structures achieved the quality required to observe a well-defined QCSE and enhanced electro-absorptive modulation; that is, the control of layer thicknesses down to only a few 10's of Ångströms and hetero-interface widths to ≈ 1 monolayer ($\approx 2.8\text{Å}$). This being achieved with good uniformity over wide areas. Also essential was the achievement of low background impurity doping levels in the nominally undoped MQW layers, and the ability to abruptly change the doping level and type to form the *p-i-n* diode structure.

At the beginning of this work, MBE was already established as a proven technology for the growth of low-dimensional structures and devices, and, prior to the growth of MQW modulator structures, the system used here had successfully produced QW lasers [2]. However, the MOVPE system which was used was less well developed, and had produced no doped structures containing MQWs, so there was a significant amount of development work to be done [3].

2.2.1 METAL-ORGANIC VAPOUR PHASE EPITAXY (MOVPE)

MOVPE has become popular as a commercial high-resolution epitaxial technique because of its inherent capability for large wafer throughput and fast source replacement. Growth can be carried out simultaneously on several substrates within the same reactor. It is sometimes dismissed as a lower resolution method compared to MBE. While this may be true for extremely thin layers ($\approx 10\text{Å}$), we clearly show in § 2.5 that, as far as the growth of MQW modulator structures is concerned, MOVPE achieves exactly the quality required.

Research into MOVPE was begun in the late 1960s by Manasevit [4], but device quality material did not become available until 1975. By 1978, however, the first QW injection laser operating c.w. at room temperature was demonstrated by Dupuis et al. [5] using MOVPE, and the technique has since successfully reproduced most of the achievements of MBE.

The MOVPE process essentially involves the thermal dissociation of

volatile metal-organic compounds containing the group III elements in the presence of the group V hydride. In the case of Ga(Al)As the reagents are typically trimethyl gallium (TMG), trimethyl aluminium (TMA) and arsine, with silane and dimethyl zinc as *n*-type and *p*-type dopants. Hydrogen is used as a carrier gas to transport the TMG and TMA as a vapour from the source liquid into the quartz reaction chamber, which for the materials studied here is of the horizontal, atmospheric pressure type.

Mass flow controllers on the input gas lines are used to fix the composition and the growth rate. After intermixing, the reagents flow through the chamber, dissociating only when the heated region around the substrate is reached, and forming the desired III-V compound. Valve control of the gas lines allows the TMA to be switched in and out for heterojunction growth. The switching time is of the order of 1 second, so typical growth rates for the highest quality material are ≈ 1 monolayer/sec, which translates to $\approx 1\mu\text{m/hr}$, in order to keep interfaces sharp.

A thorough review of MOVPE covering a wide range of III-V compounds has recently been given by Stringfellow [6].

The MOVPE-grown MQW *p-i-n* diodes, whose characteristics are described in § 2.5, were supplied by Dr. John Roberts and co-workers at the SERC III-V Central Facility, University of Sheffield. Initial device properties were poor due to high MQW background doping. However, this problem was eventually overcome and all optical modulation data in the chapters to follow are from high quality MOVPE-grown devices

2.2.2 MOLECULAR BEAM EPITAXY (MBE)

MBE has traditionally been used to demonstrate state of the art epitaxial III-V semiconductor structures such as QW lasers and high electron mobility transistors (HEMTs), and remains at the centre of fundamental growth work. The origins of this technique go back to the late 1960s to the work of Davey & Pankey [7], Arthur [8] and Cho [9], and as early as 1971 Cho [10] had succeeded in growing periodic GaAs-AlGaAs heterojunctions with layer thicknesses down to $\approx 1700\text{\AA}$.

In MBE growth heated elemental sources (Ga, Al, As), contained in controlled effusion cells, produce beams of atoms or molecules within an ultra high vacuum (UHV) chamber held at $\approx 10^{-10}$ – 10^{-11} torr background

pressure. The beams are directed at a heated semiconductor substrate ($\approx 600\text{-}700^\circ\text{C}$) on which growth takes place at a rate according to the flux of the group III elements, in this case Ga and Al. An overpressure of As is provided to ensure good growth. The fluxes are determined by accurate temperature control of the source cells to $\approx \pm 1^\circ\text{C}$. In order to achieve abrupt hetero-interfaces, between GaAs and AlGaAs for example, each source is provided with an externally-controlled shutter which can cut off the beam in much less than the time to grow 1 monolayer of material. As with MOVPE typical growth rates are $\approx 1\mu\text{m/hr}$ for GaAs. To reduce layer thickness variations, caused by spatial non-uniformities in the source flux, the substrate is usually rotated at least once in the time taken to grow 1 monolayer. Doping is provided typically by Si (*n*-type) and Be (*p*-type) sources.

The requirement of UHV conditions for high quality growth means that the MBE system can also incorporate a number of useful diagnostics such as RHEED (reflection high energy electron diffraction) and mass spectrometry. RHEED allows the structure of the crystal surface to be monitored and can be used to determine growth rates [11] immediately prior to the growth of a complete structure. A disadvantage of the UHV environment is the need to open the system to air in order to replace exhausted sources, which involves time-consuming "bake-out" procedures to restore clean conditions in the growth chamber.

More details of the growth mechanisms, system construction and results achieved can be found in a recent review papers by Joyce [12] and Tsang [13].

The MBE samples studied here were grown in collaboration with Dr. Karl Woodbridge at Philips Research Labs., Redhill. Initial growth was carried out in a custom-built system, the details of which have been reported elsewhere [14]. During the course of this project this system was de-commissioned to be replaced by a commercial Varian Gen II Modular system. The amount of down-time obviously limited the number of MBE samples which could be grown. Hence there is no story of development as for the MOVPE-grown material. However, the two samples reported on in § 2.6 do represent the highest quality material available to us at the particular time that they were grown.

2.2.3 THE STANDARD MQW *p-i-n* STRUCTURE

The typical layer structure for a simple MQW transmission modulator is shown in Fig. 2.2.3. In the intrinsic region of the *p-i-n* there will usually be 50-60 GaAs quantum well layers of $\approx 100\text{\AA}$ thickness separated by $\text{Al}_{0.30}\text{Ga}_{0.70}\text{As}$ barrier layers of $\approx 60\text{-}100\text{\AA}$. Occasionally, undoped regions of $\text{Al}_{0.30}\text{Ga}_{0.70}\text{As}$ of $\approx 0.05\mu\text{m}$ have been included on either side of the MQWs as a buffer to protect the undoped quantum wells from any diffusion of dopants from the doped $\text{Al}_{0.30}\text{Ga}_{0.70}\text{As}$ layers, an idea based on the use of superlattice buffers as suggested by other authors [15, 25]. However, we have observed no significant difference in the device performance by including or excluding these buffer layers. The principal effect is just to increase the bias voltage required to produce a given electric field across the MQW structure.

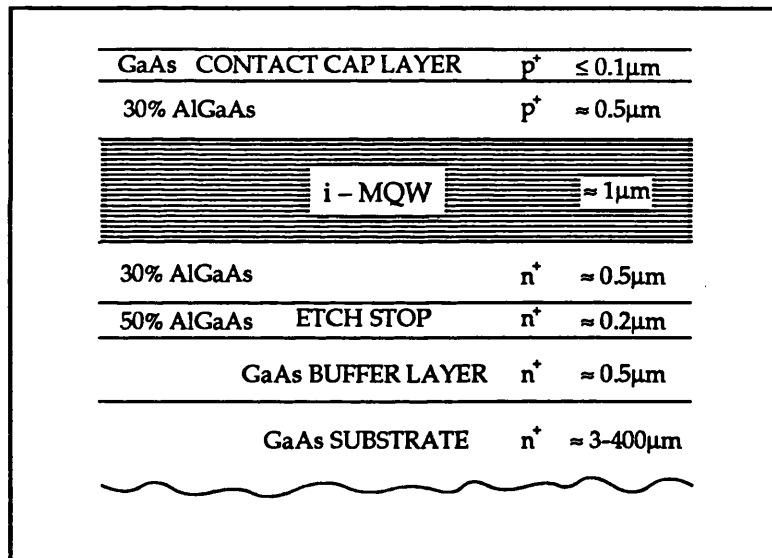


FIGURE 2.2.3:
The standard MQW *p-i-n* diode layer structure.

Doping control is essential for good electrical and optical response. The MQW region is nominally undoped but will have a background level which reflects the technology used, its state of cleanliness, and the purity of the group III and group V sources. Both MBE and MOVPE methods can now achieve an intrinsic doping level in the region of $1\text{-}2 \times 10^{15}\text{cm}^{-3}$, which is essential to minimize spectral broadening of the QCSE, as was discussed in § 1.4. The p^+ and n^+ layers are generally doped to a level of $\approx 5 \times 10^{17}\text{-}1 \times 10^{18}\text{cm}^{-3}$. High doping levels are needed to limit the carrier

depletion outside of the MQW i-region, thus maintaining high fields, and to allow low-resistivity, ohmic contacting. However, attempts to increase the level much above 10^{18}cm^{-3} can result in diffusion of the dopants into the MQWs, resulting in rather poor devices.

Growth of a GaAs buffer layer is a standard technique for smoothing the prepared substrate prior to the growth of the device layer. The etch stop layer of high Al mole fraction AlGaAs was included in early device structures to allow the absorbing substrate and buffer layer to be removed with a selective wet etch [16]. With the development of dry etching techniques, which appear to be more sensitive to smaller Al mole fractions, there has ceased to be a need for this layer. Both the buffer and etch stop layers must be doped to a level similar to that of the substrate in order to achieve low resistivity contact between substrate and device.

Because of the tendency of AlGaAs to oxidize on exposure to air, which makes the achievement of ohmic contacts difficult and sensitive to the Al mole fraction [17], a p^+ GaAs cap layer is necessary to provide a good ohmic contact.

2.3 FABRICATION AND ASSESSMENT OF MQW MESA PHOTODIODES

2.3.1 FABRICATION OF THE MQW *p-i-n* PHOTODIODE

Besides providing a device which allows the QCSE to be observed, the process described here, illustrated in Fig. 2.3.1, is also the first stage in the fabrication of the complete transmission modulator.

The main steps in the *p-i-n* diode process are:

(a) A positive photoresist layer spun on the top surface of the sample is patterned and developed for the *p*-contact metallization.

(b) A thin film of chromium and gold ($\approx 100\text{\AA}$ Cr, $\approx 2000\text{\AA}$ Au) is evaporated over the whole of the patterned sample.

(c) The *p*-contact is defined by dissolving the photoresist in acetone, thus removing the excess metal. This is known as the "lift-off" technique. To allow the free passage of light into the device the contact has a window $400\mu\text{m}$ square; with an outer dimension of $500\mu\text{m}$. The extended area to the right of the window is the wire bonding pad.

(d) In some structures the GaAs *p*-contact layer has been up to 1000\AA thick, which absorbs $\approx 10\%$ of the incident light in a single pass at wavelengths close to the MQW absorption edge. The removal of this layer from the device window requires a photoresist masking stage to protect the metallization from the selective GaAs etch. In more recent *p-i-n* structures this GaAs layer has been reduced to $\approx 200\text{\AA}$, so that losses are only $\approx 2\%$ and its removal unnecessary.

(e) To define the device electrically, so that we can apply useful bias voltages without serious leakage currents or breakdown, a mesa is etched around the top contact. A photoresist mask protects the device area.

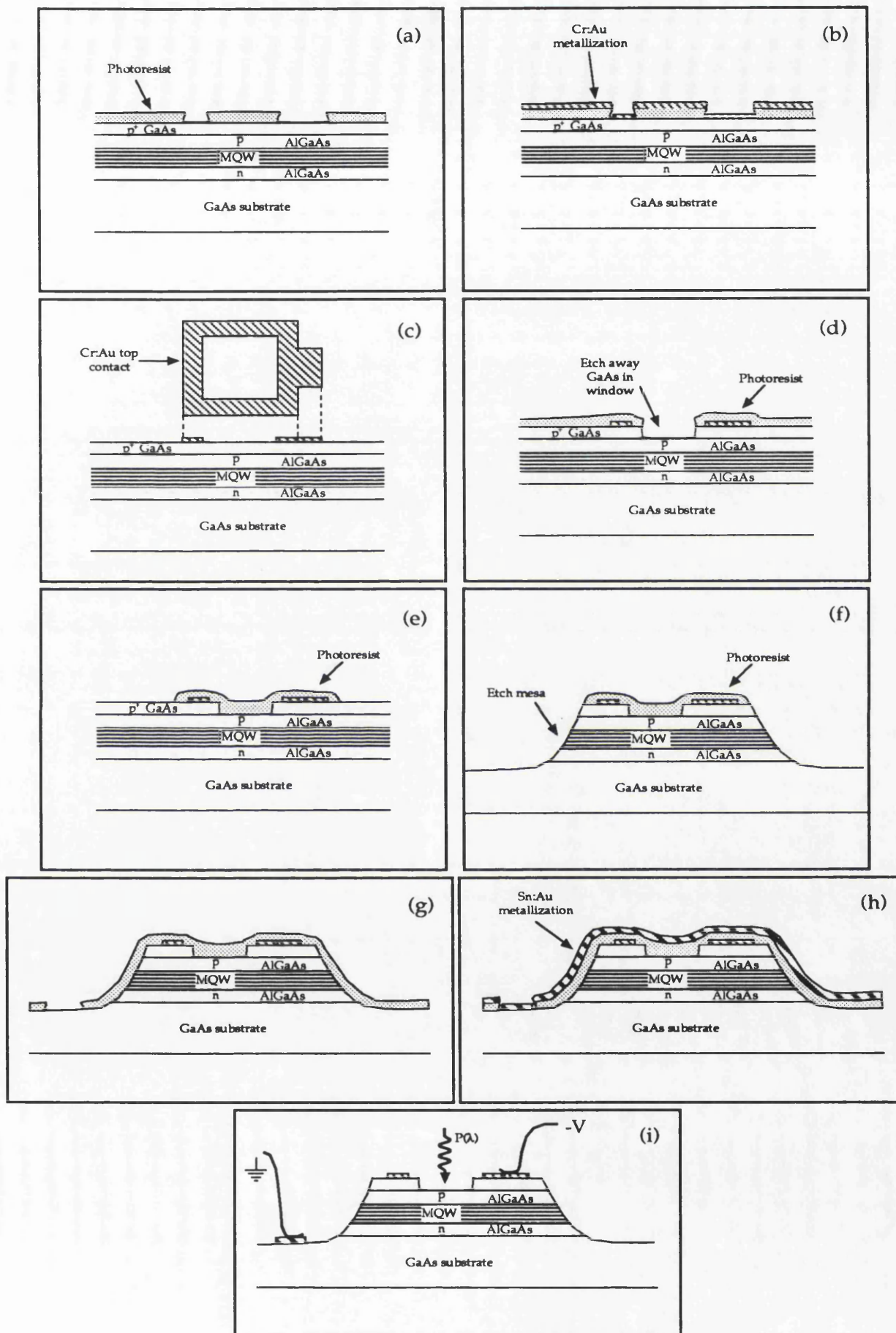


FIGURE 2.3.1: Steps in the fabrication of an MQW photodiode, as described in the text.

(f) The mesa is etched using one of number of non-selective wet etches, the favoured one being $\text{H}_3\text{PO}_4:\text{H}_2\text{O}_2:\text{H}_2\text{O}$ in the ratio 3:4:1 since it leaves a very smooth substrate surface for the n -contact. The wet etches produce smoother mesa side-walls, and thus better electrical characteristics, than existing in-house dry etching methods, which are used later in the transmission modulator fabrication scheme (see § 4.2).

(g) Photoresist is spun over the whole sample once more and patterned for the n -contact, which is a simple rectangular pad.

(h) The n -metallization ($\approx 100\text{\AA}$ Sn, 2000\AA Au) is evaporated over the whole sample and the excess "lifted off" as in steps (a)-(c). The metal contacts are then alloyed at $\approx 440^\circ\text{C}$ in a nitrogen atmosphere for 120s.

(i) Upwards of 20 devices are usually fabricated on one piece of material. After alloying the sample is mounted device side down with wax on a polishing block. The substrate is then ground down using fine grade carborundum to $\approx 100\mu\text{m}$ to make cleaving up of the individual devices easier. For measurements, pairs of devices are mounted on standard TO5 transistor headers and electrical connections made by bonding $25\mu\text{m}$ gold wires to top and bottom contact pads. With devices of this size, in the absence of a commercial bonding machine, it has been possible to hand-bond the wires using a silver-loaded conducting epoxy.

2.3.2 ELECTRICAL ASSESSMENT OF DEVICES

Prior to being mounted for optical measurements, each device fabricated on the chip is tested for its current-voltage (I-V) characteristics. The important features of the I-V characteristics which are noted are the breakdown voltage, where the reverse current typically increases above the μA level, and the bias voltage required to produce a leakage current of 10nA . This latter figure is generally in the 10-20V range for our mesa-processed structures with $\approx 1\mu\text{m}$ intrinsic region. Breakdown voltages are normally in the region of 20-30V, but will be lowered by high background doping as explained in § 1.4. The breakdown and 10nA leakage limits are not usually a problem in the MQW devices studied here since we generally need to apply only $\approx 10\text{V}$ to achieve the necessary Stark shift of

the absorption edge for strong modulation, and the amount of ohmic heating produced by 10nA @ 10V is negligible and, in any case, will be less than the power generated due to the absorbed light.

Capacitance-voltage (C-V) measurements, carried out on an automated 1MHz Hewlett-Packard C-V profiler, provide an estimate of the background doping in the MQW structure and the width of the intrinsic region of the diodes. As we discussed in § 1.4, it is important that we know the background doping to be low, otherwise the device performance can be severely degraded by field-induced broadening of the excitonic absorption edge.

Some typical C-V data will be shown in §§ 2.5 & 2.6, where they are particularly relevant to the device characteristics.

2.3.3 MEASUREMENT OF PHOTOCURRENT SPECTRA

An automated experimental facility was constructed for the measurement of biased photocurrent spectra in the first instance. This is shown below in Fig. 2.3.3.1.

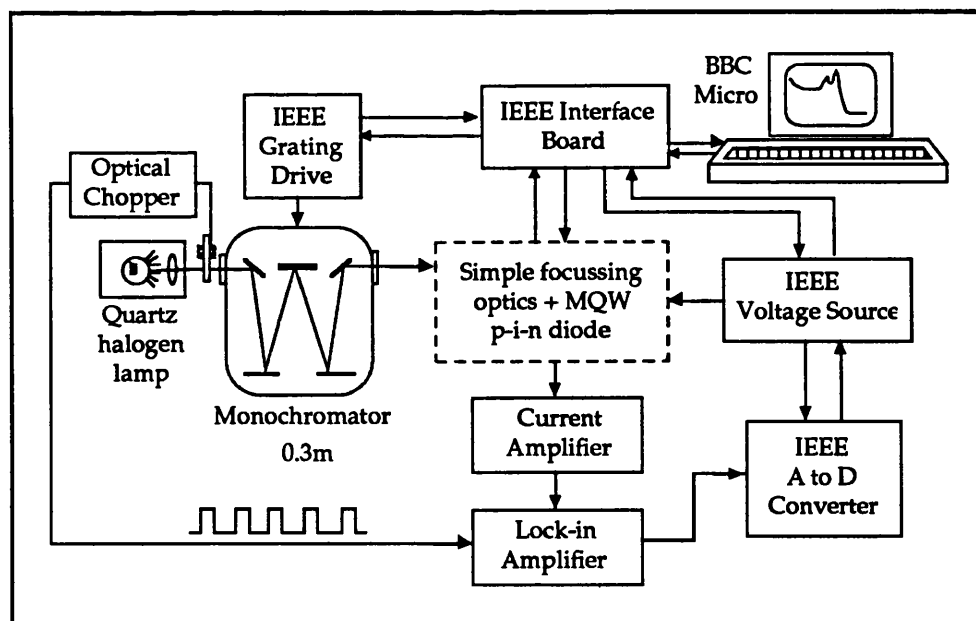


FIGURE 2.3.3.1:

Schematic of experimental set-up used for a range of optical measurements on MQW structures.

The optical source is a monochromated broad-band quartz halogen lamp, which typically delivers $\approx 100\text{nW}$ of power onto the test device, in a linewidth of $\approx 0.6\text{nm}$. The light is modulated by a rotating-wheel chopper. This generates its own reference signal which is fed to the lock-in amplifier and used to extract only the signal (at the same frequency) which is produced in the MQW diode by the light from the monochromator. The total current from the MQW diode will include components due to stray light and reverse leakage.

The output wavelength from the monochromator and the bias applied to the MQW device are controlled via the IEEE interface bus. At each wavelength and bias the signal derived from the photocurrent is fed into the current amplifier/lock-in combination. The output of this is sampled 64 times by the ADC and the r.m.s. of the digital values is stored by the BBC Microcomputer. For each bias voltage data is normally recorded at intervals of either 0.5 or 1nm, depending on the spectral range.

The "simple focussing optics" (shown in Fig. 2.3.3.2a) consist of a pair of lenses – one for collimation and one for tight focussing onto the MQW diode, and a variable aperture (VA) to reduce the beam size. The filter, F, cuts out light below $\approx 600\text{nm}$ to prevent any contributions to the photocurrent from 2nd order light from the monochromator grating at 800-900nm.

The biasing circuit for the MQW diode (Fig. 2.3.3.2b) is kept extremely simple. We use a load resistor (10-100k Ω) to produce a voltage proportional to the current flowing through the diode.

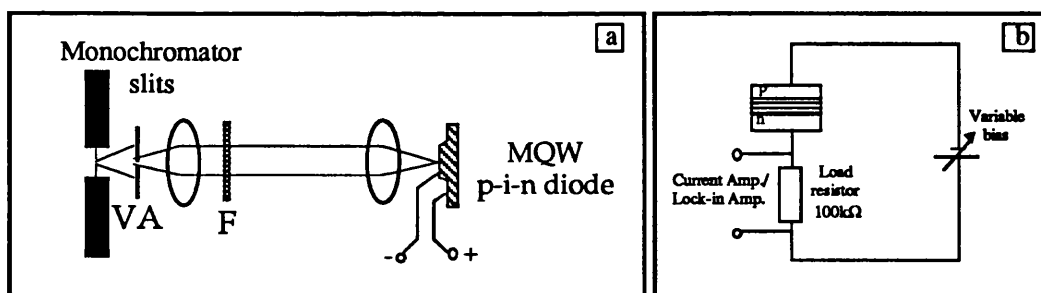


FIGURE 2.3.3.2:

(a) The simple optical arrangement for photocurrent measurements.

(b) The electrical connections made to the MQW diode in order to detect photocurrent.

Bias is applied across both these components, and, provided the input power is in the 100nW range or less and the contact resistances for the device are small, virtually all the voltage will be dropped across the

MQWs. (At $\approx 850\text{nm}$ the maximum possible responsivity is $\approx 0.67\text{A}\cdot\text{W}^{-1}$. Through the $100\text{k}\Omega$ load resistor, current of 67nA produces only 0.67mV).

Depending on the amount of sensitivity required, the signal extracted from across the load resistor can be input into the lock-in amplifier via the current amplifier, or input directly into the lock-in. Neither of these two arrangements perturbs the diode circuit. In the former case the low input impedance of the current amplifier, relative to the load resistance, effectively means that all the current in the circuit will by-pass the load resistor, so the current amplifier will appear to be in series with the MQW diode as for a standard current measurement. In the latter case the high input impedance of the lock-in ($\approx 100\text{M}\Omega$) means that it will draw virtually no current. All the current in the diode circuit will therefore pass through the load resistance and produce the full photovoltage to be measured by the lock-in.

The same experimental system has also been used for other optical measurements such as field-dependent transmission and reflection spectra. These require only a simple reconfiguration of the optics and the use of a separate photodetector. Such measurements will be described in § 4.2 and the results reported in Chapters 4 and 6.

2.4 PHOTOCURRENT AND ABSORPTION

Where the drift current dominates over that due to diffusion, i.e. in the presence of an electric field, the photocurrent generated at a wavelength λ by a power P incident on a p - i - n diode can be expressed as:

$$I_{ph}(\lambda, V) = P(\lambda)(1 - R_f(\lambda)) \left(\frac{q\lambda}{hc} \right) \eta(V) [1 - e^{-\alpha(\lambda, V)d}] \quad \dots(2.1)$$

where V is the bias applied, R_f is the reflectivity of the front surface, q is the electronic charge, h is Planck's constant, c is the velocity of light, η is the internal quantum efficiency, α is the absorption coefficient of the material in the i -region and d is its thickness. $P(1 - R_f)$ is the power which reaches the detection region. The fraction of this which is absorbed in a single pass is $[1 - e^{-\alpha(\lambda, V)d}]$. The factor $(q\lambda/hc)$ converts from absorbed power per sec. to the number of generated carriers per sec., i.e. current. The quantum efficiency, η , is the fraction of generated carriers which actually reaches the contacts and is detected externally as current.

It can be seen from Eq. 2.1 that the photocurrent is roughly proportional to the absorbed power, since the variation due to the λ -dependence is only $\approx 20\%$ over a typical spectral range of perhaps 750-900nm, and any factors which reduce the quantum efficiency, η , such as carrier capture by the quantum wells and subsequent recombination, are assumed to be only voltage-dependent. We would also expect R_f to be reasonably constant over the same spectral range, and, although the absorbed power term depends on the inverse exponential of αd , the deviation from a linear dependence is monotonic and quite slow as αd increases. Thus the most significant variations in the photocurrent spectrum will be due to the variation in the absorption coefficient, α , and the photocurrent spectrum will be a fair representation of the absorption spectrum, provided αd does not become so large (> 3 roughly) that at all wavelengths above the absorption edge there is almost complete absorption of the incident light within the MQW region. In particular we should be able to resolve excitonic features in the spectrum and observe their behaviour under an applied electric field.

As we discuss in the next chapter, our initial attempts to observe electro-absorptive effects in MQW transmission spectra were fraught with problems, but it was soon realised that the same qualitative effects could

be observed more easily in photocurrent spectra. Around the same time other workers were also independently starting to use this convenient method in MQW experiments to observe, for example, low-temperature excitonic Stark shifts, tunnelling dynamics of photocarriers and the relative oscillator strengths for different excitonic transitions [18-23]

Photocurrent spectroscopy has now become commonplace as a probe of Stark shifts and transport in quantum wells, and is often used in tandem with photoluminescence [18, 21]. Although photocurrent measurements require metallic contacts and some simple device processing, they can be carried out at room temperature without the need for high power laser sources (incident powers of significantly less than $1\mu\text{W}$ will suffice, unlike photoluminescence spectroscopy) and with a higher degree of sensitivity owing to the detection of current rather than re-radiated photons. As an example, we shall show in the next section extremely noise-free photocurrent spectra from a *single* quantum well.

If certain assumptions are made about R_f and η it is possible to rescale photocurrent spectra to represent absorption [24]. In Chapter 3 we shall discuss this further and show some typical calculated spectra.

2.5 PHOTOCURRENT STUDIES OF MOVPE-GROWN DEVICES

The initial results from the samples supplied by the III-V Central Facility at Sheffield University were rather poor. The early samples were the first attempts to grow MQWs as part of a *p-n* junction device and, understandably, there was a period of development before sufficient quality was achieved that we could observe the optical modulation properties of the MQWs undistorted by deficiencies in the *p-i-n* structure.

Here we give a chronological account of the modifications which were made in order to produce device quality material. Each structure reported is referred to by its original (Central Facility) name and the important dimensions of the MQW region and particular growth features are given. Note that the well widths given here are estimated from a comparison of the room-temperature e1-hh1 exciton peak wavelength with the theoretical curve of $\lambda(\text{e1-hh1})$ vs well width in § 1.3.1. The barrier widths given are the nominal values specified in the design of the structures or are calculated on the basis of growth times and known growth rates relative to the GaAs well. Figures quoted for the applied electric field are simply an average value equal to the bias voltage divided by the total thickness of the intrinsic region.

2.5.1 SAMPLE CPM7 (55 x \approx 97Å WELL, \approx 100Å BARRIER)

As we have previously said, the major problem with initial structures was the high level of free carriers present in the MQW region, due to carbon acceptor impurities ($N_A \approx 1-2 \times 10^{16} \text{ cm}^{-3}$), intrinsic to the growth of the $\text{Al}_{0.30}\text{Ga}_{0.70}\text{As}$ barriers. In § 1.4 we described the effect of background doping on the uniformity of the electric field in the *p-i-n* diode; here in Figures 2.5.1.1 & 2.5.1.2 we can see the effect of the field non-uniformity on the absorption spectrum of the MQWs via the photocurrent. The design of this structure was based on that used by Wood et al [25] for the first MQW electro-absorption modulator. However, we could not observe the distinct red shift of the excitonic absorption edge which they had seen. Instead, the differential Stark shifts experienced by each well sum to produce an overall broadening of the edge, reminiscent of the bulk Franz-Keldysh effect [26], but with a higher

field sensitivity.

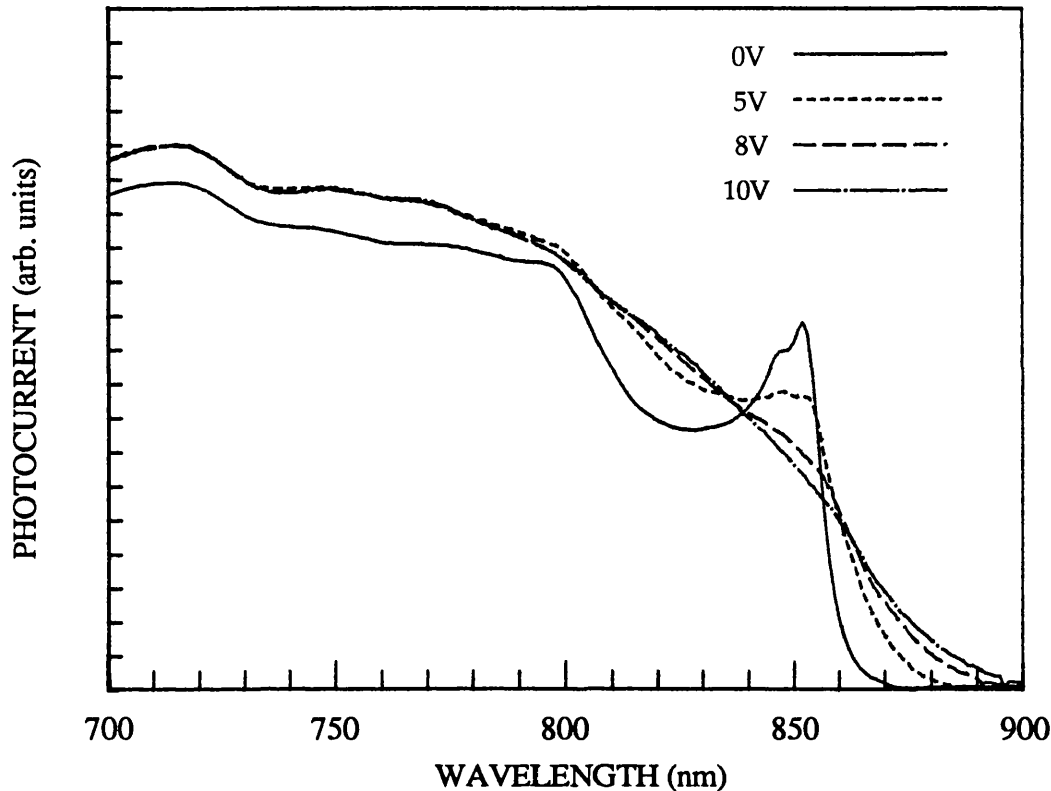


FIGURE 2.5.1.1:

Photocurrent spectra for MQW structure CPM7 (100Å wells) taken at room temperature.

In Fig. 2.5.1.1 we have plotted the raw photocurrent spectra. At zero bias close to 850nm there are features which we ascribe to the $n=1$ heavy- and light-hole excitons, but which are not well resolved compared to the data for MBE-grown material which existed at the time this structure was grown [25]. This loss of resolution may be due to the inhomogeneity of the internal field, or thickness variations (both within the plane of a single well, and from well to well), or a combination of the two. In this figure it can be seen that the general level of the photocurrent increases from zero bias up to $\approx 5V$ then saturates. This is a standard observation in $p-i-n$ diodes where the intrinsic doping is not ideally low. As bias increases, the depletion region will extend further and further into the undoped region, increasing the probability that photo-generated free carriers will reach the doped contact regions under the influence of the applied field.

It is seemingly not necessary for the undoped region to be fully depleted for photocurrent to be detected. In Fig. 2.5.1.2 below we show the

calculated background doping profile in the MQW region of this material. The calculation is based on the measurement of the bias dependence of the device capacitance. Referring back to Fig. 1.4.2, we note that the unbiased depletion depth for a device with an intrinsic doping level of $\approx 1-1.5 \times 10^{16} \text{ cm}^{-3}$, which we see here, is only $\approx 0.5 \mu\text{m}$, yet we clearly observe a photocurrent. There must therefore be some transport mechanism, for example diffusion, which permits carriers to pass through the undepleted part of the i-region where there is no driving field.

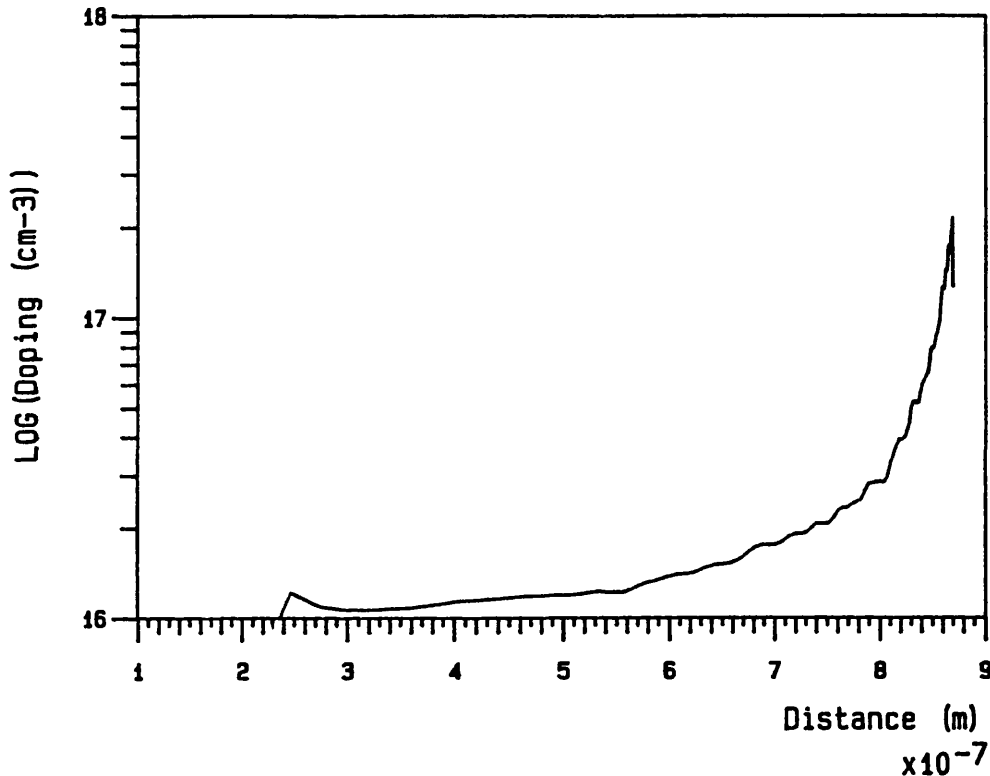


FIGURE 2.5.1.2:

The doping level in the undoped region of the MQW *p-i-n* diode CPM7, as determined by C-V measurements.

For this particular device C-V measurements indicate full depletion at 8–10V. The quantum efficiency, however, has saturated at $\approx 5\%$. The exact nature of the transport process is not clear as the situation is complicated in MQWs by the AlGaAs barriers, which obstruct the movement of photo-generated free carriers in the direction of the applied field (normal to the plane of the wells). It has been proposed that the escape of electrons and holes is via a combination of phonon interactions and tunnelling from higher-lying confined states into which the free carriers are scattered [27], and from which the tunnelling probability will

be significantly greater than for the low-lying states. In all the measurements presented here we are not specifically concerned with how carriers reach the contacts to produce a photocurrent, but we can make some qualitative comments on the quantum efficiency as related to the material quality and applied bias.

In Figure 2.5.1.3 we have scaled up the low bias spectra to account for the lower quantum efficiencies in order to make the extent of the field-induced changes in the absorption edge more clear. The photocurrent values for each bias are matched at a wavelength where no excitonic effects are seen and thus where no significant electro-absorptive changes are expected.

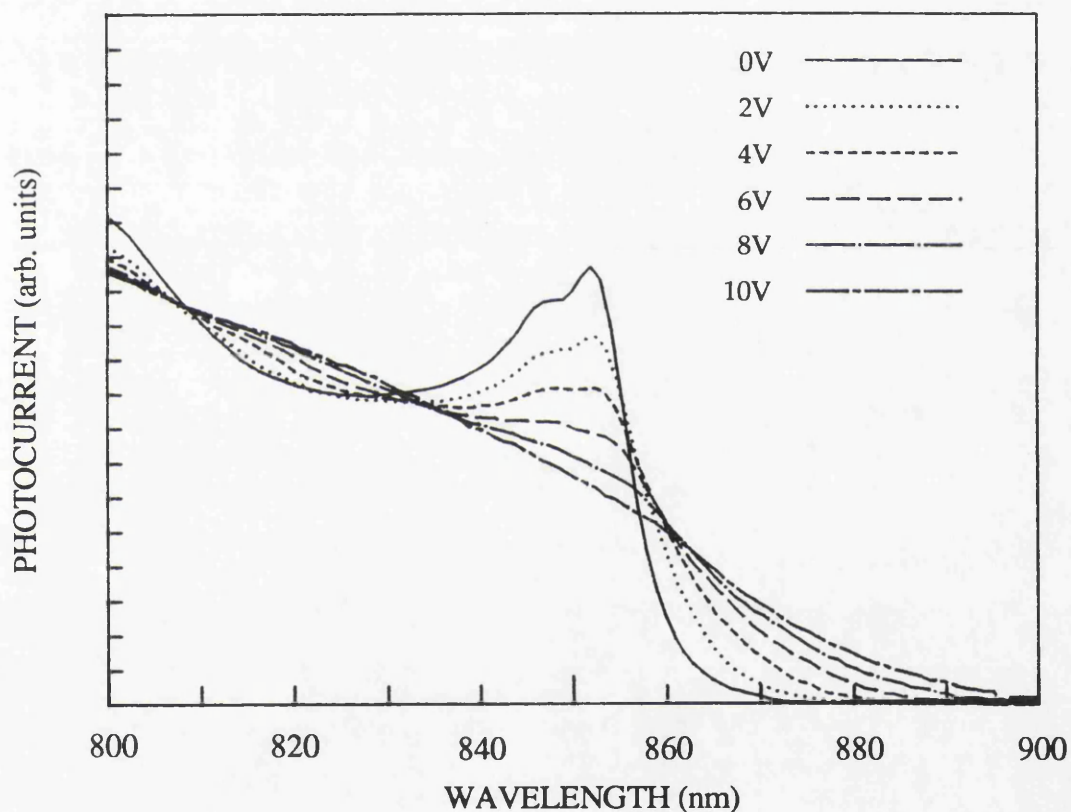


FIGURE 2.5.1.3:
Photocurrent spectra for CPM7 scaled to remove variation due to quantum efficiency at low bias.

Even at 4V, where excitonic features are still just visible, there is very little apparent shift. It is therefore likely that the wells which contribute to the peak which remains reasonably well-defined close to 850nm at 4V are in the low field region of the MQW structure. These spectra correlate well with the modelled spectra of Fig. 1.4.3.1, with a background doping level of 10^{16} cm^{-3} .

2.5.2 SAMPLE CPM147 (25 x $\approx 90\text{\AA}$ WELL, $\approx 100\text{\AA}$ BARRIER)

Having seen the problems with doping broadening in the CPM7 structure, we first decided to simply reduce the total thickness of the MQW region in order to reduce the extent of the variation in the internal electric field over the quantum wells. However, with hindsight, this line of reasoning is slightly erroneous. By halving the thickness of the MQW region we simply reduce the bias required for full depletion. The slope of the electric field is not reduced since it depends only on the background doping level. Thus for this device at full depletion we should only expect to see roughly the same broadened spectrum as for the CPM7 structure at its half-depletion voltage, without the effect of the extra undepleted wells which see no field.

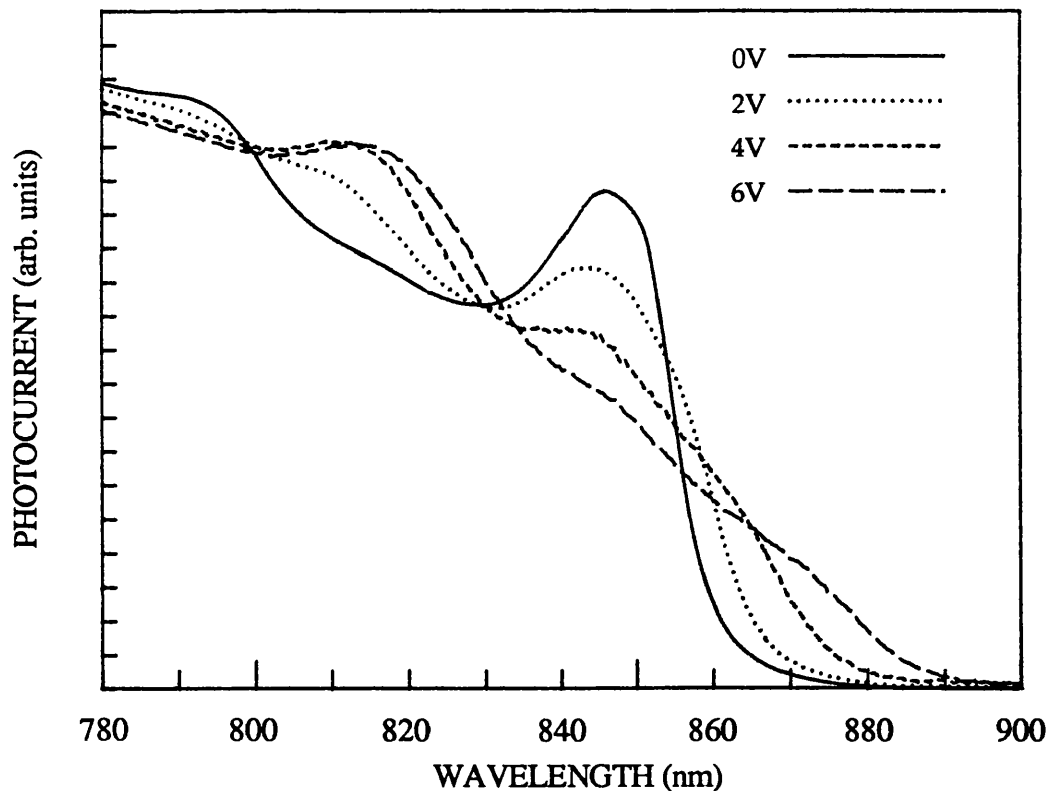


FIGURE 2.5.2:
Room-temperature photocurrent spectra for sample CPM 147 ($\approx 100\text{\AA}$ wells).

This is confirmed in Figure 2.5.2, where it is noticeable that the bias dependence of the quantum efficiency has been eliminated, but the spectra are still dominated by field-broadening of the absorption edge. In fact the excitonic peak is, if anything, less well defined than for the CPM7 structure at low bias. One possible explanation for this is that, as we have

already suggested, the apparent heavy- and light-hole excitonic features just visible in the CPM7 spectra at low biases are due to the quantum wells which are experiencing electric fields close to zero. In this sample, even at zero bias, all the wells will fall within the depleted (finite field) region in which the maximum electric field will have increased compared to the CPM7 structure. (See Fig. 1.4.2. Assuming that the background doping levels are the same in both cases, then the slope of the internal electric field remains the same. The built-in voltage across the intrinsic region must also be the same, so the maximum electric field must increase as the thickness of the i-region goes down in order to maintain the total area under the electric field profile.). So for the CPM147 sample the net absorption spectrum will be the sum of 25 differentially shifted spectra, the relative shifts being greater than for CPM7 because of the higher average field, with no contributions from wells experiencing close to zero field.

2.5.3 SAMPLE CPM244 ($100 \times \approx 51\text{\AA}$ WELL, $\approx 60\text{\AA}$ BARRIER)

The next approach to overcoming the i-doping problem was to reduce the quantum well width. The thinking behind this was that the exciton binding energy for the narrower well would be increased and in theory should be retained to higher electric fields, which might allow a clear quantum-confined Stark effect (QCSE) to be observed. What we see in Fig. 2.5.3. is obviously not the case. The bias dependence of the quantum efficiency has been re-introduced by growing $\approx 1\mu\text{m}$ of MQWs once more. In this case the barrier thickness was also reduced to keep the average intrinsic doping at the same level as in previous devices.

The heavy- and light-hole excitons are now clearly resolved, which is as expected since their energy separation increases with decreasing well width. Also, the broadening at low fields due to field variation will be reduced in this case since the shift of the exciton is reduced for narrower wells. However, the broadening due to well width fluctuations will increase, since a typical well:barrier interface roughness of ± 1 monolayer represents a larger fractional well width fluctuation the narrower the well.

It may well be that the underlying excitonic linewidth for the wells in this structure is broader than for the CPM7 structure. If we consider the

height of the hh excitonic transition relative to the flat continuum, it is reduced here compared to the low bias CPM7 data, indicating perhaps a loss of oscillator strength, when we might have expected an increase (The reduced dimensions of the well should give a greater spatial overlap of electron and hole wavefunctions).

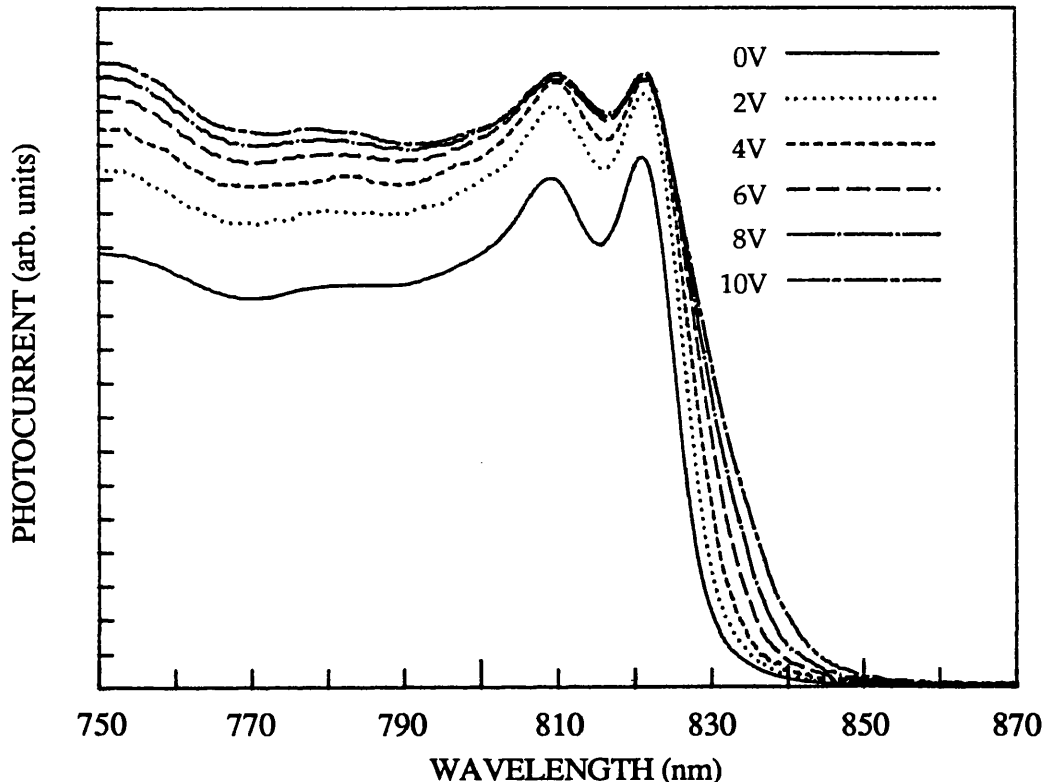


FIGURE 2.5.3:
Room-temperature photocurrent spectra for sample CPM244 (51 Å wells).

Again we see no shift of the absorption edge, merely a broadening, and the changes which do occur are over a noticeably smaller spectral region than for the CPM7 device, where the field per volt is the same. However a maximum bias of only 10V was applied to the devices which were tested from this sample, so it is probable that the maximum applied field was not high enough to induce a significant Stark shift of the excitons in all the wells.

2.5.4 SAMPLE CPM363 (60 x \approx 100 Å WELL, \approx 60 Å BARRIER)

Being still unable to directly engineer a reduction in the MQW intrinsic doping at this time, we then attempted to effectively reduce it by reducing

the barrier width relative to the well width, the AlGaAs barrier being the source of the background impurity. It was felt that the reduction of the AlGaAs barrier to $\approx 60\text{\AA}$ would still prevent electronic coupling between wells and preserve the QCSE, since with the CPM244 sample, where any coupling should be stronger because of the narrower wells, excitons were still resolvable with this reduced barrier width. With the corresponding increase in the proportion of the essentially undoped GaAs material, the average intrinsic doping should be only $\approx 75\%$ of its previous level, and therefore reduce the exciton broadening under bias.

The photocurrent spectra in Fig. 2.5.4 show an improvement in the zero-bias spectrum, with light and heavy hole excitons more clearly resolved compared to the previous structures with this well width. The $e2\text{-}hh2$ exciton (at $\approx 800\text{nm}$) is also more prominent than before. This suggests some improvement in sample quality, especially in view of the fact that this MQW structure is $\approx 1\mu\text{m}$ thick.

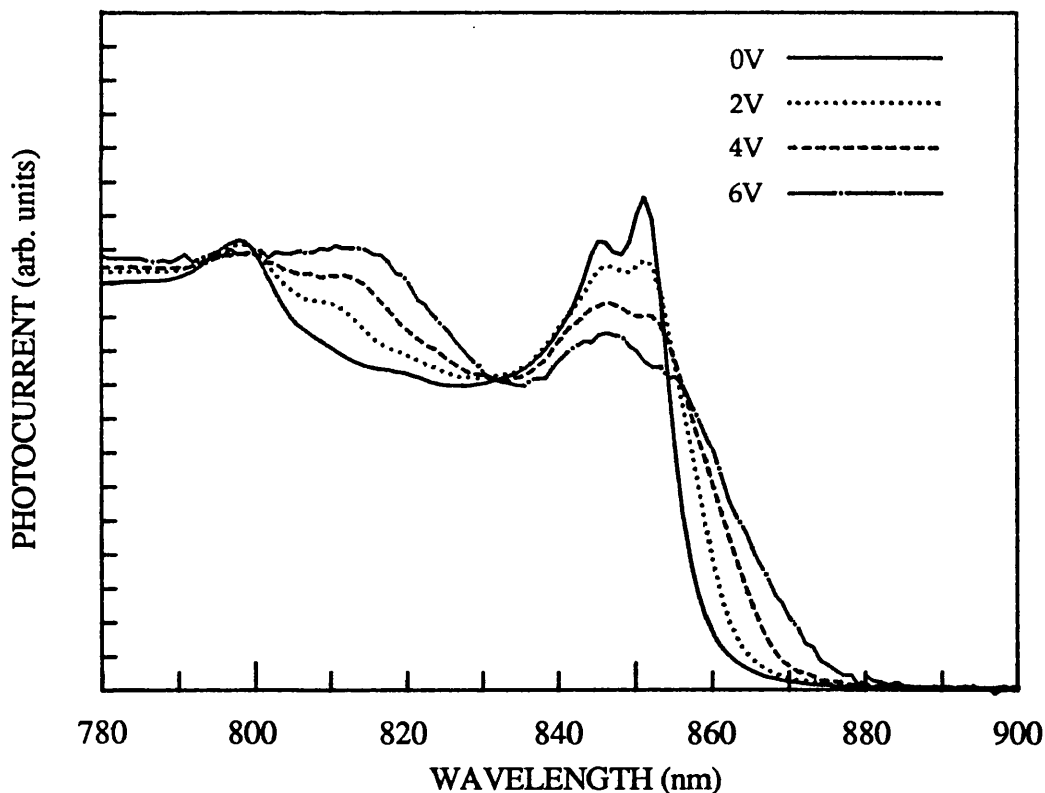


FIGURE 2.5.4:
Room-temperature photocurrent spectra for sample CPM363 (100\AA wells).

However, the biased spectra do not show any significant improvement. There is no clear shift of the excitonic edge – broadening still dominates, although it appears to be not quite so severe as for the CPM7 structure for

example. Again the background doping is the problem. The C-V profile for this sample indicates that the doping is as low as $4 \times 10^{15} \text{ cm}^{-3}$ in some parts of the i-region, but climbs to the high 10^{15} s in other areas, the effects of which will be more prominent.

2.5.5. SAMPLES CPM401 & 405 (50/60 \times \approx 85/87Å WELL, \approx 60Å BARRIER)

The conclusion from the data which have already been presented in this section was that the only way of obtaining clear, strong quantum-confined Stark shifts in *p-i-n* modulator structures was to somehow produce significantly lower doped AlGaAs than had been observed so far. This was eventually achieved by securing a supply of purer metalorganic reagents for the Ga and Al, drying of the arsine source and a lowering of the growth temperature for the MQW part of the structure. The full details of the growth optimization have been described by Roberts et al. [28].

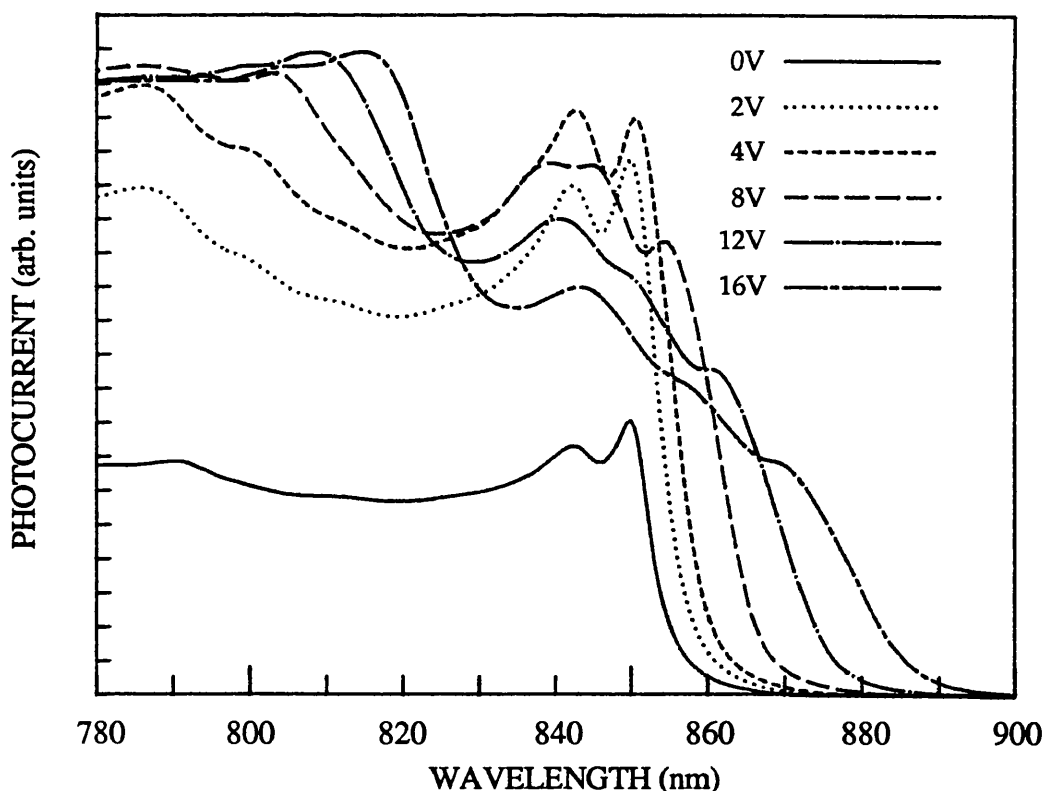


FIGURE 2.5.5.1:

Room-temperature photocurrent spectra for sample CPM405 (\approx 87Å wells).

In Fig. 2.5.5.1 we see the first evidence of improved growth. The CPM405

spectra show an obvious sharpening up of the biased excitonic features and a clear shift in response to an applied field. This was, to our knowledge, the first clear observation of the QCSE in a GaAs-AlGaAs MQW *p-i-n* diode grown by MOVPE and is reported in more detail in Ref. [29].

The splitting of the light- and heavy-hole excitons at the absorption edge is now very clear and they remain resolvable up to fields of more than 10^5 V.cm⁻¹. Another indication of the material quality is the emergence of so-called "forbidden" excitons in the 800-810nm range with increasing bias. These peaks are due to transitions between the hh and lh $n=1$ levels and the electron $n=2$ level (e2-hh1, e2-lh1). They are forbidden in the flat band condition because of the orthogonality of wavefunctions for a transition requiring $\Delta n=1$. The presence of an electric field, however, tilts the quantum wells, polarizing electron and hole wave functions towards opposite sides of the wells in such a way that increasing spatial overlap of wavefunctions occurs for these previously disallowed excitons. Another forbidden transition can be seen growing on the high energy side of the e1-lh1 exciton. This can be identified as the e1-hh2 exciton.

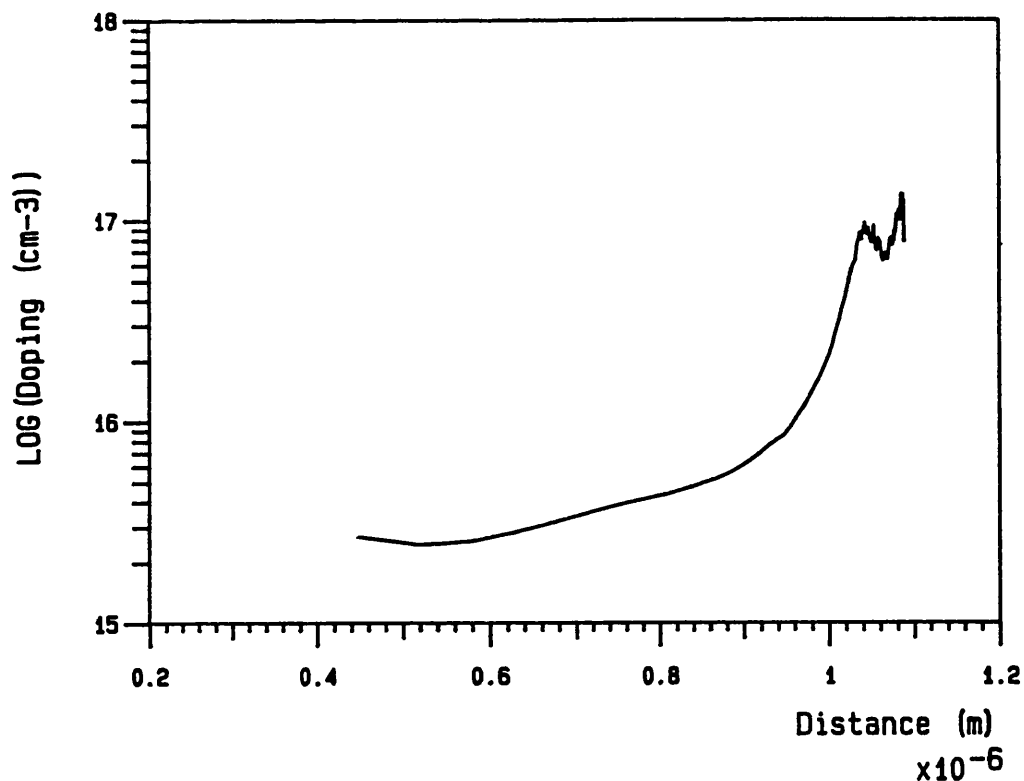


FIGURE 2.5.5.2:

Intrinsic doping profile of the improved MQW *p-i-n* CPM405, with the MQW grown at a lower temperature in order to reduce impurity levels.

That the improved performance is due to the reduction of background impurities is confirmed by C-V measurements (see Fig. 2.5.5.2) which indicate a doping level of $\approx 3\text{-}5 \times 10^{15} \text{ cm}^{-3}$. The differences between the spectra for this sample and those for CPM7 agree well with the previously modelled effects of background doping (§ 1.4).

As an indication of the amount of field-broadening which still remains in the CPM405 photocurrent response, a sample with the same well and barrier dimensions, but 10 fewer wells, was grown just prior to this. The photocurrent spectra for this structure, CPM401, are shown in Fig. 2.5.5.3.

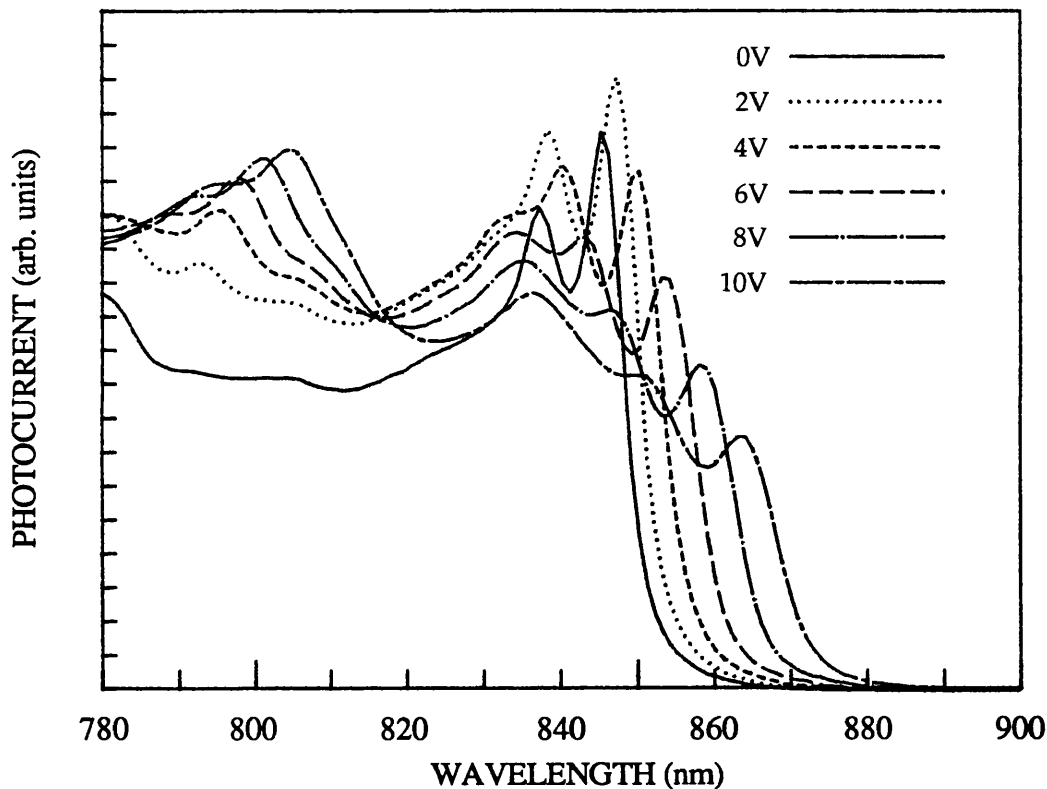


FIGURE 2.5.5.3:

Room-temperature photocurrent spectra for sample CPM401 ($\approx 85\text{\AA}$ wells).

According to C-V measurements the background doping is very similar to that of CPM405. However, there are some obvious differences in the spectra for the two samples grown under almost exactly the same conditions. The excitonic peaks in the CPM401 spectra are better resolved at zero bias and remain so with bias if we compare, for example, the 10V curves for the two cases. Also, the quantum efficiency for the sample with fewer wells requires significantly less bias to saturate. The simple calculation of Fig 1.4.2 predicts that full depletion should occur in

structures of this doping and thickness ($\approx 0.73\text{-}0.88\mu\text{m}$) at only $\approx 1\text{-}2\text{V}$, which agrees well with the CPM401 data.

It would appear that even after this reduction of the intrinsic doping, though the optical response of the devices has significantly improved, the doping level is still not quite low enough to avoid field-broadening effects when the total MQW thickness begins to approach $1\mu\text{m}$, which as we shall see later is a typical device requirement.

2.5.6 SAMPLE MV245 ($45 \times \approx 145\text{\AA}$ WELL, $\approx 53\text{\AA}$ BARRIER)

With material quality improved, at this stage of our investigations we were interested to determine whether there were any advantages to be gained from using quantum wells of widths other than the standard $90\text{-}100\text{\AA}$ which had been used by most other workers in this field up to that time. It was known theoretically that the wider the well, the greater the shift of the absorption edge with field, but also the greater the loss in strength of the exciton at the edge. With this sample containing 145\AA wells and the following one of 47\AA wells it was possible to make some initial qualitative comparison of the QCSE with the data for the CPM401/405 samples.

The photocurrent data for the 145\AA wells is shown in Fig. 2.5.6 (over page). We notice that there is no longer a resolvable splitting of the light- and heavy-hole excitons at the absorption edge, which is reasonable to expect considering the increased well width. Having increased the ratio of well to barrier material the effective background doping should be even lower than in the CPM401/405 structures. C-V measurements confirm this, giving a figure of $\approx 2\text{-}3 \times 10^{15} \text{cm}^{-3}$, and only $2\text{-}3\text{V}$ are needed to raise the quantum efficiency up to its maximum level. Even before reaching this point there are changes taking place in the photocurrent spectrum.

At only 1V the height of the $n=1$ exciton(s) relative to the $n=2$ continuum has decreased considerably, and other peaks, due to previously disallowed transitions, have begun to appear. The richer structure here compared to the case of the 87\AA wells is due to an increased number of quasi-bound states within the wider wells.

As the bias is increased the QCSE manifests itself more as a broadening of the absorption edge rather than a discernible shift, with the $n=1$ exciton

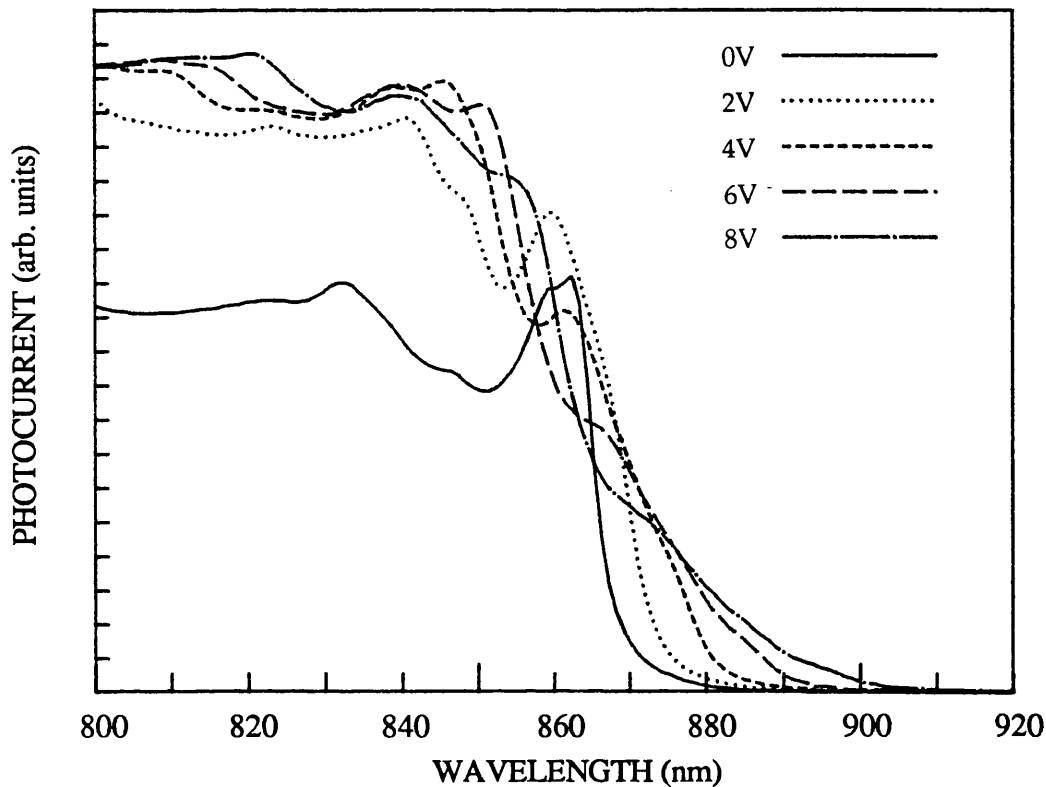


FIGURE 2.5.6.:
Room-temperature photocurrent spectra for MQW sample MV245 (145Å wells).

virtually disappearing at only 6-8V ($\approx 67\text{-}90 \text{ kV}\cdot\text{cm}^{-1}$). The most likely reason for this is that, even with the low background doping which is evident in this sample, the variation in the internal field is enough to separate spectrally the excitonic absorption in each well because of the increased sensitivity of the Stark shift to applied field with the wider wells¹. Added to that the excitonic oscillator strength will be reduced more easily with field as the electron and hole are more strongly polarized to opposite sides of the well.

The low-field shift and loss of oscillator strength in the exciton which exists at zero bias suggests the idea of using this type of structure in a different manner than the normal MQW transmission modulator, which switches off with bias as the exciton is Stark-shifted into the operating wavelength. That is, we operate at the wavelength of the unbiased exciton, quenching the absorption with bias, to make the device switch on. The potential of this mode of operation is assessed in Chapter 4.

¹In his Ph. D. thesis, my colleague Peter Stevens has calculated that by reducing the background doping for a $1\mu\text{m}$ MQW structure with 150\AA wells from 10^{17} cm^{-3} to $\approx 2 \times 10^{14} \text{ cm}^{-3}$, the maximum transmission change can be increased by a factor of 2. This is simply due to the reduction in background doping broadening. The same structure containing 100\AA wells shows little improvement in performance with this doping reduction.

2.5.7 SAMPLE MV246 ($75 \times \approx 47\text{\AA}$ WELL, $\approx 53\text{\AA}$ BARRIER)

In marked contrast to the spectra for the previous sample, and in line with theoretical predictions, with the reduction of the well width to only 47\AA we see in Fig. 2.5.7 that the zero-field excitons remain well resolved on the application of a field, but high bias voltages are needed to induce any sort of spectral shift. There is only a small shift of 3-4nm below 12V ($\approx 160\text{kV.cm}^{-1}$), and to observe any appreciable absorption changes at a wavelength well into the tail of the unbiased absorption edge we need to apply 16V ($\approx 213\text{ kV.cm}^{-1}$).

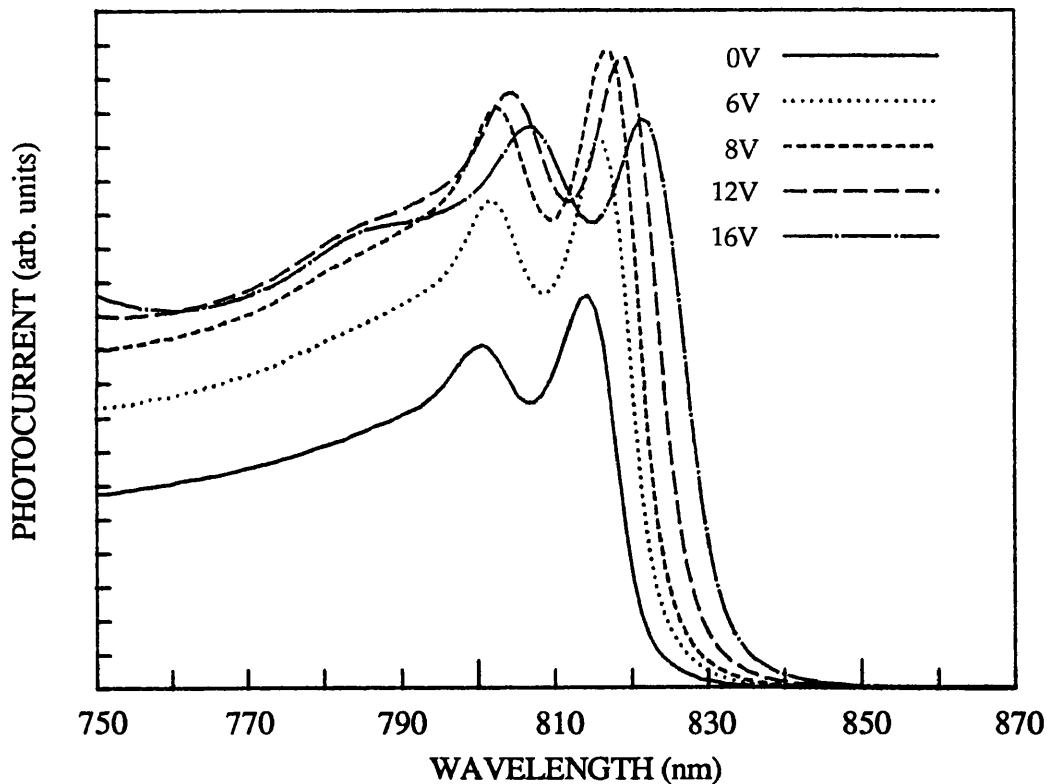


FIGURE 2.5.7:
Room-temperature photocurrent spectra for MQW sample MV246 (47\AA wells).

The MQW structure here is very similar to that of sample CPM244 (§ 2.5.3) in which we were unable to observe any Stark shift due to the limiting bias of 10V ($\approx 90\text{ kV.cm}^{-1}$) and the high background doping. Having achieved a general lowering of the background doping in the intrinsic region, and using only $\approx 0.75\text{ }\mu\text{m}$ of MQWs, we can actually discern a Stark shift at 10V with this sample, although the average field is $\approx 133\text{kV.cm}^{-1}$ in this case.

It is noticeable here that the quantum efficiency once again requires a

significant amount of bias to be applied before it saturates, levelling out at 8-10V compared with only 2-3V for the previous sample. This effect may be explained to some extent by the increase in the average background doping because of the higher proportion of barrier material in this MQW structure, almost twice that in the MV245 structure for example.

One problem which arises with narrow quantum wells is that the position of the absorption edge is more sensitive to well width. At only $\approx 50\text{\AA}$ thickness there are less than 20 monolayers of GaAs per well, so typical thickness fluctuations of around 1 monolayer have more effect. For this particular sample, in photocurrent and transmission measurements, we have found that the wavelength of the $n=1$ e-hh exciton was anywhere between 813-820nm, depending on the part of the sample from which devices were made.

This sample is assessed for its transmission modulation properties in Chapter 4, but it is already apparent from these photocurrent spectra that significant modulation will only be achieved at the expense of a high operating voltage, if at all.

2.5.8 SAMPLE MV301 (SINGLE $\approx 83\text{\AA}$ WELL)

A number of single well *p-i-n* diodes were grown with different well widths in order to observe the QCSE in the absence of the usual field-variation broadening associated with multiple wells. Fig. 2.5.8 shows the data for a single 83\AA well clad on either side by $\approx 0.4\mu\text{m}$ of undoped $\text{Al}_{0.3}\text{Ga}_{0.7}\text{As}$.

The spectra are generally similar to the multiple well CPM401 structure (§ 2.5.5) but notice that the exciton peaks are better resolved and higher relative to the continuum even under bias; a consequence of the reduced field-variation. The bias at 8V is equivalent to an average applied field of $\approx 100\text{kV.cm}^{-1}$. For this particular sample we see no bias dependence of the quantum efficiency, with an estimated background doping level of $2-3 \times 10^{15}\text{cm}^{-3}$.

In the limit of very thin absorbing regions, where $\alpha d \ll 1$, the expression for the photocurrent generated in a *p-i-n* diode (see Eq. 2.1) becomes:

$$I_{\text{ph}} = P(1 - R_f) \frac{\eta q \lambda}{hc} \alpha d \quad \dots(2.2)$$

since $1 - e^{-\alpha d} \approx \alpha d$. Thus, over a typical range of interest of around 60-100nm, with a flat input power spectrum and adjustment for the bias-dependence of the quantum efficiency, the photocurrent from a single quantum well will be a direct measure of the absorption coefficient,

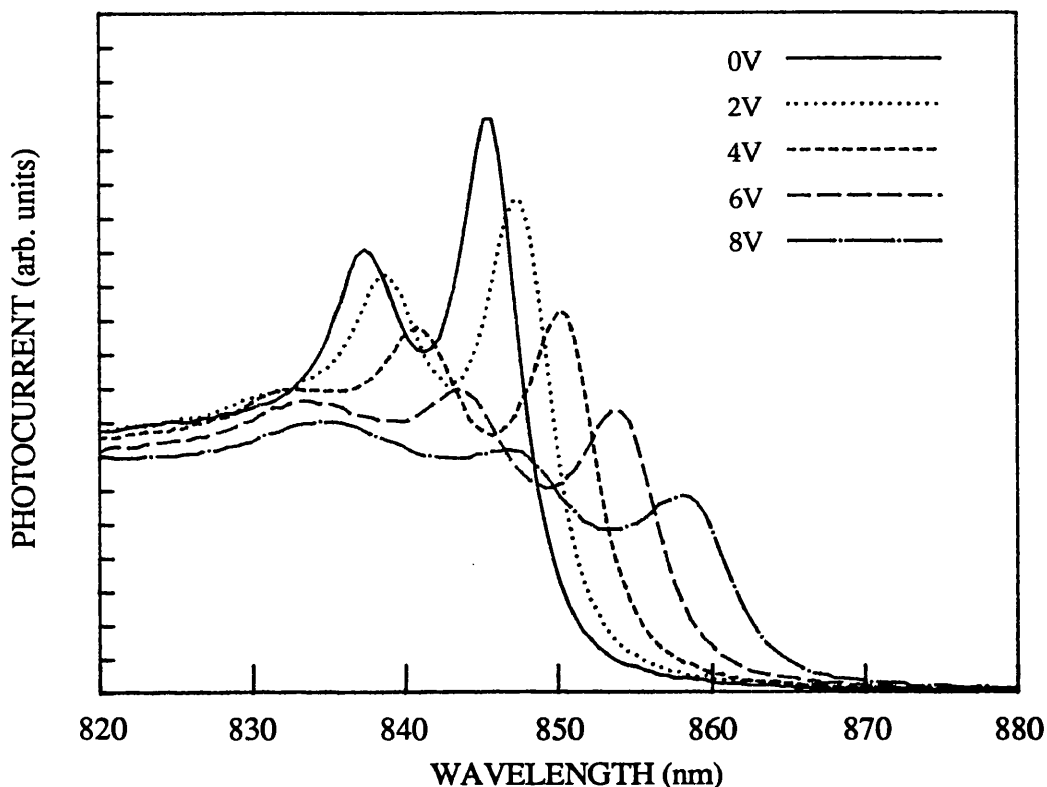


FIGURE 2.5.8:

Room-temperature photocurrent spectra for a *single* quantum well sample, MV301. The well width is estimated to be $\approx 83\text{\AA}$.

neglecting the small variations in R_f and λ . Furthermore, the biased spectra will be free of the field-variation broadening observed in samples with multiple wells. Providing the well is at the centre of a fully-depleted intrinsic region, the field at the quantum well will be simply the average electric field, given by $V/(\text{Intrinsic width})$, irrespective of the level of the background doping.

The growth of single QW *p-i-n* diodes is a useful technique for the assessment of the QCSE in material systems which are not yet fully developed enough to provide the very low doping or high structural uniformity which has been achieved in GaAs-AlGaAs MQWs, e.g. InGaAs-InP [30], which is the popular choice for devices intended to operate at the wavelengths of lowest loss in optical fibres. Measurements cannot be made accurately using transmission spectroscopy since the αd factor is far too low. Data such as that displayed here are useful in

modelling the ultimate performance of modulators containing multiple wells. As we shall discuss in Chapter 3, the single well photocurrent spectra can easily be rescaled to represent absorption, and broadening factors such as background doping and well width fluctuations incorporated into the model [31].

2.5.9 SAMPLES MV367 (77 x \approx 100Å WELL, \approx 35Å BARRIER) & MV370 (50 x \approx 85Å WELL, \approx 67Å BARRIER)

These two samples are considered together as an indication of the limit to which the AlGaAs barriers between the quantum wells may be reduced before the QCSE is lost, or at least severely degraded. We know that at zero field the coupling of quantized carrier states will increase as the barrier width decreases, and thus the excitonic oscillator strength will be reduced with the decrease in the overlap integral of the electron and hole wave functions.

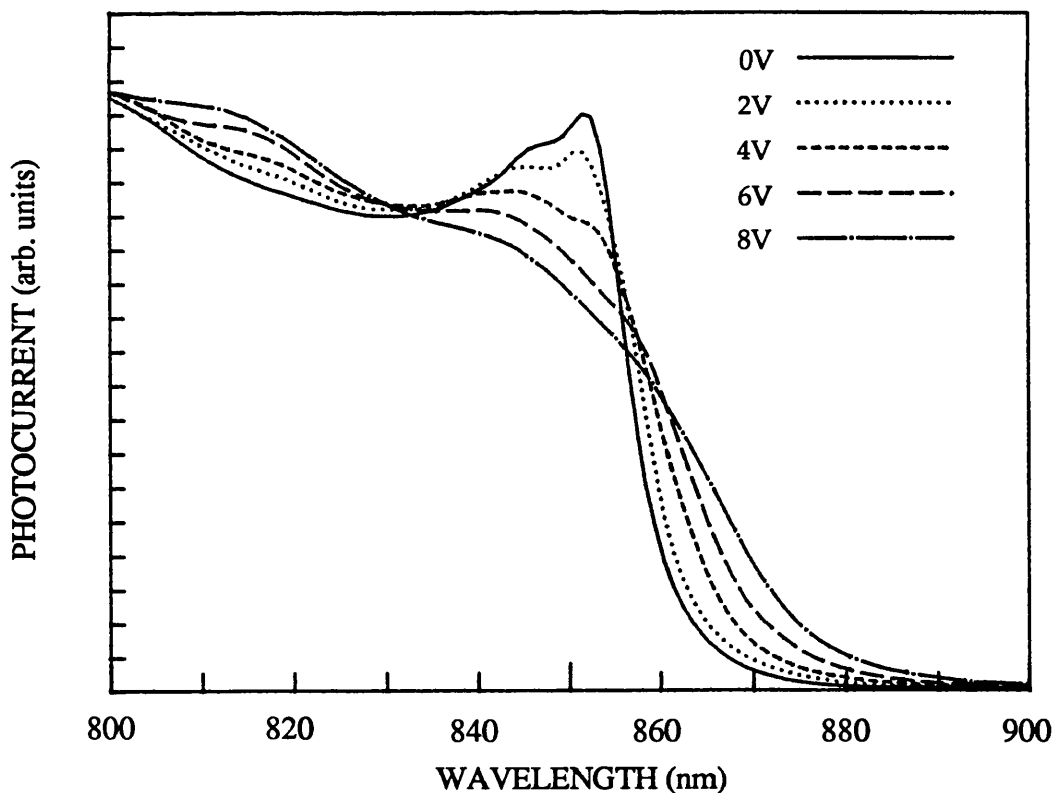


FIGURE 2.5.9.1:

Room-temperature photocurrent spectra for MQW sample MV367 (\approx 100Å wells), showing the exciton broadening effects of reducing the barriers to 30-35Å.

As an electric field is applied we expect the broadening due to tunnelling of electrons and holes to become dominant, since at some point the tunnelling time for one of the carriers out of the well will become comparable with the characteristic ionization time of the exciton due to phonon interactions, and the exciton will effectively cease to be created.

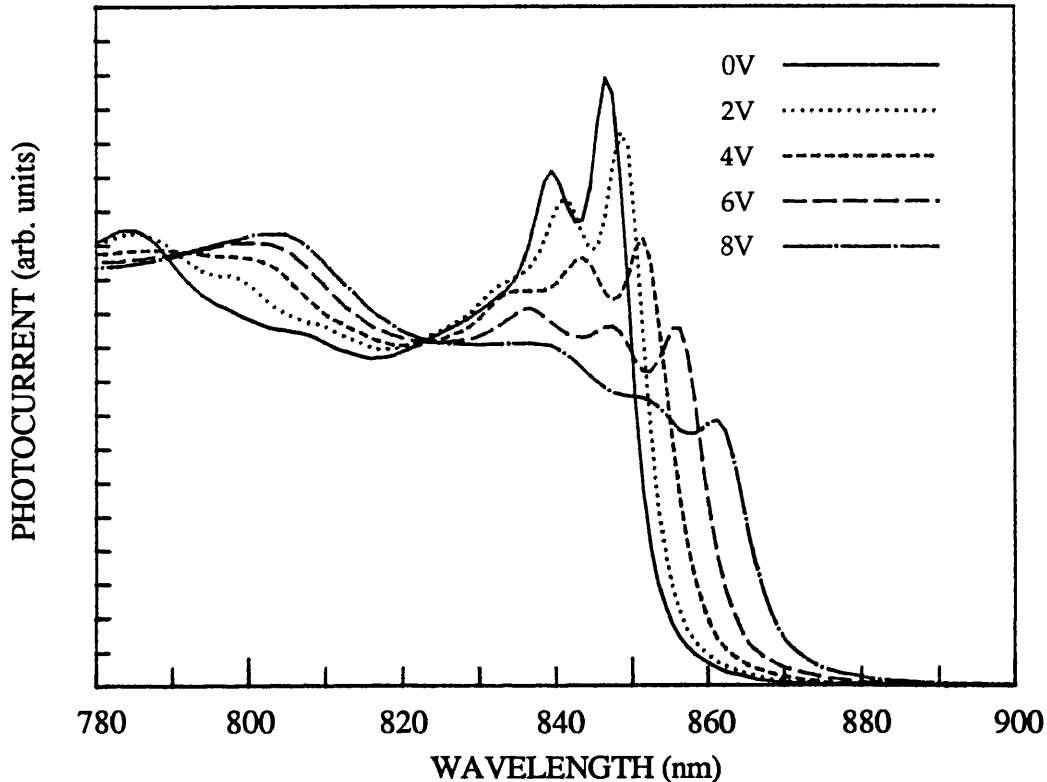


FIGURE 2.5.9.2:

Room-temperature photocurrent spectra for MQW sample MV370 ($\approx 85\text{\AA}$ wells). The barriers in this case are sufficiently thick to retain the quantum-confined Stark effect. To be compared with MV367 in Fig. 2.5.9.1.

The spectra for sample MV367 in Fig. 2.5.9.1 (previous page) clearly show broadening effects due to the reduction of the barrier to only 35\AA . The resolution of light- and heavy-hole excitons has been lost, although some evidence of the two separate transitions can still be seen. The height of the remnant excitonic peak has been strongly reduced relative to the $n=1$ continuum, and the absorption tail now extends well beyond 870nm . There is no visible shift in the absorption edge; instead the electro-absorptive changes appear as a broadening of the edge, very similar in fact to the first structure we looked at, CPM7. In this case, however, the lack of clear QCSE is not due to the background doping. This was estimated to be even lower than normal for this sample, being $\approx 1\text{-}2 \times 10^{15}\text{cm}^{-3}$, and

presumably improved by the lower than usual proportion of barrier material (which is effectively the sole contribution to the intrinsic doping).

Just to confirm that there were no material growth problems contributing to the MV367 properties, sample MV370, which was grown very soon after MV367, has barriers of 67\AA and in Fig. 2.5.9.2 on the previous page shows exactly the same clear QCSE as other MQW samples which have barriers thick enough for isolation of the individual wells. Interestingly, the quantum efficiency in this sample is very close to its maximum value at zero bias. The photocurrent only begins to be reduced when more than $\approx 0.6\text{V}$ is applied in the forward direction.

2.5.10 SAMPLE CB93 ($100 \times \approx 100\text{\AA}$ WELL, $\approx 60\text{\AA}$ BARRIER)

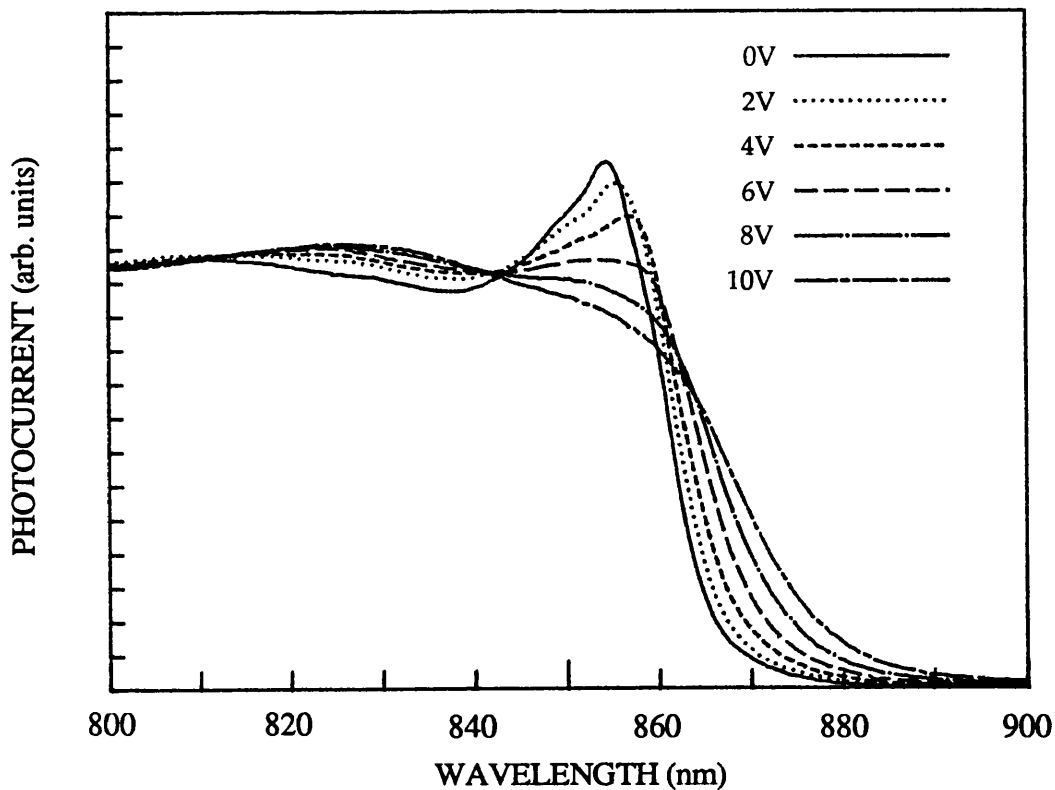


FIGURE 2.5.10:

Room-temperature photocurrent spectra for MQW sample CB93 ($\approx 100\text{\AA}$ wells). Shows the effect of growing a thick structure (100 wells) at too high a growth rate ($\approx 3\mu\text{m/hr}$), even when the intrinsic doping level is as low as $2 \times 10^{15} \text{ cm}^{-3}$.

This final set of data illustrates the problem of growing MQW *p-i-n* structures too thick and at too high a growth rate. The field-variation

broadening becomes apparent, even though the C-V profile indicates a background doping level of only $2-4 \times 10^{15} \text{ cm}^{-3}$, simply because we are once again in a situation where the internal field falls to zero within the MQW region. As we see in Fig. 2.5.10 (previous page), the effect is a loss of resolution of the light- and heavy-hole excitons, a lowering of the height of the exciton relative to the $n=1$ continuum, and a Stark shift which, although just apparent up to 4V, rapidly becomes dominated by field-variation broadening. The results are not dissimilar to the data for sample MV367, where the strong broadening is due to a reduced barrier thickness leading to interwell coupling of the confined states.

The first problem is that the whole structure is now $\approx 1.6\mu\text{m}$ thick and even with the lowest estimate of the background doping the depletion distance is only $\approx 0.9\mu\text{m}$ at zero bias. Hence, when bias is applied the variation in the electric field will be similar to that in previous, more highly doped structures with thinner MQW regions (e.g. CPM7, CPM363). This will be one broadening component. Further exciton line broadening will be due to non-abrupt interfaces and well width fluctuations. The gas switching in the MOVPE system is only capable of $\approx 1\text{s}$ cut-off for the Al source (trimethyl aluminium). In this case the growth rate was $\approx 3\mu\text{m/hr}$ or roughly 8\AA/s , so if the growth time is defined as 13 ± 1 seconds the well width will be somewhere in the range $96-112\text{\AA}$, and the interfaces will become rather ill-defined. This introduces a broadening of the excitonic features, due to well-width fluctuations both in the plane of each individual well and from well to well through the whole MQW structure.

2.6 PHOTOCURRENT STUDIES OF MBE-GROWN DEVICES

We shall restrict the discussion of MBE-grown material to two particular samples, the first of which provided useful source data for calculations of electro-absorption and electro-refraction (see §§ 3.4, 3.5), and the second of which is of the highest quality required of MQW *p-i-n* diode structures for optical modulation.

2.6.1 SAMPLE KLB461 (25 x $\approx 100\text{\AA}$ WELL, $\approx 100\text{\AA}$ BARRIER(40% Al))

This was the first MQW sample in which we were able to observe the QCSE clearly. It was known at the time that the MBE system in which this structure was grown was capable of producing high quality QW laser material [2] with background impurity levels of $\approx 5 \times 10^{15} \text{ cm}^{-3}$. This is confirmed by the C-V profile for the KLB461 sample shown below in Fig. 2.6.1.1.

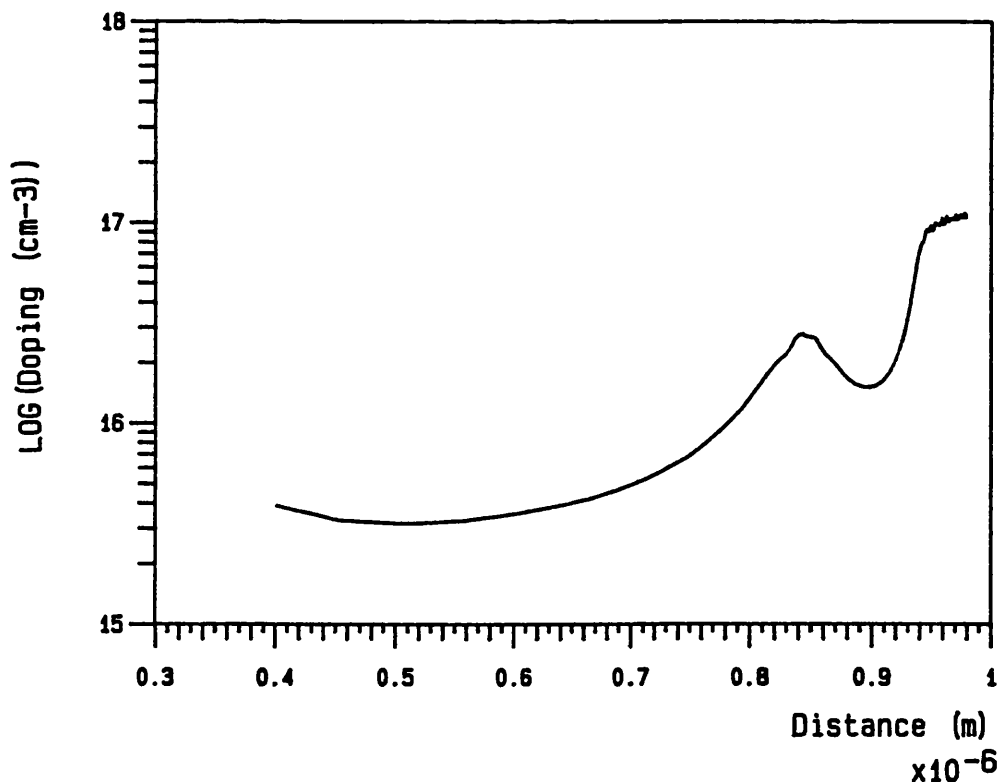


FIGURE 2.6.1.1:

Doping profile of MQW region of sample KLB461 as derived from C-V measurements.

Having already observed strong excitonic broadening in the photocurrent spectra of MOVPE-grown samples, we were aware that even this lower

level of doping for the MBE material would broaden the spectra for thick MQW structures. Therefore the sample was grown with only 25 wells as a compromise between reducing doping broadening and having enough absorbing material to observe a strong photocurrent signal or transmission change.

The room-temperature photocurrent spectra, displayed below in Fig. 2.6.1.1, clearly show the e1-hh1 and e1-lh1 excitons at the unbiased absorption edge, with the e2-hh2 peak at the n=2 sub-band edge close to 790nm.

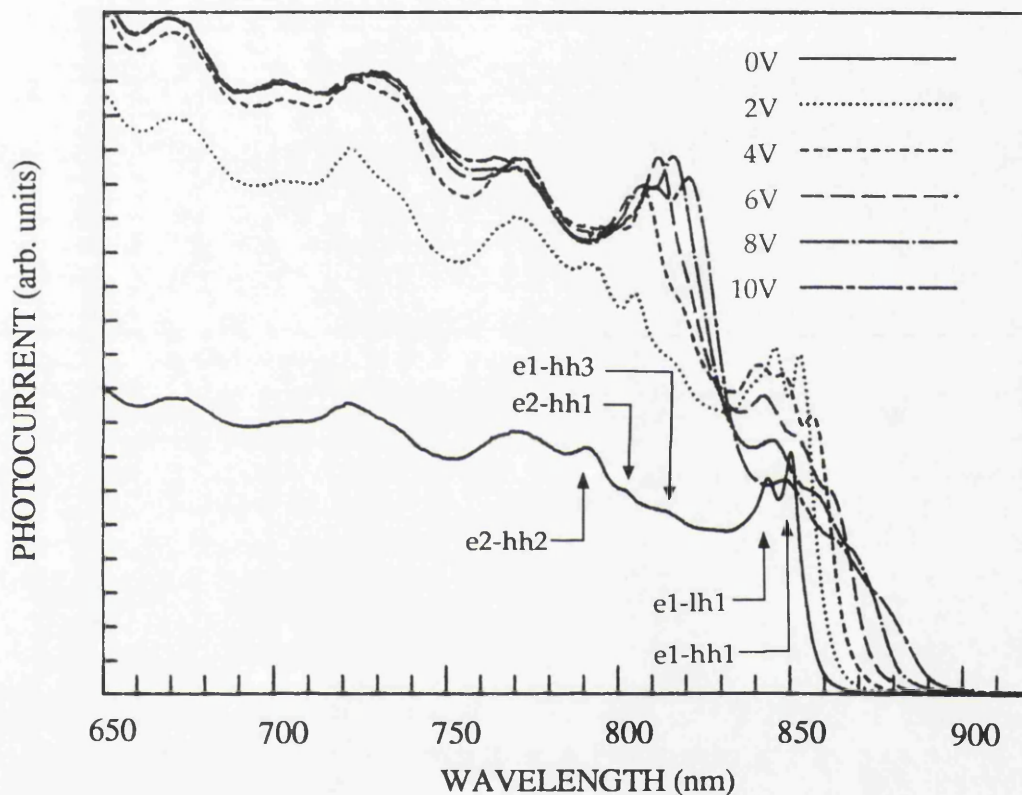


FIGURE 2.6.1.2:

Un-normalized room-temperature photocurrent spectra for sample KLB461 ($\approx 100\text{\AA}$ wells). Sample grown by M.Whitehead under the supervision of Dr. K. Woodbridge.

There is little change in the spectral features at wavelengths below $\approx 780\text{nm}$, which is as expected, the lowest lying confined levels being most sensitive to the changes in the potential. We tentatively ascribe the peak at $\approx 720\text{nm}$ to the e3-hh3 transition. Between the n=1 and n=2 sub-band edges at zero bias there is evidence of two further transitions. The lower energy one would appear to be the e1-hh3 exciton, which is weakly allowed for a finite potential well even at zero field. The higher energy transition is the normally forbidden e2-hh1 exciton. The peak appears

even in the unbiased spectrum because of the built-in field of the *p-i-n* diode in which the wells are embedded. As the electric field is increased, the strength of this transition grows markedly, whilst the originally allowed excitons lose their strength to the extent that the spectra at the highest biases are dominated by the e2-hh1 peak. At 10V the average applied field is estimated to be $\approx 167\text{kV/cm}$, since the total width of the intrinsic region is padded out by buffer regions of 500\AA undoped $\text{Al}_{0.4}\text{Ga}_{0.6}\text{As}$ either side of the MQWs.

These effects have previously been observed in MQWs at low temperatures [19, 20] and are due to changes in overlap integral between the various electron and hole wavefunctions as the potential profile of the well is skewed by an applied bias and carriers are polarized to opposite sides of the well.

For some of the MOVPE-grown samples we observed photocurrent spectra even though the diodes were not fully depleted. The depletion region should, in principle, extend completely across the MQWs in this structure even at zero bias (see Fig 1.4.2 for the zero bias field profile for a $5 \times 10^{15} \text{ cm}^{-3}$ impurity level). However, there is a significant bias dependence in the quantum efficiency which only saturates at about 5V, suggesting that the barriers are preventing carriers escaping from the wells before recombination. This is possibly due to the increased barrier height in this sample compared with the MOVPE-grown structures. We chose an Al mole fraction of 0.4 for the 100\AA barriers in an attempt to minimize any coupling between adjacent wells. The higher barrier will reduce the probability of carrier escape from the well for both thermal and tunnelling mechanisms. It may also explain the stronger forbidden excitons seen in these spectra compared to other samples. Increasing the Al mole fraction from the usual 0.3 should make the $n=2$ states in the well more highly confined, with longer tunnelling lifetimes.

Although the spectra for this sample show a clear QCSE, the response of the absorption to an applied field is not ideal. The excitons at the absorption edge are of most interest to us for modulation purposes, and there is still doping broadening apparent in the biased spectra, even for this doping level with only 25 wells. Low temperature (4K) photocurrent spectra [32] have confirmed this by showing increasingly asymmetric exciton lines with applied field.

There have also been problems in fitting the observed QCSE with

theory. A model for the MQW absorption spectrum [31] was developed by Peter Stevens of UCL, based on tunnelling resonance calculations which had previously been shown to give accurate field-dependent energy levels [33], and incorporating broadening effects such as phonon interactions, well width fluctuations and background doping. In the next section we show the model to give good agreement with the spectra for a much higher quality sample. Here, however, we see in Fig. 2.6.1.3 that there is some discrepancy between the experimental and theoretical Stark shifts for the e1-hh1 exciton peak. The well width has been derived from the unbiased e1-hh1 photocurrent peak. The actual shape of the curve is reasonably correct and a good fit can be obtained if a voltage offset of 1.4V is subtracted from the experimental bias, shifting the data points to the left by $\approx 20\text{kV/cm}$. The reason for this offset has not become clear, but it is not required for higher quality samples

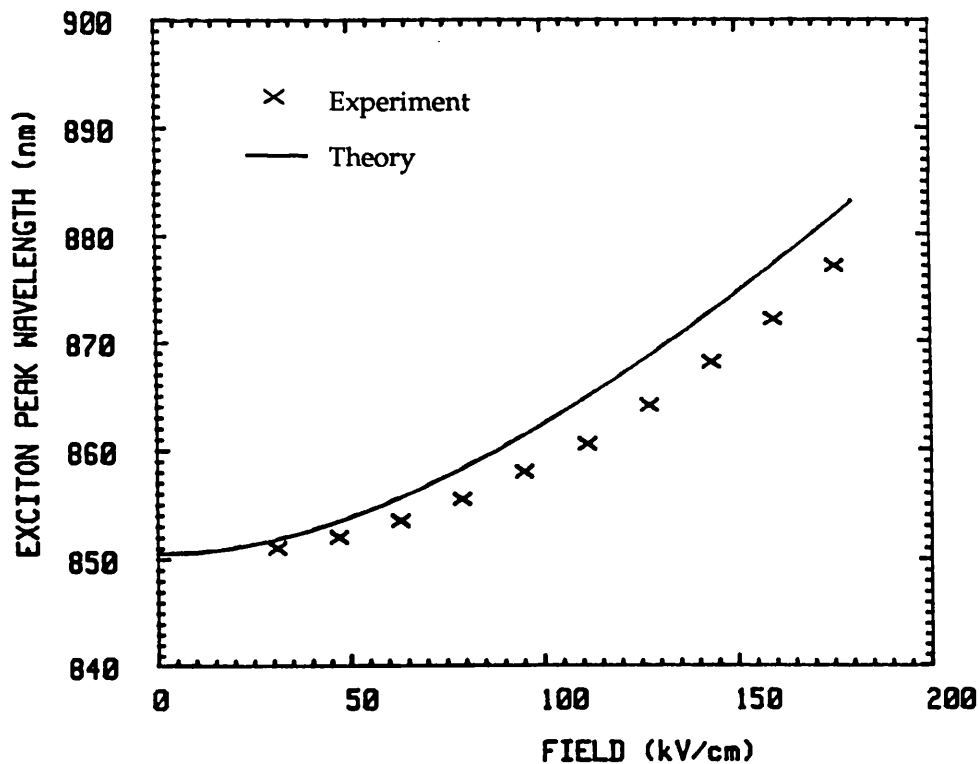


FIGURE 2.6.1.3:

Calculated and observed Stark shift of the e1-hh1 exciton peak for the KLB461 MQW sample ($\approx 100\text{\AA}$ wells). Calculated data supplied by Peter Stevens, UCL.

One final point which becomes relevant in the absorption calculations of the next chapter is the apparent wavelength dependence of the quantum efficiency for the low bias spectra in Fig. 2.6.1.2. If we compare the

photocurrent levels for the $n=1$ and $n=3$ continuum regions we find that at 700nm the photocurrent increases by a factor of ≈ 2.2 as bias changes from 0V to 6V, whereas the increase at 830nm is only ≈ 1.9 . At these two wavelengths the change in absorption with field should be very small, since there are no field-sensitive excitonic peaks. Therefore the difference must be due to quantum efficiency variation. It is not clear what the reason for this is. For shorter wavelengths we would expect a higher escape probability for carriers out of the well as they see less of a barrier, especially at low fields, but the difference in the photocurrent scaling factors seems to suggest that the quantum efficiency at short wavelengths is lower than that at the $n=1$ continuum at low bias. The alternative is that somehow the quantum efficiency around 830nm is enhanced at low bias, which is equally difficult to contemplate. We are assuming that the quantum efficiency is roughly the same for the whole of the spectrum at high bias. Whatever the reason for this effect, it means that we cannot simply scale up the low bias spectra in order to eliminate the quantum efficiency variation for the calculation of absorption spectra. This will be discussed further in §§ 3.4.1, 3.4.2. As with the Stark shift discrepancy, this effect has not been seen in higher quality samples.

2.6.2 SAMPLE M33 (20 \times $\approx 100\text{\AA}$ WELL, $\approx 100\text{\AA}$ BARRIER)

We saw in § 1.4 from the modelled spectra provided by Peter Stevens [31] that, at least for wells of $\approx 100\text{\AA}$ and total MQW thicknesses of $\approx 1\mu\text{m}$ or less, the electro-absorptive effects should become independent of background doping at levels below $\approx 1 \times 10^{15} \text{ cm}^{-3}$. This sample, grown in what was a newly-commissioned Varian Gen II MBE system at Philips Research Labs., has a background doping as low as $\approx 5 \times 10^{14} \text{ cm}^{-3}$. The profile from C-V measurements is shown over the page in Fig. 2.6.2.1. With only 20 wells in the intrinsic region the field variation across the MQW is very small at this doping level. Hence, in the biased photocurrent spectra in Fig. 2.6.2.2, we find that the $e1\text{-}hh1$ exciton remains much better resolved as it is field-shifted than is the case for the KLB461 sample. Although not shown here, we have observed a well-resolved $e1\text{-}hh1$ exciton shifted as far as 900nm at $\approx 20\text{V}$ bias. At zero bias the $e1\text{-}hh1$ peak stands higher above the continuum, indicating also that well width fluctuation broadening is reduced, giving a higher average absorption for the peak.

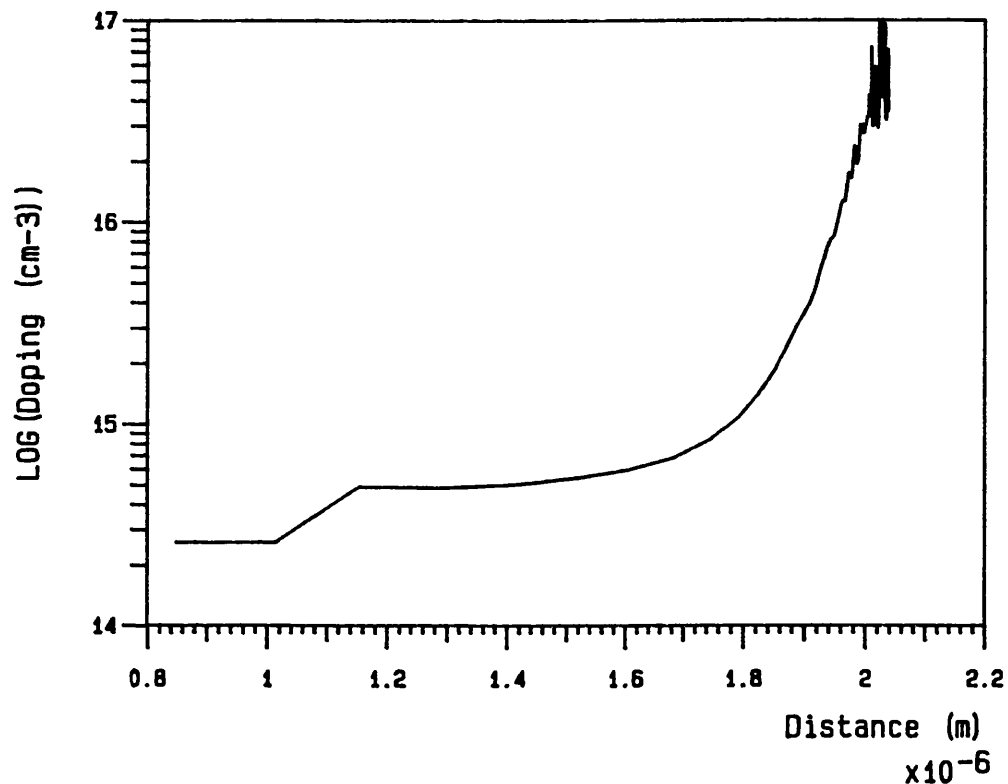


FIGURE 2.6.2.1:
Doping profile of MQW region of sample M33 as derived from C-V measurements.

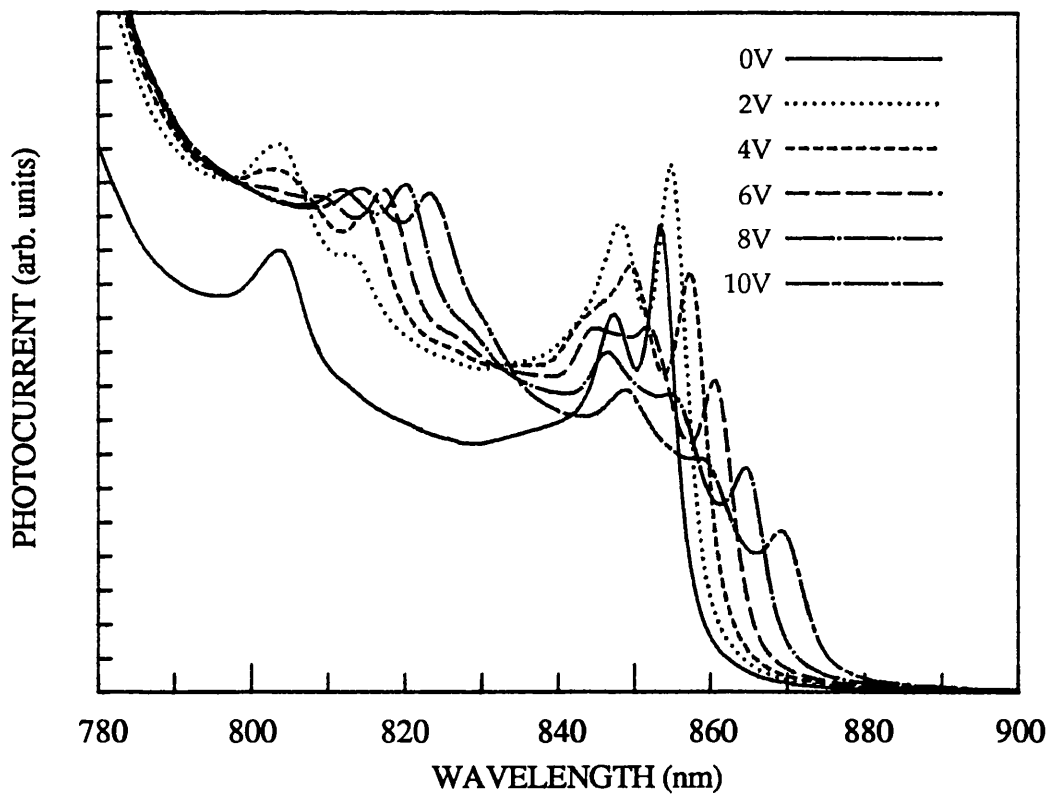


FIGURE 2.6.2.2:
Un-normalized room-temperature photocurrent spectra for very low doped MQW sample M33 ($\approx 100\text{\AA}$ wells) grown by Dr. Karl Woodbridge at Philips Research Labs, Redhill.

We note here that the quantum efficiency is again bias dependent, despite the full depletion of the intrinsic region at zero bias, although in this case the saturation voltage is only $\approx 2\text{V}$. The barriers in this case were $\approx 100\text{\AA}$, which as we found in § 2.5 is thicker than absolutely necessary to retain the QCSE. In device applications it will be desirable to operate at the lowest possible bias voltage, and so, in the case where the photodetection properties of the MQW diode are used, the barrier thickness should be minimized to achieve the highest quantum efficiency.

Apart from the increased sharpness of the shifted peaks the bias response for this structure is qualitatively similar to the KLB461 sample. The intrinsic region in this sample included $\approx 0.3\ \mu\text{m}$ undoped AlGaAs buffers either side of the wells, making a total thickness of $\approx 1\ \mu\text{m}$, so voltages are not directly comparable with those for KLB461. In Fig. 2.6.2.3 we again compare the experimental and modelled Stark shifts, with excellent agreement this time. No offset voltage is required now. With the improved quality of this sample it becomes clear that, even when free of doping broadening, the loss in the height of the e1-hh1 peak, which is theoretically expected, is quite considerable for 100\AA wells.

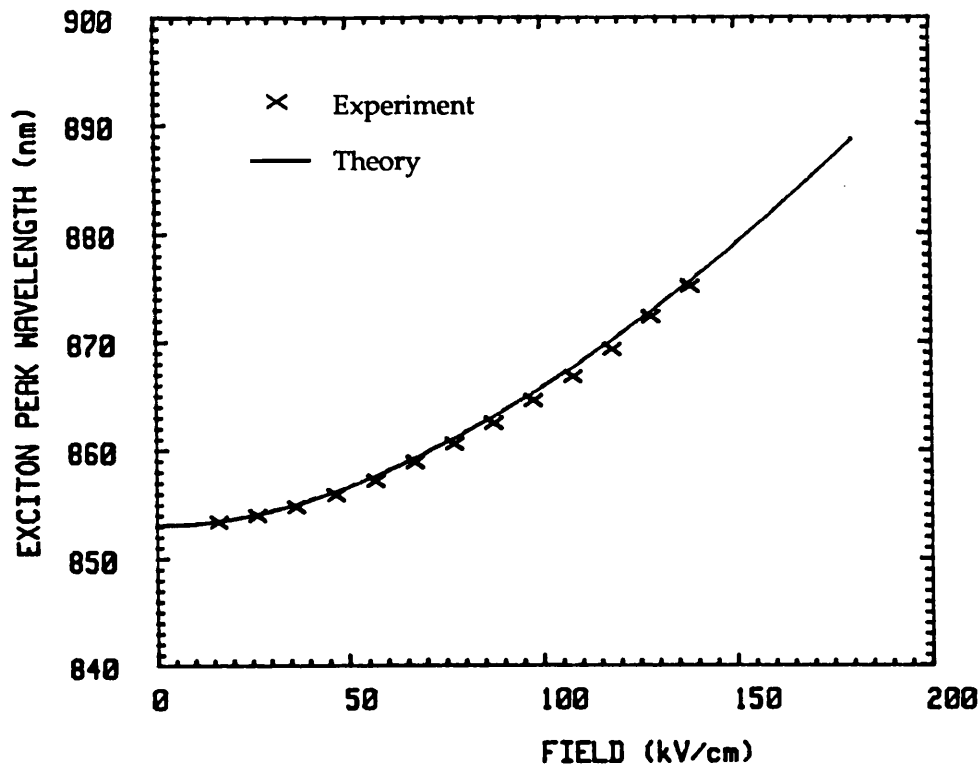


FIGURE 2.6.2.3:

Calculated and observed Stark shift of the e1-hh1 exciton peak for the M33 MQW sample ($\approx 100\text{\AA}$ wells). Calculated data supplied by Peter Stevens, UCL.

Modulation off the unbiased absorption edge will thus be limited to absorption changes of, at best, roughly half the height of the unbiased e1-hh1 exciton.

2.7. SUMMARY

In this chapter we have discussed the assessment of GaAs MQW *p-i-n* diodes using photocurrent spectroscopy, relating where possible the observed field effects to growth parameters, in particular background doping. We have shown that, if the background doping level is reduced to levels of $\approx 2 \times 10^{15} \text{ cm}^{-3}$, MOVPE can be used as successfully as MBE to grow MQW structures suitable for optical modulation, at least in terms of the observed quantum-confined Stark shifts.

A variety of MOVPE-grown devices have allowed us to draw some conclusions concerning optimization of the MQW structure for modulation purposes. Compared to the traditionally-used well width of $\approx 100\text{\AA}$, the absorption edge for wider wells of $\approx 150\text{\AA}$ begins to shift at lower fields ($\approx 2 \times 10^4 \text{ V/cm}$ cf $\approx 7 \times 10^4 \text{ V/cm}$), but also loses the strength of the exciton more quickly. With wells of $\approx 50\text{\AA}$ the excitonic strength appears to be retained at very high fields ($> 2 \times 10^5 \text{ V/cm}$). However, the shift of the edge is much reduced and the 16V+ needed to achieve this field becomes rather unattractive.

Barrier thickness appears to be important in determining the diode quantum efficiency at low bias voltages. A device with barriers of 60-70 \AA (§ 2.5.9) has shown saturated quantum efficiency even at zero bias, whereas thicker barriers of $\approx 100\text{\AA}$ introduce a bias dependence into the photocurrent response, requiring 2-6V for saturation (§ 2.6.1-2). We have also seen that the reduction of the barriers still further, to $\approx 30\text{-}35\text{\AA}$, loses the QCSE (§2.5.9), presumably due to strong coupling between wells.

With a very high quality MBE-grown structure (§ 2.6.2) we have observed good agreement between experimental and theoretical Stark shifts confirming the suitability of the fairly simple model for the theoretical optimization of MQW modulators [34].

REFERENCES (Chapter 2)

- [1] P. D. DAPKUS, "A critical comparison of MOCVD and MBE for heterojunction devices", *J. Crystal Growth* (1984), **68**, 345-55.
- [2] K. WOODBRIDGE, P. BLOOD, E. D. FLETCHER and P. J. HULYER, "Short wavelength (visible) GaAs quantum well lasers grown by molecular beam epitaxy", *Appl. Phys. Lett.* (1984), **45**, pp. 16-18.
- [3] J. S. ROBERTS, N. J. MASON and M. ROBINSON, "Factors influencing doping control and abrupt metallurgical transitions during atmospheric pressure MOVPE growth of AlGaAs and GaAs", *J. Crystal Growth* (1984), **68**, pp. 422-30.
- [4] H. MANASEVIT, "Single crystal GaAs on insulating substrates", *Appl. Phys. Lett.* (1968), **12**, p.156.
- [5] R. D. DUPUIS, P. D. DAPKUS, N. HOLONYAK JR., E. A. REZEK and R. CHIN, "Room-temperature laser operation of quantum-well Ga_(1-x)Al_xAs-GaAs laser diodes grown by metalorganic chemical vapour deposition", *Appl. Phys. Lett.* (1978), **32**, pp. 295-7.
- [6] G. B. STRINGFELLOW, "Organometallic vapor-phase epitaxial growth of III-V semiconductors", *Semiconductors and Semimetals* (1985), **22A**, pp. 209-59.
- [7] J. E. DAVEY and T. PANKEY, "Epitaxial GaAs films deposited by vacuum evaporation", *J. Appl. Phys.* (1968), **39**, p.1941.
- [8] J. R. ARTHUR, "Interaction of Ga and As₂ molecular beams with GaAs surfaces", *J. Appl. Phys.* (1968), **39**, p.4032.
- [9] A. Y. CHO, "Morphology of epitaxial growth of GaAs by a molecular beam method: the observation of surface structures", *J. Appl. Phys.* (1970), **41**, p.2780.
- [10] A. Y. CHO, "Growth of periodic structures by the molecular beam method", *Appl. Phys. Lett.* (1971), **19**, pp. 467-8.
- [11] J. H. NEAVE, B. A. JOYCE, P. J. DOBSON and N. NORTON, "Dynamics of film growth of GaAs by MBE from RHEED observations", *Appl. Phys. A* (1983), **31**, pp. 1-8.
- [12] B. A. JOYCE, "Molecular beam epitaxy", *Rep. Prog. Phys.* (1985), **48**, pp. 1637-97.
- [13] W. T. TSANG, "Molecular beam epitaxy for III-V compound semiconductors", *Semiconductors and Semimetals* (1985), **22A**, pp. 95-207.
- [14] K. WOODBRIDGE, P. DAWSON, J. P. GOWERS and C. T. FOXON, "Structural and optical properties of GaAs-Al_xGa_{1-x}As quantum wells", *J. Vac. Sci. Technol.* (1984), **B2**, pp.

163-66.

- [15] T. HAYAKAWA, T. SUYAMA, M. KONDO, K. TAKAHASHI, S. YAMAMOTO, S. YANO and T. HIJIKATA, "High-purity AlGaAs grown by molecular beam epitaxy using a superlattice buffer layer", *J. Appl. Phys.* (1985), **58**, pp. 4452-4.
- [16] J. J. LEPORE, "An improved technique for selective etching of GaAs and $Ga_{1-x}Al_xAs$ ", *J. Appl. Phys.* (1980), **51**, pp. 6441-2.
- [17] See for example V. L. RIDEOUT, "A review of the theory and technology for ohmic contacts to group III-V compound semiconductors", *Solid State Electron.*, **18**, pp. 541-50.
- [18] H.-J. POLLAND, Y. HORIKOSHI, E. O. GÖBEL, J. KUHL and K. PLOOG, "Photocurrent and picosecond photoluminescence spectroscopy in GaAs/AlGaAs quantum wells", *Surf. Sci.* (1986), **174**, pp. 278-82.
- [19] R. T. COLLINS, K. von KLITZING and K. PLOOG, "Photocurrent spectroscopy of GaAs/ $Al_xGa_{1-x}As$ quantum wells in an electric field", *Phys. Rev. B* (1986), **33**, 4378-81.
- [20] K. YAMANAKA, T. FUKUNAGA, N. TSUKADA, K. L. I. KOBAYASHI and M. ISHII, "Photocurrent spectroscopy in GaAs/AlGaAs multiple quantum wells under a high electric field perpendicular to the heterointerface", *Appl. Phys. Lett.* (1986), **48**, pp. 840-2.
- [21] L. VIÑA, R. T. COLLINS, E. E. MENDEZ and W. I. WANG, "Comparative study of the effect of an electric field on the photocurrent and photoluminescence of GaAs-GaAlAs quantum wells", *Phys. Rev. B* (1986), **33**, pp. 5939-42.
- [22] R. T. COLLINS, K. von KLITZING and K. PLOOG, "Photoexcited transport in GaAs/AlAs quantum wells", *Appl. Phys. Lett.* (1986), **49**, pp. 406-8.
- [23] P. W. YU, G. D. SANDERS, D. C. REYNOLDS, K. K. BAJAJ, C. W. LITTON, J. KLEM, D. HUANG AND H. MORKOÇ, "Determination of transition energies and oscillator strengths in GaAs- $Al_xGa_{1-x}As$ multiple quantum wells using photovoltage-induced photocurrent spectroscopy", *Phys. Rev. B* (1987), **35**, pp. 9250-8.
- [24] M. WHITEHEAD, G. PARRY, K. WOODBRIDGE, P. J. DOBSON and G. DUGGAN, "Experimental confirmation of a sum rule for room temperature electroabsorption in GaAs-AlGaAs multiple quantum well structures", *Appl. Phys. Lett.* (1988), **52**, pp. 345-7.
- [25] T. H. WOOD, C. A. BURRUS, D. A. B. MILLER, D. S. CHEMLA, T. C. DAMEN, A. C. GOSSARD and W. WIEGMANN, "High speed optical modulation with GaAs/GaAlAs quantum in a *p-i-n* diode structure", *Appl. Phys. Lett.* (1984), **44**, pp. 16-18.
- [26] D. R. WIGHT, A. M. KEIR, G. J. PRYCE, J. C. H. BIRBECK, J. M. HEATON, R. J. NORCROSS, and P. J. WRIGHT, "Limits of electro-absorption in high purity GaAs, and the optimisation of waveguide devices", *IEE Proc. Pt. J* (1988), **135**, pp. 39-44.

- [27] A. LARSSON, P. A. ANDREKSON, S. T. ENG and A. YARIV, "Tunable superlattice p-i-n photodetectors: Characteristics, theory and applications", *IEEE J. Quantum Electron.* (1988), **24**, pp. 787-801.
- [28] J. S. ROBERTS, M. A. PATE, P. MISTRY, J. P. R. DAVID, R. B. FRANKS, M. WHITEHEAD and G. PARRY, "MOVPE grown MQW p-i-n diodes for electro-optic modulators and photodiodes with enhanced electron ionisation coefficients", *J. Crystal Growth* (1988), **93**, pp. 877-84.
- [29] M. WHITEHEAD, G. PARRY, J. S. ROBERTS, P. MISTRY, P. LI KAM WA and J. P. R. DAVID, "Quantum confined Stark shifts in MOVPE-grown GaAs-AlGaAs multiple quantum wells", *Electron. Lett.* (1987), **23**, pp. 1048-50.
- [30] A. J. MOSELEY, D. J. ROBBINS, A. C. MARSHALL, M. Q. KEARLEY and J. I. DAVIES, "Quantum confined Stark effect in GaInAs/InP single quantum wells grown by low pressure MOVPE", *Electron. Lett.* (1988), **24**, pp. 1301-2.
- [31] P. J. STEVENS, M. WHITEHEAD, G. PARRY and K. WOODBRIDGE, "Computer modeling of the electric field dependent absorption spectrum of multiple quantum well material", *IEEE J. Quantum. Electron.* (1988), **QE-24**, pp.2007-16.
- [32] M. WHITEHEAD, P. J. DOBSON and K. WOODBRIDGE, unpublished data.
- [33] D. A. B. MILLER, D. S. CHEMLA, T. C. DAMEN, A. C. GOSSARD, W. WIEGMANN, T. H. WOOD and C.A. BURRUS, "Electric field dependence of optical absorption near the band gap of quantum well structures", *Phys. Rev. B* (1985), **32**, pp. 1043-60.
- [34] P. J. STEVENS and G. PARRY, "Limits to normal incidence electro-absorption modulation in GaAs/(GaAl)As multiple quantum well diodes", *J. Lightwave Tech.* (1989), **LT-7**, pp. 1101-8. Also see P. J. STEVENS, Ph. D. Thesis, University of London 1990.

CHAPTER THREE

ABSORPTION, ELECTRO-ABSORPTION & ELECTRO-REFRACTION IN GaAs MQWs

3.1 Introduction

3.2 Limits to the Accurate Measurement of Absorption

3.2.1 The Problem of Unwanted Fabry-Perot Effects

3.2.2 Problems in the Fabrication of Modulators

3.2.3 The Use of Anti-Reflection Coatings to Reduce FP Effects

3.2.4 Analysis of the Effect of FP Resonance on Transmission Spectra

3.3 Calculation of Absorption from Transmission Measurements

3.4 Calculation of Absorption Spectra from Photocurrent Measurements

3.4.1 The Factors Affecting the Photocurrent:Absorption Relationship

3.4.2 Example Calculations of Absorption Spectra (Samples KLB461 & M33)

3.4.3 Agreement with the Electro-Absorption Sum Rule

3.5 Calculation of Electro-Refraction

3.5.1 General Points Concerning Electro-Refraction

3.5.2 Index Changes Based on Photocurrent Measurements

3.5.3 Index Changes Based on Transmission Measurements

3.6 Summary

3.1 INTRODUCTION

This chapter details how electro-absorption and electro-refraction data are obtained for GaAs: AlGaAs MQWs; the principal sections being:

- (i) A discussion of the difficulties of making accurate estimates of absorption coefficients in GaAs MQWs, due to the need to remove the absorbing GaAs substrate, which results in strong Fabry-Perot oscillations in the transmission spectra. We include a quantitative analysis of the Fabry-Perot interference effects on transmission. Calculated absorption data are presented, derived from the transmission modulation measurements of Chapter 4, for varying degrees of resonance.
- (ii) An explanation of how reasonably accurate absorption spectra may be derived from photocurrent measurements. From the spectra calculated for an MBE-grown MQW structure we are able to verify that even when large changes take place in the absorption spectrum under the influence of an applied electric field the total absorption is conserved [1, 2].
- (iii) The Kramers-Krönig (KK) transformation of MQW electro-absorption spectra to provide estimates of the electro-refractive effect. Data derived from both photocurrent and transmission measurements are shown.

In the context of this thesis there were two reasons for the interest in measuring absorption in MQW structures. The first was that, although some theoretical analyses existed [3, 4], there was little experimental data in the literature, apart from photoluminescence [5], showing the well width dependence of the QCSE and, more importantly, none showing the associated absorption changes. Most devices which had been studied contained wells of $\approx 100\text{\AA}$, so we wished to know how strongly the absorption changes in MQWs were dependent on well width, and whether the optimization of well width might significantly improve modulation. This idea is pursued in Chapter 4.

The second reason was a need for reasonably accurate electro-absorption spectra for device modelling. In Chapters 5 and 6 we shall model the performance of Fabry-Perot cavity modulators containing MQWs. In that case, particularly for high-finesse structures, as well as the MQW absorption spectra, $\alpha(\lambda, V)$, it is necessary to include the change in

refractive index, Δn , which occurs when the absorption edge is field-shifted. According to the KK integral, the index changes can be calculated from the absorption changes given sufficient spectral range.

3.2 LIMITS TO THE ACCURATE MEASUREMENT OF ABSORPTION

3.2.1 THE PROBLEM OF UNWANTED FABRY-PEROT EFFECTS

- (i) The simple method of determining absorption spectra involves the measurement of transmission, which is the ratio of transmitted intensity to input intensity. Where interference effects do not occur, transmission, T , is given by:

$$T = T_0 \exp(-\alpha d) \quad \dots(3.1)$$

where α is the absorption coefficient, d the thickness of the absorber and T_0 the limiting transmission as $\alpha \rightarrow 0$, which is a function of the reflectivity at the entrance and exit facets of the sample under test.

With GaAs MQWs there is a two-stage barrier to the accurate measurement of absorption. Firstly the MQW structure always has its absorption edge at a shorter wavelength than that of the GaAs substrate on which it is grown, so the substrate must be completely removed from the optically-probed region. Fortunately there exist highly selective chemical etches – both wet and dry [6,7] – which will remove GaAs in preference to AlGaAs. Thus we can incorporate an abrupt etch-stop within the epitaxial structure. However, the ability to cleanly remove the absorbing substrate leaves us with a second problem. The MQW *p-i-n* structure left behind is typically 2-3 μm thick, with extremely smooth, parallel surfaces front and back, which act as mirrors with $\approx 30\%$ reflectivity and cause very strong interference effects according to the simple Fabry-Perot (FP) cavity model [8]. The equations governing transmission and reflection in an absorptive FP cavity can be found in the appendix. Figure 3.2.1.1. below shows the typical effect observed with an MQW sample containing 25 \times 100 \AA wells. A piece of the sample roughly 2-3mm square was mounted epitaxial side down with epoxy adhesive on a sapphire disk for support. The substrate was ground down to 80-100 μm thickness (from typically $\approx 400\mu\text{m}$) using a fine grade carborundum, then the remainder etched away using a selective wet etch consisting of a mixture of 30% H_2O_2 and NH_4OH in the ratio 19:1 [6]. The etch-stop layer of $\text{Al}_{0.6}\text{Ga}_{0.4}\text{As}$ included as part of the n^+ layer of the MQW *p-i-n* was left microscopically smooth after complete removal of the substrate.

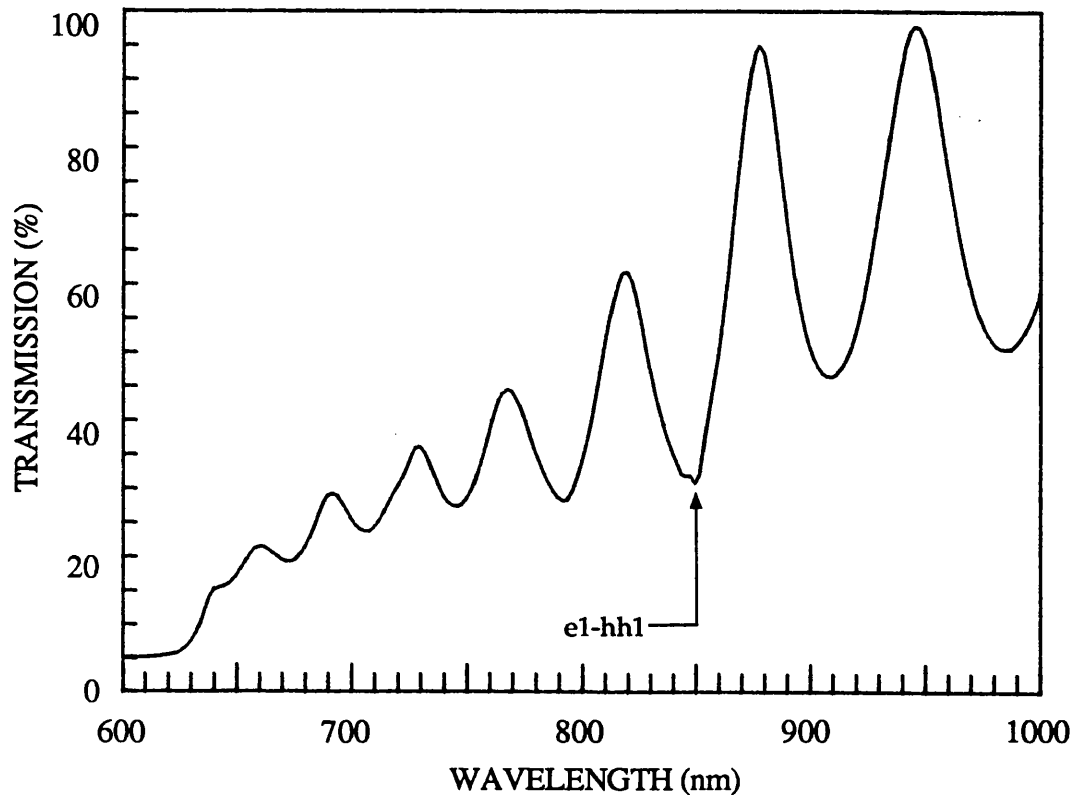


FIGURE 3.2.1.1:

Unbiased, room-temperature transmission spectrum of an MBE-grown MQW sample (KLB 461) containing $25 \times 100 \text{ \AA}$ GaAs wells. The spectrum is strongly modulated by Fabry-Perot interference effects due to substrate removal. (Sample grown at Philips Research Labs., Redhill by M. Whitehead under the supervision of K. Woodbridge).

The two highest transmission peaks at 875nm and 940nm are in the region where MQW absorption is roughly zero. Maximum and minimum values of transmission in this region are in good agreement with a front surface reflectivity of $\approx 30\%$ (air:semiconductor interface) and a back surface reflectivity of $\approx 10\%$ (semiconductor: epoxy interface). The relevant equations for T_{\max} and T_{\min} can be found in § 3.2.4.

Strong absorption is expected in the MQWs at wavelengths below $\approx 850\text{nm}$. However, this is insufficient to dampen the FP resonances, and evidence of the e1-hh1 excitonic absorption peak is only just observable at 851nm. The positions of the transmission resonances are dependent on the cavity thickness and the refractive index, which is in turn dependent on temperature and wavelength. This factor, coupled with uncertainties in the actual values of the surface reflectivities, makes the calculation of absorption rather difficult. In § 3.2.4 we discuss the accuracy of estimating absorption from spectra with residual FP effects.

3.2.2 PROBLEMS IN THE FABRICATION OF MODULATORS

Aside from the problem of interference effects in transmission, the fabrication of GaAs MQW samples for unbiased measurements is straightforward compared to making a device structure for electro-absorption or transmission modulation experiments. The modulator obviously requires the removal of the substrate. However, to retain some mechanical strength in the device the substrate must be windowed, rather than being completely removed over the whole of the sample.

The modulator is electrically defined by the *p-i-n* diode mesa process described earlier in § 2.3.1. The difficulty comes in accurately aligning a photolithographic mask with this mesa on one side of the wafer in order to produce a window etch pattern in photoresist on the other side. Commercial mask aligners do exist with IR illumination and monitoring to allow features on the back of semiconductor substrates to be viewed, but this facility was not available to us.

In the next chapter a method of obtaining reasonably accurate window alignment is described. Once this has been achieved there is unfortunately the further problem of etching uniform, clean windows when the substrate thickness is roughly the same as the diameter of the hole being etched. In this case it appears to be difficult to keep a uniform flow of the etchant around the hole being etched in order to remove etch products and maintain the reaction rate. With the simple wet selective etch, distortion of the window profile due to preferential etching along certain crystal axes, and non-uniformities due to the formation of bubbles in the etch mixture have been observed.

The final drawback with the fabrication of MQW devices for electro-absorption measurements is the fragility of the structure which is left when all the other problems have been surmounted. Devices with windows large enough (200-400 μm square) to allow easy assessment in the automated monochromator set-up are prone to damage. The stresses induced (in the sample and the student!) simply in handling the devices with tweezers during the mounting stage are enough to cause the active "membrane" which remains after etching to crack or fall out completely, rendering the device useless.

3.2.3 THE USE OF ANTI-REFLECTION COATINGS TO REDUCE FP EFFECTS

A standard method of reducing FP interference effects is to apply dielectric anti-reflection (AR) coatings to one or both facets of the cavity by a vacuum technique such as plasma deposition or sputtering. The AR layer must have a refractive index somewhere between 1 (air) and ≈ 3.6 (GaAs) in order to smooth the index discontinuity. The simplest form of AR coating is a single layer of index n with a thickness $\lambda/(4n)$. In theory zero reflectance may be achieved with such a coating when

$$n = \sqrt{(n_1 n_2)} \quad \text{.....(3.2)}$$

where n_1 and n_2 are the indices of the two media to be matched. So for air : GaAs at 850nm we require a matching index of ≈ 1.897 and a layer thickness of 1120Å. However, it is not usually possible to satisfy Eq. 3.2 exactly, and the compromise matching layer will give a residual minimum reflectance given by [9]:

$$R_{\min} = \frac{(n_1 n_2 - n^2)^2}{(n_1 n_2 + n^2)^2} \quad \text{.....(3.3)}$$

There is obviously only one wavelength at which the quarter-wave condition is satisfied, so how much does the reflectance increase away from this minimum? In Fig. 3.2.3.1 (over page), we have modelled the reflectance spectrum of a typical silicon nitride AR coating, as used in the fabrication of the modulators to be described in Chapter 4. The calculation has been carried out using the matrix formulation of § 6.5.1.

The reflectance reaches a minimum of ≈ 0.0003 at 838nm, and does not rise above 1% between 760-930nm, which is generally wider than the range over which we measure the electro-absorptive effects in MQWs. There will normally be some uncertainty in the exact index and thickness of a silicon nitride coating, but without being too concerned about the exact position of R_{\min} we can be reasonably certain that the front surface reflectance will be at most 1% over the range.

A preliminary attempt to AR-coat a transmission sample was made by thermally evaporating $\approx 1000\text{Å}$ of SiO on the front surface of the MQW structure KLB461, as described in Fig. 3.2.1.1. Oxidation occurs during deposition leaving a mixed oxide of SiO/SiO₂.

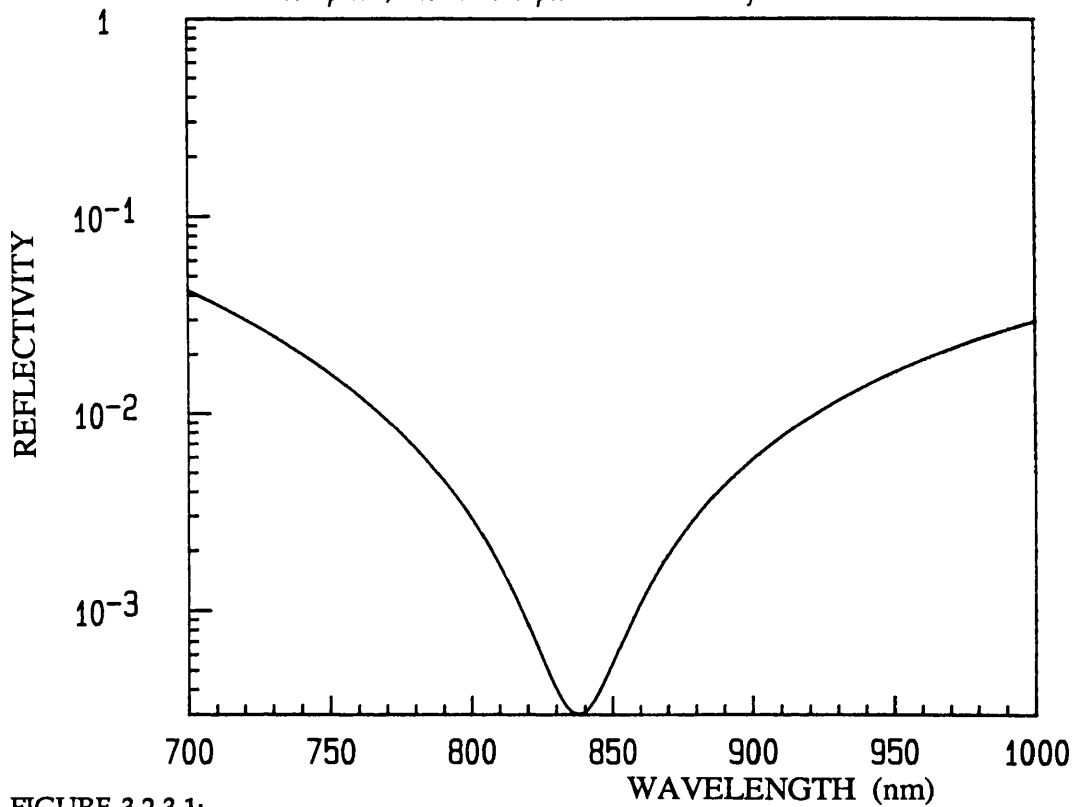


FIGURE 3.2.3.1:
Simulated reflection spectrum of an 1120Å AR layer of silicon nitride ($n = 1.87$) on GaAs ($n = 3.62$).

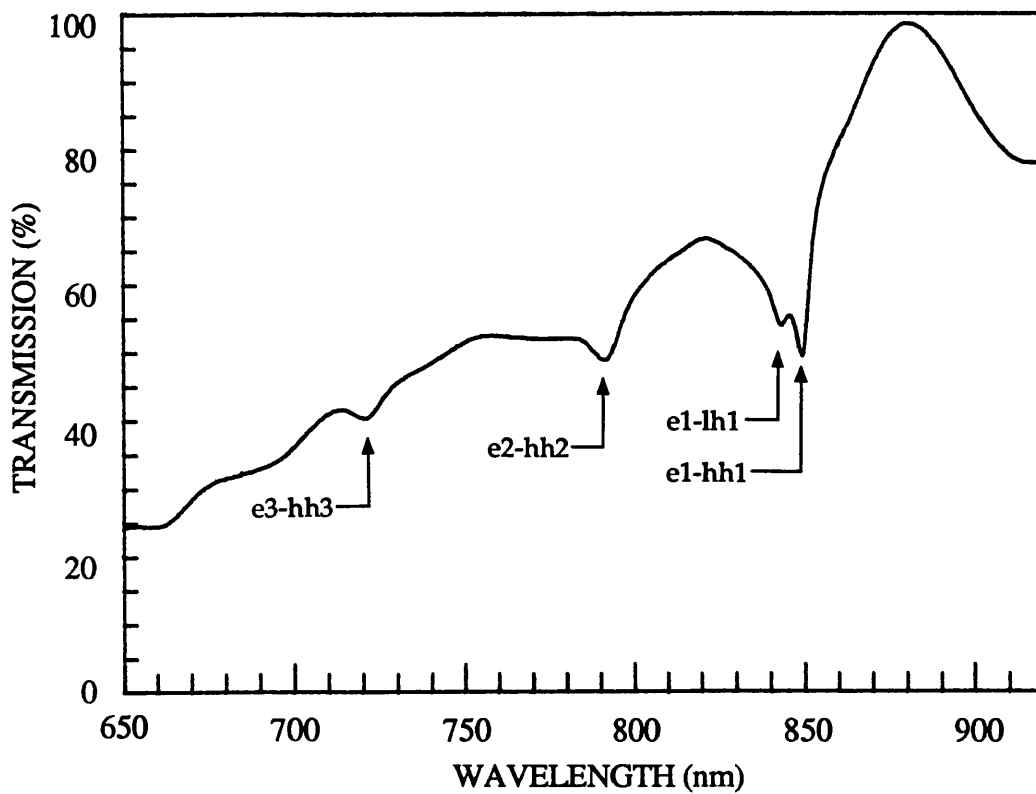


FIGURE 3.2.3.2:
The room-temperature transmission spectrum of the MQW structure of Fig. 3.2.1.1 after the deposition of $\approx 1000\text{\AA}$ of a mixture of SiO/SiO_2 on the front surface.

The refractive indices for the monoxide and dioxide at 850 nm are ≈ 1.92 and 1.45 respectively [10]. If we assume an average index value for the mixed oxide of 1.685, then the theoretical R_{\min} is $\approx 1.5\%$ according to Eq. 3.3. In Fig. 3.2.3.2 we see that the AR coating, although far from optimized, has significantly reduced the FP effects compared to Fig. 3.2.1.1. Excitonic absorption peaks can now clearly be seen for the $n = 1, 2$ and 3 sub-bands at $\approx 850, 790$ and 720nm respectively, with the splitting of light and heavy holes at the $n=1$ absorption edge. Distortion of the transmission spectrum still occurs in the region where absorption falls off beyond $\approx 850\text{nm}$, and this will be considered in detail in the next section.

Finally, it is worth noting that an elegant method for adjusting AR layers after deposition has been recently published by Jelley and Engelmann [11]. The method was specifically designed for GaAs MQW transmission modulators and involves back etching of the AR coating whilst monitoring the transmission spectrum, stopping when FP oscillations are minimized at the most appropriate wavelength.

3.2.4 ANALYSIS OF THE EFFECT OF FP RESONANCE ON TRANSMISSION SPECTRA

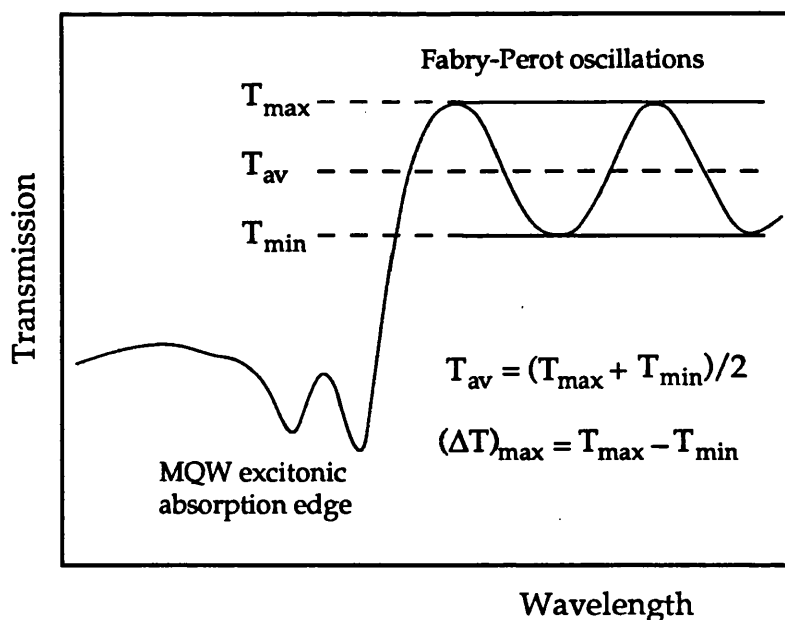


FIGURE 3.2.4.1:
Schematic of the MQW transmission spectrum with residual Fabry-Perot effects.

Consider the standard GaAs MQW transmission modulator with its thin active region as a low finesse FP cavity. We can only AR-coat the front surface of the device because of the fragility of the structure left behind when the substrate is etched away. How low must the front reflectivity (R_f) be in order to make reasonably accurate absorption calculations, or so that the transmission modulation is not significantly dependent on the FP characteristics?

Figure 3.2.4.1 (previous page) shows schematically the important points in the MQW transmission spectrum when FP oscillations are still present.

In the absence of absorption, the FP equations (see Appendix) for transmission at resonance ($\phi = 0, m\pi, T = T_{\max}$) and anti-resonance ($\phi = m(\pi/2), T = T_{\min}$) can be reduced to:

$$T_{\max} = \frac{(1 - R_f)(1 - R_b)}{(1 - \sqrt{R_f R_b})^2} \quad \dots(3.4)$$

and

$$T_{\min} = \frac{(1 - R_f)(1 - R_b)}{(1 + \sqrt{R_f R_b})^2} \quad \dots(3.5)$$

In this case, as the front reflectivity, R_f , tends to zero, T_{\max} and T_{\min} converge towards their average, T_{av} , which has the limiting value of $(1 - R_b)$. It is interesting to see how large the amplitude of the FP oscillations remains even when an anti-reflection coating is applied to lower the front reflectivity. The amplitude, $(\Delta T)_{\max}$, is simply $(T_{\max} - T_{\min})$ and is given by:

$$(\Delta T)_{\max} = \frac{4\sqrt{R_f R_b}(1 - R_f)(1 - R_b)}{(1 - R_f R_b)^2} \quad \dots(3.6)$$

In Figure 3.2.4.2 (over page) we have plotted this amplitude as a function of R_f for the case where the back reflectivity of the cavity, R_b , remains at 0.30. The dotted line marks the 1% reflectivity point, which perhaps might have been considered low enough to eradicate the FP effects. However, the amplitude of the oscillations is still around 15% even for such an apparently low-finesse cavity. This is typical of the MQW electro-absorption modulators described in Chapter 4.

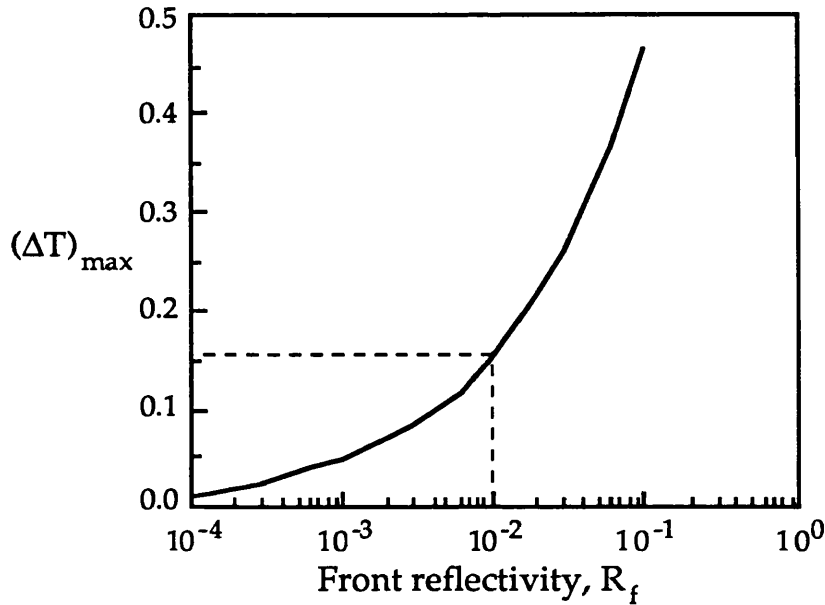


FIGURE 3.2.4.2:

The dependence of the amplitude of Fabry-Perot oscillations on the cavity front reflectivity in the absence of absorption. The back reflectivity is fixed at 0.30.

As R_f decreases, $(\Delta T)_{\max}$ is dominated by the $\sqrt{R_f}$ term in the numerator of Eq. 3.6, so the oscillations will only be reduced by a factor of 10 when R_f is reduced 100-fold. Should we wish to reduce the amplitude to $\approx 1\%$ then R_f must be lower than 0.0001, requiring very accurate control of the AR layer thickness and a refractive index very close to that prescribed by Eq. 3.2.

We now consider the situation when both absorption, α , and FP interference effects are present and we wish to calculate α from the transmission spectrum. The maximum distortion of the transmission spectrum, and therefore the largest error in calculating absorption, will occur either at resonance or anti-resonance. T_{\max} and T_{\min} now become:

$$T_{\min}^{\max} = \frac{(1 - R_f)(1 - R_b)e^{-\alpha d}}{(1 \mp \sqrt{R_f R_b} e^{-\alpha d})^2} \quad \dots(3.7)$$

where d is the absorber thickness.

As an example, if we let $\alpha d = 1$, we can calculate the maximum and minimum possible transmission from Eq. 3.7. If we imagine that these values are experimentally observed, on the assumption that the simple non-resonant equation for transmission (Eq. 3.1 with $T_o = (1 - R_b)$ or T_{av}),

holds good, we can then back-calculate values of αd corresponding to T_{\max} and T_{\min} and compare them with the real value. Table 3.1 shows the results for a range of R_f , with R_b as usual fixed at 0.3.

R_f	R_b	T_{\max}	T_{\min}	$\alpha d_{T_{\max}}$	$\alpha d_{T_{\min}}$
0.30	0.30	0.228	0.146	1.123	1.566
0.10	0.30	0.264	0.205	0.974	1.229
0.05	0.30	0.268	0.224	0.959	1.139
0.01	0.30	0.266	0.245	0.969	1.050
0.001	0.30	0.261	0.257	0.988	1.014

TABLE 3.1:

Calculated values of αd based on the assumption that FP effects can be neglected. To be compared with the real value of $\alpha d=1$, which is used to calculate T_{\max} and T_{\min} .

The error when at anti-resonance is noticeably larger than when on resonance. This is presumably due to the fact that, in the former case, absorption and FP effects both act to reduce transmission, whereas in the latter case the FP effect raises transmission, opposing the absorption. A point worth noting here is that provided $\alpha d \geq 1$, the maximum possible error is down to $\leq 5\%$ once R_f is reduced to 0.01.

Since increasing absorption will dampen the FP oscillations, the minimum R_f needed to reach a certain accuracy should increase also. To quantify this we have repeated the above calculation for four different values of αd . In Figure 3.2.4.3 (over page) the results have been plotted as the maximum fractional error, which is defined by $(\alpha d_{T_{\min}} - \alpha d)/\alpha d$, as a function of R_f , with again $R_b = 0.30$.

What these curves indicate is that it is not possible to calculate low absorption coefficients to a high degree of accuracy even when R_f has been reduced to $\approx 1\%$. A typical MQW structure would contain upwards of fifty 100\AA wells, with $\alpha \approx 22\text{-}24000\text{ cm}^{-1}$ at the absorption edge excitonic peak. This gives us $\alpha d \approx 1.10\text{-}1.20$ and an error between 3-5% with $R_f \approx 0.01$. So the estimate of α at the exciton peak will be good. However, moving into the absorption tail, as αd falls off rapidly to $\approx 0.2\text{-}0.3$, we

would be faced with errors of much more than 10%.

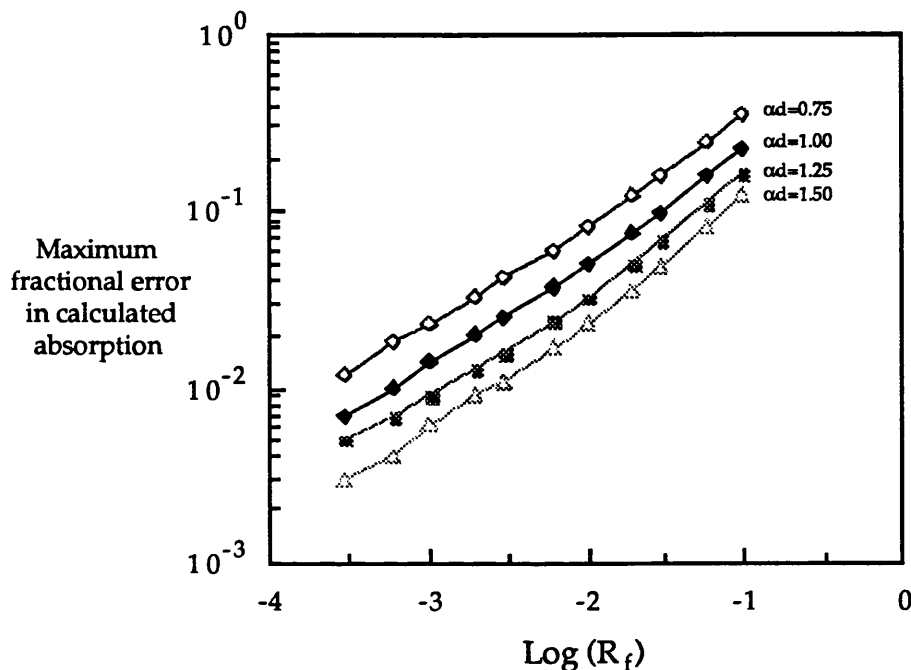


FIGURE 3.2.4.3:

The maximum fractional error in calculating absorption from experimental transmission spectra, on the basis that Eq. 3.1 is still valid even when FP oscillations are present.

It may be possible to attempt to fit suitable values for R_f , R_b and the product of the cavity index and thickness, nL , to the full expressions for the transmission of an absorptive FP cavity (see Appendix). Complete absorption spectra could then be extracted free of FP effects. One problem which may occur with this technique is the effect of assigning a fixed value for nL . The refractive index may vary slightly over the spectrum producing a mismatch of the real and modelled resonance wavelengths which could give rise to oscillations in the calculated absorption spectra and apparent negative values of α .

Finally, let us consider how the FP oscillations may affect the measured transmission modulation. Suppose we operate at a wavelength off the unbiased absorption edge, with T being reduced as a voltage, V , is applied. Inserting the following parameters in Eq. 3.7, $R_f=0.01$, $R_b=0.30$, $\alpha d_0=0.1$, $\alpha d_V=1.0$, we find that:

$$\begin{array}{llll} T_{\max}(\alpha d_0) = 0.694 & T_{\max}(\alpha d_V) = 0.266 & \rightarrow & \Delta T_{\max} = 0.428 \\ T_{\min}(\alpha d_0) = 0.569 & T_{\min}(\alpha d_V) = 0.245 & \rightarrow & \Delta T_{\min} = 0.324 \end{array}$$

So the transmission change for a fixed $\Delta\alpha$ can vary by ≈ 0.1 even when the device is reasonably AR-coated. This depends on where the absorption edge lies relative to the nearest FP resonance, with most of the variation occurring in the on-state (high T) level. In the non-resonant case, with $R_f = 0$, the transmission change obviously must lie mid-way between the two extremes, so the deviation is $\Delta T_{\text{non-res}} \pm 0.05$.

3.3 CALCULATION OF ABSORPTION FROM TRANSMISSION MEASUREMENTS

Having looked in the previous section at the problems of ascertaining accurate absorption coefficients from MQW transmission spectra in the presence of FP effects, here we present some calculations based on data obtained from MQW transmission spectra for a range of samples with and without remnant FP oscillations.

Let us firstly consider the AR-coated KLB461 sample of Fig. 3.2.3.2. In this case the average level, T_{av} , of the transmission in what is essentially the non-absorbing region is close to 0.90. This is due to the reduction of the reflectivity at the back surface of the sample, by being partially index-matched by the epoxy adhesive which holds the sample to the sapphire disc support, in addition to the reduction of the front surface reflectivity by the AR coating. By iterating Eq. 3.6 with suitable test values for the front and back reflectivities, we find the best solution is $R_f = 0.040$ and $R_b = 0.088$, which from Eqs. 3.4 and 3.5 gives $T_{max} = 0.989$, $T_{min} = 0.780$, close to the experimental values. The F figure (see Appendix), which is a measure of the cavity finesse, for these calculated reflectivities is very close to that for the case of the standard AR-coated FP cavity of the previous section, with $R_f = 0.01$, $R_b = 0.30$. Therefore we may consider the errors in estimating absorption values for this particular sample to be close to those displayed in Fig. 3.2.4.3.

Looking at the e1-hh1 exciton peak in Fig. 3.2.3.2, the transmission, T , is ≈ 0.49 . Making the approximation from Eq. 3.1 that:

$$\alpha d = \ln\left(\frac{T_{av}}{T}\right) \quad \dots(3.8)$$

we find that $\alpha d = 0.583$, with a maximum possible error, based on the method of calculation used for Fig. 3.2.4.3, of $\approx 18\%$. The MQW structure contains $25 \times 100\text{\AA}$ quantum wells. Thus we obtain an absorption coefficient, α , of around $23,320 \text{ cm}^{-1}$ at the exciton peak, calculated for the wells only. The same calculation for a wavelength of 658nm , where T is ≈ 0.24 , gives $\alpha d = 1.295$, which puts us in the region of only 5-6% error. The corresponding α value is $51,780 \text{ cm}^{-1}$. This estimate of absorption will be used in following section to rescale photocurrent spectra to represent absorption.

In the chapter which follows, where we shall discuss transmission modulation in MQW devices, we find in some cases that FP resonances are successfully suppressed by the application of a front AR-coating, whereas in others there are remnant oscillations in line with front and back reflectivities of ≈ 0.01 and 0.30 respectively. Here we estimate absorption coefficients for some of the devices.

From the CPM405 transmission spectra in Fig. 4.4.2.1 we find $T_{av} \approx 0.70$, and at the e1-hh1 exciton peak $T \approx 0.22$, giving $\alpha d \approx 1.157$. The structure contains $60 \times 87\text{\AA}$ wells, so the peak excitonic absorption coefficient is $\approx 22,160 \text{ cm}^{-1}$. The maximum error is around the 4% mark. Perhaps a more useful point to estimate the absorption is in the $n=1$ continuum region to the high energy side of the e1-lh1 excitonic peak. Here the absorption will not be affected so strongly by such line broadening mechanisms as temperature, high background doping and well width fluctuations, which would tend to reduce the peak exciton absorption strength in multiple wells. The comparison of absorption values for different well widths is then more valid [12]. Again from Fig. 4.4.2.1, the unbiased T value in the continuum at $\approx 835\text{nm}$ is ≈ 0.34 , giving $\alpha d \approx 0.72$, and an absorption coefficient of $\approx 13,800 \text{ cm}^{-1}$, with a maximum error of 8-9%. This is somewhat different from the low temperature measurements of Masumoto et al [12], who found continuum absorption values of ≈ 13400 and 16400 cm^{-1} for wells of 96\AA and 83\AA respectively. Our figure is significantly lower for the most comparable well width. This may simply be due to error in the assignment of the well width. Unfortunately, the data in Ref. 12 was recorded at 2K, and for unbiased structures only, so it is not possible to compare excitonic peak positions which we use as the indicator of the well width.

Calculated absorption coefficients based on the zero bias transmission spectra of §§ 4.4-4.6, together with the values we have already mentioned here are summarized in Table 3.2. The maximum error figure is obtained by using Eqs. 3.1 and 3.7 just as in § 3.2.4.

The continuum absorption coefficient for the 145\AA quantum well sample is in good agreement with Ref. 12 ($8,580 \text{ cm}^{-1}$ compared to $8,570 \text{ cm}^{-1}$ for 154\AA wells). However, there is again a discrepancy between the results for narrow wells. Their measurements give a continuum value of $\approx 24,000 \text{ cm}^{-1}$ for 43\AA wells, which is far outside the error range for the figure of $18,870 \text{ cm}^{-1}$ which we find for the 47\AA wells.

TABLE 3.2:

Calculated absorption coefficients at various points in the spectrum for a range of MQW structures.

Sample	Wavelength	αd	$d(\text{\AA})$	$\alpha(\text{cm}^{-1})$	Maximum error
KLB461	e1 – hh1	0.583	25x100 \AA	23,320	18%
KLB461	n = 1 continuum 835nm	0.343	25x100 \AA	13,700	35%
KLB461	658nm	1.295	25x100 \AA	51,780	5 – 6%
CPM405	e1 – hh1	1.157	60x87 \AA	22,160	3 – 4%
CPM405	n = 1 continuum 835nm	0.722	60x87 \AA	13,800	8 – 9%
MV245 *	e1 – hh1	0.847	45x145 \AA	12,980	\approx 1%
MV245 *	n = 1 continuum 853nm	0.560	45x145 \AA	8,580	\approx 1%
MV246	e1 – hh1	1.117	75x47 \AA	31,700	4%
MV246	n = 1 continuum 790nm	0.622	75x47 \AA	17,630	11%
MV246 *	e1 – hh1	1.204	75x47 \AA	34,150	\approx 1%
MV246 *	n = 1 continuum 785nm	0.665	75x47 \AA	18,870	\approx 1%

The most accurate calculations, based on transmission data unaffected by FP oscillations are denoted by *. There is a difference of \approx 5nm in the position of the e1-hh1 exciton for the two sets of measurements on sample MV246, probably due to a combination of well width variation over the wafer and temperature. Hence the n=1 continuum absorption is estimated at two different wavelengths.

We conclude this section with the complete electro-absorption spectra for samples MV245 (145 \AA wells) and MV246 (47 \AA wells) which are derived from the biased transmission spectra of § 4.5 and § 4.6. These data are the

only ones which we have been able to observe free from FP effects. They are included here to give an accurate picture of the practical wide and narrow well electro-absorption limits.

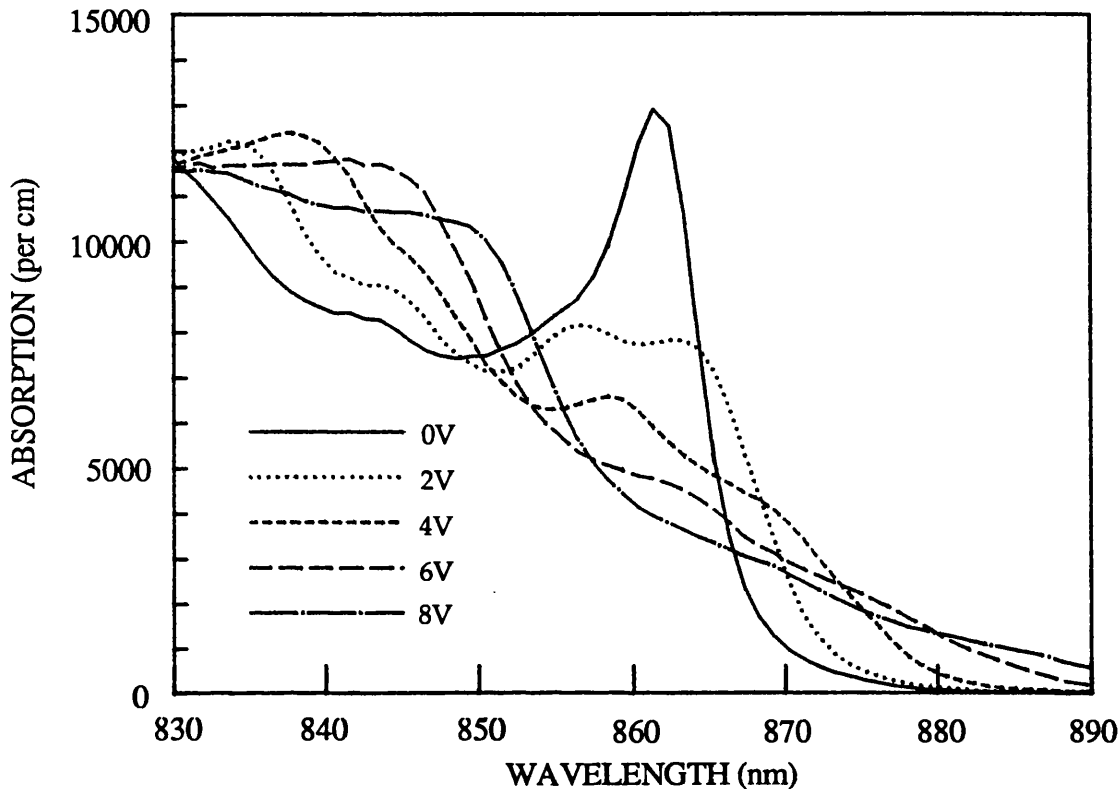


FIGURE 3.3.1:
Biased absorption spectra for MQW sample MV245 (145Å wells).

In Fig. 3.3.1 it can be seen that by far the strongest absorption changes occur at the unbiased exciton peak wavelength at $\approx 862\text{nm}$. The heavy and light hole state splitting is not large enough to be resolvable here. Quite modest voltages change the absorption coefficient by as much as -9000 cm^{-1} . The excitons at the absorption edge quickly become unresolvable as the bias is increased. This is due to some extent to the loss in oscillator strength due to increased polarization of the electron and hole wave functions towards opposite sides of the quantum well, but is more strongly affected in this case [13] by the increased sensitivity of the Stark shift for wide wells, which results in a greater spread of shifted absorption edges for each well in the MQW structure. There is generally good correlation between these spectra and the corresponding photocurrent spectra in Chapter 2, apart from the scaling required for quantum efficiency.

In Fig. 3.3.2 (over page) the increased absorption at the excitonic edge

in the narrow well structure is immediately apparent (Note the change of scale on the vertical axis compared to Fig. 3.3.1). Separate light and heavy hole absorption peaks can clearly be seen at $\approx 808\text{nm}$ and 819nm respectively. This is due to the increased energy splitting of confined states with reduced well width. The narrow well width also leads to greater spatial overlap of electron and hole wave functions, hence the much larger absorption coefficient at the e1-hh1 exciton peak for this sample compared to the 145\AA well structure. In this case the exciton remains well resolved, even when subject to very strong field, again an effect of the narrow well, which prevents a large polarization of electron and hole wavefunctions when a field is applied. Thus the largest electro-absorptive changes occur at the wavelength of the field-shifted e1-hh1 exciton. Maximum absorption change is more than $14,000\text{ cm}^{-1}$.

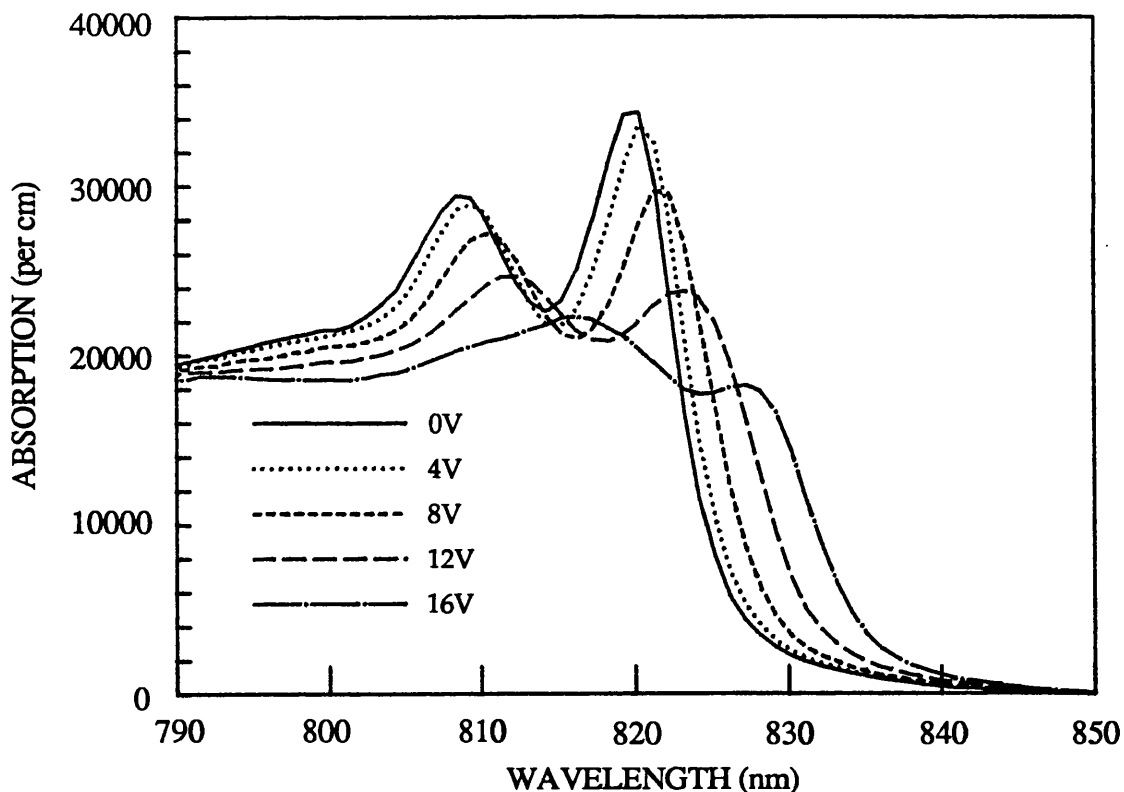


FIGURE 3.3.2:
Biased absorption spectra for MQW sample MV246 (47\AA wells).

Comparing with the photocurrent spectra in Fig. 2.5.7 it is noticeable that, although the Stark shifts at 16V are the same for the two sets of data, the height of the heavy hole peak is considerably less than that of the light hole in the absorption spectra, whereas they are of similar height in the

photocurrent spectra. The position of the unbiased heavy hole peak is also different in the two cases, being at $\approx 813\text{nm}$ for the photocurrent spectrum. The measurements were carried out on devices from different parts of the same wafer, so it is possible that growth variations are the reason for the discrepancies. Small well width variations will have a more profound effect on the exciton wavelength the narrower the well width. There could also conceivably be some well to well coupling effect due to barrier thickness reduction in some parts of the wafer. This would result in a loss of oscillator strength in the biased excitons.

3.4 CALCULATION OF ABSORPTION SPECTRA FROM PHOTOCURRENT MEASUREMENTS

We have outlined the problems of accurately determining absorption by the usual method of transmission spectroscopy. Here we shall describe an alternative method of obtaining electro-absorption spectra from measurements of the photocurrent. Since photocurrent is an almost linear function of absorbed power, by making certain assumptions we can rescale photocurrent spectra to represent absorption.

3.4.1 THE FACTORS AFFECTING THE PHOTOCURRENT:ABSORPTION RELATIONSHIP

Taking Eq. 2.1, which relates the photocurrent in a *p-i-n* diode to the absorption coefficient, we can re-cast it thus:

$$\alpha = \left(\frac{1}{d} \right) \ln \left[1 - \frac{CI_{ph}}{P(1-R_f)\eta\lambda} \right]^{-1} \quad \dots(3.9)$$

where we have replaced (hc/q) with the constant C which is equal to 1242.4 J.nm/Coulomb.

In the discussion of photocurrent measurements in Chapter 2 it was observed on a number of occasions that the quantum efficiency, η , was dependent on bias voltage up to a certain saturation level. We also saw that above the $n=2$ sub-band edge there is little change in the spectral features in the photocurrent spectrum with applied bias. Therefore, assuming that η is not wavelength dependent we can rescale our photocurrent spectra to match up at an appropriate wavelength well above the band gap.

The reflectivity at normal incidence for GaAs and AlGaAs has been measured by Aspnes et al. [14] and found to increase from 0.298 to 0.325 between 1.5 and 1.9eV (826 to 652nm) for AlGaAs with 0.3 Al mole fraction. The increase over the same range for GaAs is even smaller, being only 0.327 to 0.344. So the maximum variation in the term $(1-R_f)$ above will be $\approx 4\%$. We neglect this and assume that $(1-R_f)$ is constant and equal to 0.68.

Having normalized photocurrent spectra to account for both the

wavelength dependence in the optical source intensity and η variation, if we obtain a value for the absorption coefficient at a suitable wavelength at zero bias by an alternative measurement, such as transmission, we can then find the corresponding value of $P\eta$ in Eq. 3.9. Using this value for all other wavelengths we can generate a series of biased absorption spectra from the normalized photocurrent spectra.

This may appear to be somewhat convoluted, but the reason for employing this approach was that at the time we were particularly interested in obtaining electro-absorption data, the fabrication of MQW transmission modulators was proving to be difficult because of the need to etch away the substrate from the active part of the device. It was a much simpler process to obtain the unbiased transmission spectrum for a sample with no contacts, and to measure the photocurrent spectra for the same material.

3.4.2 EXAMPLE CALCULATIONS OF ABSORPTION SPECTRA (KLB461 & M33)

In order to model resonant device characteristics, absorption spectra at biases between zero and $\approx 10V$ are needed. The problem with the photocurrent spectra for sample KLB461, as shown in Fig. 2.6.1.2, is that there is quite a strong bias dependence in the quantum efficiency. The general level of the photocurrent does not saturate until $\approx 6V$. Worse than this, the spectra, when normalized (scaled to match) at the shortest wavelengths, where we expect minimal electro-absorptive effects, have values which appear to be far too large at wavelengths close to the e1-hh1 exciton. This indicates that there may well be a wavelength dependence in the quantum efficiency at low bias voltages. With the photocurrent spectra normalized in the standard way, the resultant low-bias absorption spectra do not agree well with the sum rule for electro-absorption [1], which we shall discuss in § 3.4.3.

For modelling purposes, where we wish to evaluate the optimum performance of a modulator, we really only need to be confident that the absorption changes involving the heavy and light hole excitons at the absorption edge are in reasonable agreement with existing electro-absorption data [15], rather than concern ourselves with the spectra over

the full range of Fig. 2.6.1.2. We can achieve the necessary agreement by arbitrarily matching the photocurrent spectra at a wavelength much closer to the absorption edge (in the $n=2$ sub-band) and ignoring the mismatch which then occurs at higher energies because of the anomalous variation of η with wavelength. Fig. 3.4.2.1 shows the photocurrent spectra for sample KLB461 close to the absorption edge in their raw form. To calculate absorption spectra we scale up the 0V and 2V spectra to match those at 4 and 6V at 785nm. At the latter bias the quantum efficiency has saturated in the higher energy part of the spectrum.

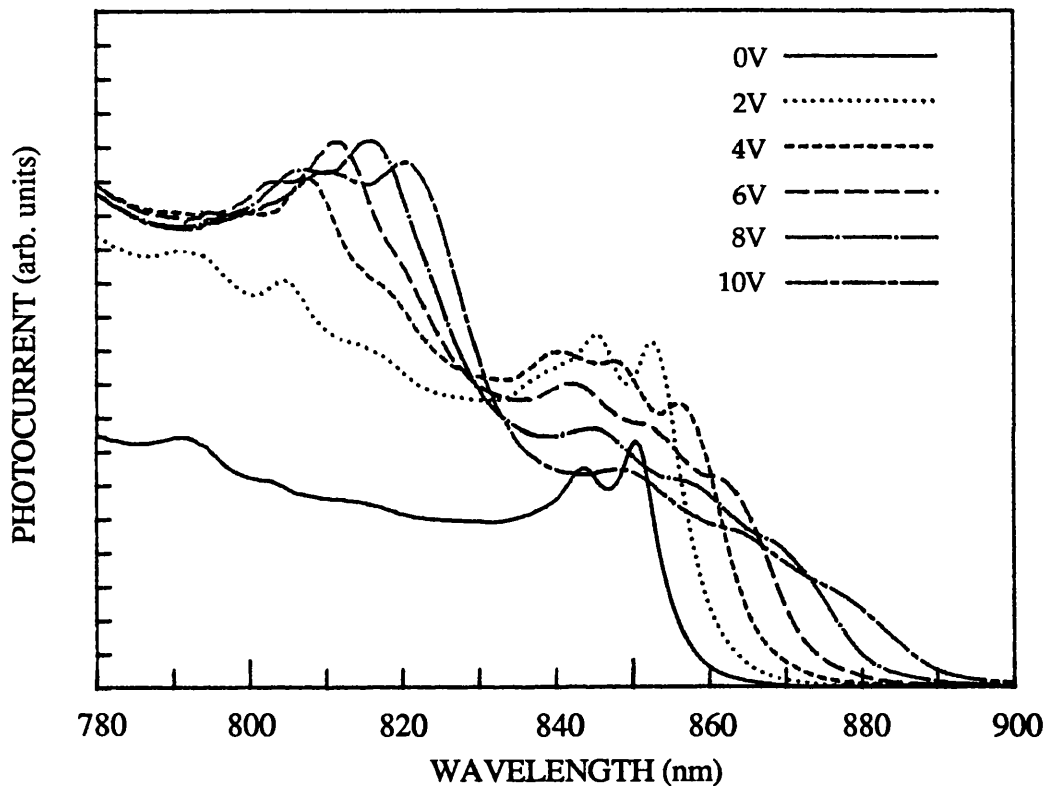


FIGURE 3.4.2.1:

Un-normalized room temperature photocurrent spectra for MBE-grown MQW sample KLB461. (Well width $\approx 100\text{\AA}$).

For this sample at 835nm we determined an absorption coefficient of $\approx 13,700\text{ cm}^{-1}$ in § 3.3. This was based on a transmission measurement in an unbiased sample and was subject to some error due to Fabry-Perot effects. However, a similar absorption value was also obtained for a similar MQW sample (CPM405) but with smaller possible error. Therefore we use this figure with some justification. Inserting the I_{ph} , α and λ values into Eq. 3.9, with $d = 25 \times 100\text{\AA} = 0.25\mu\text{m}$, $(1-R_f) = 0.7$, we calculate $P\eta$. This value is then inserted back into the equation, and all the

photocurrent data are converted to absorption values for the whole range of bias. The calculated absorption spectra are shown below in Fig. 3.4.2.2. 830-890nm is the limit over which useful absorption changes occur from a device point of view and we restrict all the modelling based on this data to this range. A maximum positive absorption change of slightly less than 8000 cm^{-1} occurs at $\approx 858\text{nm}$ for 4V bias or $\approx 67\text{kV/cm}$. At the wavelength of the unbiased exciton changes are even higher, exceeding $14,000 \text{ cm}^{-1}$ for 8V bias.

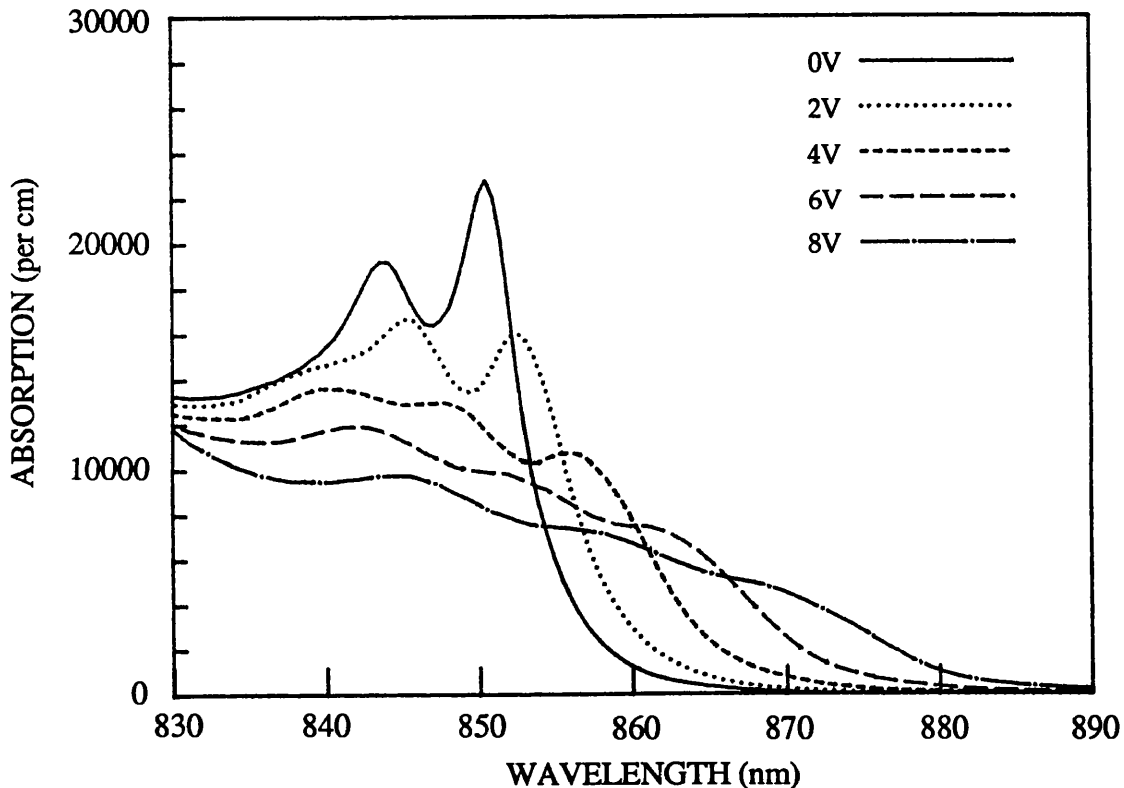


FIGURE 3.4.2.2:

Absorption spectra of MQW sample KLB461 as calculated from the photocurrent spectra of § 2.6.1. Well width is estimated to be $\approx 100\text{\AA}$. The average applied electric field at 8V is $\approx 133\text{kV/cm}$.

A theoretical calculation of the KLB461 absorption spectra (see Fig. 3.4.2.3 over page), supplied by Peter Stevens of UCL and based on the tunnelling resonance model mentioned previously [16], shows generally good agreement with the spectra derived from photocurrent. In the model the well width is fitted to match our observed e1-hh1 peak wavelength. A value of 98\AA gives the best agreement. Other parameters used in the model are an estimated background doping of $\approx 5 \times 10^{15} \text{ cm}^{-3}$ and an r.m.s. well width fluctuation of 1 monolayer. The magnitude of the absorption

changes and the increased broadening in the field-shifted exciton are reproduced very well, although the forbidden $e1-hh2$ transition, which appears on the shoulder of the $e1-hh1$ and $e1-lh1$ peaks, is a little too strong.

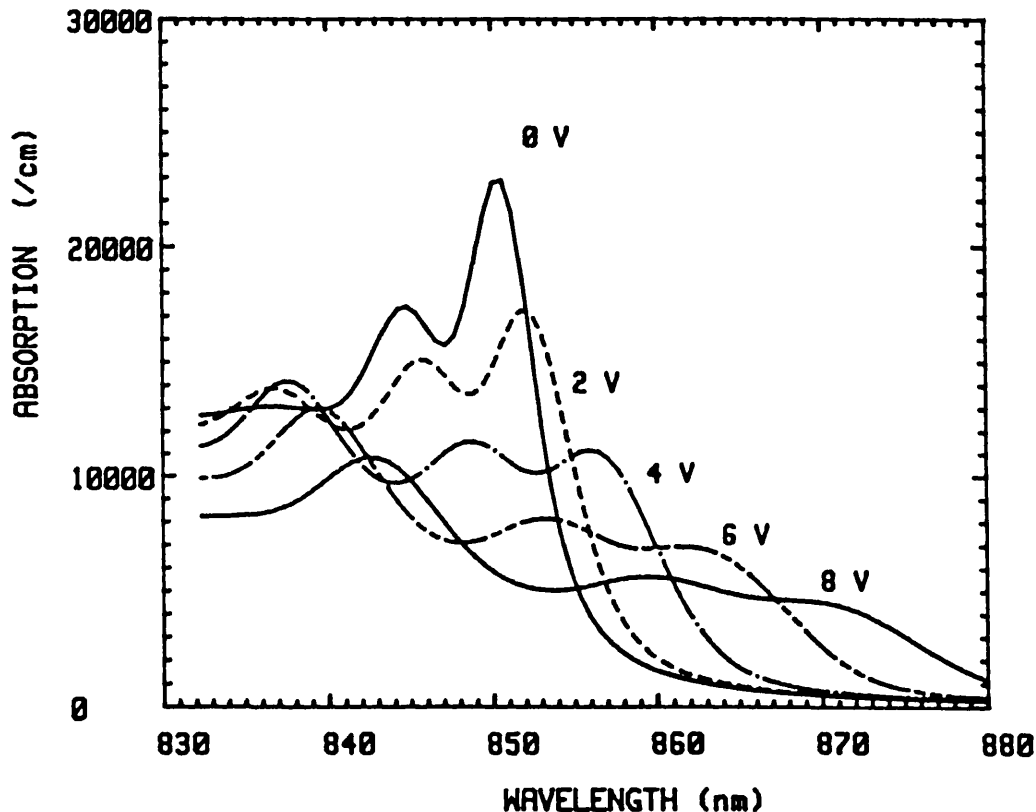


FIGURE 3.4.2.3: Modelled absorption spectra for the KLB461 structure ($\approx 100\text{\AA}$ wells). Calculation by Peter Stevens, UCL.

To give some idea of the ultimate electro-absorptive modulation which may be achieved using quantum wells of $\approx 100\text{\AA}$, we have also rescaled the photocurrent spectra for the high-quality M33 sample of Fig. 2.6.2.2. The same absorption value as for the KLB461 sample was used to "seed" the calculation of the absorption spectra, since the wells are of roughly equal dimensions in the two cases, and at the continuum the absorption level should be insensitive to broadening mechanisms.

Fig. 3.4.2.4 (over page) shows the calculated M33 absorption spectra. The first thing to notice is the increased height of the $e1-hh1$ peak above the continuum. There is an increase of $\approx 3000\text{ cm}^{-1}$ compared to the KLB461 sample due to the reduced doping broadening in this structure. Background doping was shown in § 2.6.2 to be in the region of $5-6 \times 10^{14}\text{ cm}^{-3}$. The shifted $e1-hh1$ peak therefore remains more clearly resolved as field is increased, resulting in a larger maximum absorption change off

the edge than for KLB461. Between 4-5V the absorption change is as high as $11,000 \text{ cm}^{-1}$, although this is not shown here.

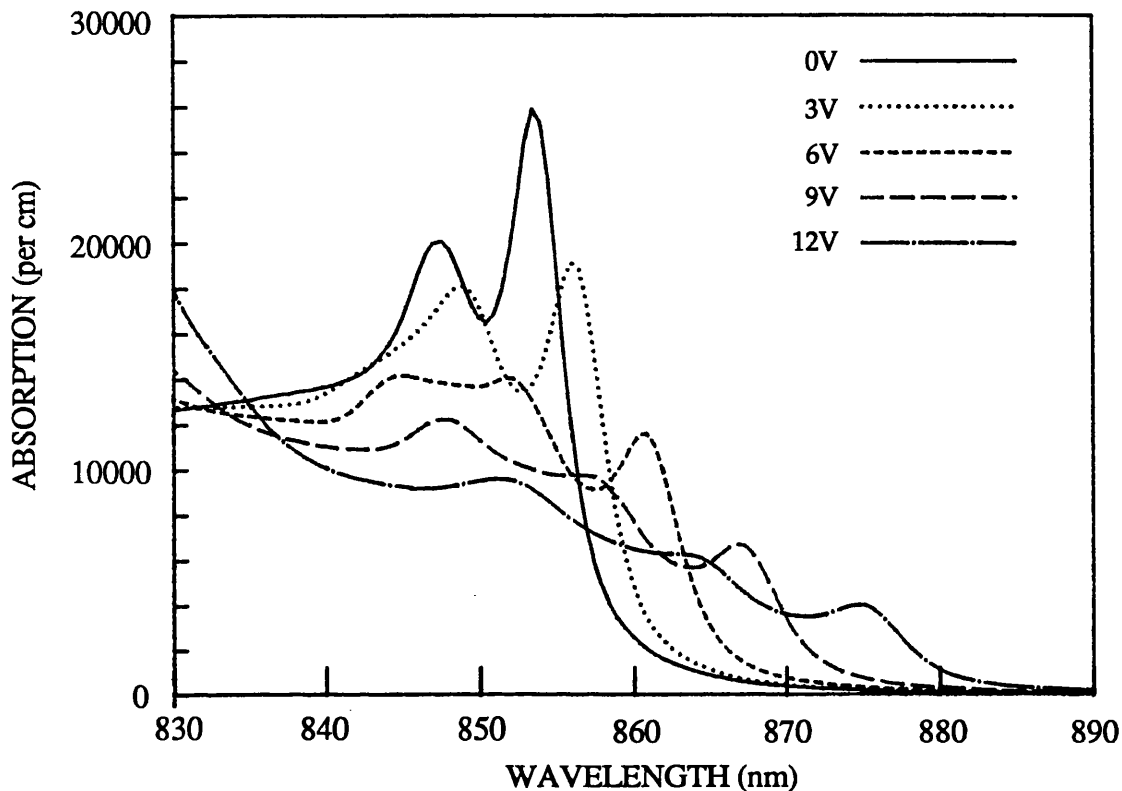


FIGURE 3.4.2.4:

Absorption spectra of very high quality MQW sample M33 as calculated from the photocurrent spectra of § 2.6.2. Well width is $\approx 100 \text{ \AA}$. The average applied electric field at 12V is $\approx 120 \text{ kV/cm}$.

As for the KLB461 sample, the M33 spectra have also been modelled. Fig. 3.4.2.5 (over page) shows once more the good agreement between the modelled absorption spectra and those derived from photocurrent measurements, especially for the $e1\text{-hh}1$ exciton. There seems to be more loss in oscillator strength than theoretically predicted, even though the original $e1\text{-hh}1$ peak is higher. However, as we saw in § 2.6.2, the Stark shift agreement is almost exact. Again there are discrepancies in the region of the $e1\text{-lh}1$ and $e1\text{-hh}2$ peaks where absorption falls strongly with bias, but the accuracy of these transitions is less crucial to the modelling of device performance.

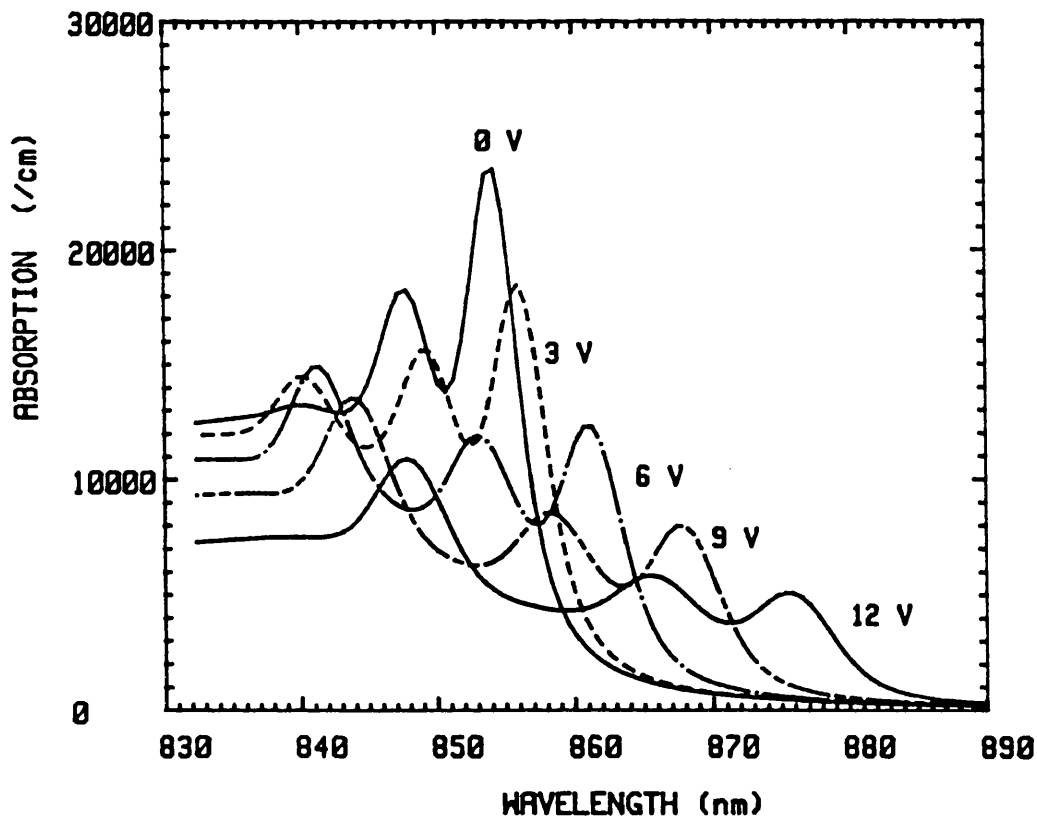


FIGURE 3.4.2.5:
Modelled absorption spectra for the M33 structure ($\approx 100\text{\AA}$ wells). Calculation by Peter Stevens, UCL.

3.4.3 AGREEMENT WITH THE ELECTRO-ABSORPTION SUM RULE

A number of sum rules pertaining to the absorption in QW structures subject to an applied electric field have been derived by Miller et al [1].

The simple statement of the first electro-absorption sum rule is that the integrated absorption, A , over the whole spectrum should remain constant, i.e.

$$\Delta A = \int_0^{\infty} [\alpha_v(\hbar\omega) - \alpha_0(\hbar\omega)] d(\hbar\omega) = 0 \quad \dots(3.10)$$

This rule actually applies to the more general case of electro-absorption in bulk materials and for electric fields applied in the directions other than perpendicular to the plane of the quantum wells.

Here we use absorption spectra derived from the KLB461 photocurrent data to examine how quickly the sum rule converges over the absorption spectrum. The absorption calculations are carried out over a much wider wavelength range (650-920nm) than for the spectra in the previous

section.

We have previously remarked on the apparent wavelength dependence of the quantum efficiency for photocurrent at low bias voltages in the KLB461 sample. In order to avoid this problem, for the sum rule calculation we consider only the photocurrent spectra for bias voltages $\geq 5V$ (see Fig. 2.6.1.2), where the quantum efficiency appears to have levelled out and no scaling is required. These spectra are converted into absorption spectra by the method explained above. In this case the "seeding" value of absorption is $51,780 \text{ cm}^{-1}$ at 658nm which is taken from the AR-coated transmission spectrum in Fig. 3.2.3.2.

In Fig. 3.4.3 we have plotted the calculated absorption spectra for $5V$ and $10V$ bias only for clarity. It can be seen that the $e2\text{-}hh1$ forbidden transition is already appearing strongly (at $\approx 810\text{nm}$), and that the major electro-absorptive changes are confined to wavelengths greater than $\approx 800\text{nm}$, which coincides with the $n=2$ sub-band edge at zero bias (see the photocurrent spectra in Fig. 2.6.1.2).

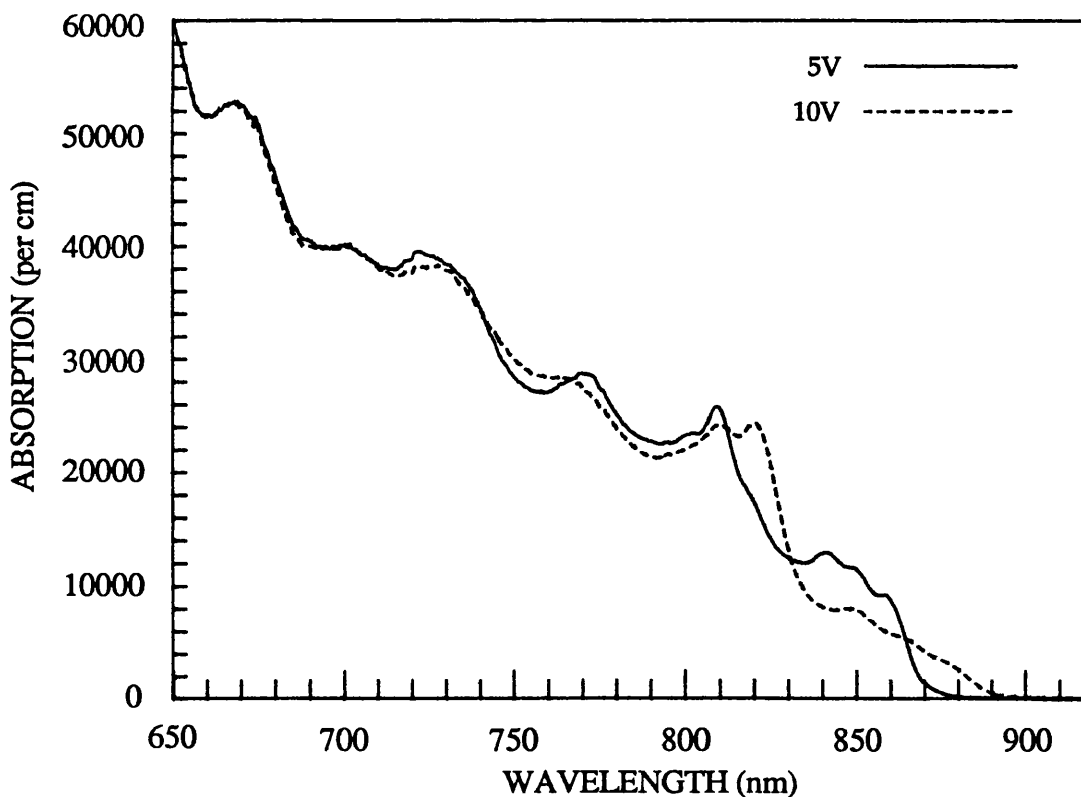


FIGURE 3.4.3:

Absorption spectra for MQW sample KLB461 showing the regions where strong electro-absorptive effects occur.

The integrated absorption for the spectra above and those at the intermediate bias voltages has been calculated for three wavelength ranges, with the appropriate conversion of the integrand in Eq. 3.10 for the integration over λ rather than ω . Results are tabulated below. All values have been normalized to the integral at 10V.

TABLE 3.3

Normalized integrated absorption for MQW sample KLB461

	<u>650-920nm</u>	<u>770-920nm</u>	<u>830-920nm</u>
A(5V)	0.990	0.997	1.132
A(6V)	0.997	1.003	1.105
A(7V)	0.999	1.003	1.074
A(8V)	0.999	1.002	1.044
A(9V)	1.000	1.001	1.018
A(10V)	1.000	1.000	1.000

There is excellent conservation of the absorption over the full range of 650-920nm and the reduced range of 770-920nm, with less than 1% variation. When we ignore the contribution of the forbidden transitions which grow just below the $n=2$ sub-band edge, the sum rule breaks down and the variation in the integral is more than 13%. It appears that oscillator strength is being transferred from the e1-hh1 and e1-lh1 "allowed" excitons to the initially forbidden e1-hh2, e2-hh1 and e2-lh1 excitons as field increases. We are careful to include the forbidden transitions when calculating the electro-refractive effect in the next section.

Sum rule calculations have also been carried out for the M33 sample, with absorption conservation being observed for 2V and upwards, which coincides with the saturation of the quantum efficiency in this higher quality sample. The same spectral convergence is seen as for the KLB461 sample.

3.5 CALCULATION OF ELECTRO-REFRACTION

3.5.1 GENERAL POINTS CONCERNING ELECTRO-REFRACTION

- (i) The change in absorption, $\Delta\alpha$, induced by an applied electric field is simultaneously accompanied by spectral changes in the real part of the refractive index, n . The two properties are linked by the Kramers-Krönig (KK) relations, which can be summarized as follows:

For any material a complex dielectric function can be defined thus:

$$\epsilon = \epsilon_1 + i\epsilon_2 \quad \text{.....(3.11)}$$

which is simply related to the complex refractive index, \tilde{n} , by $\epsilon = \tilde{n}^2$.

The complex index is usually expressed as:

$$\tilde{n} = n - ik \quad \text{.....(3.12)}$$

where n , the real part, is the term which is commonly meant when referring to refractive index, and k is called the *extinction coefficient*, defined as:

$$k = \alpha\lambda/4\pi \quad \text{.....(3.13)}$$

with λ as usual the optical wavelength.

So the components of the complex dielectric function are:

$$\epsilon_1 = n^2 - k^2 \quad \text{.....(3.14)}$$

$$\epsilon_2 = -2nk \quad \text{.....(3.15)}$$

The KK relations are the link between ϵ_1 and ϵ_2 and are normally cast in the following form, as a function of the angular frequency, ω ($\omega = 2\pi c/\lambda$, c = velocity of light).

$$\epsilon_1(\omega) = 1 + \frac{2}{\pi} P \int_0^\infty \frac{\omega' \epsilon_2(\omega')}{[\omega']^2 - \omega^2} d\omega' \quad \text{.....(3.16)}$$

and

$$\epsilon_2(\omega) = -\frac{2\omega}{\pi} P \int_0^\infty \frac{\epsilon_1(\omega')}{[\omega']^2 - \omega^2} d\omega' \quad \text{.....(3.17)}$$

P represents the Cauchy principal value of the integral, which means avoiding the critical point $\omega' = \omega$ in the integrand by integrating in two parts, from 0 to $\omega - \delta$, and from $\omega + \delta$ to ∞ , with $\delta \rightarrow 0$. A tutorial discussion of these integral relationships can be found in Ref. [17].

A more practical form of the KK integral, based on Eqs. 3.13-3.17, which relates the directly measurable properties of absorption and the real

part of the index is also given in standard texts [18].

$$n(\omega) - 1 = \frac{hc}{2\pi^2} P \int_0^\infty \frac{\alpha(\omega')}{(\omega')^2 - \omega^2} d\omega' \quad \dots(3.18)$$

In theory, knowledge of the complete absorption spectrum is required to compute the real part of the refractive index, or vice versa, since the integral covers the range 0 to ∞ . In practice, for the MQW structures, we shall only be interested in the possibility of using the *changes* taking place to produce a modulation, and so we restrict the range of integration to the region of the absorption spectrum close to the fundamental absorption edge, where the notable changes in absorption occur.

Substituting λ , which we measure experimentally, for ω , the change in refractive index, Δn , caused by an applied voltage, V , becomes:

$$\Delta n(\lambda, V) \approx \frac{1}{2\pi^2} P \int_{\lambda_1}^{\lambda_2} \frac{\Delta\alpha(\lambda', V)}{\left[1 - \left(\frac{\lambda'}{\lambda}\right)^2\right]} d\lambda' \quad \dots(3.19)$$

where $\lambda_2 > \lambda_1$. Thus, given a reasonably wide range of absorption data for different bias voltages, we can compute the corresponding electro-refractive effects.

The electro-refractive effect or quadratic electro-optic effect has been calculated by Weiner et al [15] using the KK transformation of directly measured electro-absorption data, with good agreement with some of our results in the following sections. Other authors have determined QW electro-refraction from measurements of the field-induced phase shift in waveguides [19-21] or by electro-reflectance [22], all of whom observed the strong quadratic behaviour of the index changes associated with the excitons at the absorption edge. The actual magnitude of the index changes reported shows some variation, but the effect is seen to be considerably stronger than the linear electro-optic effect close to the MQW absorption edge, with peak changes of up to 1% at fields of $\approx 10^5$ V/cm.

The thickness of the active region in normal-incidence MQW device structures is generally around $1\mu\text{m}$ in order to obtain a substantial absorption. If the refractive index were to change by 1% ($n \approx 3.4$ - 3.5 for GaAs MQWs) on the application of an external electric field, then the phase change imparted to a transmitted beam of light would be

$\Delta\phi \approx 2\pi\Delta nL/\lambda$, which at $\approx 850\text{nm}$, with $L = 1\mu\text{m}$, would still only be $\pi/12$. To determine noise-free spectra of refractive index change, using for example a Mach-Zehnder interferometer [21, 23, 24] to measure phase changes of the above magnitude and less, requires both a stable, tunable, coherent optical source and a thermally and mechanically stable experimental environment. It was therefore decided to avoid direct measurement and proceed with calculation of the index changes in MQWs by KK transformation of existing absorption data.

The index change at any wavelength is influenced by absorption changes at all other wavelengths according to Eq. 3.19. However, the absorption changes at wavelengths away from the MQW absorption edge either tend to zero (longer λ) or are diminished by the denominator of the integral (forbidden transitions), so that we can confine the integral to a fairly small spectral region and retain accuracy.

3.5.2 CALCULATION OF INDEX CHANGES BASED ON PHOTOCURRENT DATA

In this section we use the absorption spectra determined from photocurrent measurements on the two MBE-grown samples, KLB461 and M33, to generate spectra of refractive index change. For all the KK calculations in this and the following section we take electro-absorption spectra (defined as the absorption changes from unbiased to biased state, $\alpha(\lambda, V) - \alpha(\lambda, 0)$) and integrate the absorption changes numerically according to Eq. 3.19. A simple trapezoidal rule is used, which is adequate for the 0.5nm point spacing in our spectra. The integral is split into two parts, one either side of the singularity at $\lambda' = \lambda$ and truncated one point spacing away from it. We ignore any contribution to the integral from the region $\lambda - \Delta$ to $\lambda + \Delta$, where Δ is the point spacing, since for small Δ the contributions will tend to cancel each other out on either side of the singularity, especially when $\Delta\alpha$ is slowly varying.

Table 3.4 (over page) shows how the integral converges for decreasing point spacing. The test calculation is for a linearly decreasing positive $\Delta\alpha$ over the range 850-880nm, with the singular point at 865nm. We see that for the 0.5nm spacing used here the integral is only 3-4% down on the asymptotic limit.

TABLE 3.4:

The convergence of the Kramers-Krönig integral with point spacing for the trapezoidal integration rule.

<u>Point Spacing(nm)</u>	<u>Normalized integral</u>
3.0	0.799
1.5	0.900
1.0	0.934
0.5	0.967
0.2	0.987
0.1	0.994
0.05	0.997
0.01	1.000

Looking at the denominator in the integrand of Eq. 3.19, the contribution of an absorption change at 770nm to the index change at 860nm will be more than a factor of 17 smaller than the contribution from the same absorption change at 855nm. Therefore, in the following KK calculations we shall restrict the integral to the wavelength range 770-920nm, where, as we have already seen, the major absorption changes occur, including the forbidden transitions.

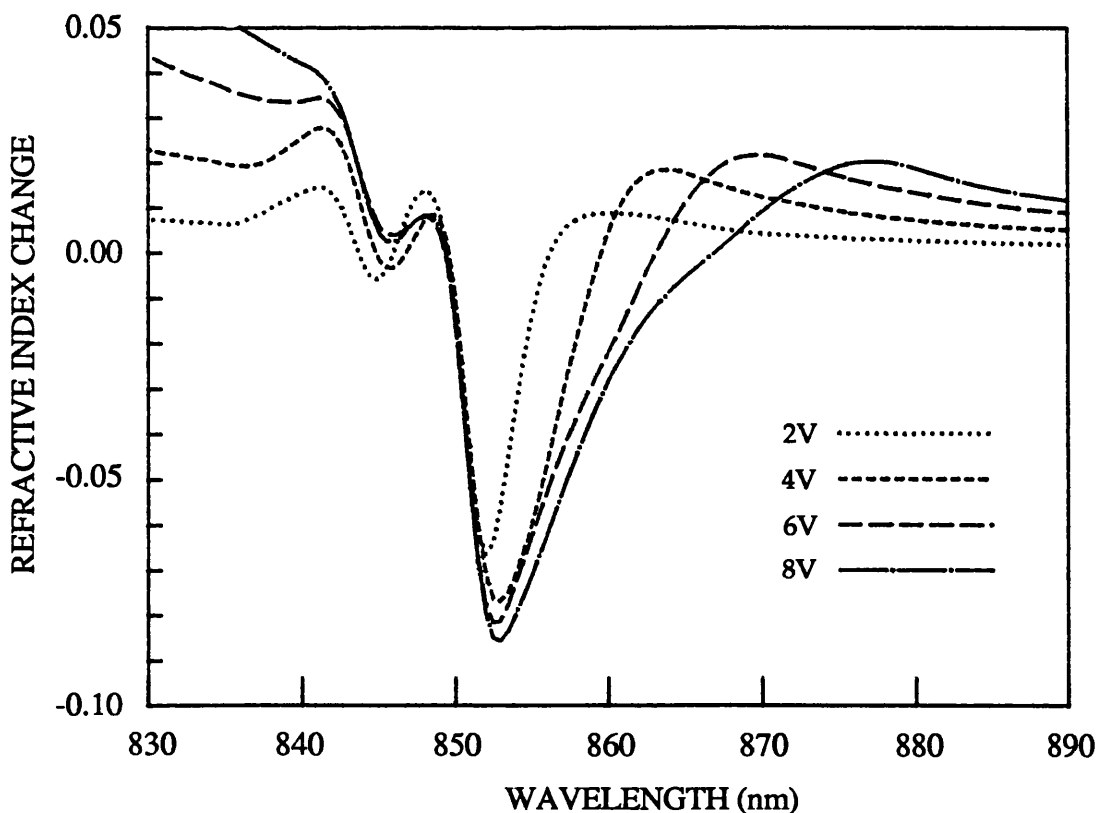


FIGURE 3.5.2.1:

Calculated electro-refraction spectra for sample KLB461 based on electro-absorption data derived from photocurrent measurements.

The calculated Δn spectra for sample KLB461, on the previous page in Fig. 3.5.2.1, show an extremely large negative change of more than 2% of the index. However, this maximum change appears in all cases very close to the position of the unbiased e1-hh1 exciton, thus we could not expect obtain phase modulation without accompanying large changes in the signal intensity due to electro-absorption. Of more interest for phase modulation are the positive changes in the 860-880nm region which red shift with increasing electric field, driven by the shift of the e1-hh1 exciton absorption peak. The index changes here are still large by comparison with the linear electro-optic effect for bulk GaAs. The linear electro-optic coefficient, r_{41} , is $\approx 1.1 \times 10^{-10}$ cm/V close to 900nm (quoted in Ref. [21]). This gives an index change of $\approx 2.5 \times 10^{-4}$, almost two orders of magnitude smaller than the peak electro-refractive effect calculated.

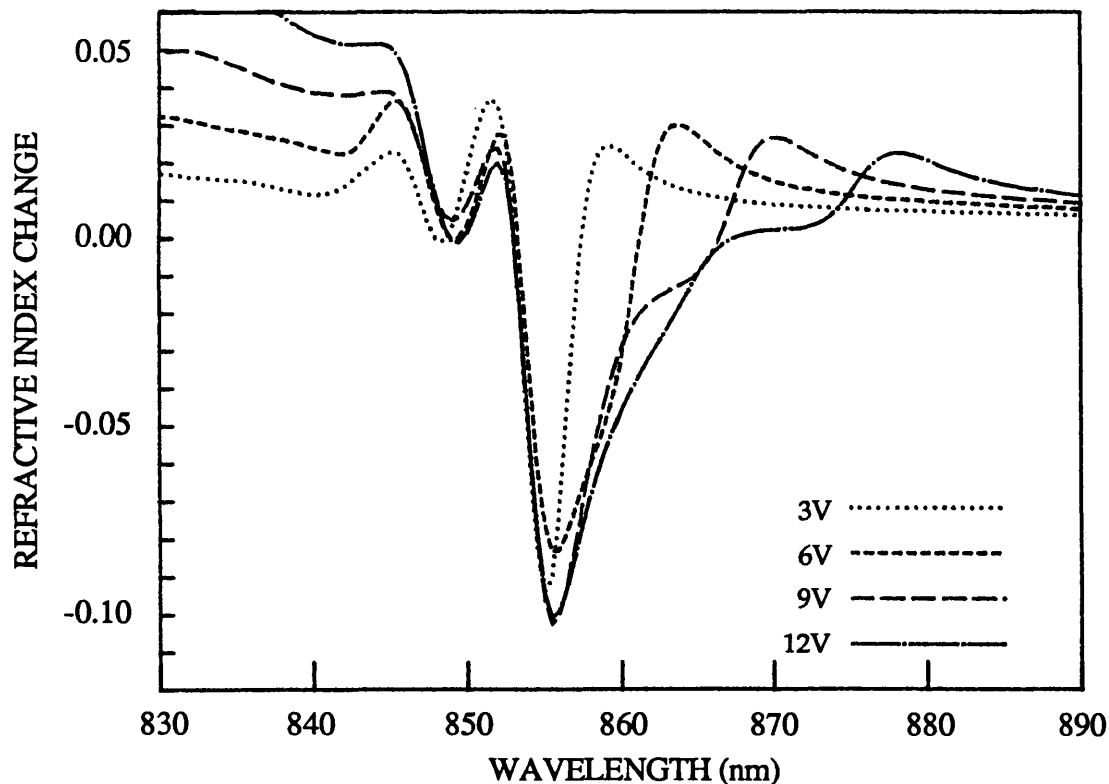


FIGURE 3.5.2.2:

Calculated electro-refraction spectra for MQW sample M33 based on electro-absorption data derived from photocurrent measurements.

To compare with the KLB461 spectra, the KK calculations have also been carried out for the M33 sample. The spectra are shown above in Fig. 3.5.2.2. Maximum index changes in both senses are increased by the sharper absorption peaks for this sample, but the qualitative appearance is

very similar.

In the two samples above the index change is limited to a maximum of $\approx 0.02-0.03$. To achieve a phase change of π radians will therefore require a total thickness of quantum wells of at least $20\mu\text{m}$. This is not practical in a normal incidence modulator, but by using a waveguide with light propagating along the QW layers to increase the interaction length, efficient phase modulators can be designed [23-26]. The main problem in the optimization of such devices is to avoid as much as possible the intensity modulation which occurs due to electro-absorption at the same wavelengths as the maximum index changes.

3.5.3 CALCULATION OF INDEX CHANGES BASED ON TRANSMISSION DATA

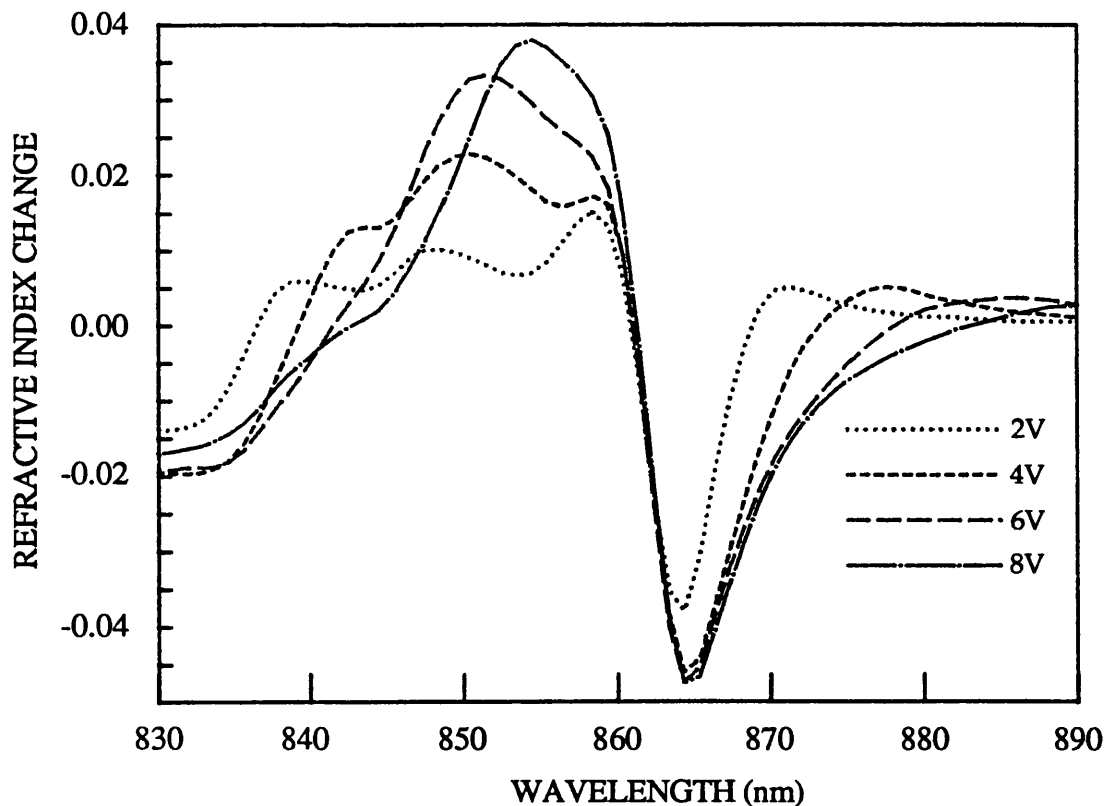


FIGURE 3.5.3.1:

Calculated electro-refraction spectra for MQW sample MV 245 (145\AA wells) based on electro-absorption data derived from transmission measurements.

Using the same KK integration method as above, we calculate here the electro-refraction spectra for the wide and narrow well MQW samples for which we derived the absorption spectra in § 3.3. The aim is simply to

show how the spectra differ from those for the more standard 100Å wells.

As might be expected, for the MV245 sample with $\approx 145\text{\AA}$ wells, where the electro-absorption is much reduced in the region just off the unbiased edge (Fig. 3.3.1), we see that the maximum index changes in Fig. 3.5.3.1 are about a factor of 4-5 down compared to the 100Å well structures, although in this case the peak value of 0.005 is achieved at very low field.

With the 47Å well MV246 sample the peak index changes are large, in line with the electro-absorption, being as much as $\approx 4\%$ in the negative sense. The maximum positive change is, however, no bigger than that for the M33 sample and requires 3-4 times the field.

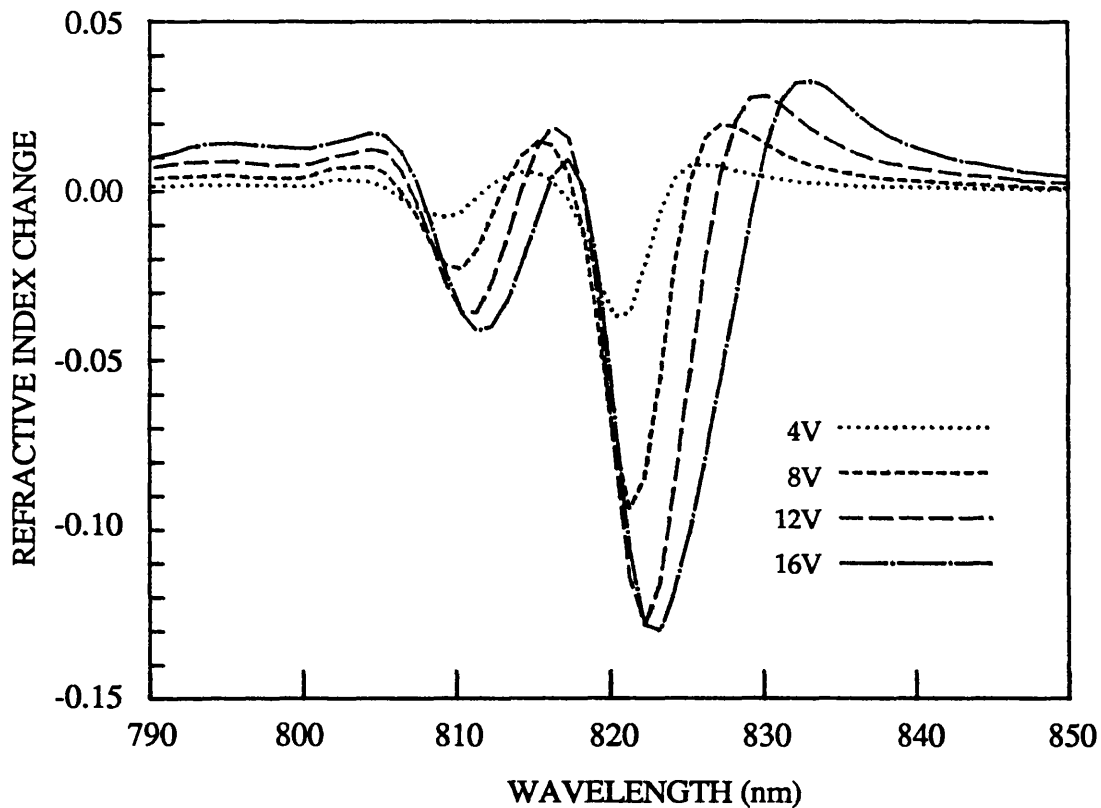


FIGURE 3.5.3.2:

Electro-refraction spectra for MQW sample MV246 (47Å wells) based on electro-absorption data derived from transmission measurements.

For all the calculated electro-refraction spectra in this section it is quite clear that it will not be possible to access the maximum index changes without the attendant effects of background absorption, which will cause both insertion loss and intensity modulation in the case where only phase modulation may be desired. This is a significant problem in waveguide modulators [23-26], where the operating wavelength for optimum phase modulation must be well away from the QW absorption

edge, thus diminishing the enhanced modulation expected of the QW structure. In Chapter 5, where we consider FP cavity modulators we will examine whether the electro-refraction and electro-absorption can be successfully combined.

3.6 SUMMARY

In this chapter, as in the previous one, we have investigated the optical properties of GaAs MQWs. In this case we have attempted to quantify the more fundamental properties such as absorption, the changes in absorption which may be induced by an electric field, and the associated change in the refractive index. All of these are of interest for optical modulators.

We first discussed the effect of Fabry-Perot oscillations on the accuracy of calculating absorption coefficients because this is an effect which is intrinsic to GaAs-AlGaAs MQW transmission device structures. The problems encountered in removing the FP effects by AR-coating have been outlined and we have determined the reduction in surface reflectivity required to reduce them to acceptable levels, such that transmission spectra are not strongly distorted. Following on from this we have defined accuracy limits for calculated absorption according to the amplitude of the remnant FP oscillations and the product of the absorption coefficient and absorber thickness, αd . Typically, we find that with a front surface reflectivity reduced to 0.01 (from ≈ 0.30), we can calculate a value of αd from the transmission spectrum with errors of only a few % possible.

Absorption coefficients have been calculated at certain points in the spectrum for a range of samples with well widths between 47Å and 145Å, and varying degrees of remnant FP oscillations, and we have found general agreement with the results of other workers, apart from the data for the narrowest quantum wells. For transmission spectra which were free from FP effects we have calculated complete absorption spectra for a range of bias voltages. For a structure containing wells of $\approx 47\text{Å}$ the maximum absorption change occurs off the unbiased absorption edge and is $\approx 14,000\text{ cm}^{-1}$ at a field of $\approx 213\text{ kV/cm}$. When the wells are increased to $\approx 145\text{Å}$ the maximum absorption changes occur at the wavelength of the unbiased e1-hh1 exciton. With an applied field of $\approx 67\text{ kV/cm}$ the absorption falls by more than 8000 cm^{-1} . These well widths are likely to represent the practical limits for MQW modulators. At the narrow well width end the fields required to shift the exciton by at least its own linewidth lead to rather unattractive bias voltages of around 20V. Whilst at the wider well end, although the absorption is more sensitive to field, the oscillator strength is lost very rapidly in the shifted exciton.

Maximum absorption changes at the unbiased exciton peak are also limited by the reduction in oscillator strength as the well width increases, tending towards the bulk material characteristics.

Absorption spectra for $\approx 100\text{\AA}$ wells have also been calculated from photocurrent spectra using supplementary data obtained from transmission measurements. These spectra agree well with data on $\approx 100\text{\AA}$ wells determined previously from transmission spectra by other authors, and also with a theoretical model for MQW electro-absorption developed by Peter Stevens at UCL. Wells of this size offer a good compromise between the absorption change achievable and the field required. For high quality material we estimate a maximum $\Delta\alpha$ of $\approx 11,000\text{ cm}^{-1}$ at a field of only $\approx 50\text{ kV/cm}$.

We shall use the calculated absorption spectra in Chapter 5 to simulate MQW devices where FP cavity characteristics are deliberately incorporated. Such devices can be made to modulate strongly on the basis of phase changes induced in the cavity. Therefore we have also calculated the electro-refractive effects which go hand in hand with the electro-absorption. The maximum usable index changes for 100\AA wells appear to be about 0.01-0.02, which means in principle that efficient MQW cavity modulators can be designed and constructed. Derivation of electro-absorption and electro-refraction spectra by the method described here has also been used successfully in the optimization of MQW waveguide modulators [26].

REFERENCES (Chapter 3)

- [1] D. A. B. MILLER, J. S. WEINER and D. S. CHEMLA, "Electric-field dependence of linear optical properties in quantum well structures: Waveguide electroabsorption and sum rules", *IEEE J. Quantum Electron.* (1986), **QE-22**, pp. 1816-30.
- [2] M. WHITEHEAD, G. PARRY, K. WOODBRIDGE, P. J. DOBSON and G. DUGGAN, "Experimental confirmation of a sum rule for room-temperature electroabsorption in GaAs-AlGaAs multiple quantum well structures", *Appl. Phys. Lett.* (1988), **52**, pp. 345-7.
- [3] E. J. AUSTIN and M. JAROS, "Electric field induced shifts and lifetimes in GaAs-GaAlAs quantum wells", *Appl. Phys. Lett.* (1985), **47**, pp. 274-6.
- [4] T. HIROSHIMA and R. LANG, "Well size dependence of Stark Shifts for heavy-hole and light-hole levels in GaAs/AlGaAs quantum wells", *Appl. Phys. Lett.* (1986), **49**, pp. 639-41.
- [5] H. -J. POLLAND, L. SCHULTHEIS, J. KUHL, E. O. GÖBEL, AND C.W. TU, "Lifetime enhancement of two-dimensional excitons by the quantum-confined Stark effect", *Phys. Rev. Lett.* (1985), **55**, pp. 2610-3.
- [6] J. J. LEPORE, "An improved technique for selective etching of GaAs and $Ga_{1-x}Al_xAs$ ", *J. Appl. Phys.* (1980), **51**, pp. 6441-2.
- [7] K. HIKOSAKA, T. MIMURA and K. JOSHIN, "Selective dry etching of AlGaAs-GaAs heterojunction", *Jpn. J. Appl. Phys.* (1981), **20**, pp. L847-50.
- [8] See for example M. BORN and E. WOLF, "Principles of Optics" 6th Edition, Pergamon Press, 1980.
- [9] POCHI YEH, "Optical Waves in Layered Media", Wiley Series in Pure and Applied Optics, Wiley Interscience 1980.
- [10] "HANDBOOK OF OPTICAL CONSTANTS OF SOLIDS", Ed. Edward Palik, Academic Press, N.Y., 1985.
- [11] K. W. JELLEY and R. W. H. ENGELMANN, "An etch tunable antireflection coating for the controlled elimination of Fabry-Perot oscillations in the optical spectra of transverse modulator structures", *IEEE Photon. Technol. Lett* (1989), **1**, pp.235-7.
- [12] Y. MASUMOTO, M. MATSUURA, S. TARUCHA and H. OKAMOTO, "Direct experimental observation of the two-dimensional shrinkage of the exciton wave function in quantum wells", *Phys. Rev. B* (1985), **32**, pp. 4275-8.
- [13] P. J. STEVENS private communication.

- [14] D. E. ASPNES, S. M. KELSO, R. A. LOGAN and R. BHAT, "Optical properties of $\text{Al}_x\text{Ga}_{1-x}\text{As}$ ", *J. Appl. Phys.* (1986), **60**, pp. 754-767.
- [15] J. S. WEINER, D. A. B. MILLER and D. S. CHEMLA, "Quadratic electro-optic effect due to the quantum-confined Stark effect in quantum wells", *Appl. Phys. Lett.* (1987), **50**, pp. 842-4.
- [16] P. J. STEVENS, M. WHITEHEAD, G. PARRY and K. WOODBRIDGE, "Computer modeling of the electric field dependent absorption spectrum of multiple quantum well material", *IEEE J. Quantum. Electron.* (1988), **QE-24**, pp.2007-16.
- [17] F. STERN, "Elementary theory of the optical properties of solids", in *Solid State Physics* Vol. 15, eds. Seitz & Turnbull, Academic Press (New York) 1964, pp. 328-33.
- [18] See for example J. I. PANKOVE, "Optical processes in semiconductors", Dover Publications (New York) 1971, pp. 392-4.
- [19] M. GLICK, F. K. REINHART, G. WEIMANN and W. SCHLAPP "Quadratic electro-optic light modulation in a GaAs/AlGaAs multiquantum well heterostructure near the excitonic gap", *Appl. Phys. Lett.* (1986), **48**, pp. 989-91.
- [20] T. H. WOOD, R. W. TKACH and A. R. CHRAPLYVY, "Observation of large quadratic electro-optic effect in GaAs/AlGaAs multiple quantum wells", *Appl. Phys. Lett.* (1987), **50**, pp. 798-800.
- [21] J. E. ZUCKER, T. L. HENDRIKSON and C. A. BURRUS, "Electro-optic phase modulation in GaAs/AlGaAs quantum well waveguides", *Appl. Phys. Lett.* (1988), **52**, pp. 945-7.
- [22] Y. KAN, H. NAGAI. M. YAMANISHI and I. SUEMUNE, "Field effects on the refractive index and absorption coefficient in AlGaAs quantum well structures and their feasibility for electrooptic device applications", *IEEE J. Quantum Electron.* (1987), **QE-23**, pp. 2167-79.
- [23] P. J. BRADLEY, Ph. D. Thesis, University of London 1989.
- [24] J. E. ZUCKER, T. L. HENDRIKSON and C. A. BURRUS, "Low-voltage phase modulation in GaAs/AlGaAs quantum well optical waveguides", *Electron. Lett.* (1988), **24**, pp. 112-3.
- [25] P. J. BRADLEY, G. PARRY and J. S. ROBERTS, "Optimised multiple quantum well phase modulator", *Electron. Lett.* (1989), **25**, pp. 1349-50.
- [26] P. J. BRADLEY, M. WHITEHEAD, G. PARRY, P. MISTRY and J. S. ROBERTS, "Effect of device length and background doping on the relative magnitudes of phase and amplitude modulation in GaAs/AlGaAs PIN multiple quantum well waveguide optical modulators", *Appl. Opt.* (1989), **28**, pp. 1560-4.

CHAPTER FOUR

ELECTRO-ABSORPTIVE GaAs-AlGaAs MQW MODULATORS

- 4.1 Introduction**
- 4.2 Fabrication and Characterization of MQW Transmission Modulators**
 - 4.2.1 Modulator Fabrication
 - 4.2.2 Measurement of Transmission Modulation
 - 4.2.3 Modulation: Transmission Change and Contrast
- 4.3 The CPM7 (100Å well) Transmission Modulator**
- 4.4 The CPM405 (87Å well) Transmission Modulator**
 - 4.4.1 Device with no Anti-Reflection Coating
 - 4.4.2 AR-Coated Modulator
- 4.5 The MV245 (145Å well) Transmission Modulator**
- 4.6 The MV246 (47Å well) Transmission Modulator**
 - 4.6.1 Device with Imperfect AR-Coating
 - 4.6.2 Device with FP Effects Removed
- 4.7 The CPM405 (87Å well) Reflection Modulator**
- 4.8 Limits to Modulation at Normal-Incidence in MQWs**
- 4.9 Summary**
 - 4.9.1 Comparison of MQW Modulation with Bulk GaAs
 - 4.9.2 Optimum Well and Barrier Widths
 - 4.9.3 General Comments

4.1 INTRODUCTION

In the preceding chapter we investigated the field-induced changes in absorption and refractive index in MQWs in order to provide data necessary to model the performance of devices, be they amplitude or phase modulators or a combination of the two. For example, as we shall see in Chapter 5, absorption and index changes will both cause amplitude modulation in a high-finesse Fabry-Perot cavity. Typical values of the peak absorption change, $\Delta\alpha_{\max}$, were estimated to be $\approx 9\text{-}15,000\text{ cm}^{-1}$ for a range of well widths at an applied field of $\approx 1\text{-}2 \times 10^5\text{ V.cm}^{-1}$. In a single-pass transmission modulator, with a total quantum well thickness, d , of $\approx 0.5\mu\text{m}$, this translates to a contrast ratio, $e^{\Delta\alpha d}$, of between 1.6 and 2.1:1, or $\approx 1\text{-}3\text{dB}$ (see Eq. 4.2).

If we are constrained by limitations on the operating voltage of the modulator, dictated for example by some integrated application, such that we may use no more than 10V, then the total thickness of quantum wells plus barriers will be limited to roughly $1\mu\text{m}$ in order to maintain the electric field required to produce a significant shift of the absorption edge. Therefore it is necessary to achieve the right balance between using a thicker MQW structure in order to increase the $\Delta\alpha d$ factor, and reducing the thickness to reduce the operating voltage (or maintain the necessary electric field).

Even with a fixed thickness for the MQW region of our modulator we are still allowed the choice of well and barrier widths. As we saw in Chapters 1-3, in theory and practice wider wells exhibit a greater Stark shift for a given field, but have reduced absorption coefficient at the important e1-hh1 excitonic peak, and increased field-ionization broadening. In narrower wells the opposite is the case. However, for device purposes we must also consider the effect of the barrier material which is essentially "dead", optically speaking. The ratio of well to barrier material must ultimately decrease as well width decreases. We cannot simply keep on reducing the barrier in proportion because there is a lower limit at which the barrier can no longer prevent significant electronic coupling between neighbouring quantum wells (in the limit the material becomes a superlattice), and at this point the QCSE is severely degraded. Witness in Chapter 2 the photocurrent spectra of sample MV367, which was nominally a $100\text{\AA}/30\text{\AA}$ MQW structure, where the biased spectra are dominated by broadening effects. This is important to remember when

the total MQW thickness is fixed – we obviously wish to have as large a proportion of active material within the MQW as possible without losing the essential MQW properties.

Typical MQW structures in previous studies of the QCSE [1,2] have consisted of wells and barriers of $\approx 100\text{\AA}$ – even thicker barriers being used in some cases, with the aim of minimizing quantum mechanical coupling of carrier states between wells. We choose 60\AA as our barrier thickness for these experiments to increase the proportion of well material that can be packed into the whole structure. Photocurrent spectra (see Chapter 2) indicate that the quantum-confined Stark effect is adequately retained with this reduced barrier.

After some preliminary measurements on the first MQW modulator produced by the MOVPE process, which suffered from the effects of high background doping, we examine devices with three different well widths: 47, 87 and 145\AA , to determine the qualitative and quantitative effects on the transmission spectra under reverse bias. The total thickness of wells plus barriers is kept roughly constant in the three different structures to allow a comparison of performance on a modulation per volt basis.

The results presented here for the transmission modulators have been published previously in a less detailed form [3].

We conclude the experimental section of this chapter with an attempt to improve the modulation achievable with a given thickness of MQWs by operating in reflection, thus making a double-pass through the absorber.

Finally the experimental results obtained here are compared with the work of other authors concerning the limits of electro-absorptive modulation in MQW devices.

4.2 FABRICATION AND CHARACTERIZATION OF MQW TRANSMISSION MODULATORS

As discussed in the preceding chapter, there are significant problems in producing transmission modulators in the GaAs-AlGaAs MQW material system because of the need to remove the absorptive substrate. Here we describe the details of how the aligned window is achieved in the substrate beneath the *p-i-n* mesa which defines the modulator, the deposition of single quarter-wave layer SiN_x anti-reflection coatings in an attempt to remove the unwanted FP effects from the transmission spectrum, and the measurement of transmission modulation. All the modulators studied were of the standard *p-i-n* diode structure as described in Chapters 1 & 2, and grown by the MOVPE process.

4.2.1 MODULATOR FABRICATION

The first stage in the process is to define the MQW *p-i-n* mesa as described in Chapter 3. Figure 4.2.1.1 shows the form of the device at this point.

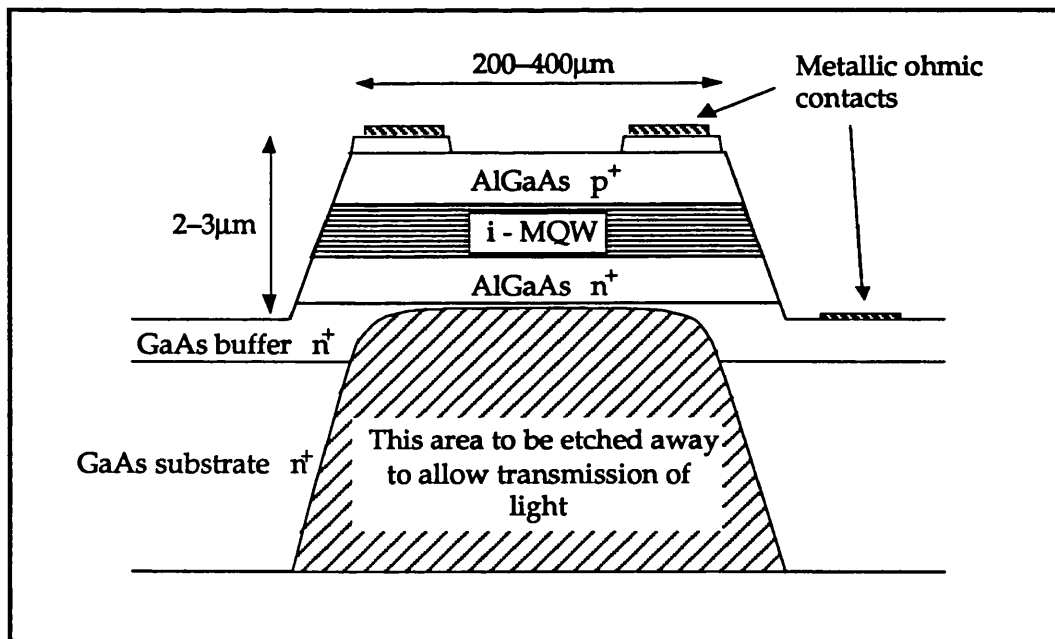


FIGURE 4.2.1.1:
The GaAs-AlGaAs MQW modulator structure prior to window etching.

An anti-reflection (AR) layer of SiN_x is formed on the top surface of the mesa by plasma-enhanced chemical vapour deposition from a mixture of 5% silane in argon and pure nitrogen. The exact composition of the nitride is unknown – but it is certainly not the stoichiometric form, Si_3N_4 . The thickness is intended to be $\lambda/4$ at $\approx 850\text{nm}$, which for the nitride, with an index of ≈ 1.85 , means $\approx 1000\text{-}1100\text{\AA}$. The thickness is determined by a controlled time deposition according to a prior calibration. In theory, zero reflectivity with a single quarter-wave AR coating can be achieved when $n_{AR} = \sqrt{(n_1 n_2)}$, where n_1 and n_2 are the refractive indices of the two media to be matched [4]. With our particular nitride layer on GaAs ($n = 3.62$) we can expect a minimum reflectivity, according to Eq. 3.3:

$$R_{\min} = \frac{(3.62 - 1.85^2)^2}{(3.62 + 1.85^2)^2}$$

which is less than 0.1%.

The AR coating is deposited over the surface of the whole sample, patterned with photoresist to leave the window areas of the mesa diodes covered, then the excess nitride is removed by plasma etching using a Freon-14: O_2 (92%:8%) mixture to leave behind AR "caps" on the mesas.

The rest of the fabrication process, illustrated in Fig. 4.2.1.2 (i)–(viii) over the next two pages, is as follows:

- (i) The back of the GaAs substrate is ground down using a fine grade carborundum. The final thickness is $\approx 100\text{-}120\mu\text{m}$ – thick enough to prevent the sample from shattering, and thin enough to avoid excessive etch time.
- (ii) The sample is fixed device side down, using photoresist, onto a thin glass microscope cover slip. More photoresist is then spun over the back of the sample, extending out over the surface of the cover slip, and pre-baked.
- (iii) Observing the devices through the glass cover slip, the photo-lithographic mask for the back window pattern is aligned with the mesas. The photoresist is then exposed *through* the glass.
- (iv) The photoresist pattern is developed in the area surrounding the sample.
- (v) Turning the sample and cover slip over, the same mask is aligned with the developed pattern surrounding the sample, and is therefore also aligned with the device mesas on the hidden side of the sample.

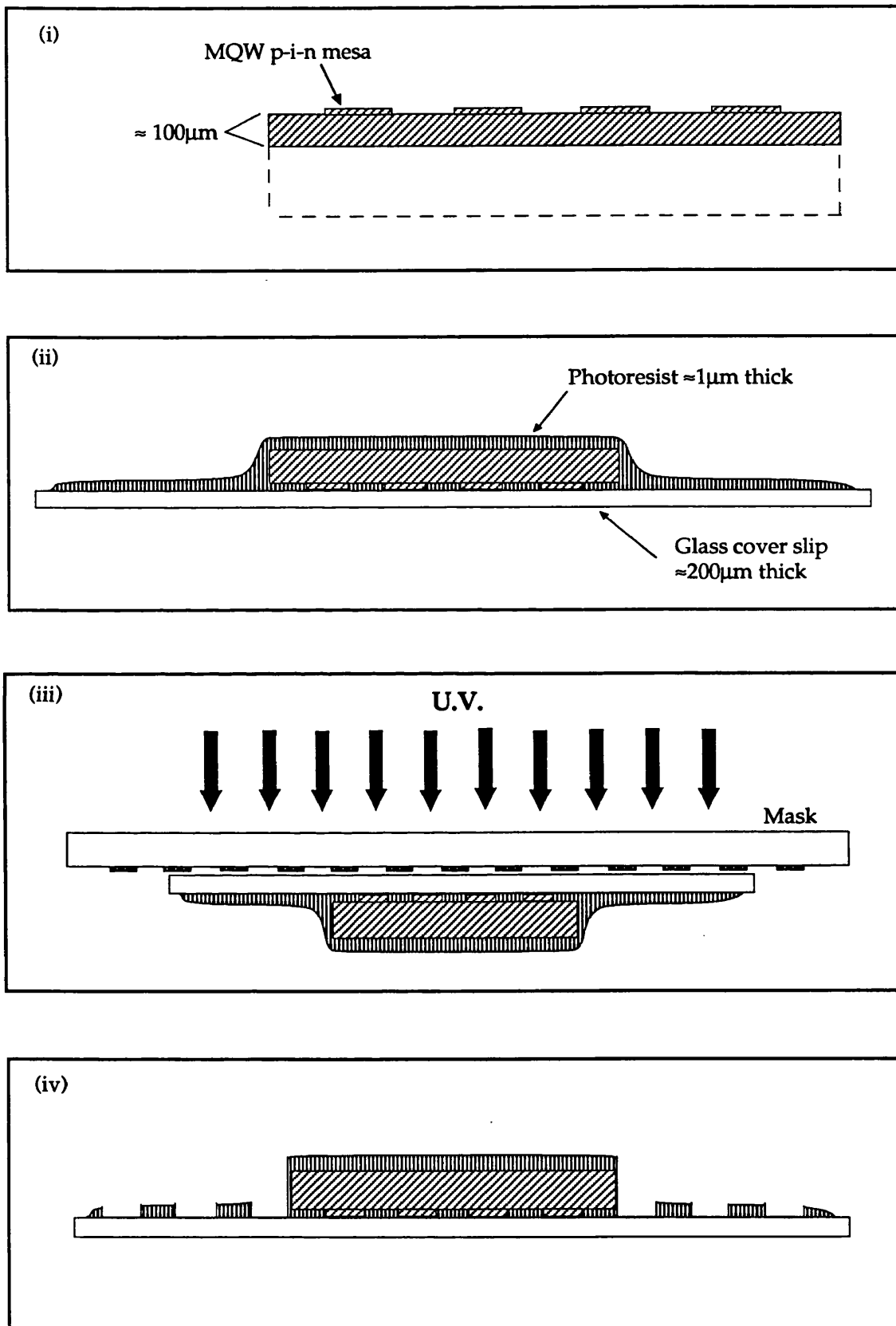


FIGURE 4.2.1.2:
Stages in the fabrication of MQW transmission modulators

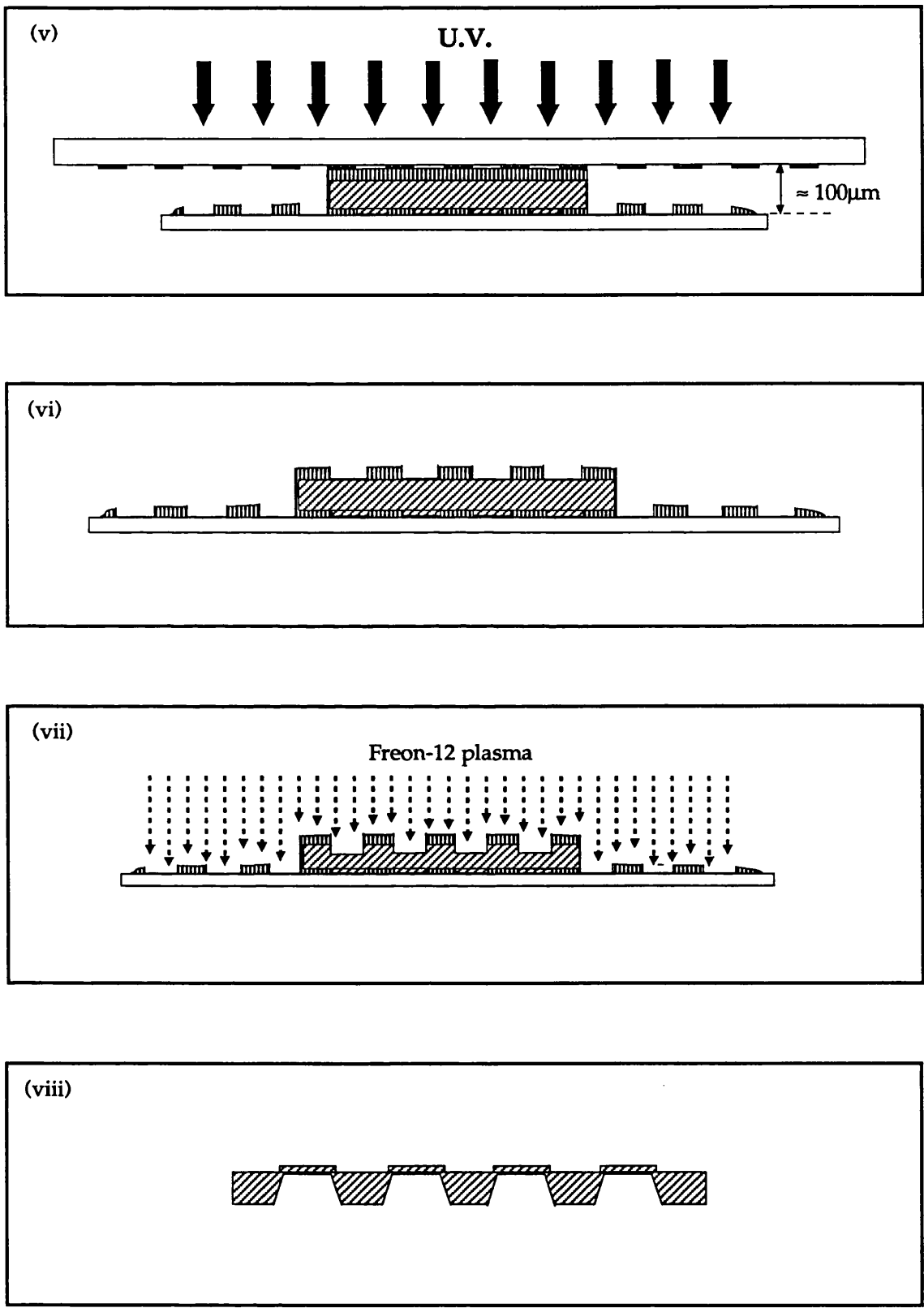


FIGURE 4.2.1.2:
Stages in the fabrication of MQW transmission modulators

The photoresist on the back of the sample is then exposed with the window pattern. With the separation of $\approx 100\mu\text{m}$ of the mask from the registration marks in the photoresist there are obviously limitations to the accuracy of this alignment method. However, devices with mesa widths from $800\mu\text{m}$ down to $200\mu\text{m}$ have been fabricated successfully.

- (vi) The photoresist pattern is developed to open up the areas of the substrate which are to be etched away.
- (vii) Using Freon-12 in a reactive ion etching (RIE) system, the windows in the substrate are dry etched. The etch is selective, with the rate for GaAs reported as high as 200 times that for AlGaAs [5], and so stops abruptly at the interface between the GaAs n^+ buffer and $\text{Al}_{0.3}\text{Ga}_{0.7}\text{As } n^+$ layers. This stage was originally carried out using the wet selective etch described in § 3.4.1 [6]. With the wet process the etching is often prone to problems such as incomplete GaAs removal due to oxide formation, loss of selectivity due to pH imbalance and severe distortion of the window profile due to preferential etching along certain lattice planes. However, the dry process has been found to offer much cleaner etch profiles, selectivity and reproducibility.
- (viii) The remaining photoresist is dissolved in acetone to remove the finished devices from the glass cover slip. Great care must be taken when blowing the sample dry with nitrogen, especially with large area devices, because of the inherent fragility of the final modulator structure, the active area of which is a "membrane" only $2\text{--}3\mu\text{m}$ thick.

It should be pointed out that most of the development of this process to its current level of sophistication has been carried out at UCL by Tony Rivers, based on initial work by Malcolm Pate at the III-V Central Facility, University of Sheffield.

The appearance of the finished transmission modulator is shown in Figs. 4.2.1.3 & 4 over the page. (The photographs were supplied by Tony Rivers of UCL and taken using a scanning electron microscope (SEM)).

Fig. 4.2.1.3 shows the diode mesa as seen from the usual light-input side. Fig. 4.2.1.4 shows a modulator cleaved in half to display the cross-sectional structure, in particular the very thin MQW "membrane" left after substrate etching. This results in the bowing of the window which can be clearly seen in the second photograph of Fig. 4.2.1.3.

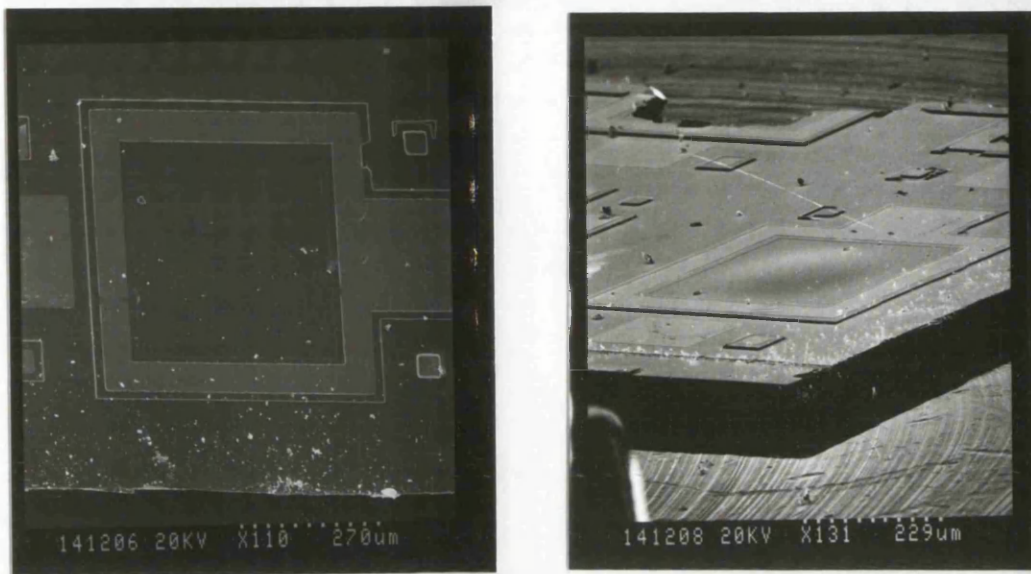


FIGURE 4.2.1.3:
SEM photographs of MQW transmission modulator (Plan view and angled top view).

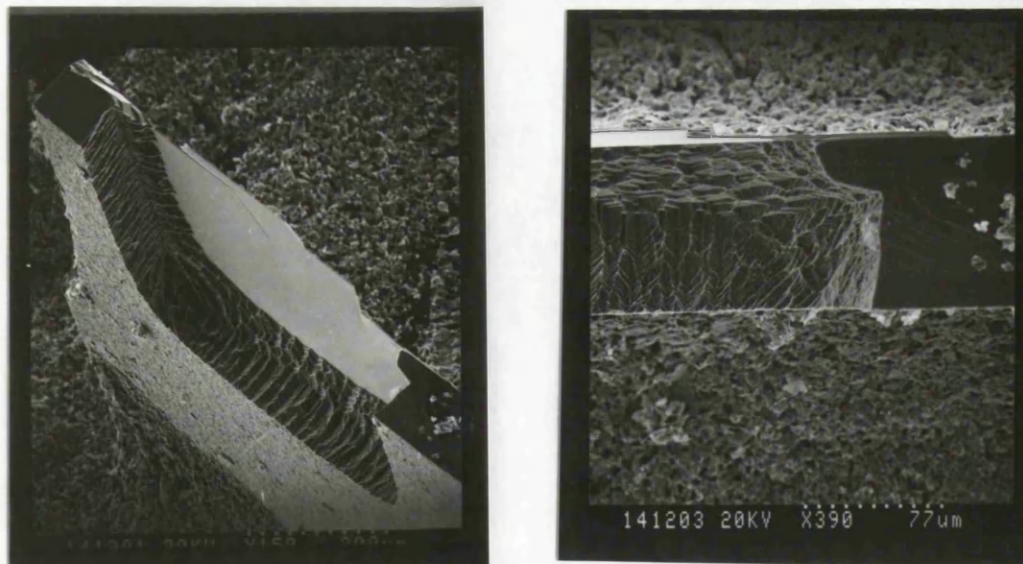


FIGURE 4.2.1.4:
SEM photograph of MQW transmission modulator in cross-section. Angled view shows the smoothness of the etch stop surface. Normal view shows the mesa height

4.2.2 MEASUREMENT OF TRANSMISSION MODULATION

Transmission measurements were made using the automated scanning monochromator system, as described previously in Chapter 2 for photocurrent measurements, for the broadband optical source and data acquisition. Figure 4.2.2.1 shows the simple optical arrangement used.

We measure calibrated transmission using a sample in: sample out method, rather than having two detectors operating simultaneously to record source and transmitted intensity spectra. Although this requires an extra scan without the sample in position, it removes the need to calibrate the splitting ratio of beamsplitters (BS) and detector responsivity.

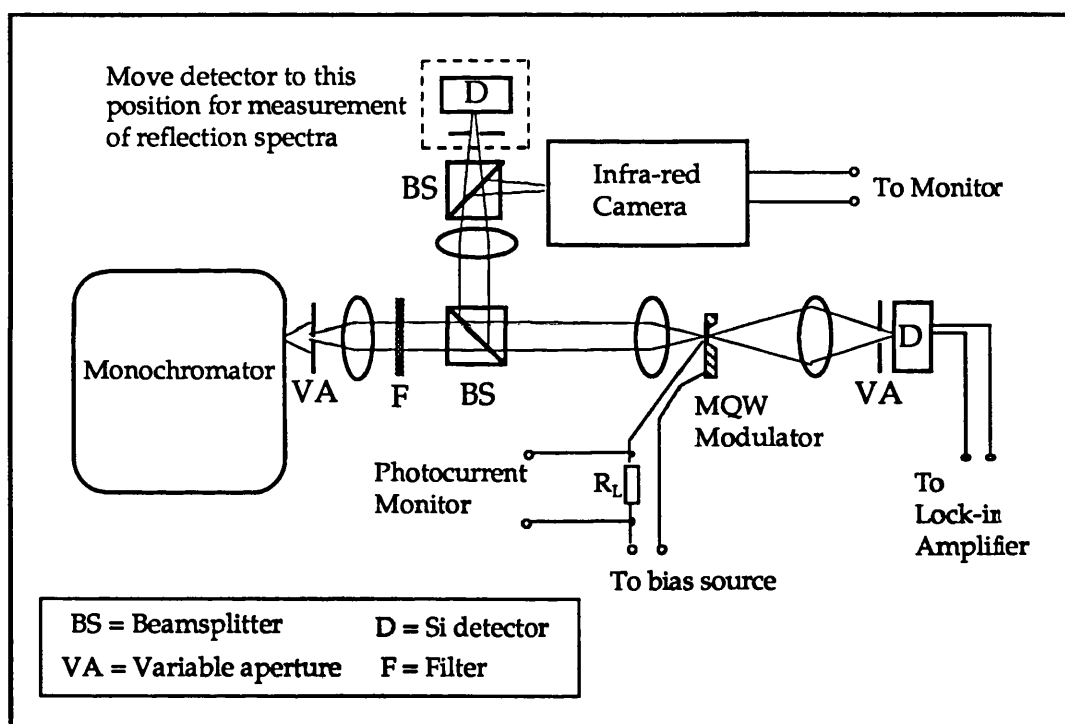


FIGURE 4.2.2.1:

The experimental set-up routinely used to measure transmission spectra, also adaptable for reflection spectra.

Small variable apertures (VA) are used to cut down the focussed spot size and confine light within the modulator window and also to prevent excessive background light from reaching the Si detector. A Schott colour glass filter, F, which passes wavelengths above $\approx 700\text{nm}$ is used to remove 2nd order light from the monochromator, i.e. in the 800-900nm band there is a measurable amount of blue/near UV light transmitted.

The devices are mounted in a variety of ways – some on a glass microscope slide with a large-area Au contact pattern; some on a sapphire disk, also pre-metallized, in turn fixed on a standard TO5 transistor header for simpler biasing. Electrical connections to the modulator are made by hand-bonding 25 μ m diameter Au wire with Ag-loaded epoxy adhesive out from the on-chip contact pads to larger remote metal pads on the device mount. The whole package is then mounted on an x,y,z translation stage for fine control of the device position.

Alignment of the modulator with the optical signal is not difficult to achieve due to its large size ($\approx 500\mu$ m mesa typically). It is possible to use the photocurrent signal to align – we simply maximize the signal by x,y,z movement. There is also an IR camera available to view reflected light from the front surface of device. However, when light is actually focussed onto the device and stopped down, then it is not possible to view the whole of the device. The condition for light being focussed simultaneously on device and camera was found difficult to achieve.

Measurements are all taken at room temperature (in the range 20–25 $^{\circ}$ C) with DC bias applied by a computer-controlled voltage source, which provides 10mV resolution. The output from the monochromator, generally ≈ 100 nW or less when stopped down, is mechanically chopped to reduce noise in detection. Chopping frequencies are kept to below ≈ 1 kHz in order to obtain good response from the lock-in amplifier and keep well below the roll-off frequency of the modulator, which is estimated to be of the order of a few MHz for a 500 μ m square device which is not 50 Ω -matched. No measurement has been made here of the high-speed response of these devices [7], where it has recently been found that modulation is ultimately dependent on the transport time of excess photo-generated carriers out of the quantum wells [8,9].

Normalized transmission spectra are obtained by first measuring the transmitted intensity spectra for the desired range of wavelength and bias voltage. The modulator is then moved out of the path of the beam and the source intensity spectrum measured. The transmission, T, is simply the transmitted intensity spectrum divided by the source spectrum. Care must be taken to ensure that all the light incident on the device falls only within the windowed area, so that no light transmitted through the MQWs is lost in the GaAs substrate. In some cases the normalized spectra show lower transmission than expected in the non-absorbing region. This can be attributed to scattering from roughness at the selectively etched window surface or perhaps to absorption in GaAs if the substrate is

incompletely etched away. Where this was found to be the case the spectra have been scaled to an average transmission of $\approx 70\%$ in the non-absorbing region, which is the limit for a device with one side perfectly AR-coated ($T_{\max} = 1 - R$; $R \approx 0.30$, see § 3.2.4). By "average" we mean the average of the maximum and minimum transmission in the region where FP oscillations remain present.

4.2.3 MODULATION: TRANSMISSION CHANGE AND CONTRAST

Before going on to describe the experimental results it is perhaps worthwhile clarifying what we mean by "modulation". There are usually two adjacent spectral regions in which significant field-induced effects occur with MQWs – around the unbiased e1-hh1 exciton peak, and in the 10-15nm band to the long wavelength side of this peak. In the former case transmission will increase with applied field due to the red shift and loss of oscillator strength, so here we can term the modulation *bias transmitting* (BT). In the latter case transmission falls with applied field as the excitonic absorption is shifted into the operating wavelength, therefore modulation is termed *bias absorbing* (BA). For both these modes of operation the modulation can be defined as transmission *contrast*, C_T , or transmission *change*, ΔT . Contrast is the on:off ratio, "on" being the high transmission state, which may be expressed as the simple ratio or in dB ($10 \log(C_T)$). Note that we may sometimes refer to a contrast without specifying whether the device is switching on or off with applied bias – this depends on whether the device is being operated in BA or BT mode.

Neglecting Fabry-Perot effects, ΔT and C_T are given by the following equations:

$$\Delta T = T(0) - T(V) = (1 - R_b)(e^{-\alpha(0)d} - e^{-\alpha(V)d}) \quad \dots(4.1)$$

$$\begin{aligned} C_T &= T(0)/T(V) \text{ [bias absorbing (BA)]} \\ &= T(V)/T(0) \text{ [bias transmitting (BT)]} \\ &= e^{|\alpha(0) - \alpha(V)|d} = e^{|\Delta\alpha|d} \quad \dots(4.2) \end{aligned}$$

$$\therefore |\Delta T| = T(0)[1 - 1/C_T] \quad \dots(4.3)$$

(0) and (V) refer to the unbiased and biased states respectively, α is the

absorption coefficient, d the total thickness of quantum wells and R_b (≈ 0.30) the reflectivity of the exit (back) facet of the modulator. We assume the front surface to be perfectly AR-coated.

Quoting only the contrast for a modulator can be misleading in that it says nothing about the on and off levels, both of which may be low whilst still giving a high contrast ratio. For example, a contrast of 5 could be achieved by switching between 50% and 10% transmission, or between 5% and 1%. The former case is preferable because the *insertion loss*, i.e. the output "on" state in dB relative to the input signal, is rather high for the latter, and would require more amplification stages for the optical signal. Also, if we only consider transmission changes, then ΔT of 60% could mean a contrast of 4 (80% to 20%) or 61 (61% to 1%). Which of these is the best device characteristic depends on the application in mind. High contrast would, for example, be required in a spatial light modulator or where signals are combined such as in an optoelectronic logic gate, in order to discriminate between 1's and 0's. In a communications link, however, it is more important for the absolute transmission change to be high to achieve highest signal to noise ratio at the detector.

4.3 THE CPM7 (100Å WELL) TRANSMISSION MODULATOR

This was the first attempt to demonstrate an MQW modulator grown by MOVPE. The MQW region consists of 55 x 100Å GaAs wells with 100Å Al_{0.3}Ga_{0.7}As barriers. Unfortunately the performance was seriously affected by background doping in the i-MQW region, which as we stated in Chapter 2 was $\approx 1.3 \times 10^{16} \text{cm}^{-3}$. This was confirmed by photocurrent and C-V measurements. In Fig. 4.3.1 the transmission spectra have been plotted for up to 6V reverse bias. The voltage range is limited by the low breakdown observed with this device – a feature of the immature modulator fabrication process at the time, and to some extent due to the high background doping level.

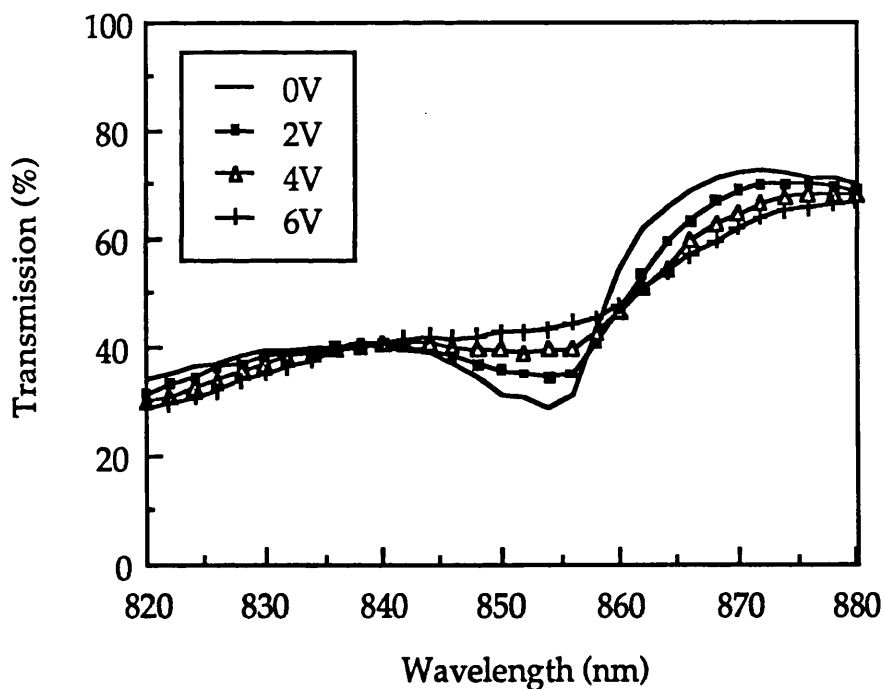


FIGURE 4.3.1:
Room-temperature transmission spectra with reverse bias for MQW sample CPM7.

Evidence for the excitonic absorption is seen only as a fairly broad minimum around 854nm, with no clear resolution of the expected heavy and light hole effects. This is thought to be due to the field-broadening effect of background doping, present even when no bias is applied (see §§ 1.4, 2.5.1), and made worse by well:barrier interface roughness and interwell thickness variations. There is a distinct lack of FP oscillations in

the spectra, despite there being no AR coating applied, which is probably due to a roughened back surface and/or absorption in GaAs not completely removed by the window etch. The spectra have been scaled so that the transmission in the non-absorbing region lies at $\approx 70\%$. The maximum transmission as measured was $\approx 53\%$. In this case the bias response is qualitatively similar to that of a bulk GaAs modulator [10] in that we see no distinct shift of the absorption edge, instead strong broadening occurs due to each quantum well experiencing a different electric field. However, as we shall show at the end of this chapter, for comparable fields the modulation is still stronger even for this poor MQW device.

Figures 4.3.2 and 4.3.3 show the modulation achieved as transmission change and contrast respectively. Maximum transmission changes are only in the 10-15% range, with contrast limited to 0.90dB (BA) and 1.76dB (BT).

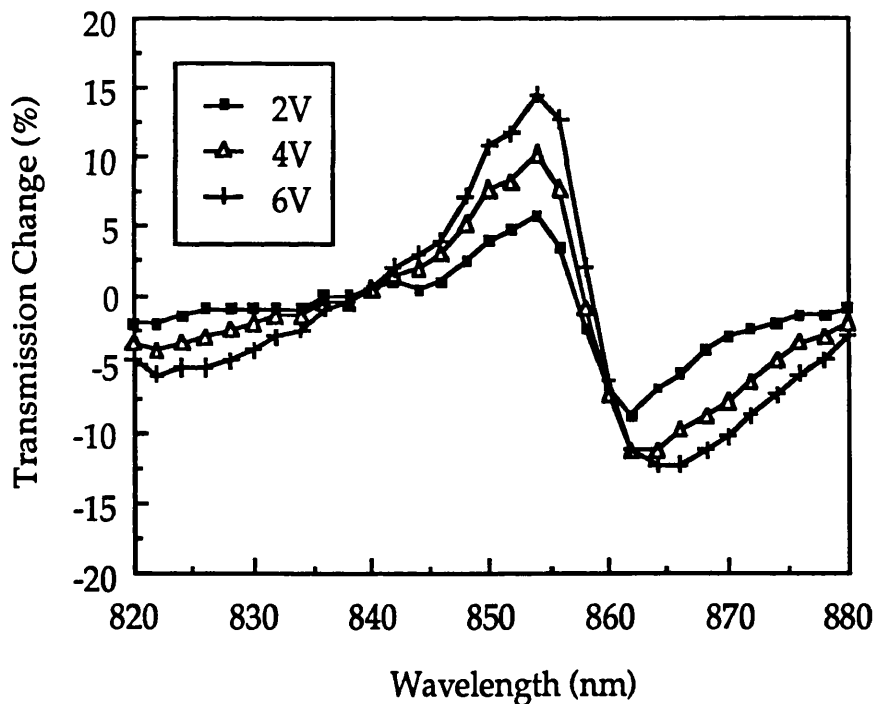


FIGURE 4.3.2:
Transmission changes for the CPM7 modulator.

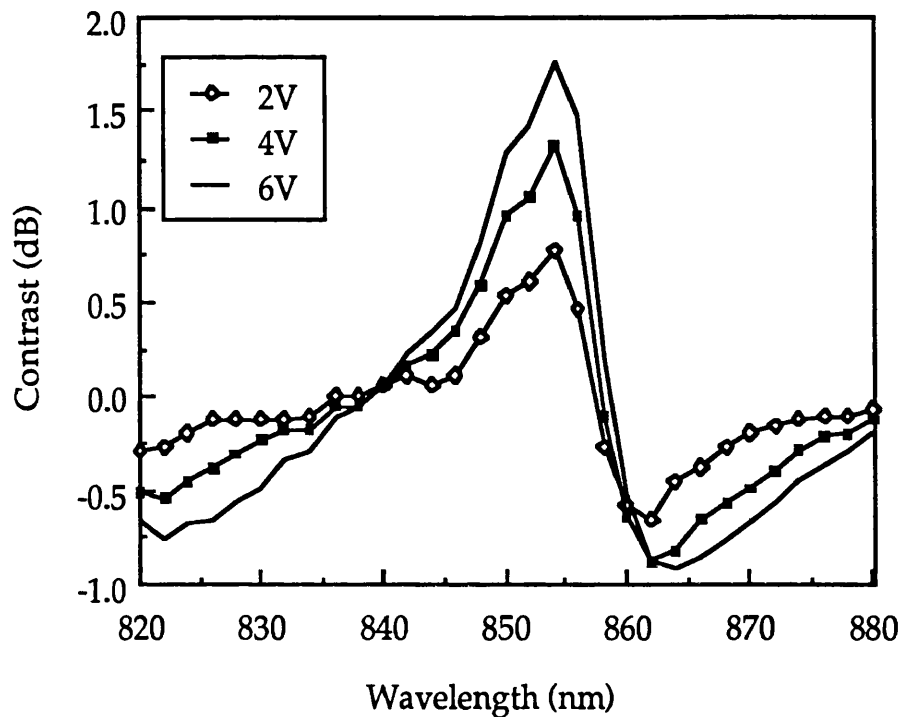


FIGURE 4.3.3:
Transmission contrast for the CPM7 modulator.

By current standards this is a poor example of an MQW modulator. Nevertheless it is useful to include the data here as an indication of a lower limit to performance and to underline how growth optimization has significantly improved devices.

4.4 THE CPM405 (87Å WELL) TRANSMISSION MODULATOR

To our knowledge, this was the first MOVPE-grown MQW *p-i-n* structure to show a clear quantum-confined Stark shift [11]. The improvements in growth which led to this have already been described in Chapter 2. The most crucial achievement was the lowering of background impurity concentrations in the MQW region to $\approx 3-4 \times 10^{15} \text{cm}^{-3}$. The MQW region consists of 60 wells with an estimated thickness of $\approx 87\text{\AA}$ and AlGaAs barriers (0.3 Al mole fraction) of $\approx 60\text{\AA}$. The estimate of the well width comes from comparison of the observed e1-hh1 exciton peak wavelength with the theoretical curve in § 1.3. Spectra from two different devices from the same sample are presented here. The first has no AR coating applied to the front surface, and therefore exhibits pronounced FP resonances. The second has an AR layer of $\approx 1000\text{\AA}$ of SiN_x which reduces the resonance effects to a level which is tolerable according to the analysis in Chapter 3, but does not eliminate them. We discuss the modulation in the light of these effects.

4.4.1 DEVICE WITH NO ANTI-REFLECTION COATING

As we saw in the photocurrent spectra from this sample, there are clearly defined heavy and light hole excitonic absorption peaks which account for the two minima either side of 840nm in the unbiased transmission spectrum of Figure 4.4.1.1. The other important feature of the optical response is the fairly strong FP transmission peak at about 880nm, which, however, is not quite consistent with the reflectivities expected at the front and back surfaces – T_{max} should be closer to 1, and T_{min} closer to 0.30. As with the CPM7 device, transmission is probably slightly affected by scattering and absorption in unetched GaAs substrate. Were there no absorption in this cavity structure then we would expect to see another FP transmission peak very close to where the MQW absorption edge is seen here. With a resonance situated almost on the absorption edge, as we shall show in the next chapter, the transmission spectra are strongly distorted and, in this case, the transmission changes reduced compared to what would be expected from a device with a reasonable AR coating (see § 4.4.2).

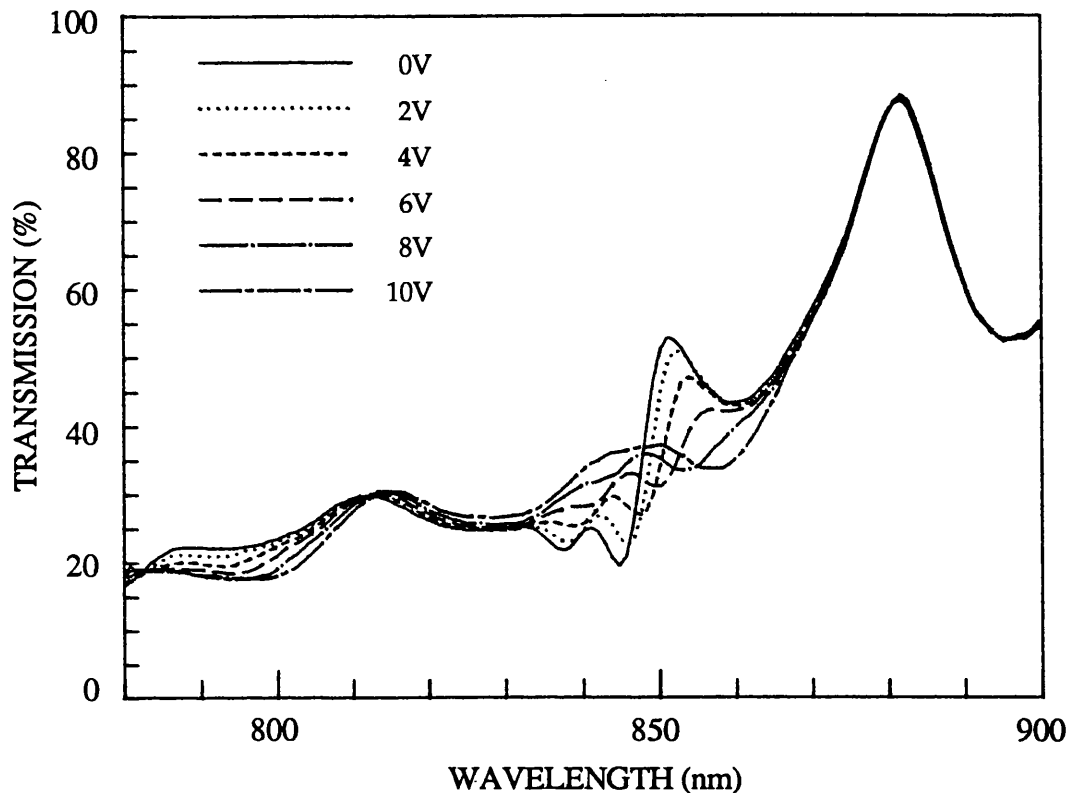


FIGURE 4.4.1.1:

Room-temperature biased transmission spectra for MQW modulator CPM405 with no AR coating.

The FP peak can also be positioned so as to improve the modulation. This depends on the thickness of the cavity, which for this type of modulator is determined by how far the substrate window etching process penetrates into the n -AlGaAs layer of the p - i - n .

Despite the non-optimal FP effects, this device shows larger transmission changes than the CPM7 device, with maximum values of $\approx \pm 20\%$ (shown in Figure 4.4.1.2). The improved quality of the p - i - n allows us to apply higher biases than previously and thus clearly observe the shift of the $e1$ - $hh1$ exciton by almost 10nm. At the unbiased exciton wavelength (≈ 845 nm) the contrast is close to 3dB with 12V applied. As with all the devices operating in the BT mode, the insertion loss is more than 3dB. These are typical figures for quantum wells of this size, with or without the FP effects, which are damped out by the high background absorption at the BT wavelengths.

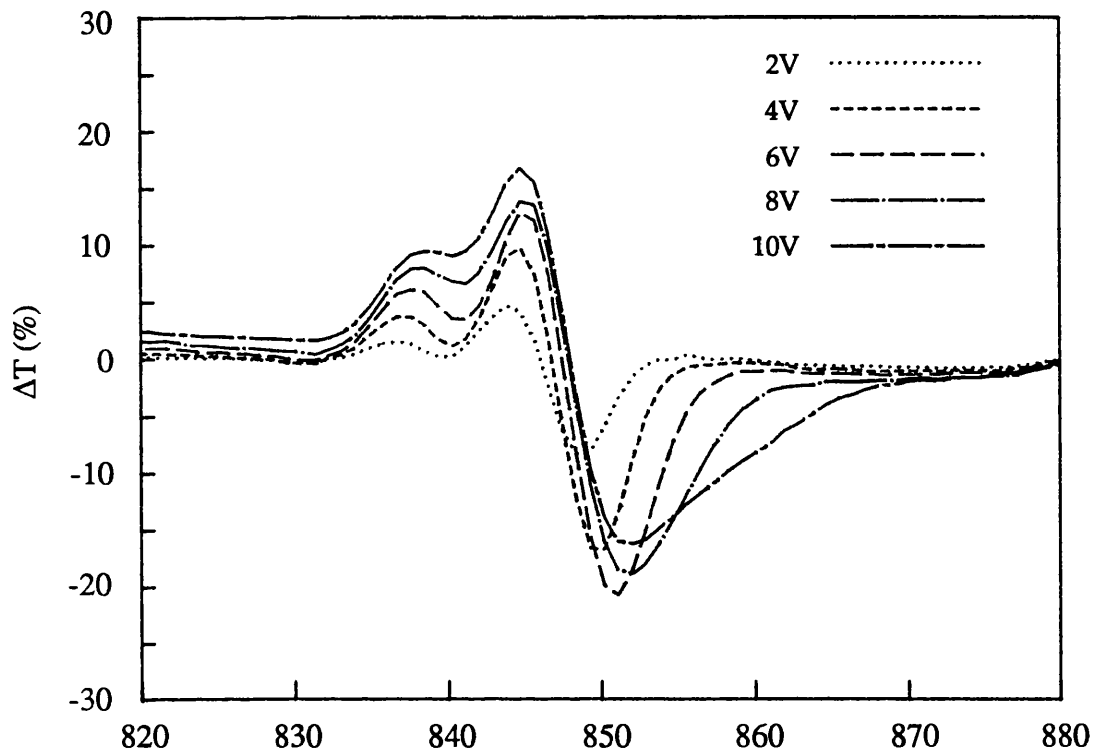


FIGURE 4.4.1.2:
Transmission changes for the uncoated CPM405 modulator.

4.4.2 AR-COATED MODULATOR

With the application of a silicon nitride AR coating the FP structure evident in Fig. 4.4.1.1 is noticeably reduced in the transmission spectra of Fig. 4.4.2.1. From the calculations of § 3.2.4. the remaining oscillations are consistent with a front reflectivity of $\approx 1\%$ (with 30% at the back). The separation between heavy and light hole excitons appears to be less well resolved in this case than in Fig. 4.4.1.1. This may be to some extent caused by the position of the excitons relative to the underlying FP structure, but more likely due to some variation in the sample over the wafer. However the exciton peaks and the absorption edge are much more clearly visible when shifted under bias than before.

It appears that the FP structure is more advantageously sited with respect to the absorption spectrum here – an FP peak coinciding roughly with the foot of the absorption edge, rather than with the peak of the exciton, as was the case in § 4.4.1.

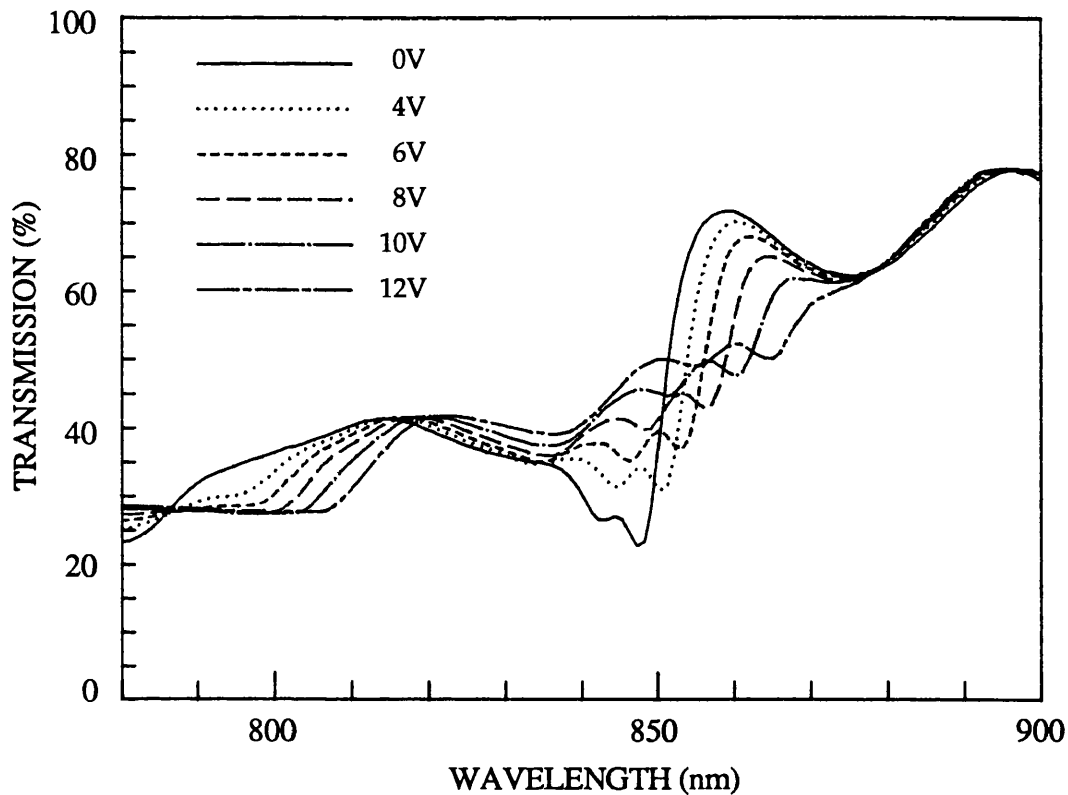


FIGURE 4.4.2.1:

Room-temperature transmission spectra with bias for the AR-coated CPM405 MQW modulator.

Consequently the changes in transmission, plotted in Fig. 4.4.2.2, show an improvement of about 5-7% at both BT and BA wavelengths. The insertion loss at both operating points has also improved, the on state for BT modulation being 0.49 compared with 0.39. The modulation bandwidth is just determined by the linewidth of the band-edge excitons, so that in the BA case it increases as field is applied, although the maximum modulation eventually falls. Between 6V and 10V a change in transmission of -20% is achieved over at least 3-4.5nm.

In contrast terms BT operation offers the largest modulation of ≈ 3.4 dB, but at 12V and with a greater insertion loss than the BA case (Figs. 4.4.2.3-4). In fact at 6V bias, where the best BA contrast occurs, the contrast is roughly the same for both modes, being close to 2dB. The linewidth for 2dB contrast is ≈ 7.5 nm for bias ≥ 10 V in the BA mode. However, in the BT mode it is a maximum of 5nm for only 1.5dB.

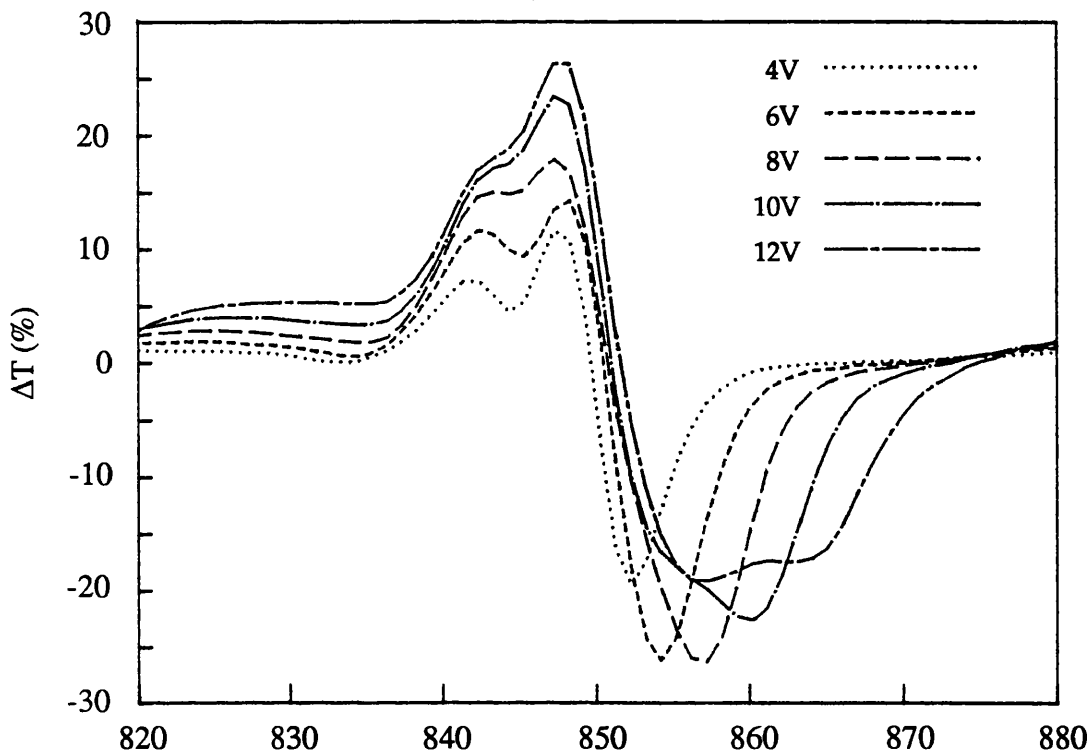


FIGURE 4.4.2.2:
Transmission changes with bias for AR-coated MQW modulator CPM405

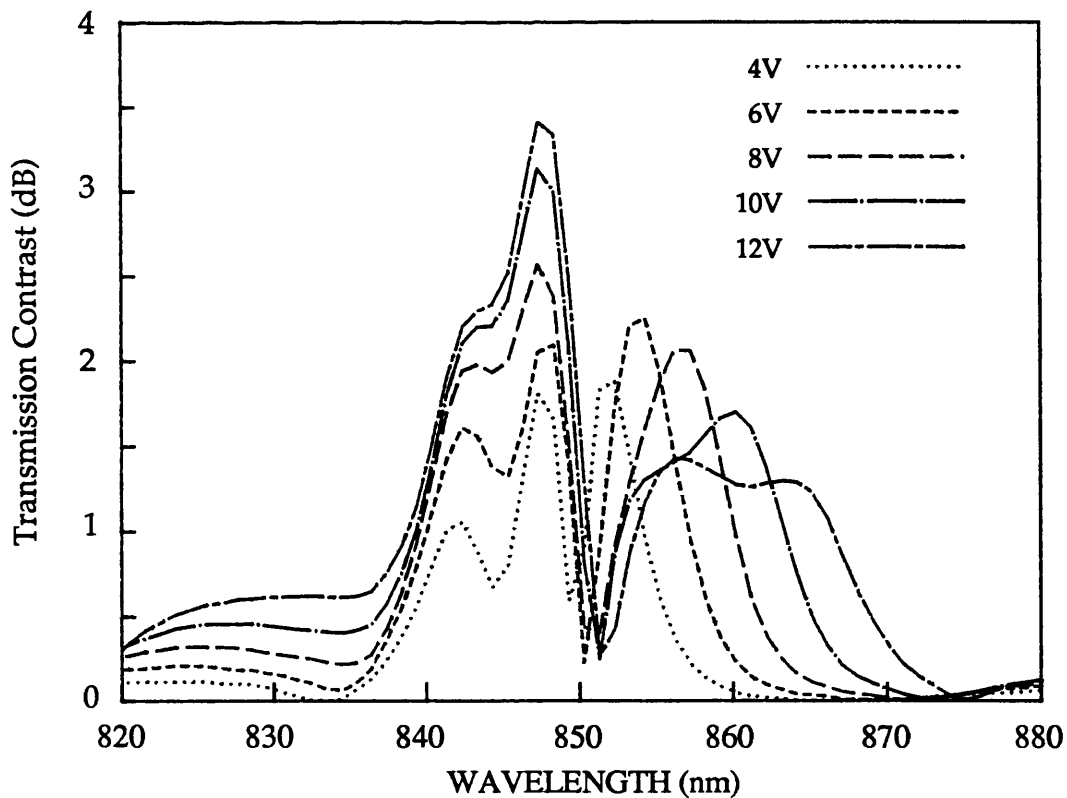


FIGURE 4.4.2.3
Transmission contrast with bias for AR-coated MQW modulator CPM405.

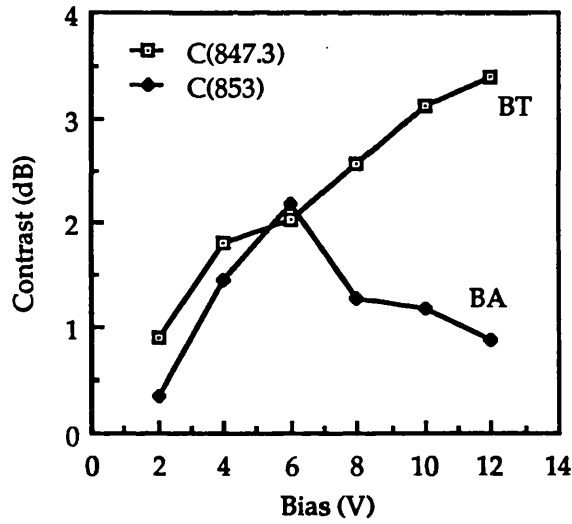
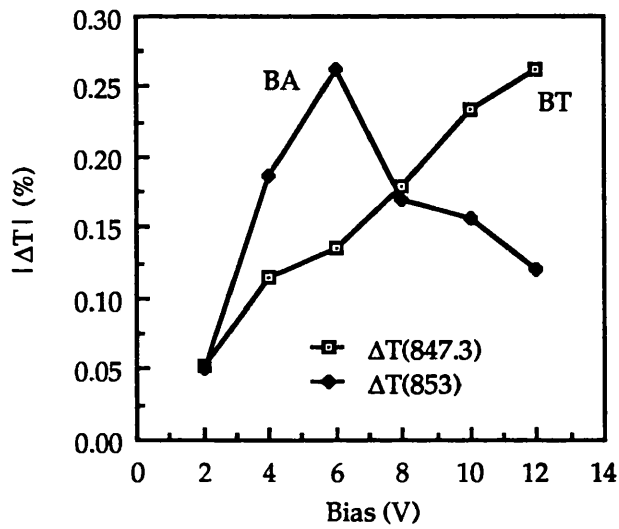


FIGURE 4.4.2.4:
Transmission change and contrast as a function of bias at the optimum bias-absorbing and bias-transmitting wavelengths for the CPM405 AR-coated modulator.

4.5 THE MV245 (145Å WELL) TRANSMISSION MODULATOR

The MQW region of this device was designed to have $45 \times 160\text{\AA}$ quantum wells with 60\AA $\text{Al}_{0.3}\text{Ga}_{0.7}\text{As}$ barriers. The optical evidence from the unbiased transmission spectrum in Fig. 4.5.1 indicates that, as with the CPM405 structure, the as-grown well width is slightly less than specified, the position of the exciton peak being consistent with $\approx 145\text{\AA}$. The real barrier thickness will therefore be less than 60\AA , and is estimated to be $\approx 53\text{\AA}$, based on the apparent well width, the known relative growth rates for GaAs and $\text{Al}_{0.3}\text{Ga}_{0.7}\text{As}$ and the specified growth time of the barriers.

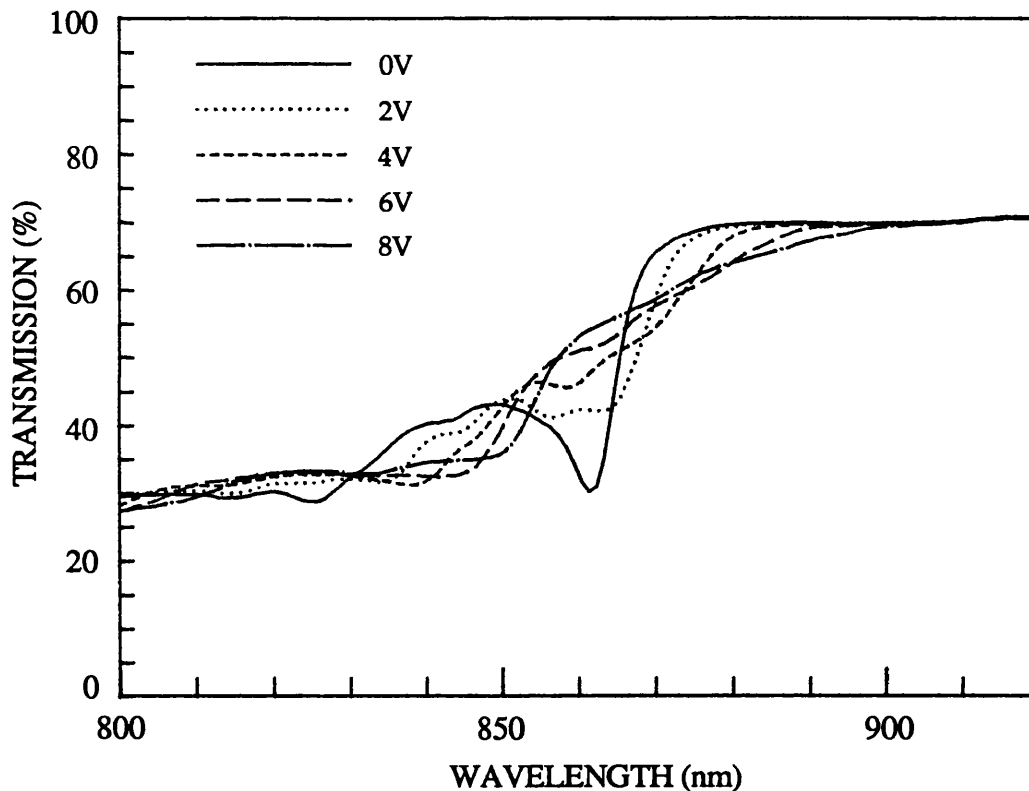


FIGURE 4.5.1:

Room-temperature transmission spectra with bias for the AR-coated MV245 MQW modulator.

The fact that the FP effects are undiscernible means that the AR coating is close to optimum and the net front reflectivity must be $\approx 0.01\%$ or less (see § 3.2.4). The maximum transmission level of $\approx 70\%$ needed no scaling in this instance. Accurate absorption data have been calculated for this structure and are to be found in § 3.3. Note the general decrease in the depth of absorption compared to the 87\AA well structure, i.e. the

minimum transmission at the unbiased exciton ($\approx 860\text{nm}$) is about 10% higher, and this for an MQW containing $\approx 25\%$ more absorptive material. This loss in strength of the exciton is in qualitative agreement with theory – we expect the overlap integral between electron and hole, which determines the oscillator strength for the optical transition, to become smaller as the well width increases and electron and holes are allowed greater spatial separation. A further consequence of the increased well width is the convergence of light and heavy hole states in the valence band. Hence it is not possible here to resolve lh and hh excitons.

The estimate of well width becomes less accurate here because the variation in the wavelength of the exciton peak is reduced at larger well widths – tending asymptotically towards the bulk optical characteristics. The QCSE is very much more field-broadened than in § 4.4, with immediate loss of exciton oscillator strength with bias. Therefore BA modulation is poor (Figure 4.5.2). A maximum transmission change of 12% is observed in this mode, however this is achieved at only 3V.

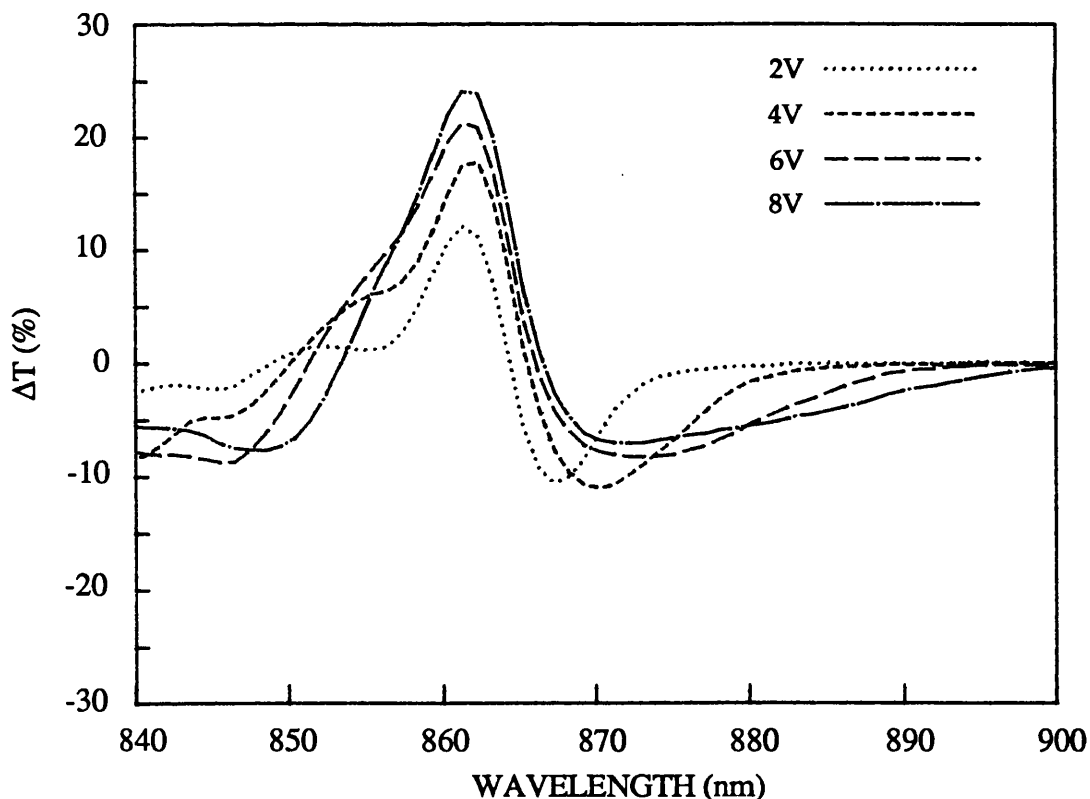


FIGURE 4.5.2:
Transmission changes with bias for the AR-coated MV245 modulator.

In the BT mode the transmission change is close to that for the 87\AA well device, with a lower insertion loss ($<3\text{dB}$), and contrast is a respectable 2.58dB at only 8V (Figures 4.5.3-4). We cannot expect any better than this with increased bias, even though the spectra are not shown here, because of the red shift of the "forbidden" transitions into the operating wavelength. This can be seen as a shoulder in the 8V transmission spectrum at $\approx 850\text{nm}$.

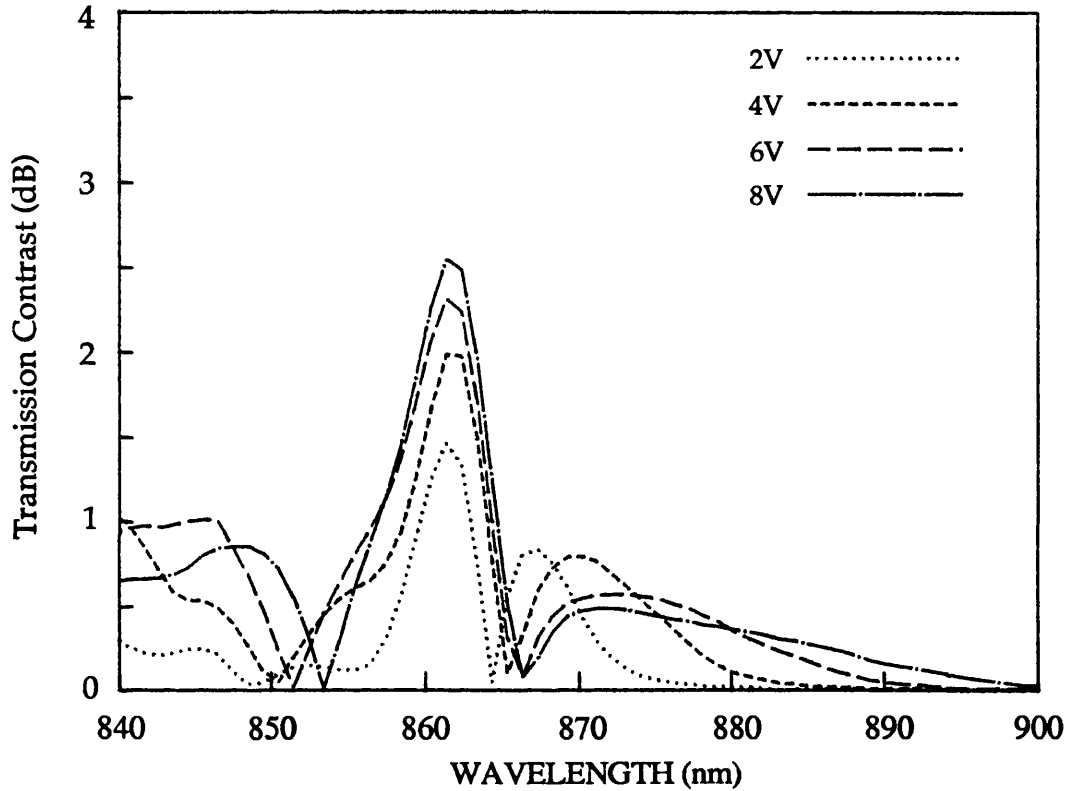


FIGURE 4.5.3:
Transmission contrast with bias for AR-coated MQW modulator MV245.

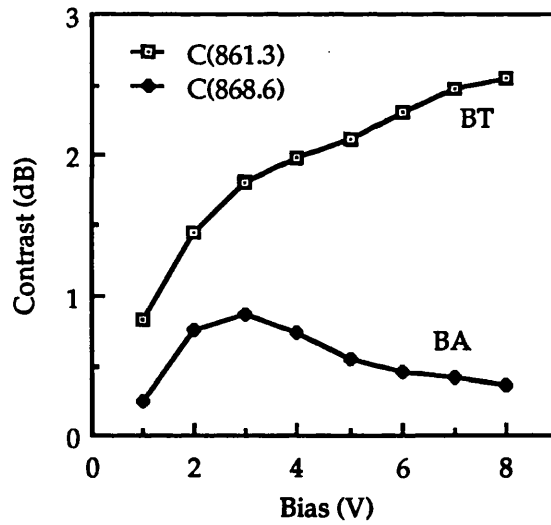
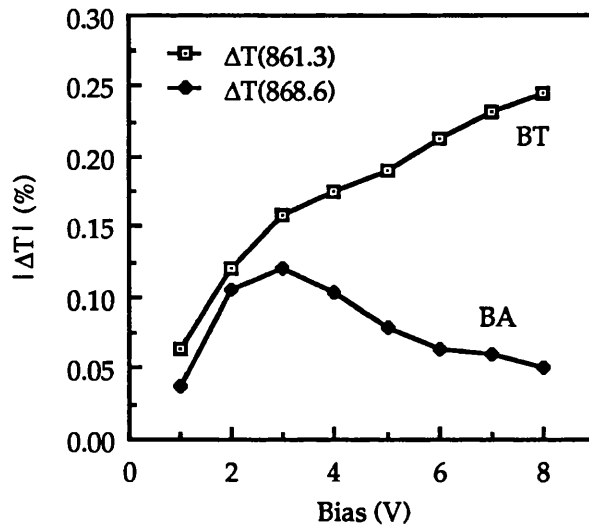


FIGURE 4.5.4: Transmission change and contrast as a function of bias at the optimum bias-absorbing and bias-transmitting wavelengths for the MV245 AR-coated modulator.

4.6 THE MV246 (47Å WELL) TRANSMISSION MODULATOR

In this section we shall again compare two different modulators fabricated from the same MQW structure. However, unlike in § 4.4, both devices are AR-coated. The difference is in the quality of the coating – in one case there are remnant FP effects, in the second these are almost totally removed. This enables us to comment on the effect of a small amount of resonance on the modulation. The modulator in question contained 75 quantum wells with a nominal width of 60Å, separated by 60Å barriers. From optical measurements we deduce that the real well width is $47 \pm 3\text{Å}$, and from relative growth rates and times the barrier width is estimated to be closer to 53Å. It should be pointed out that at this reduced well width, the wavelength of the e1-hh1 exciton (which we use to identify the well width) can vary more significantly with small fluctuations in the well width. We therefore expect some noticeable variation in the exciton peak wavelength for devices from different parts of the same sample, as is the case for the two modulators tested here.

4.6.1 DEVICE WITH IMPERFECT AR COATING

Looking at Figure 4.6.1.1 where we have plotted transmission spectra for a range of bias voltages, one difference between this narrow well device and the previous modulators is in the amount of bias required to induce significant transmission changes. Very little happens until more than ≈ 10 volts are applied, equivalent to a field of $\approx 1.3 \times 10^5 \text{ V.cm}^{-3}$, which agrees qualitatively with theory. It is apparent that a large increase in the absorption *coefficient* has occurred by reducing the well thickness down to 47Å. Even with only $\approx 0.32 \mu\text{m}$ total well thickness, the transmission at the exciton absorption peak still drops to $\approx 20\%$ – the same as for the CPM405 device (with $0.52\mu\text{m}$) and lower than for the MV245 device (with $0.65\mu\text{m}$).

It appears from Fig. 4.6.1.1 that the excitonic oscillator strength is retained at higher fields for this structure, so that in Fig. 4.6.1.2 the transmission change spectra are dominated by the bias-absorbing modulation. This device shows the largest transmission change of any of the devices studied – almost 34% at 825nm and 16V, and the lowest insertion loss, but the effect may be enhanced by a fortuitous positioning of the remaining FP oscillations.

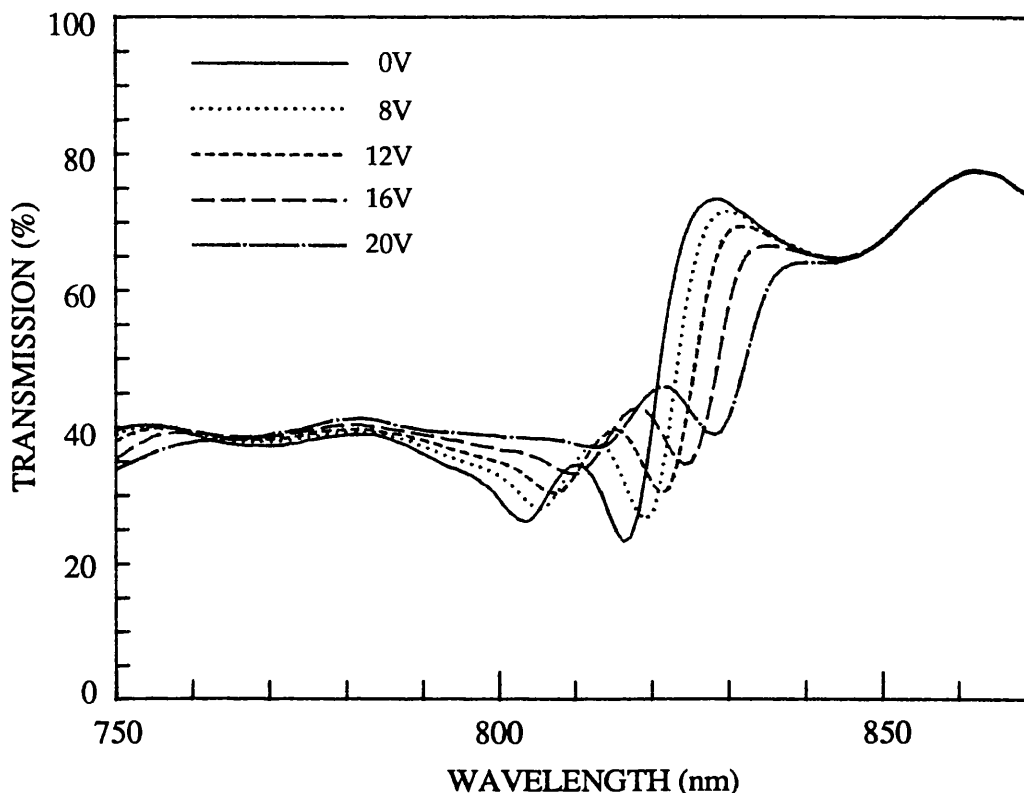


FIGURE 4.6.1.1:
Room-temperature transmission spectra with bias for the AR-coated MV246 MQW modulator (with remnant FP effects).

Just as for the AR-coated CPM405 device, the FP effects here are roughly consistent with a residual front reflectivity of $\approx 1\%$ (30% at the back). The minimum transmission at 16V seems to occur at almost the same wavelength as an FP maximum in the zero bias spectrum, giving rise to such a large modulation. Indeed this is the only modulator to achieve close to 3dB contrast in the BA mode (Fig. 4.6.1.3). In Fig. 4.6.1.4 we note that the contrast in BA mode at low biases remains well above that for the BT mode and is $\approx 2\text{dB}$ at 9V, which is not much less than observed in the wider well devices. The modulation in this case seems due not to field-induced loss of exciton strength, but to the large separation of the heavy and light hole excitons – the heavy hole shifts but the light hole does not follow immediately behind it, giving a noticeable increase in transmission.

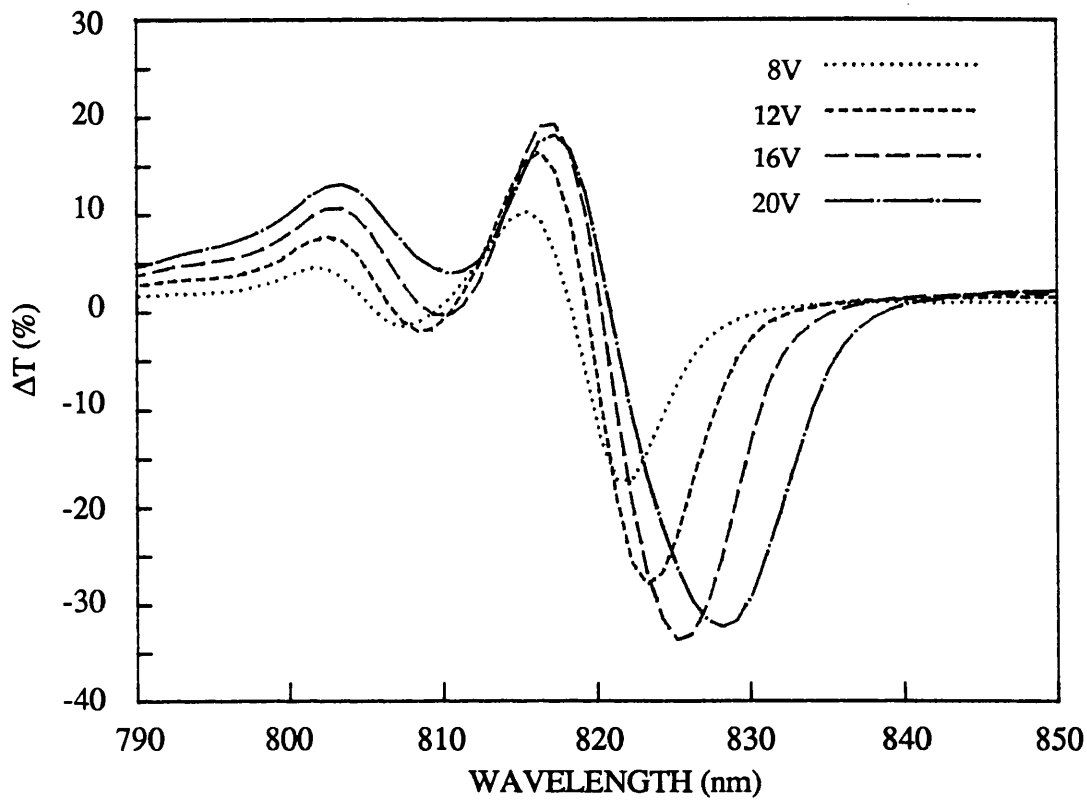


FIGURE 4.6.1.2:
Transmission changes for AR-coated MQW modulator MV246 (with remnant FP effects).

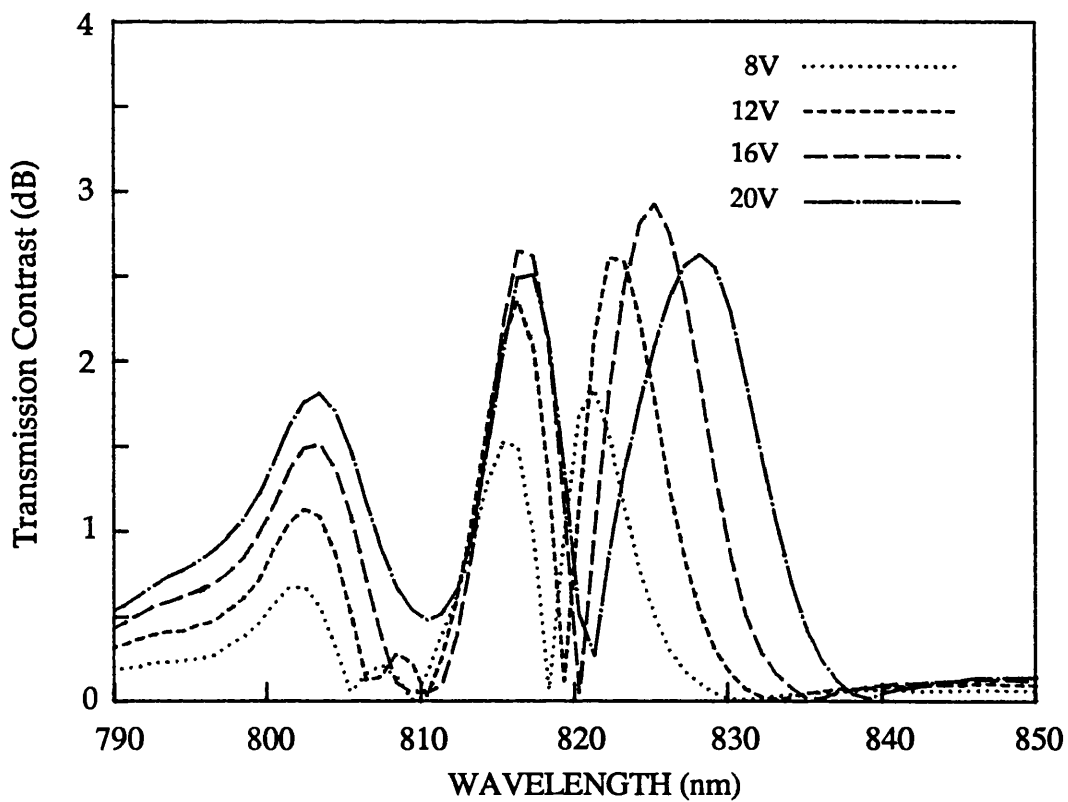


FIGURE 4.6.1.3:
Transmission contrast for AR-coated MQW modulator MV246 (with remnant FP effects).

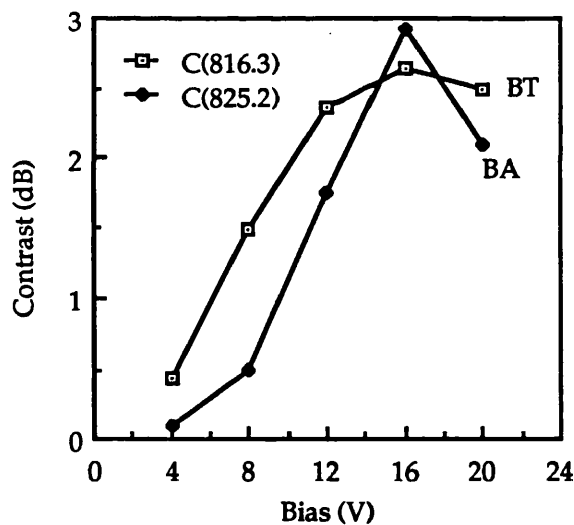
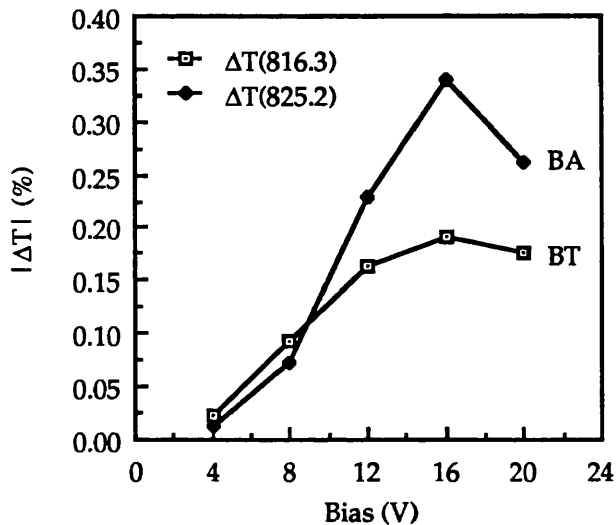


FIGURE 4.6.1.4:

Transmission change and contrast as a function of bias at the optimum bias-absorbing and bias-transmitting wavelengths for the MV246 AR-coated modulator (with remnant FP effects).

4.6.2 DEVICE WITH FP EFFECTS REMOVED

In Fig. 4.6.2.1 we see the transmission spectra for the MV246 modulator almost undistorted by FP oscillations. There is still a small amount of curvature in the part of the spectrum where there is effectively zero

absorption. This is consistent with a front reflectivity of only 0.1% or less.

Comparing with Fig. 4.6.1.1 the main thing to notice is the apparent loss of resolution of the effect of absorption peaks in the shifted spectra. We conclude that the clear appearance of the excitons in the previous spectra is enhanced by the remaining FP oscillations. If the two sets of spectra are overlaid and the zero-bias absorption edges aligned we find that the Stark shifts at 12V and 16V are identical, and the transmission level due to the continuum absorption and at the exciton peak is roughly the same in both cases, so there is no problem due to variation in the sample quality across the wafer. The biggest difference occurs in the on state level at the wavelength of maximum transmission change (825-830nm). By removing the FP effects the on state transmission is reduced from $\approx 70\%$ to $\approx 61\%$, and consequently the maximum BA transmission change falls from $\approx 34\%$ to 24% (compare Fig. 4.6.2.2 with Fig. 4.6.1.2).

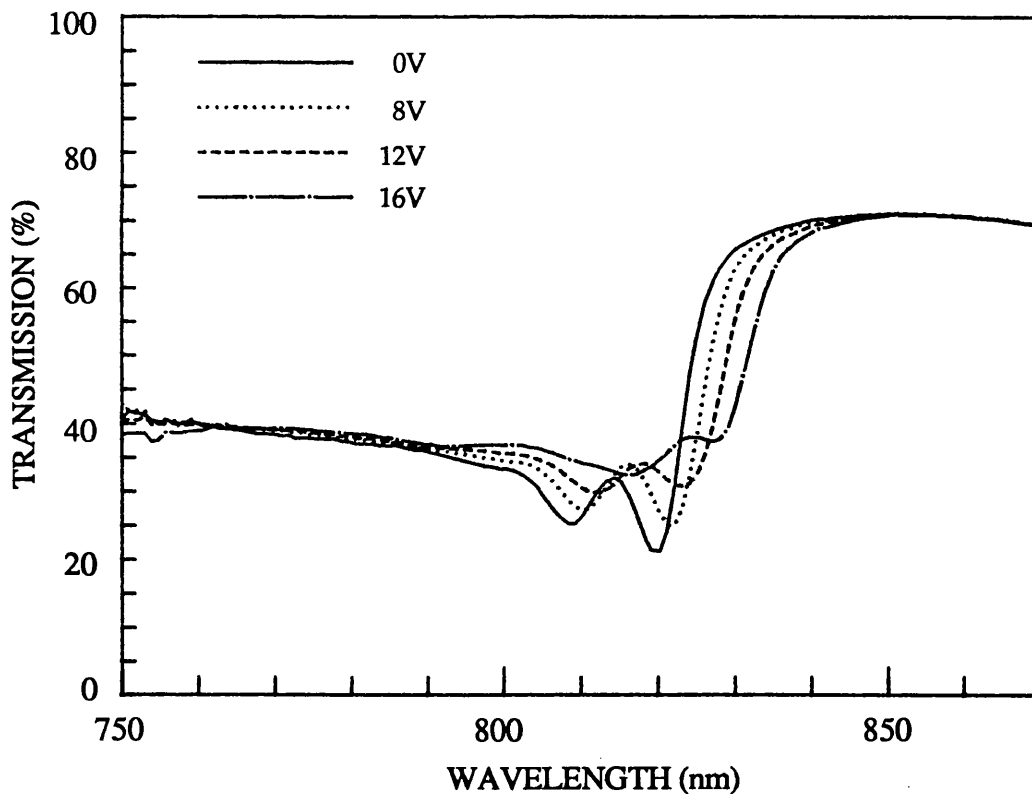


FIGURE 4.6.2.1:
Room-temperature transmission spectra with bias for the AR-coated MV246 MQW modulator (without FP effects).

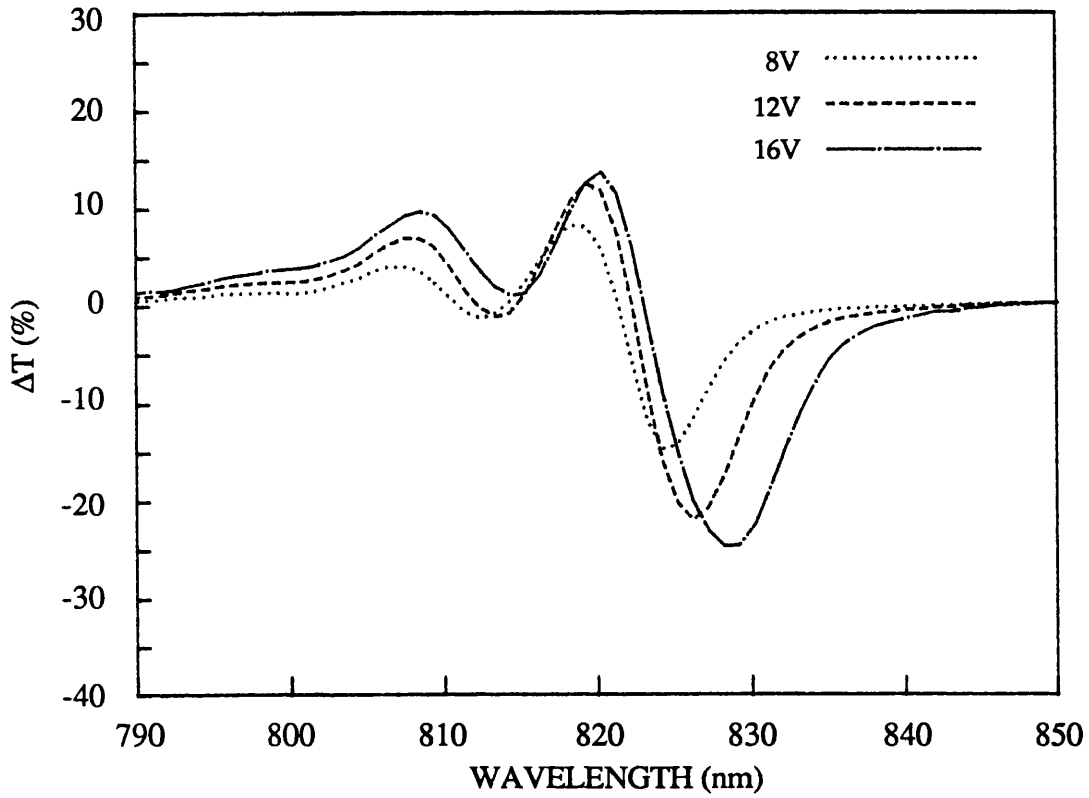


FIGURE 4.6.2.2:
Transmission changes with bias for AR-coated MQW modulator MV246 (No FP effects).

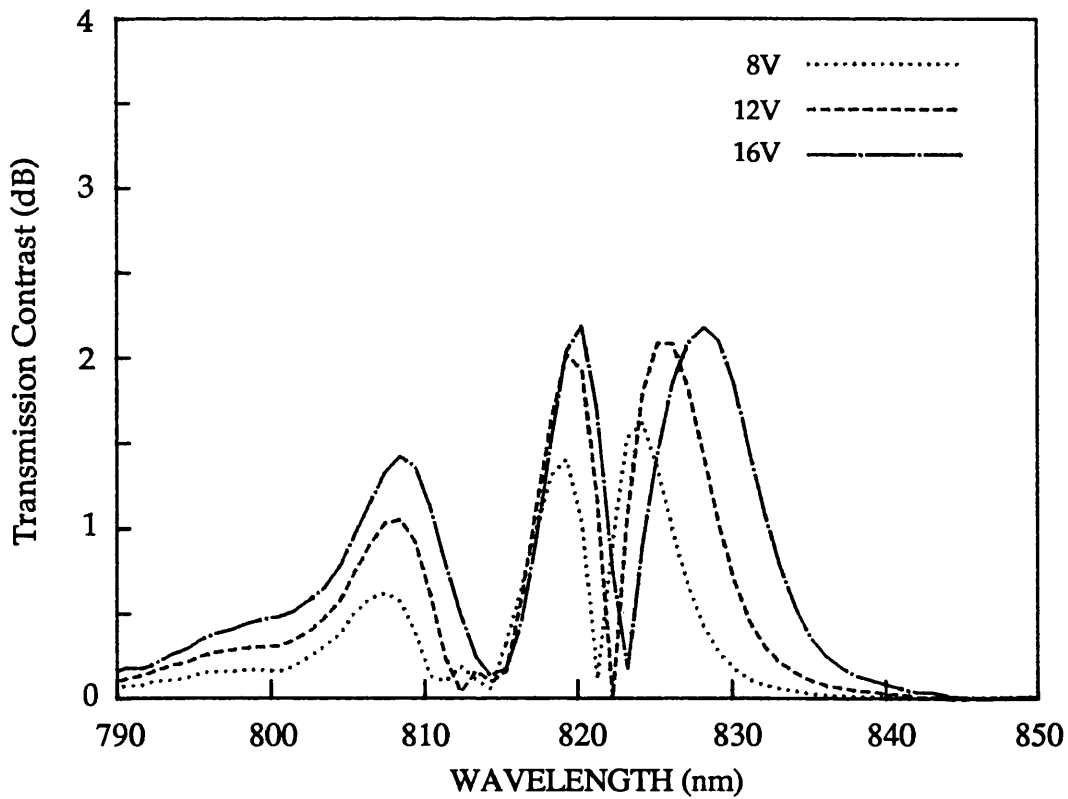


FIGURE 4.6.2.3:
Transmission contrast with bias for AR-coated MQW modulator MV246 (No FP effects).

As a result of the reduction in BA transmission change the contrast is also smaller than before (Figs. 4.6.2.3-4), with a maximum value of ≈ 2.2 dB, which is similar to that of the AR-coated CPM405 modulator, except that the bias voltage required is more than twice as high.

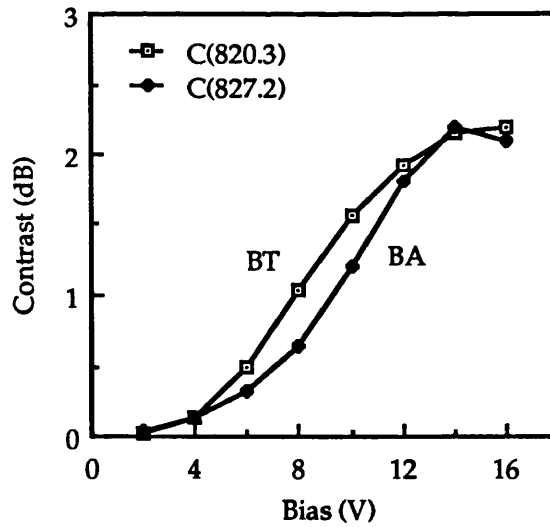
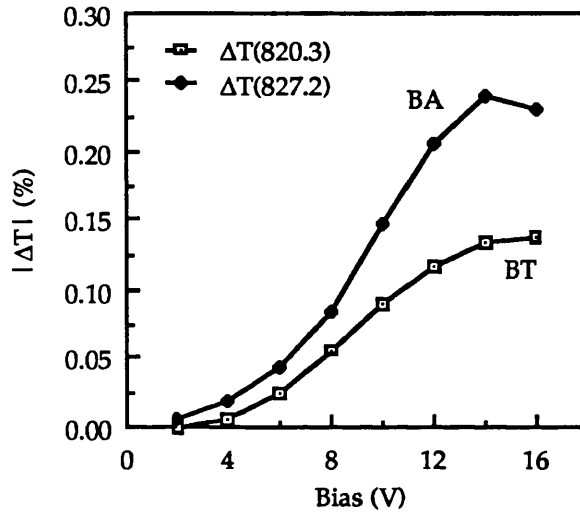


FIGURE 4.6.2.4: Transmission change and contrast as a function of bias at the optimum bias-absorbing and bias-transmitting wavelengths for the MV246 AR-coated modulator (without FP effects).

4.7 THE CPM405 (87Å WELL) REFLECTION MODULATOR

In an attempt to improve the modulation attainable with the basic MQW *p-i-n* structure a highly-reflective gold coating was deposited on the back surface of a CPM405 device originally fabricated to operate in transmission. If one assumes that the gold acts as a perfect reflecting surface, then the contrast ratio for this type of device, which is effectively like a double-pass transmission modulator, will be the square of that for the single pass device since the optical path length is doubled in the simplest approximation. A device of this type was used as a combined modulator and photodetector in a fibre-optic transmission system by Wood et al [12].

A GaAs-AlGaAs MQW modulator operating in reflection with an integral quarter-wave stack reflector was demonstrated by Boyd et al. in 1987 [13]. Contrast of 8:1 was achieved but at the expense of a relatively high insertion loss (R_{on} was only $\approx 25\%$), the device operating best at the unbiased exciton peak wavelength. The metal coating used here to realize a reflection device was the simplest alternative available at the time, having ourselves not yet investigated the growth of semiconductor multilayer stacks.

Figure 4.7.1 shows the result of this first rough attempt at making a reflection modulator. Unfortunately, the effects of FP resonance were not considered, and the possibility of applying an AR coating to the front surface of the modulator was not available in this instance. We used the experimental apparatus of Figure 4.2.2.1 with the detector suitably positioned to record spectra of reflected intensity at various bias voltages. The absolute reflection was calibrated by normalizing the reflected intensity spectra from the MQW device to that from a freshly-deposited gold film. It is immediately obvious from the reflection spectra that strong interference effects are occurring which not even the absorption in the MQWs can damp out. The effect of the $e1-hh1$ absorption peak can be seen as a reflection minimum at about 846nm. The strongest modulation occurs between 850-860nm, with an apparent maximum reflection change of only $\approx 15\%$ and a contrast ratio of $\approx 2:1$. The fact that these figures are not better than those for the single-pass transmission device can be ascribed to the depth of the FP resonance which coincides exactly with the wavelength band in which the largest absorption changes occur, and reduces the on-state reflection to only $\approx 25\%$. We would normally expect

the metallic coating at the back of the device to provide a reflectivity of at least 90% in this part of the optical spectrum. This, coupled with a front reflectivity of $\approx 30\%$, should produce much shallower interference fringes, where absorption is low, than observed here.

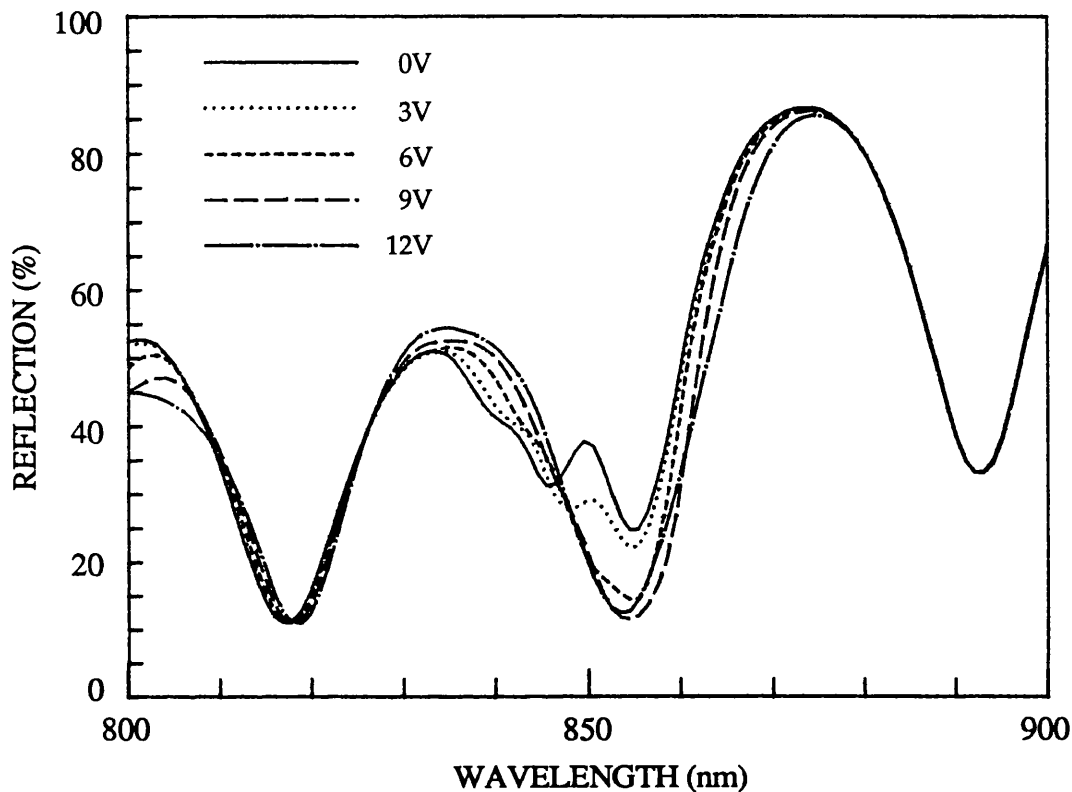


FIGURE 4.7.1:

Room-temperature reflection spectra for MQW modulator CPM405 with gold coating on back surface.

For example, with $R_f = 0.30$, $R_b = 0.90$, we can calculate a reflection maximum and minimum of ≈ 0.97 and ≈ 0.70 respectively, where $\alpha = 0$ (see Eq. A19). This is obviously not the case experimentally. One reason for this may be that the gold layer, which was estimated to be $\approx 160\text{\AA}$, is not thick enough to make the back reflectivity as high as 90%.

Further calculation indicates that the observed reflection values in the low absorption region of the spectrum are consistent with $R_f = 0.30$, $R_b = 0.73$. From the transmission spectra in Fig. 4.4.2.1 we can deduce that the αd factor for this material is ≈ 0.56 at $\approx 817\text{nm}$, the wavelength at which an FP resonance occurs in Fig. 4.7.1. In theory, with this amount of absorption, we should observe less than 1% reflection at resonance (see Eq. A17). In subsequent measurements on reflection modulators it was

discovered that there was a significant amount of background scattered light (see § 6.6.2) and this is certainly the most likely reason for the 10% minimum reflection observed for this device. Had the background light been removed then the real contrast for this device would probably have been at least 15:1 (11.8dB), but with an insertion loss of more than 8dB, much larger than that of the CPM405 transmission modulator for example.

We shall consider MQW reflection modulators further in the next two chapters.

4.8 LIMITS TO MODULATION AT NORMAL INCIDENCE IN MQWS

Recently Stevens and Parry [14] have theoretically assessed the ultimate performance of normal-incidence GaAs-AlGaAs MQW modulators. The model which they used has previously been used successfully to predict Stark shifts and absorption changes in MQW structures, as deduced from some of the room-temperature photocurrent measurements reported in Chapter 2 [15]. Extending this basic work, the modulation achievable in single- or double-pass MQW devices, with line-broadening effects such as well width fluctuations and background doping, was optimized. The devices under consideration were confined to the BA mode of operation, i.e. the operating point is at a longer wavelength than that of the unbiased $e1-hh1$ absorption peak. It was found that for a given operating voltage there exists a maximum transmission/reflection change (or contrast) defined by an optimum number of quantum wells. This is illustrated in Figure 4.8.1.

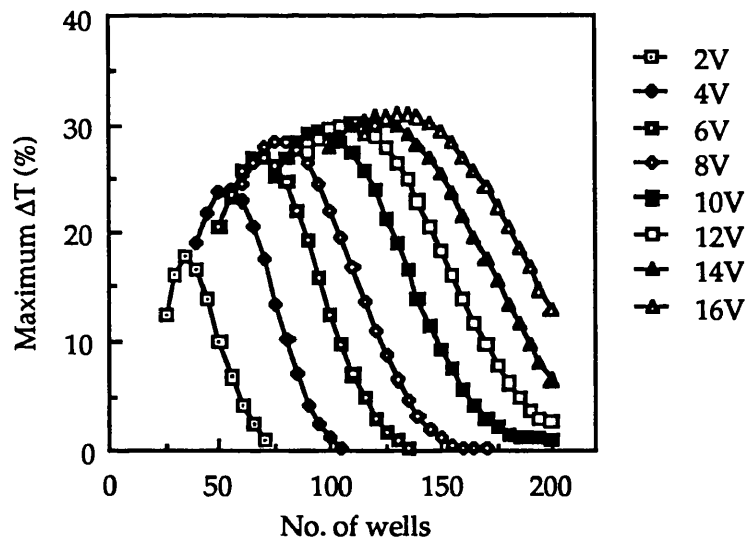


FIGURE 4.8.1:

Calculated maximum transmission change as a function of the absorber thickness and bias voltage for an MQW transmission modulator with one surface perfectly AR-coated. (Adapted from Stevens and Parry, Ref. 14).

With a lower number of wells than optimum the modulation is reduced by the decrease in the amount of absorbing material (although the change

in absorption coefficient can remain high), while a higher than optimum number begins to reduce the electric field and thus the Stark shift of the absorption edge to the extent that the absorption change is reduced. The edge-broadening effect of background doping is also increased.

This calculation is for a device with $2 \times 10^{15} \text{cm}^{-3}$ background doping in the MQW region, r.m.s. well width fluctuations of the order of 1 monolayer ($\approx 2.8 \text{\AA}$) and the front surface perfectly AR coated.

In the case of 100\AA wells with 60\AA AlGaAs barriers, which is the nearest comparison with our CPM405 (87\AA well) device, the maximum calculated transmission change for 60 wells is around the 26% mark, at 5V bias. This is shown in Figure 4.8.2, where we have plotted the "envelope" of maximum transmission change, optimized for a given bias voltage. It is worth noting that, although the optimum number of wells increases almost linearly with bias voltage, there is little to be gained in modulation by using more than ≈ 70 wells and 6V bias. The transmission change limits because of background doping broadening of the excitonic absorption edge.

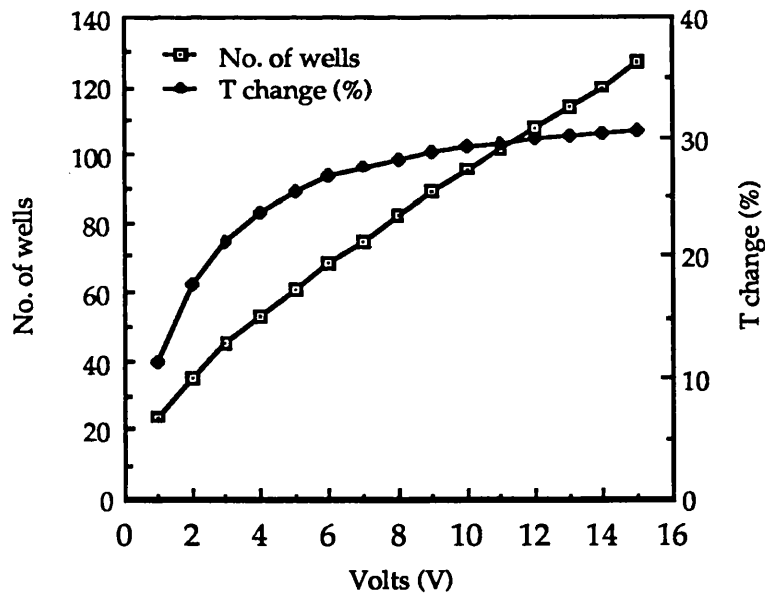


FIGURE 4.8.2:

Optimum number of quantum wells and maximum transmission change as a function of bias voltage for an MQW transmission modulator with one side AR-coated. Well width is 100\AA and barrier width 60\AA , with 0.3 Al mole fraction (adapted from Stevens and Parry, Ref. 14).

In practice we have observed a maximum ΔT of 26.3% with a bias of 6V,

which is in excellent agreement with the data above. The small discrepancy in bias voltage could be due to the difference in well width between the experiment and the model. For our smaller experimental well width we would expect to need a slightly higher field to obtain the optimum Stark shift, hence the higher bias, and also achieve a slightly higher maximum absorption change because of the higher peak excitonic absorption with narrower wells, hence the larger transmission change.

We must also consider the possibility that the good agreement may be due to an enhancement of the underlying modulation by the residual FP oscillations. Since we have no spectra for the CPM405 modulator which are unaffected by resonance we cannot directly check this. However, when we consider the MV246 device, with $\approx 47\text{\AA}$ wells, we find there is a marked difference in the maximum ΔT achieved with or without FP effects, even though the magnitude of the oscillations is consistent with only $\approx 1\%$ reflectivity remaining at the front surface. With FP effects left in we get 33.9% maximum ΔT , when they are removed this is reduced to 24.0%, in both cases at 16V (see Table 4.1, Figs. 4.6.1.2, 4.6.2.2). Stevens and Parry calculate that, with an optimum bias of 15V for $75 \times 50\text{\AA}$ quantum wells, we should expect a maximum transmission change of 24.5–25.6% [14], which is in better agreement with the data for the modulator which has the FP effects removed.

A complementary experimental study of the effect of well width on electro-absorption in GaAs-AlGaAs MQWs has recently been carried out by Jelley et al [16, 17]. They investigated 5 well widths in the range 50–260 \AA , and in all devices held the total GaAs (quantum well) thickness constant at 0.5 μm , with all wells separated by 100 \AA $\text{Al}_{0.32}\text{Ga}_{0.68}\text{As}$ barriers. The emphasis in their work was on the optimization of well width for maximum *absorption change*, which as we have outlined is not the only factor determining the modulation achievable, however it is useful to compare our experimental absorption changes with theirs.

In Fig. 4.8.3 we have plotted the data of Jelley et al. for maximum absorption change as a function of applied field. The well widths of 105 \AA and 50 \AA are closest to our CPM405 and MV246 devices respectively, for which we have also plotted the estimated maximum absorption change taken from Table 4.1 (see § 4.9). The agreement for the wider well is quite reasonable, our device requiring a slightly higher field to achieve maximum $\Delta\alpha$, which can simply be explained by the well width difference (our 87 \AA compared with their 105 \AA).

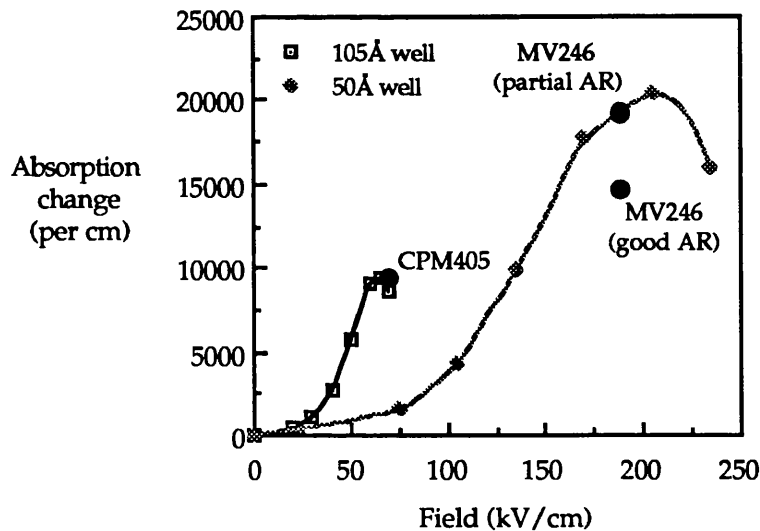


FIGURE 4.8.3: Maximum absorption change as a function of applied electric field for two different well widths (after Jelley et al., Reference 16) with experimental data from this chapter superimposed for comparison.

For the narrow well $\Delta\alpha_{\max}$ is much lower for our modulator with the best AR coating (§ 4.6.2). However, if we consider the device with remnant FP effects (§ 4.6.1) the agreement is much better. The problem is that in this case the assumption made in calculating the absorption change is less accurate, so the agreement is likely to be coincidental. It may be that the disagreement is simply due to inaccuracy in assigning the well width. If the well widths are in actual fact significantly different, e.g. 55Å & 43Å, rather than 50Å & 47Å, this could strongly affect the electro-absorption, since the exciton peak height and QCSE change more rapidly with well width when the wells are narrow.

Figure 4.8.4 shows more data taken from reference [16], which gives some indication of the optimum choice of well width for an MQW modulator. The interesting point is that there is a fairly broad maximum in the curve of $\Delta\alpha_{\max}$ per unit electric field, which suggests that an optimum well width may be $\approx 120\text{\AA}$. The question remains whether the decrease in $\Delta\alpha_{\max}$ due to using a slightly wider well width is more than offset by being able to use a larger number of wells for a given bias (since the field for $\Delta\alpha_{\max}$ is lower).

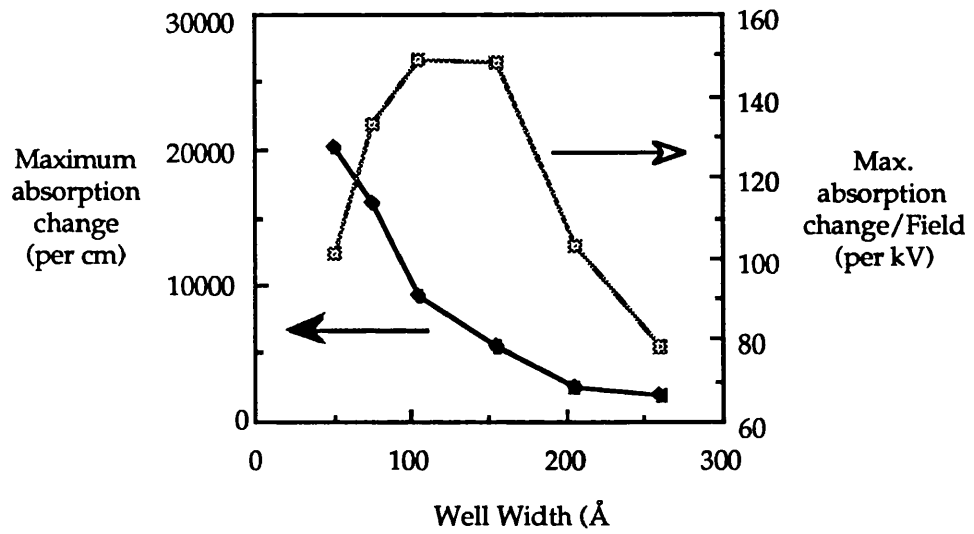


FIGURE 4.8.4:
Well width dependence of the maximum absorption change for GaAs quantum wells separated by $\text{Al}_{0.32}\text{Ga}_{0.68}\text{As}$ barriers (after Jelley et al., Reference 16).

4.9 SUMMARY

4.9.1 COMPARISON OF MQW MODULATION WITH BULK GaAs

The performance of the devices studied in §§ 4.3-4.6 is summarized below in Table 4.1. Maximum absorption changes are based on the measured maximum contrast and Eq. (4.2). Operating wavelengths are dependent on the well width used and cover the range ≈ 820 - 870 nm, the particulars for each device being given in the relevant section of this chapter.

TABLE 4.1:

Summary of the characteristics of the MQW transmission modulators reported in §4.3-4.6.

Device Name	Absorber Thickness (μm)		Maximum Contrast (dB)	Maximum Transmission Change (%)	Insertion Loss (dB)	Operating Voltage (V)	Maximum Change in Absorption Coefficient (cm^{-1})
CPM7	0.550 (55x100A)	BT	1.76	+14.5	3.76	6	$\approx -7,370$
		BA	0.90	-12.5	1.80	6	$\approx +3,770$
CPM405* ($R_f \approx 1\%$)	0.522 (60x87A)	BT	3.38	+26.3	3.19	12	$\approx -15,220$
		BA	2.21	-26.3	1.80	6	$\approx +9,750$
MV245 (Good AR)	0.652 (45x145Å)	BT	2.58	+24.2	2.65	8	$\approx -9,110$
		BA	0.87	-12.0	1.77	3	$\approx +3,070$
MV246* ($R_f \approx 1\%$)	0.353 (75x47A)	BT	2.62	+19.0	3.75	16	$\approx -17,090$
		BA	2.91	-33.9	1.61	16	$\approx +18,980$
MV246 (Good AR)	0.353 (75x47A)	BT	2.19	+13.7	4.60	16	$\approx -14,280$
		BA	2.19	-24.0	2.00	14-16	$\approx +14,280$

* signifies devices for which there were still noticeable Fabry-Pérot effects in the transmission spectra, even after AR coating

BT = Bias transmitting, i.e. transmission increasing with bias

BA = Bias absorbing, i.e. transmission decreasing with bias

We have clearly demonstrated the improvement in modulation to be gained from using MQW GaAs-AlGaAs rather than bulk GaAs in normal-incidence electro-absorptive optical modulators. The MQW devices all outperform their bulk counterpart, regardless of the width of the quantum wells used, in contrast and transmission change. In Table 4.2 we show some projected optimum performance figures for GaAs transmission modulators based on recent measurements on high purity

GaAs *p-i-n* diodes by Wight et al. [10].

TABLE 4.2:
Performance of bulk GaAs normal-incidence modulators

	GaAs thickness (μm)	$\alpha(0)$ (per cm)	$\alpha(V)$ (per cm)	T_{on} (%)	T_{off} (%)	ΔT (%)	Contrast (dB)	Insertion Loss (dB)	Bias (V)
BA	1.0	940	2500	64	55	-9	0.64	1.94	≈ 8.5
	2.0	940	2500	58	42	-16	1.35	2.37	≈ 17
BT	1.0	9400	4600	44	27	+17	2.12	3.56	≈ 20
	1.5	9400	4600	35	17	+18	3.13	4.60	≈ 30

BA = bias absorbing,
Operating wavelength $\approx 877\text{-}880\text{nm}$ ($F=85$ kV/cm)

BT = bias transmitting,
Operating wavelength $\approx 868\text{-}870\text{nm}$ ($F=200$ kV/cm)

The modulation figures are calculated for a device with a perfect front anti-reflection coating. Electro-absorption data have been taken from Wight et al., Ref. 10.

Referring back to Table 4.1 we find that the MQW devices generally achieve higher maximum contrast ratios and maximum transmission changes than a bulk modulator. Furthermore smaller bias voltages are needed. Modulation achievable with MQWs is as high as 0.37dB per volt and typically 0.2-0.3 dB per volt, with transmission changes of up to 4.4% per volt, whereas with bulk GaAs we can only expect a maximum of 0.11dB per volt and 1.1% per volt respectively.

The most recent available modulation data for a high quality, epitaxially-grown bulk GaAs modulator working at normal incidence further underlines the superiority of MQWs. Leeson et al [16] have observed a maximum transmission change of 20% with 20V bias in the BA mode. They also suggest that the performance of their device was enhanced by Fabry-Perot effects.

MQW modulators exhibit lower insertion losses, whether working in the BA or BT mode. In the first case this is due to the sharpness of the excitonic absorption edge (particularly in the case of narrow quantum wells), and in the second case due to the ability to Stark shift the exciton strongly from its zero-bias wavelength, with the quantum confinement helping to maintain the oscillator strength up to high fields.

4.9.2 OPTIMUM WELL AND BARRIER WIDTHS

The choice of well width for an ideal modulator depends very much on what is required of the device. It is not possible to say that a particular well width is the absolute optimum because no single structure offers the best performance in terms of contrast, transmission change, insertion loss and operating voltage simultaneously (see Table 4.1). In fact, because the total thickness (wells + barriers) of the MQW structures used here was kept to less than $1\mu\text{m}$, there is not a huge variation in performance of the three different devices. We note that there are qualitative changes in the appearance of the excitonic structure with increasing bias, but because the expected *reduction* in the achievable change in absorption coefficient with increasing well width is roughly offset by the *increase* in the ratio of well:barrier thickness, the important factor for transmission, $e^{-\alpha d}$, changes less dramatically.

Barrier thickness is an important consideration. As far as modulation is concerned the barriers are excess material, and only serve to increase the total thickness of the MQW structure and hence the bias required for a given Stark shift. However, in minimizing the thickness of the barriers one must also consider the limit at which significant electronic coupling starts to occur between adjacent wells. This is an undesirable effect which will simply degrade the QCSE. Thus we are faced with a lower limit to the barrier thickness which we estimate to be in the region of 40\AA^1 , and which would tend to discourage the use of well thicknesses of less than $\approx 80\text{\AA}$, firstly to keep the well:barrier thickness ratio high, and secondly because the probability of coupling increases as well width is reduced.

We can make one or two points about limits to the choice of well width. If low voltage operation is required, e.g. 10V or less, then firstly the total MQW thickness must be kept to about $1\text{-}1.5\mu\text{m}$ so that the fields being applied are in the $70\text{-}100\text{kV}\cdot\text{cm}^{-1}$ range, and secondly the well width must be in the range $\approx 80\text{-}150\text{\AA}$, depending on whether the device is operated as BA or BT. The only justification for using narrow wells is to obtain the maximum BA transmission *change*. The drawback is the 16-20V

¹ Very recently we have observed well resolved excitons in an MQW structure consisting of 95\AA quantum wells separated by 40\AA barriers. With bias, significant absorption changes occur far from the absorption edge, unlike the MV368 sample of Ch.3 where the barriers are $\approx 35\text{\AA}$. It therefore appears that we have found roughly the minimum barrier width to avoid strong inter-well coupling – at least for wells of $\approx 100\text{\AA}$.

required to achieve this. Narrower wells would further exacerbate the problem and may result in poorer modulation because of the reduction in well:barrier ratio.

To emphasise further the point that there is not a great deal to be gained by changing the well width from the usual 90-100Å, in a very recent theoretical optimization of modulation, Cho and Prucnal [18] concluded that the bias-absorbing contrast ratio for a single-pass transmission modulator could in principle be improved by only $\approx 20\%$ using a 1 μm thick 75Å/78Å GaAs/Al_{0.45}Ga_{0.55}As MQW structure, rather than a more conventional 95Å/98Å GaAs/Al_{0.30}Ga_{0.70}As structure. This, however, requires a two-fold increase in the required electric field/bias voltage, in line with what we find on reducing the well width from $\approx 87\text{Å}$ to $\approx 47\text{Å}$.

4.9.3 GENERAL COMMENTS

Comparison with modelling by other authors [14, 18] shows good agreement between predicted and measured device performance, with the appropriate scaling. Even though the devices tested here may have fewer wells than prescribed for maximum modulation, their performance is not significantly less than optimum, as we have shown in transmission change. Furthermore, if the operating voltage is limited, then the 87Å well device does indeed achieve the ultimate performance for MQW transmission modulators.

Although a comprehensive investigation of a wide range of well widths has not been carried out here, the recent work of Jelley et al. [16], which defines the maximum absorption changes per unit applied field, leads us to conclude that the devices investigated here roughly represent the practical upper and lower well width limits ($\approx 150\text{Å}$ and 50Å) for MQW modulators, within our specified voltage constraints.

It appears that FP effects may have noticeably enhanced the maximum transmission change for one of the devices with a non-ideal AR coating, namely the MV246 structure. We can compare the performance of MV246 with and without the FP effects, and see the reduction in modulation as resonance is removed. Of course it is also possible for interference effects to reduce the modulation. Simple calculations already described in Chapter 3 show that, for typical changes in absorption (see

Table 4.1), the transmission change can deviate by $\approx \pm 5\%$ when the FP oscillations are of the amplitude which we have observed experimentally.

In the chapter which follows we shall pursue the idea of modulators based on MQWs within Fabry-Perot cavities, where, in this case, the use of resonance effects is intended to be beneficial.

REFERENCES (Chapter 4)

- [1] D. A. B. MILLER, D. S. CHEMLA, T. C. DAMEN, A. C. GOSSARD, W. WIEGMANN, T. H. WOOD and C.A. BURRUS, "Electric field dependence of optical absorption near the band gap of quantum well structures", *Phys. Rev. B* (1985), **32**, pp. 1043-60.
- [2] L. VIÑA, R. T. COLLINS, E. E. MENDEZ and W. I. WANG, "Comparative study of the effect of an electric field on the photocurrent and photoluminescence of GaAs-GaAlAs quantum wells", *Phys. Rev. B* (1986), **33**, pp. 5939-42.
- [3] M. WHITEHEAD, P. STEVENS, A. RIVERS, G. PARRY, J. S. ROBERTS, P. MISTRY, M. PATE and G. HILL, "Effects of well width on the characteristics of GaAs/AlGaAs multiple quantum well electroabsorption modulators", *Appl. Phys. Lett.* (1988), **53**, pp. 956-8.
- [4] POCHI YEH "Optical Waves in Layered Media", Wiley Series in Pure and Applied Optics, 1988, p.152.
- [5] K. HIKOSAKA, T. MIMURA and K. JOSHIN, "Selective dry etching of AlGaAs-GaAs heterojunction", *Jpn. J. Appl. Phys.* (1981), **20**, pp. L847-50.
- [6] J. J. LEPORE, "An improved technique for selective etching of GaAs and Ga_{1-x}Al_xAs", *J. Appl. Phys.* (1980), **51**, pp. 6441-2.
- [7] T. H. WOOD, C. A. BURRUS, D. A. B. MILLER, D. S. CHEMLA, T. C. DAMEN, A. C. GOSSARD and W. WIEGMANN, "131ps optical modulation in semiconductor multiple quantum wells (MQW's)", *IEEE J. Quantum Electron.* (1985), **QE-21**, pp. 117-8.
- [8] R. J. MANNING, P. J. BRADLEY, A. MILLER, J. S. ROBERTS, P. MISTRY and M. A. PATE, "Photoconductive response time of a multiple quantum well *pin* modulator", *Electron. Lett.* (1988), **24**, pp. 854-5.
- [9] G. LIVESCU, A. M. FOX, T. SIZER, W. H. KNOX and D. A. B. MILLER, "Optical detection of resonant tunneling of electrons in quantum wells", *Topical Meeting on Quantum Wells for Optics and Optoelectronics*, 1989 Technical Digest Series, Vol. 10, pp. 254-7.
- [10] D. R. WIGHT, A. M. KEIR, G. J. PRYCE, J. C. H. BIRBECK, J. M. HEATON, R. J. NORCROSS, and P. J. WRIGHT, "Limits of electro-absorption in high purity GaAs, and the optimisation of waveguide devices", *IEE Proc. Pt. J* (1988), **135**, pp. 39-44.
- [11] M. WHITEHEAD, G. PARRY, J. S. ROBERTS, P. MISTRY, P. LI KAM WA, and J. P. R. DAVID, "Quantum-confined Stark shifts in MOVPE-grown GaAs-AlGaAs multiple quantum wells", *Electron. Lett.* (1987), **23**, pp. 1048-50.

- [12] T. H. WOOD, E. C. CARR, B. L. KASPER, R. A. LINKE, C. A. BURRUS and K. L. WALKER, "Bidirectional fibre-optical transmission using a multiple-quantum-well (MQW) modulator/detector", *Electron. Lett.* (1986), **22**, pp. 528-9.
- [13] G. D. BOYD, D. A. B. MILLER, D. S. CHEMLA, S. L. McCALL, A. C. GOSSARD and J. H. ENGLISH, "Multiple quantum well reflection modulator", *Appl. Phys. Lett.* (1987), **50**, pp. 1119-21.
- [14] P. J. STEVENS and G. PARRY, "Limits to normal incidence electro-absorption modulation in GaAs/(GaAl)As multiple quantum well diodes", *J. Lightwave Tech.* (1989), **LT-7**, pp. 1101-8.
- [15] P. J. STEVENS, M. WHITEHEAD, G. PARRY and K. WOODBRIDGE, "Computer modeling of the electric field dependent absorption spectrum of multiple quantum well material", *IEEE J. Quantum. Electron.* (1988), **QE-24**, pp.2007-16.
- [16] K. W. JELLEY, K. ALAVI and R. W. H. ENGELMANN, "Experimental determination of electroabsorption in GaAs/ $\text{Al}_{0.32}\text{Ga}_{0.68}\text{As}$ multiple quantum well structures as a function of well width", *Electron. Lett.* (1988), **24**, pp. 1555-7.
- [17] M. S. LEESON, F. P. PAYNE, R. J. MEARS, J. E. CARROLL, J. S. ROBERTS, M. A. PATE and G. HILL, "Design and fabrication of a planar, resonant Franz-Keldysh optical modulator", *Electron. Lett* (1988), , pp. 1546-7.
- [18] H. S. CHO and P. R. PRUCNAL, "Effect of parameter variations on the performance of GaAs/AlGaAs multiple-quantum-well electroabsorption modulators", *IEEE J. Quantum Electron.* (1989), **QE-25**, pp. 1682-90.

THE USE OF FABRY-PEROT EFFECTS TO ENHANCE THE PERFORMANCE OF MQW OPTICAL MODULATORS

5.1 Introduction

5.2 Simulation of MQW Fabry-Perot Cavity Modulators

5.2.1 Basic Features of the Cavity Model

5.2.2 Optimization of Modulators

5.3 Low-Finesse MQW Transmission Modulators

5.3.1 AR-Coated Transmission Modulators ($R_f \leq 0.01$, $R_b = 0.30$)

5.3.2 The Uncoated Transmission Modulator ($R_f = 0.30$, $R_b = 0.30$)

5.4 Low-Finesse MQW Reflection Modulators

5.4.1 The AR-coated Reflection Modulator ($R_f = 0.0001$, $R_b = 0.30$)

5.4.2 The Uncoated (Asymmetric Cavity) Reflection Modulator ($R_f = 0.30$, $R_b = 0.95$)

5.5 High-Finesse MQW Reflection Modulators

5.5.1 The Symmetric Cavity Modulator ($R_f = 0.95$, $R_b = 0.95$)

5.5.2 The Absorption-Compensating Cavity ($R_f = 0.90$, $R_b = 0.95$)

5.6 Sensitivity of FP Cavity Modulators

5.7 Summary

5.1 INTRODUCTION

The results from the work described in the previous chapter show that the modulation achievable, within certain operating constraints such as low bias voltage, using only a single pass in a MQW transmission modulator is limited to around 2–3dB with a minimum of ≈ 6 V bias. It was noted that using various well widths affects the bias voltage needed and the optimum operating wavelength. However, it does not help to increase the contrast. Therefore we must seek a way of improving the device performance (contrast or T/R changes) other than altering the MQW structure itself. Merely increasing the total number of quantum wells can obviously give higher contrast [1], but this is achieved at the expense of increased bias and insertion loss. Ideally we wish to keep the thickness of the region over which the modulating field is applied, i.e. the MQWs, as small as possible in order to minimize bias voltage and the detrimental effect of background doping, whilst making the incident light interact as strongly as possible with the MQWs. Hence we must increase the path length for light passing through the device.

One method of increasing the interaction region for an optical modulator is to use a waveguiding structure in which the light is confined to propagate parallel to the plane of the quantum wells, and in this case, perpendicular to the direction of the applied field [2, 3]. However, this mode of operation presents its own particular problems in getting the light into and out of the device (by end-fire or grating coupling), and makes the fabrication of 2-D arrays of modulators extremely difficult. Because the interaction length of waveguide devices is typically of the order of 100's of microns, and propagation is restricted to discrete modes, the optimization [4, 5] of such structures incorporating quantum wells is markedly different from that of normal-incidence modulators, and further discussion is beyond the scope of this thesis.

The alternative method of increasing the effective optical path through a normal-incidence device is to incorporate it into a resonant or Fabry-Perot (FP) cavity, which in the most general sense means having a finite reflectivity at the input and output facets to the device. Light travelling through the device is made to bounce back and forth through the active MQW layer, incurring increasing field-induced attenuation (electro-absorption) and phase shift (electro-refraction) as the cavity mirror reflectivities are increased. The basic MQW transmission

modulator with no anti-reflection coatings is intrinsically a low-finesse FP cavity. To achieve maximum effect it is normally considered necessary to use reflectivities as high as possible, and indeed, initially, the ultimate aim of this project was to investigate the properties of an MQW modulator built in to a high-finesse cavity. It was expected that as the electro-absorptive effects were known to be strong, then, because of the link through the Kramers-Krönig integral, electro-refraction would be likewise. Efficient modulation would therefore be achieved by the phase shift of sharp transmission or reflection resonances due to electro-refraction as shown in Figure 5.1.1.

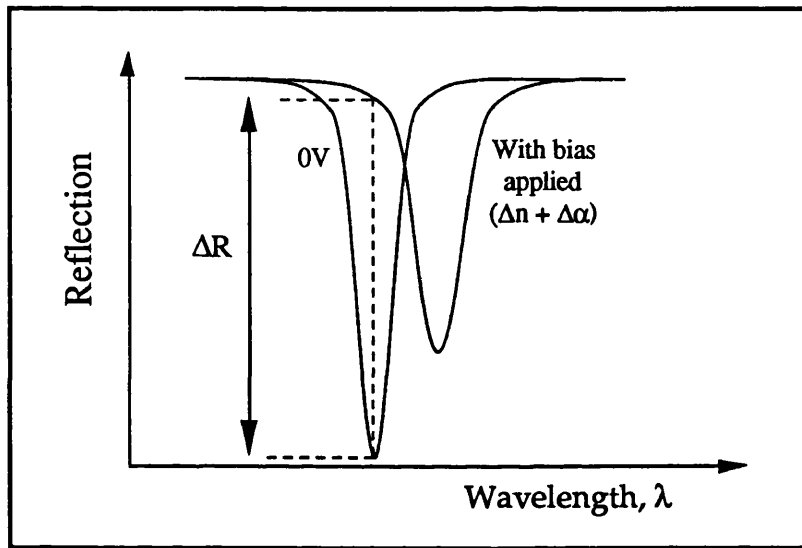


FIGURE 5.1.1:

Schematic of modulation principle in a high finesse FP cavity. Electro-refraction shifts the cavity resonance. Electro-absorption raises the reflection minimum.

During the course of this work this particular idea was independently proposed and investigated by a number of other research groups, both theoretically [6, 7] and experimentally [8, 9].

In this chapter we shall investigate theoretically how combining a variety of front and back surface reflectivities with the electro-absorptive and electro-refractive properties of MQWs may improve the performance of both transmission and reflection modulators. We discover that, in the case of high finesse devices, it is not possible to consider only electro-refractive effects. The presence of even small amounts of electro-absorption can have a marked effect on device performance, increasing

insertion loss and decreasing modulation. As an alternative, we shall demonstrate how efficient modulation may be achieved in a low-finesse cavity, with only one high reflector at the back of a device and optimized use of resonant electro-absorption.

5.2 SIMULATION OF MQW FABRY-PEROT CAVITY MODULATORS

5.2.1 BASIC FEATURES OF THE CAVITY MODEL

We have modelled the MQW FP cavity modulator in a simple way, choosing to concentrate on the way the electric field-induced changes in absorption and refractive index within the MQWs combine with the resonances of the cavity to improve modulation, rather than considering in detail the subtleties of the optical properties of the multiple semiconductor layers which may make up the cavity. Here, for example, we avoid the matrix-type calculations [6, 7] required to simulate the high reflectivity band for cavity mirrors constructed from semiconductor multilayer stacks (MLS), which consist of multiple quarter-wavelength layers of two materials of differing refractive index. That problem is addressed in Chapter 6.

Figure 5.2.1.1 shows the structure of the Fabry-Perot cavity for which we have modelled the transmission and reflection modulation characteristics for light at normal incidence.

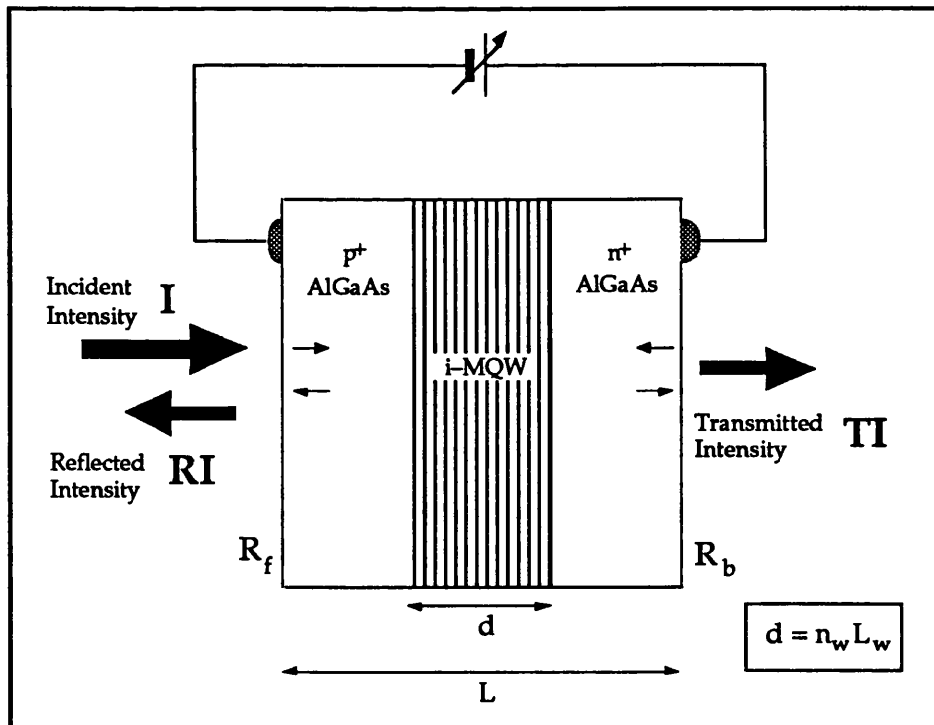


FIGURE 5.2.1.1:
Schematic diagram of the Fabry-Perot cavity model used in the calculations.

The cavity thickness, L , is set at 20 half-wavelengths, which is in the region of $2.5\mu\text{m}$ – the exact value depending on the desired position of the resonant wavelength relative to the MQW absorption edge. Note that this is not the same as the total thickness of the MQW region, which is given by $(n_w L_w + n_b L_b)$, where n_w (n_b) is the number of wells (barriers) and L_w (L_b) is the well (barrier) thickness. Also $n_b = n_w \pm 1$. Where we refer subsequently to the absorber thickness, d , we mean the total thickness of the quantum wells only, i.e. $n_w L_w$.

For a Fabry-Perot cavity, such as in Fig. 5.2.1.1, with a linear absorption coefficient α (in the quantum wells only), and a mean refractive index n_m (calculated for the whole p-i-n), in the plane wave approximation with light incident normally, the transmission T and reflection R can be expressed as follows:

$$T = \frac{A}{(1 + F \sin^2 \phi)} \quad \text{.....(5.1)}$$

$$R = \frac{(B + F \sin^2 \phi)}{(1 + F \sin^2 \phi)} \quad \text{.....(5.2)}$$

where

$$F = \frac{4 R_\alpha}{(1 - R_\alpha)^2} \quad \text{.....(5.3)}$$

$$A = \frac{(1 - R_f)(1 - R_b) \exp(-\alpha d)}{(1 - R_\alpha)^2} \quad \text{.....(5.4)}$$

$$B = \frac{R_f \left[1 - \left(\frac{R_\alpha}{R_f} \right) \right]^2}{(1 - R_\alpha)^2} \quad \text{.....(5.5)}$$

and

$$R_\alpha = \sqrt{R_f R_b} \exp(-\alpha d) \quad \text{.....(5.6)}$$

$$\phi = \frac{2\pi n_m L}{\lambda} \quad \text{.....(5.7)}$$

The cavity finesse, \mathcal{F} , is expressed as:

$$\mathcal{F} = \frac{\pi\sqrt{F}}{2} \quad \dots(5.8)$$

Absorption spectra for $\approx 100\text{\AA}$ quantum wells at various applied electric fields have already been determined in Chapter 3 from room-temperature measurements of photocurrent in an MQW p-i-n diode (sample KLB461 in § 2.6.1). Using this set of data we have calculated absorption changes and hence electro-refraction spectra according to the Kramers-Krönig integral, as described in Chapter 3. Figures 5.2.1.2 & 5.2.1.3 show the spectra which have been used in the modelling of the response of the FP cavity modulator. This range of fields is sufficient to include the maximum values of $\Delta\alpha$ and Δn in both positive and negative senses and thus allows the maximum modulation to be modelled.

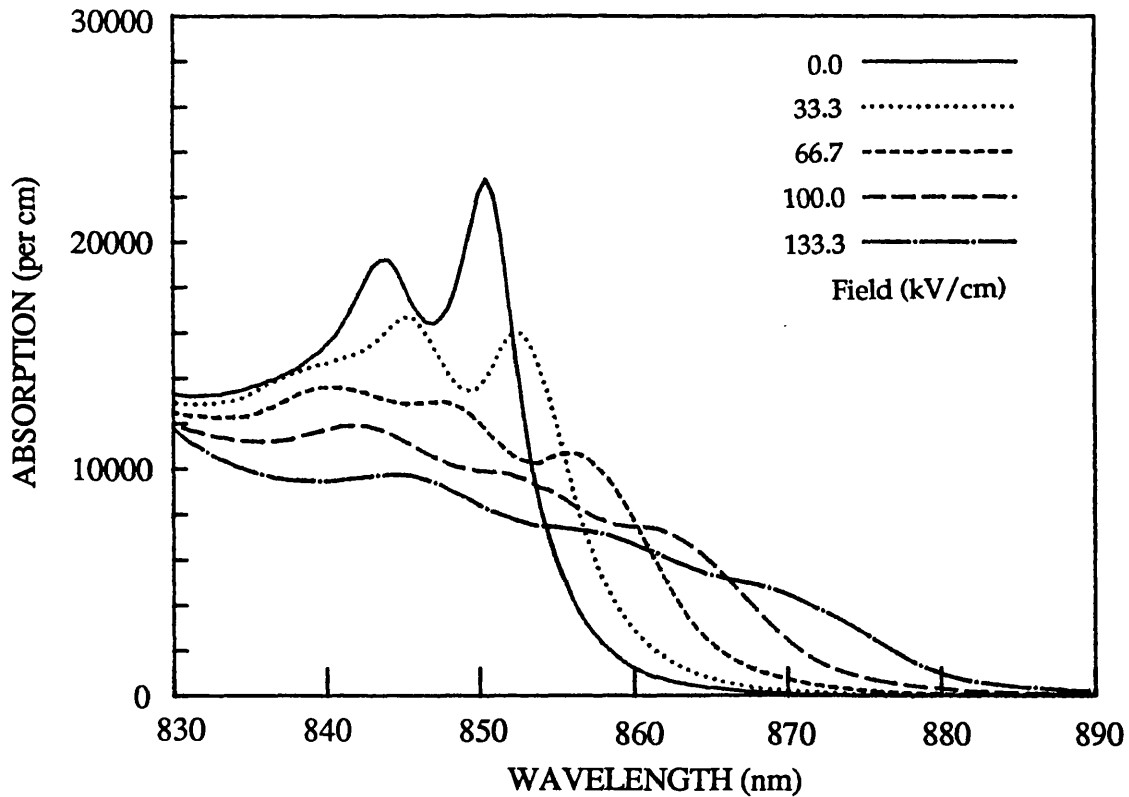


FIGURE 5.2.1.2:

Absorption spectra for $\approx 100\text{\AA}$ quantum wells derived from room temperature photocurrent spectra.

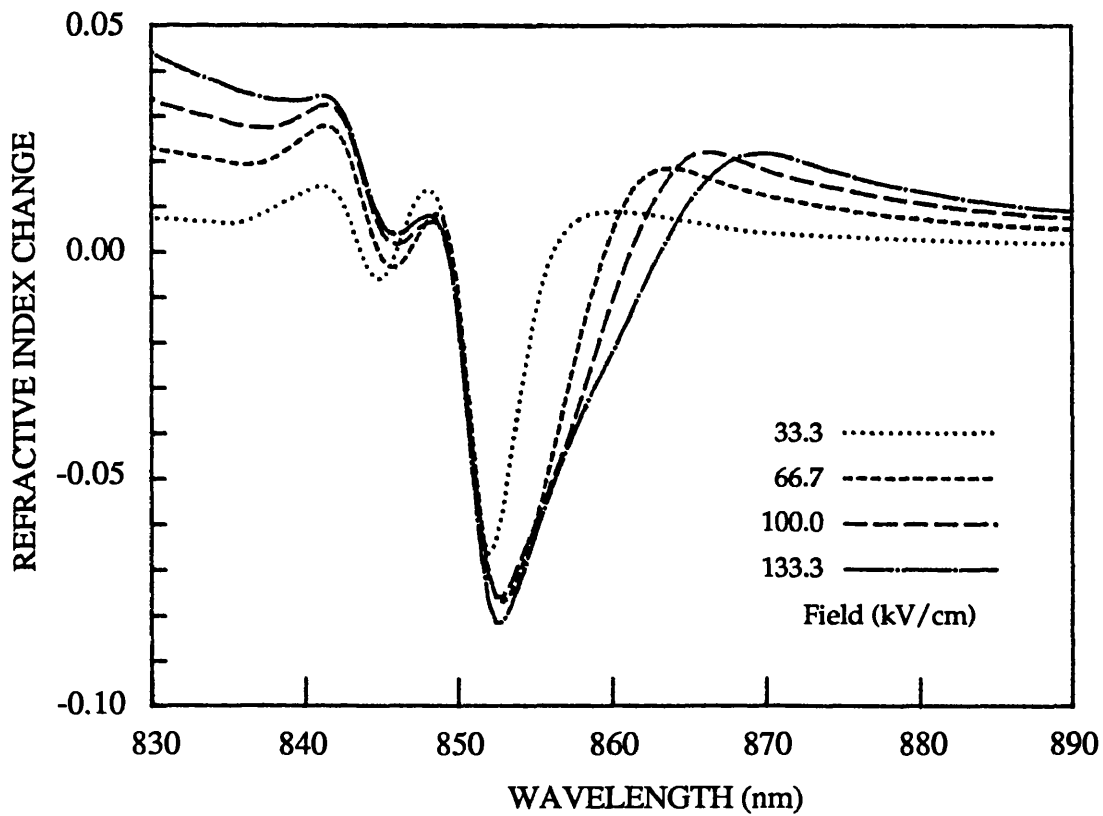
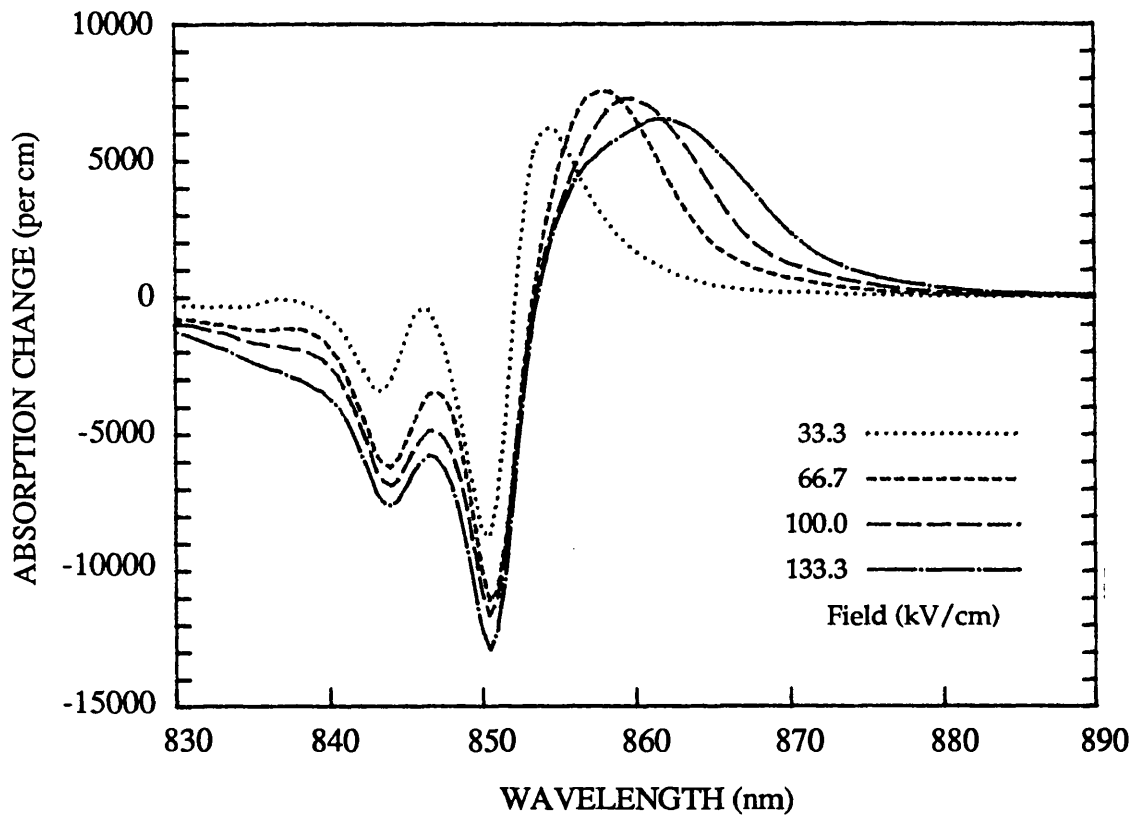


FIGURE 5.2.1.3:
Changes in absorption and refractive index for $\approx 100\text{\AA}$ quantum wells, as used in the FP cavity model. Data derived from Fig. 5.2.1.2 by Kramers-Krönig transformation.

We use these spectra, with chosen values of R_f and R_b , to calculate the transmission or reflection modulation from the unbiased state for an MQW FP cavity according to equations 5.1-5.7. With $\alpha \rightarrow \alpha + \Delta\alpha$ and $n \rightarrow n + \Delta n$ simultaneously, both the internal loss factor, $e^{-\alpha d}$, and the phase term, ϕ , in the FP equations are affected.

It should be pointed out that the calculated absorption spectra in this case do not give particularly good agreement with the electro-absorption sum rule (as explained in Chapter 3) due to bias and wavelength dependence of the quantum efficiency for fields less than $\approx 100\text{kV/cm}$. There is $\approx 10\%$ variation in the integrated absorption over the bias range. However, the calculated maximum absorption changes are in reasonable agreement with the data from the 87\AA well transmission modulator of Chapter 4. Our calculated electro-absorption and electro-refraction data are also in close agreement with the calculations of Weiner et al. [10], based on direct measurement of transmission modulation.

It was known that the absorption changes in the KLB461 sample would be affected by excitonic broadening due to background doping in the quantum well region. This was estimated to be $\approx 5 \times 10^{15} \text{ cm}^{-3}$ in Chapter 2. With more recent MQW samples, which have shown lower background doping and therefore noticeably sharper excitonic spectra with applied bias, slightly larger $\Delta\alpha$'s could be expected, and so the modelled spectra perhaps ought to be regarded as a fairly conservative estimate of resonant device performance.

The number of quantum wells can be selected in the program – fewer wells giving smaller modulation but the advantage of lower bias voltage for a given field. However, here we have chosen a fixed MQW structure of 62 GaAs wells, 100\AA thick, and 61 barriers of 60\AA $\text{Al}_{0.3}\text{Ga}_{0.7}\text{As}$. This gives a total thickness of $\approx 1\mu\text{m}$. We select this particular structure as a suitable compromise in order to keep bias voltages $\leq 10\text{V}$ for the fields which give the largest absorption changes in our data.

The applied field and cavity length, L , are varied to produce the optimum modulation for a given pair of mirror reflectivities. This is subject to the constraints that insertion loss may not exceed 3dB, i.e. the "on" state, whether in transmission or reflection, must be at least 0.5, and the bias voltage must remain below 10V. This target specification is of course somewhat arbitrary, but we believe that a number of applications for MQW modulators will require at least this level of performance.

The main approximations made in the modelling are:

- (a) Spectral dispersion and spatial variation of the unbiased refractive index of the cavity are ignored. By spatial variation we mean the change in index as one passes from AlGaAs to GaAs layers through the structure, which produces small reflected components according to the simple Fresnel equation. These reflections are considered to be negligible because of the small index mismatch ($\Delta n \approx 0.2$). A weighted mean index, n_m , of 3.37 was calculated for the cavity at a wavelength of 850nm, based on the effective AlGaAs content of the typical MQW p-i-n diode used in our experiments and published experimental index data [11, 12]. This cavity index was kept constant throughout. The justification for this is that in the small wavelength band ($\approx 10\text{nm}$) where significant modulation occurs the dispersion of the index is so small that it has no significant bearing on the modulation characteristics. Furthermore, as long as the calculated n_m lies between that of GaAs and AlGaAs at the operating wavelength there is no effect on the magnitude of the modulation achievable with a cavity of a given finesse. Any discrepancy between the real index of the cavity and that used here will simply cause a shift in operating wavelength for a particular chosen cavity thickness, which ultimately, in practice, will need to be optimized over several growth runs. The effect of the *changes* in index induced by an applied electric field is a more important consideration in calculating modulation spectra.
- (b) For the purpose of simplifying the definition of the cavity thickness the cavity mirrors are assumed to be "hard" reflectors, i.e. we assume that all reflections take place at the interfaces between the p-i-n structure and the external mirrors. This is certainly the case where the mirror is simply the semiconductor : air interface ($R \approx 0.30$), or a metallic coating on the semiconductor. It is not so when the reflector is distributed as in the MLS, which could be incorporated as one of the doped contact layers. However, the details of how the mirrors are formed are not critical to the modulation calculations. We assume that any arbitrary reflectivity can be fabricated by some technique, and also ignore any spectral variation for the same reasons that the index dispersion is neglected in (a).
- (c) The linear electro-optic (LEO) effect has not been included. At wavelengths close to the absorption edge of the MQWs, where enhanced effects due to the QCSE are observed, the quadratic electro-optic effect associated with the shift of excitonic transitions is significantly stronger. Glick et al. have observed little dispersion in the linear electro-optic

coefficient, r , and close agreement with the bulk GaAs value of $\approx 1.3 \times 10^{-10}$ cm/V, in an MQW waveguide structure at ≈ 20 nm away from the unbiased heavy-hole exciton peak [13]. The refractive index change due to the linear effect is given by $\Delta n = n^3 r E / 2$, where E is the electric field. For a field of 100 kV/cm and an index of ≈ 3.5 this gives us a Δn of $\approx 3 \times 10^{-4}$. The calculated spectra above (Fig. 5.2.1.3) show peak positive index changes of $\approx 1 \times 10^{-2}$, roughly 30 times larger, when scaled to represent the whole MQW structure.

- (d) The modelling has only been carried out for light at normal incidence, in which case there is no polarization dependence. For off-normal incidence the reflectivity of MLS cavity mirrors will have both angular and polarization dependence [14], as will the phase change on reflection in the case of metallic layers. Also, the phase change on reflection from an MLS is only π at the mid-point of the high reflectance band [14]. Although we have not taken account of phase changes other than π at the mirrors, the effect will only be to change the apparent thickness of the cavity – something that will require optimization in the growth process rather than a detailed computer simulation.

5.2.2 OPTIMIZATION OF MODULATORS

(a) *The MQW Structure, Fields and Bias:*

In the sections which follow we shall present calculated modulation spectra for a range of FP cavity devices in which the MQW structure is of a fixed thickness. In this case the bias voltage is determined for a given applied field and we can compare the range of cavities for one particular operating regime. This does not necessarily mean that all the devices are optimized, it is just a convenient way of assessing varying degrees of resonance. Optimization depends very much on what is required of the modulator, so the calculations here are only intended to give a general feel for what can be achieved.

Should a more comprehensive optimization be necessary, then, for a cavity whose front and back reflectivities and length, L , are specified, it is a reasonably straightforward matter to optimize the modulation for a given maximum bias voltage. For each of the biased spectra in our MQW electro-absorption and electro-refraction data files the average electric field is fixed, ranging from 16.7 to 100 kV.cm⁻¹. This sets an upper limit

on the number of quantum wells (each 100Å thick) for each field, according to the desired bias voltage in the model. We assume that the field non-uniformity effects due to background doping, which can become very marked for large numbers of wells, can be ignored for the total MQW thickness considered here. Thus the voltage "applied" to the modelled device is simply the product of the average electric field and the total thickness of wells + barriers. In keeping with the devices studied in the last chapter the barrier thickness has been fixed for these calculations at 60Å. As already mentioned, the barriers should be made as thin as possible, without well to well coupling occurring, so as to minimize the bias voltage. Recent modelling and measurement has indicated that barriers as thin as 40Å could be successfully used [15].

Once the maximum number of wells is determined, for each field we can calculate and compare biased and unbiased transmission (T) or reflection (R) spectra to decide which combination of field and total MQW thickness offers the best modulation, which may be in terms of ΔT , ΔR or contrast. In practice, the choice will be dependent on the application. Obviously, to keep the voltage fixed, as the chosen applied field increases, the maximum number of wells allowed must decrease, which results in a trade-off between the amount of absorption change and the Stark shift of the absorption edge.

(b) *The Cavity Length:*

The optimization of the cavity length, L , is very important since the cavity length determines the position of the FP resonance relative to the MQW absorption features in the spectrum. Thus it will have a bearing on how much modulation may be achieved, and we shall show that this may be significant even with fairly low-finesse cavities.

Once we have decided on the mirror reflectivities and MQW structure for which we want to obtain the optimum modulation characteristics, it is still possible to select a range of values for the cavity length which, for a given input wavelength, will set the initial (unbiased) detuning from resonance somewhere between $\pm \pi/2$ radians. It is therefore necessary to find the wavelength at which the presence of an FP resonance will have the most beneficial effect. To do this with a minimum of computing time we make the assumption that the maximum modulation occurs at the unbiased resonant wavelength. This is not always exactly the case, e.g. when electro-refractive effects come into play and shift the cavity resonance the largest effects may occur at the biased resonance, but even

in this case the approximation allows us to home in more quickly on the optimum cavity length.

Having made the assumption above, we then calculate the biased and unbiased transmission or reflection – whichever is more important according to the mirror reflectivities used – across the whole spectrum where significant absorption and index changes take place, with the phase term, ϕ , set to zero at all wavelengths. We call this a *zero-detuning* (ZD) spectrum, since it is equivalent to putting a resonance at every wavelength, and thus gives us an envelope of maximum modulation from which we can select the wavelength at which modulation is greatest to be the resonant wavelength for the cavity. The optimum cavity length is simply determined from this wavelength and the refractive index. The spectra can then be recalculated for the *fixed cavity* (FC) case.

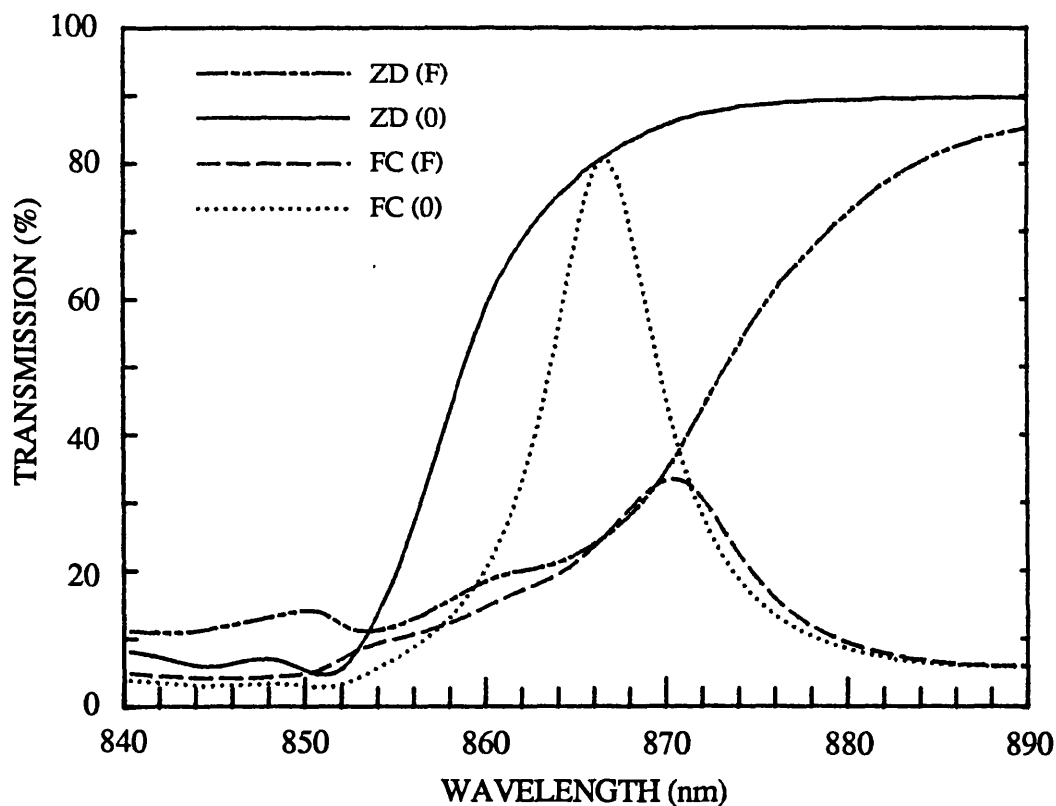


FIGURE 5.2.2.1:

Zero-detuning and fixed cavity transmission spectra for an MQW FP cavity modulator with $R_f=0.50$ and $R_b=0.70$. Applied field is 100kV/cm and the cavity length is $2.571\mu\text{m}$.

The optimization is illustrated in Figures 5.2.2.1-2, where both the ZD spectra and the optimized FC spectra are displayed to show their relationship. The calculations are for an arbitrary cavity with $R_f = 0.50$, R_b

= 0.70, the standard MQW structure mentioned above ($62 \times 100\text{\AA}$ wells), and a cavity length (in the fixed cavity case) of $2.571\mu\text{m}$.

In Fig. 5.2.2.1 (previous page) we show the transmission spectra with and without bias for the ZD and FC calculations. The former curves are generated simply by setting the cavity length to 0, which although unphysical has the same effect as making the phase, ϕ , equal to an integral multiple of π radians. It can be seen that the unbiased curve for the FC case, which has a resonance peak at $\approx 866\text{nm}$, only touches the ZD curve at the resonance. Similarly, the biased FC curve crosses the biased ZD curve at the same wavelength. In the biased case the transmission resonance has shifted due to the electro-refraction leaving a lower level of transmission at the *unbiased* resonant wavelength than if only electro-absorptive effects had occurred. Because electro-absorption and electro-refraction both reduce transmission at the unbiased resonance, one by a straightforward attenuation, the other by a shift of the peak, the ZD approximation will always home in on the optimum modulation point.

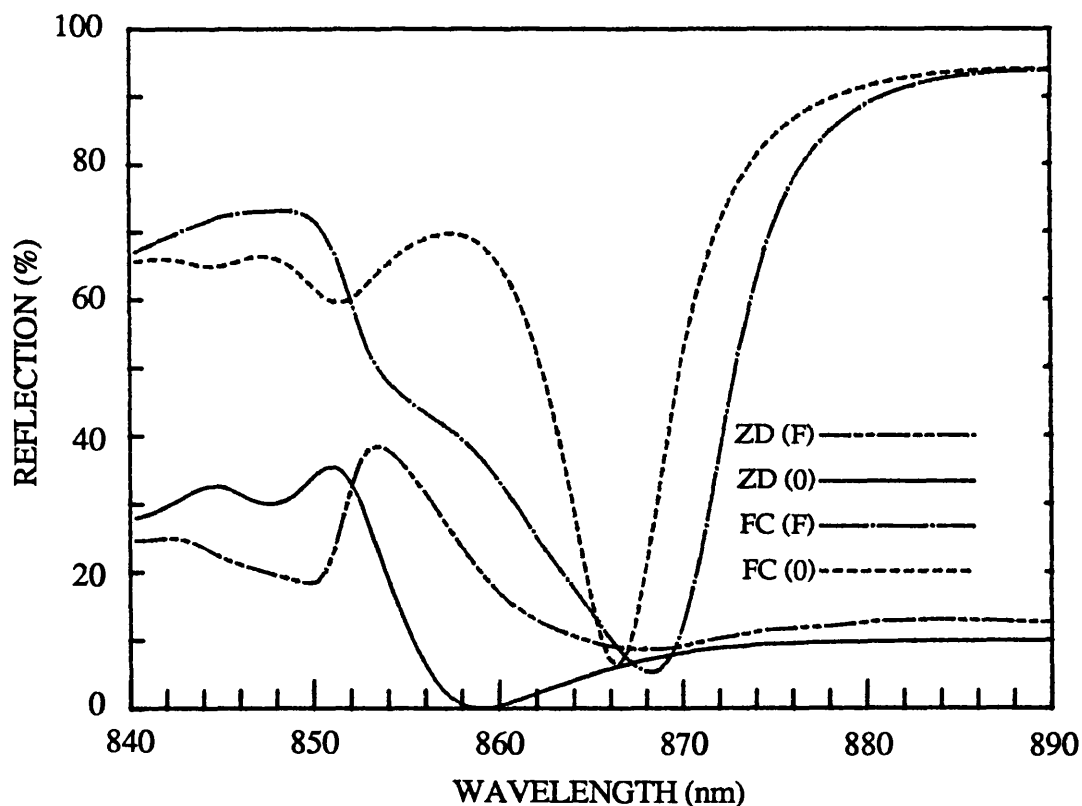


FIGURE 5.2.2.2:

Zero-detuning and fixed cavity reflection spectra for an MQW FP cavity modulator with $R_T=0.50$ and $R_b=0.70$. Applied field and cavity length are the same as for Fig. 5.2.2.1.

The situation in reflection is more subtle. If the cavity is asymmetric, i.e.

lower reflectivity at the front surface than at the back, maximum modulation can occur close to the biased resonance, where electro-refraction and electro-absorption combine to shift the resonance from the unbiased wavelength and reduce the level of the reflectance minimum respectively.

It is clear in Fig. 5.2.2.2 that the maximum modulation, whether contrast (on:off ratio) or reflection change, occurs at a longer wavelength than the unbiased resonance. This is something which the ZD calculation cannot immediately pick up, and is due to the electro-refractive shift of the resonance and the effect of electro-absorption which lowers the reflectivity minimum. In this case we have to make a series of FC calculations, usually only 2-3 iterations, each time resetting the cavity length so as to put the zero-bias resonance at the wavelength of, for example, maximum contrast (C_{\max}). It is found that C_{\max} increases initially from the value given by the zero-detuning calculation to a new maximum for the FC calculation, then decreases as the unbiased resonance is made to shift to longer and longer wavelengths, "chasing" the C_{\max} of the previous calculation.

Having defined the optimization procedure we shall now proceed to investigate MQW modulators with a variety of input/output facet reflectivities. Although the initial aim was to assess the possibility of enhancing optical modulation by use of a high-finesse cavity, with high reflectivity mirrors front and back, it is instructive to consider also the effect of FP resonance in other devices of lower finesse. In the sections to follow we shall look at three categories of MQW FP cavity modulators with a trend towards increased finesse. All the devices modelled have the same fixed MQW structure. By initially comparing the modelled results with experimental data for low-finesse structures the validity of the simple cavity model is demonstrated, and thus we can regard the results for higher finesse devices with reasonable confidence.

5.3 LOW-FINESSE MQW TRANSMISSION MODULATORS

This section covers the simplest MQW modulators, with only the exposed semiconductor surfaces as mirrors. This is the form in which they were first demonstrated [16] and typical of the devices investigated experimentally in the previous chapter [17]. Because of the nature of the GaAs-AlGaAs material system and the device fabrication process (see § 4.2.1), which leaves only a very thin active layer with smooth front and back surfaces, the basic MQW transmission modulator shows Fabry-Perot oscillations in its optical response spectrum. Anti-reflection (AR) coatings are normally applied to reduce the reflectivity of the front surface in order to remove these effects, which have been regarded as undesirable due to the non-uniformity of optical response [18, 19] which they may introduce from process to process, or indeed from device to device on a single processed wafer. Here we shall consider the possible benefits of a small amount of residual finesse and the effect of leaving out the AR coating altogether. The fragility of the MQW transmission modulator, once the window is etched in the substrate, makes it rather difficult to apply an AR layer to the back surface of the device because of the mechanical and thermal stresses involved in the extra processing, hence we keep the back reflectivity, R_b , fixed at ≈ 0.30 for these calculations, whilst we may choose a value of front reflectivity, R_f , from close to zero to ≈ 0.30 to simulate various AR coatings.

5.3.1 AR-COATED TRANSMISSION MODULATORS ($R_f \leq 0.01$, $R_b = 0.30$)

The upper limit of 1% for the front reflectivity has been chosen to compare with the experimental data of Chapter 4, where the Fabry-Perot effects in transmission spectra were consistent with this figure. It was shown in Chapter 3 that even at this apparently low level of reflectivity there remains sufficient finesse to noticeably distort the transmission spectra and make the calculation of low absorption coefficients subject to large errors. Here we wish to determine whether the modulation is influenced by the device being of low finesse, as opposed to no finesse.

Modelled spectra for the non-resonant MQW transmission modulator with R_f reduced to 0.0001 are shown below in Fig. 5.3.1.1. It was seen in § 3.2.4 that the front reflectivity must be decreased to this level in order to

reduce the amplitude of the FP oscillations in the non-absorbing part of the spectrum to only 1%. There is good qualitative agreement between these spectra and those for the AR-coated CPM405 modulator which contained 60 wells (§ 4.4.2). If anything the experimental results show a more prominent e1-hh1 exciton for the biased state (Fig. 4.4.2.1), the difference being due to the slightly poorer quality of the sample from which the absorption spectra in the model were derived, and so we may expect slightly smaller maximum transmission changes and contrast for the modelled structures.

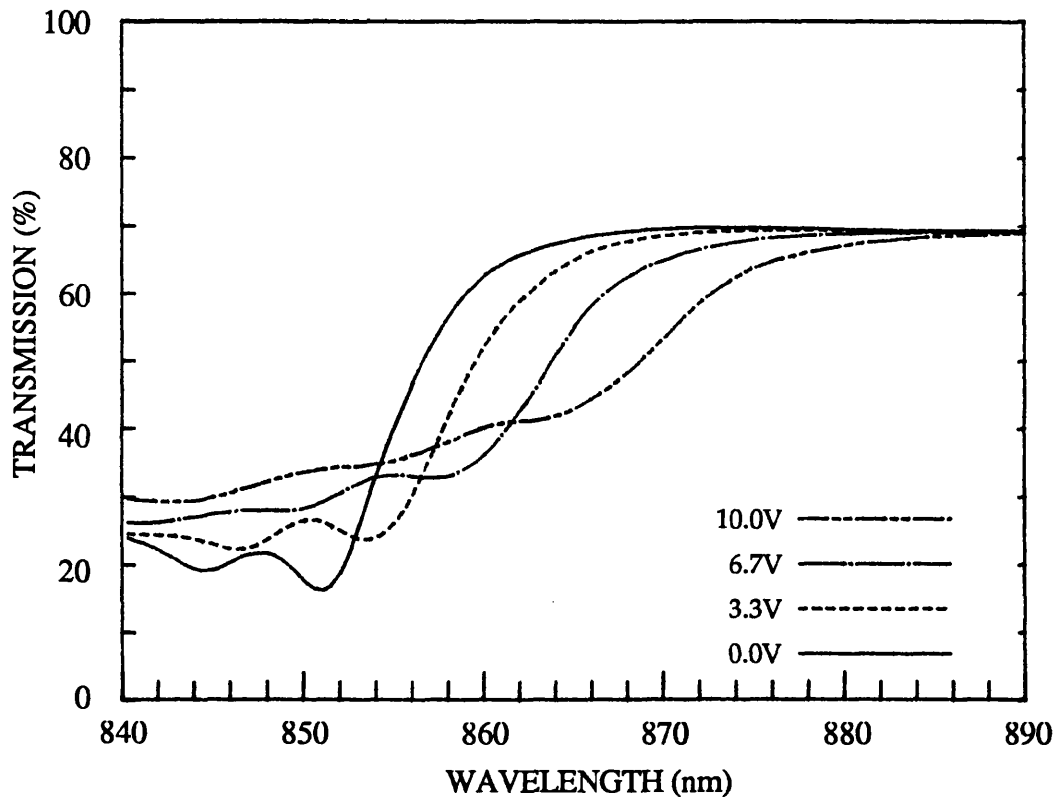


FIGURE 5.3.1.1:

Calculated transmission spectra for a non-resonant MQW modulator with $R_f = 0.0001$ and $R_b = 0.30$. Device contains $62 \times 100\text{\AA}$ GaAs wells with 60\AA AlGaAs barriers.

The modulation spectra for the non-resonant transmission modulator are shown over the page in Fig. 5.3.1.2. Maximum transmission change is $\approx -26\%$ at 6.7V.

The contrast is more than 3dB if we operate at the unbiased heavy hole exciton. However, the insertion loss at this point is also more than the 3dB limit which we set ourselves earlier, being ≈ 4.7 dB, determined by the biased absorption. Moving to the biased exciton wavelength we

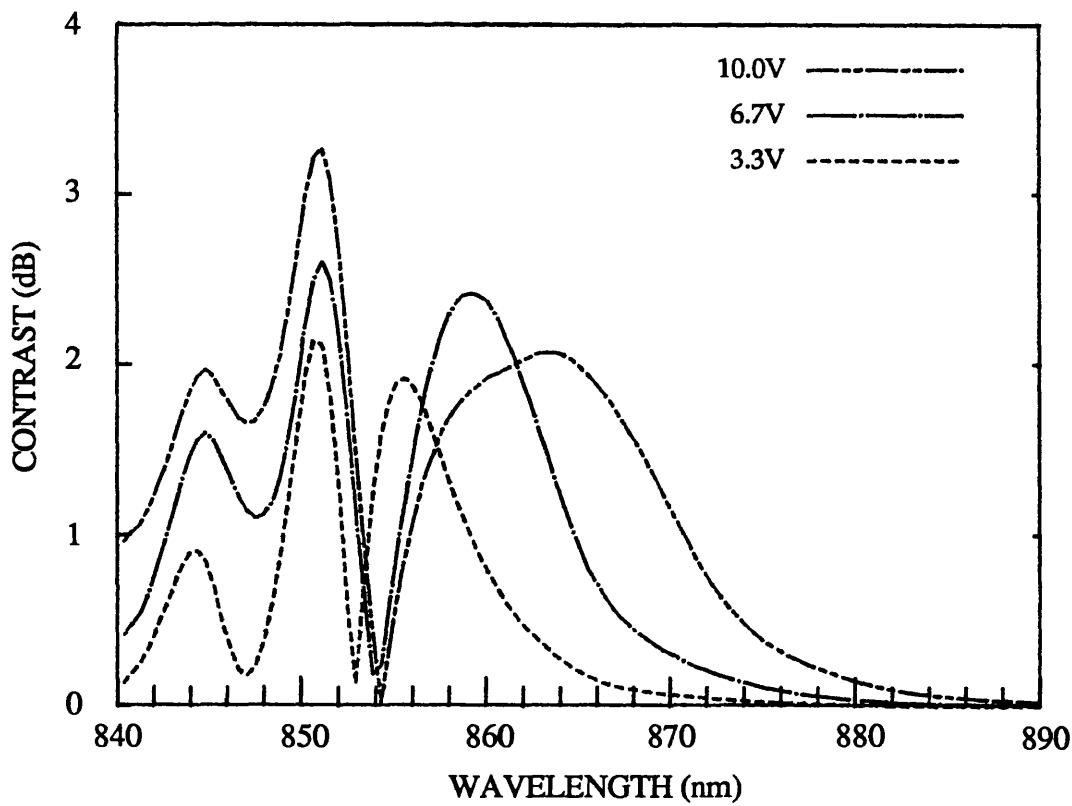
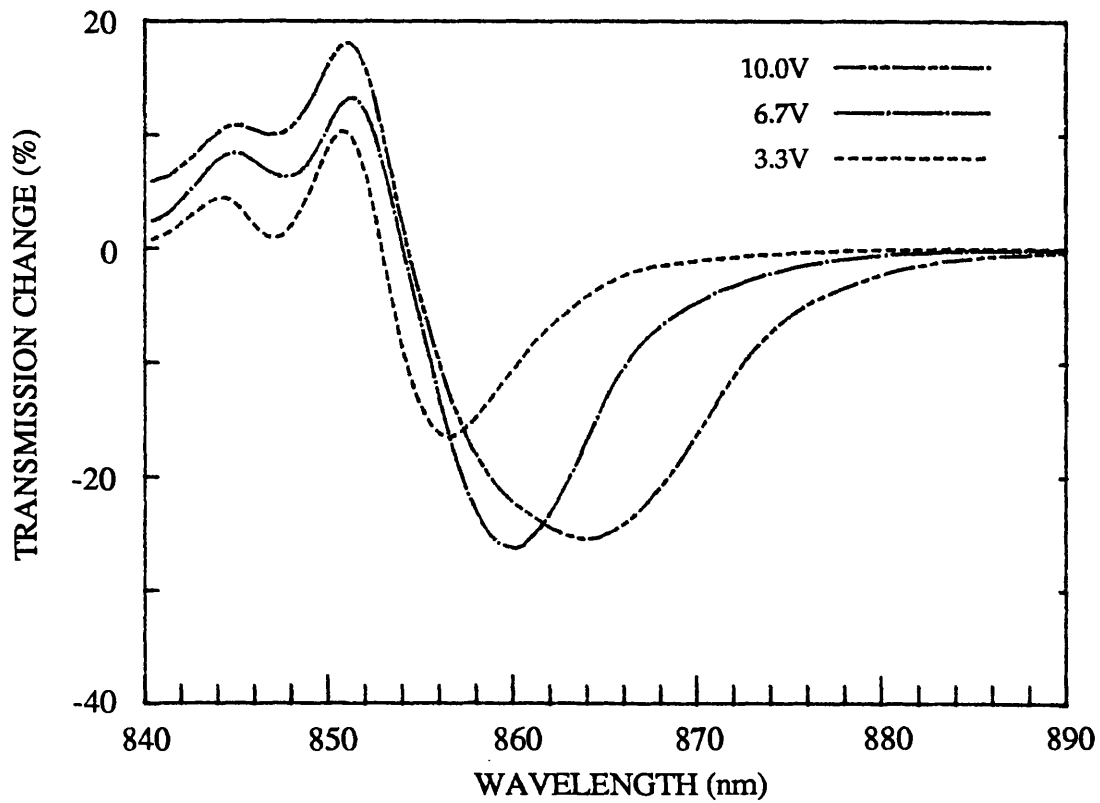


FIGURE 5.3.1.2:
 Calculated spectra of transmission change and contrast for a non-resonant MQW modulator with $R_f = 0.0001$ and $R_b = 0.30$. Derived from Fig. 5.3.1.1.

find a peak contrast of $\approx 2.4\text{dB}$, with an insertion loss of only 1.7dB . Modulation linewidths are $\approx 5\text{-}6\text{nm}$ for the 20% and 2dB limits.

We now consider the case of the AR-coated device where the residual R_f is ≈ 0.01 . This is to compare with the results of Chapter 4. The modelled transmission spectra, in Fig. 5.3.1.3 below, exhibit the characteristic oscillation in the low absorption region. The position of the peak of this FP resonance is set in the calculation scheme (see § 5.5.1) to give the optimum modulation. Generally speaking, the resonance must be close to the foot of the absorption edge. That way, insertion loss is reduced and the device makes full use of the largest electro-absorptive effects.

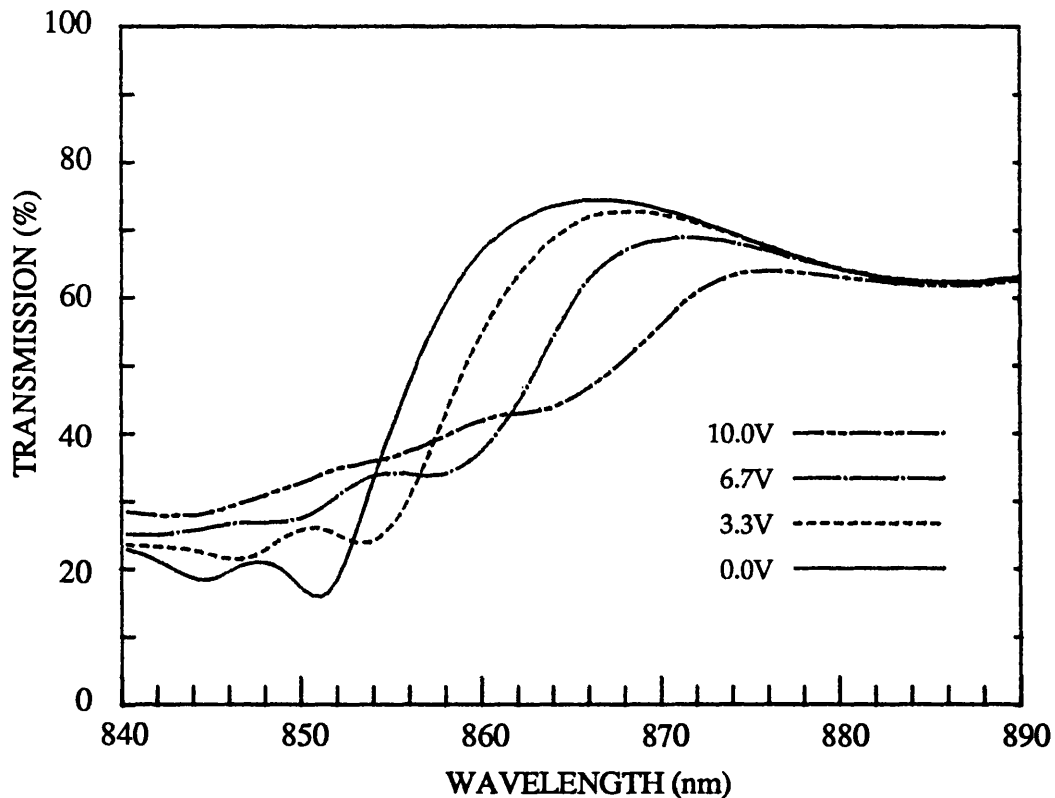


FIGURE 5.3.1.3:

Calculated transmission spectra for a non-resonant MQW modulator with $R_f = 0.01$ and $R_b = 0.30$. Device contains $62 \times 100\text{\AA}$ GaAs wells with 60\AA AlGaAs barriers.

With this small amount of finesse we find that the maximum transmission change has increased, but only to ≈ -0.30 , and the contrast has not noticeably altered. The spectra are shown in Fig. 5.3.1.4 (see over). This is in line with the simple calculation at the end of § 3.2.4 which indicated an increase of about 0.05 in the size of the transmission change with a finesse equal to that here.

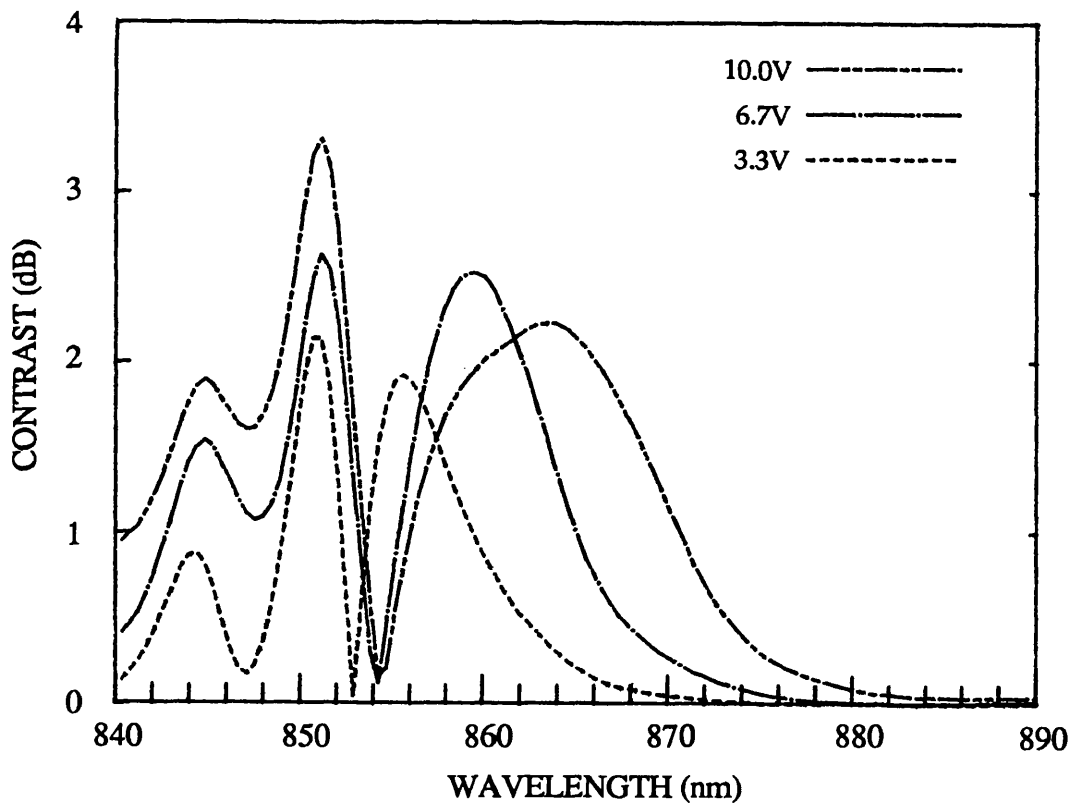
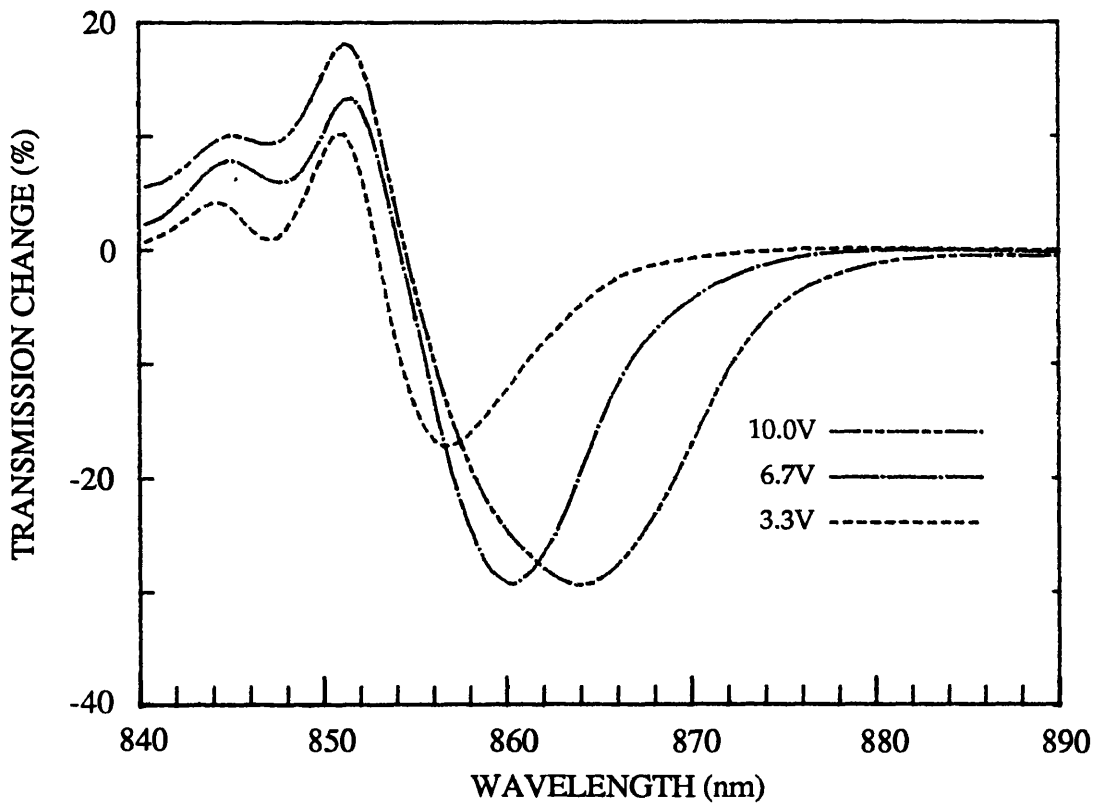


FIGURE 5.3.1.4:
 Calculated spectra of transmission change and contrast for a non-resonant MQW modulator with $R_f = 0.01$ and $R_b = 0.30$. Derived from Fig. 5.3.1.3.

The main consequence of including some resonance is an improvement in the insertion loss, as the operating point is now at a transmission peak. In this case the loss falls to $\approx 1.35\text{dB}$. Linewidths for both transmission change and contrast are unaffected.

From this initial modelling we can now be confident that the experimental modulation results are a good representation of the properties of the quantum wells alone, with only a small perturbation due to remnant FP effects. That there is good agreement with the results in § 4.4.2 is comforting, since the electro-absorption spectra used in the model are not derived from the same MQW structure. This should give us some confidence in the predictions for devices for which we have no experimental data as yet.

5.3.2 THE UNCOATED TRANSMISSION MODULATOR ($R_f \approx 0.30$, $R_b \approx 0.30$)

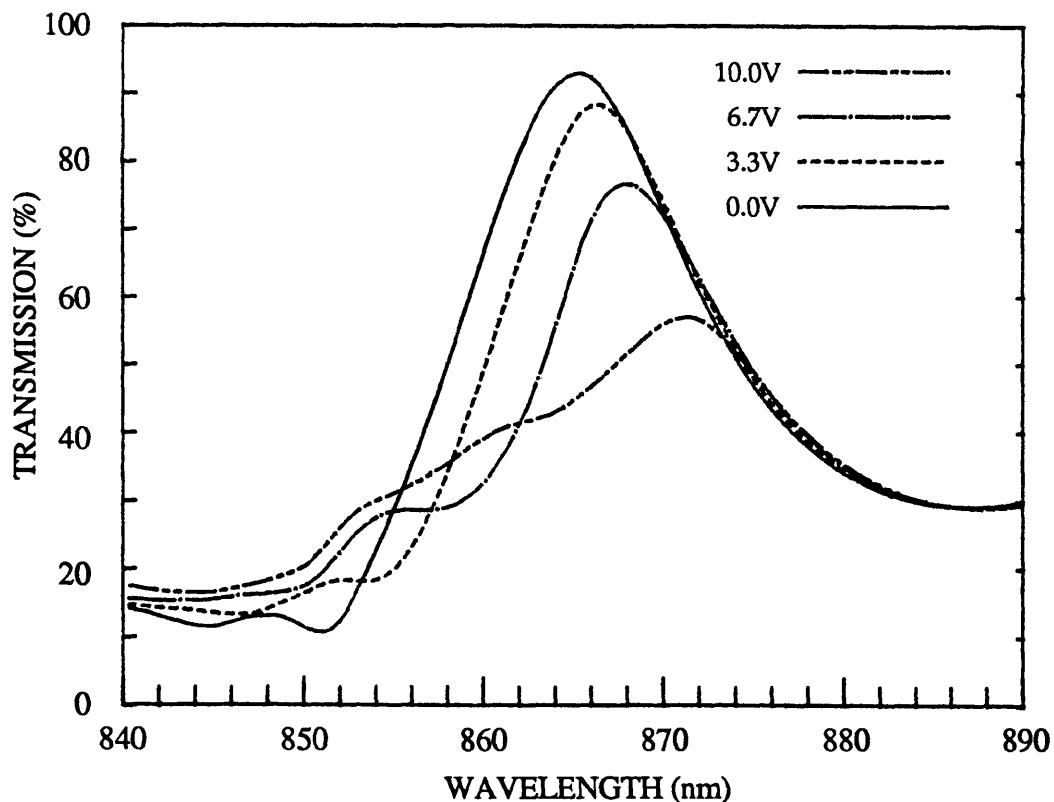


FIGURE 5.3.2.1:

Calculated transmission spectra for a resonant MQW modulator with $R_f = 0.30$ and $R_b = 0.30$. Device contains $62 \times 100\text{\AA}$ GaAs wells with 60\AA AlGaAs barriers.

In its most basic form, i.e. without any form of AR coating, the MQW transmission modulator is a symmetric FP cavity with a low finesse of

≈ 2.5 . This amount of finesse is sufficient to strongly alter the transmission spectrum, as can be seen for the uncoated CPM405 modulator in § 4.4.1. In that particular case the cavity resonance was rather unsuitably placed to enhance the device performance. The result of correctly siting the FP resonance can be seen in Fig. 5.3.2.1 on the previous page. The dominant feature in the spectrum is now the resonance rather than MQW absorption edge. This effect becomes more marked as finesse is increased.

Because of the symmetry of the cavity and the low absorption at the selected resonant wavelength the insertion loss becomes very low – only $\approx 0.4\text{dB}$ in this case.

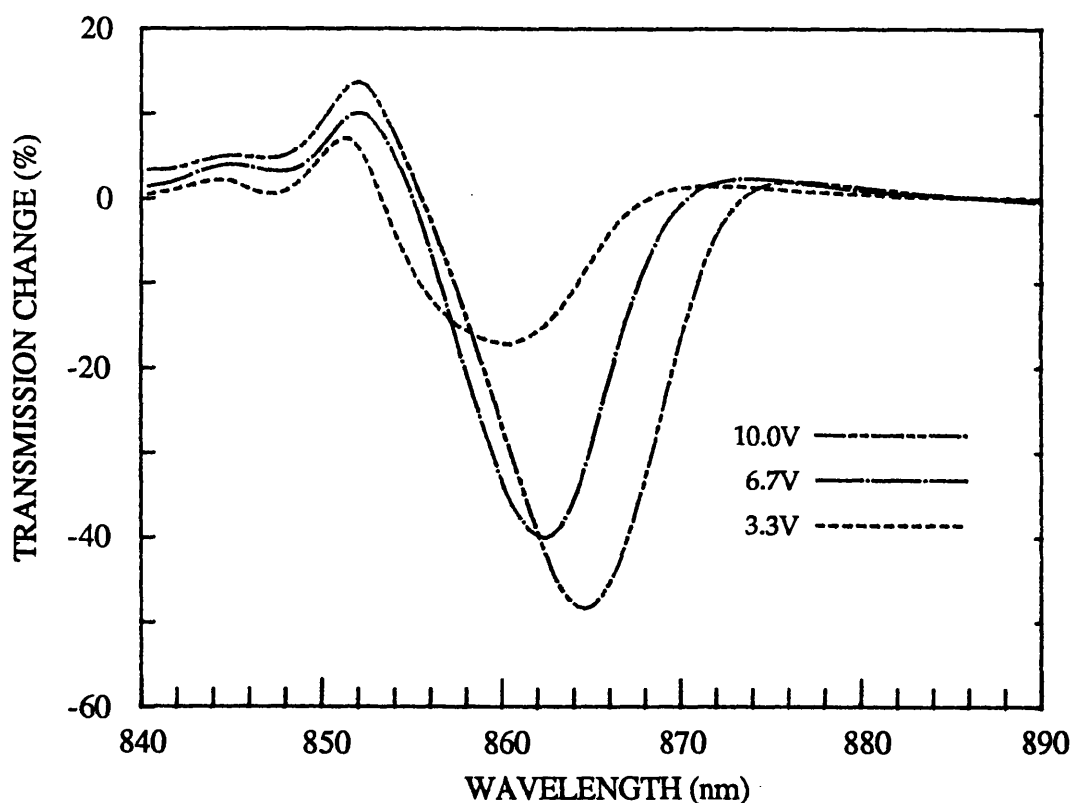


FIGURE 5.3.2.2:
Calculated transmission change spectra for a resonant MQW modulator with $R_t = 0.30$ and $R_b = 0.30$. Derived from Fig. 5.3.2.1.

The effect on transmission change is shown above in Fig. 5.3.2.2. The optimum modulation now requires 10V, in order to shift the absorption edge to the resonance, but, along with the improvement in insertion loss, the peak transmission change is now more than -48%, increased by a factor of ≈ 1.8 compared to the non-resonant modulator. A corresponding

improvement occurs in the linewidth for transmission change.

Comparing with the non-resonant device, the linewidth is now more than 10nm for a -20% change, while at -40% it is still 4.6nm. Even at the 6.7V bias the transmission change is increased to about -40%.

There is also an increase in the contrast to a peak value of ≈ 3.2 dB, with a linewidth of just under 4nm at the 3dB level (seen below in Fig. 5.3.2.3). The contrast ratio actually increases by almost the same factor as the transmission change due to most of the increase occurring in the high transmission level. This is just the effect which we saw in Chapter 3. As absorption increases, the finesse of the cavity falls, and whether we are at resonance or anti-resonance begins to have less and less effect on the transmission level.

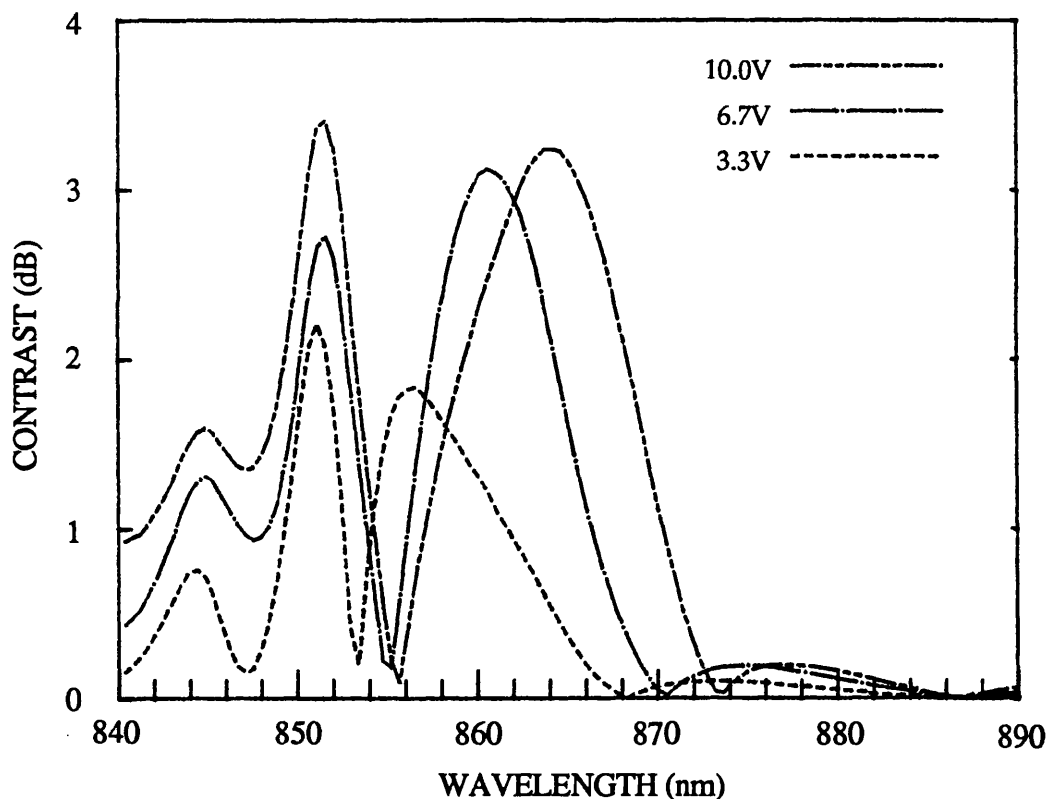


FIGURE 5.3.2.3:

Calculated transmission contrast spectra for a resonant MQW modulator with $R_t = 0.30$ and $R_b = 0.30$. Derived from Fig. 5.3.2.1.

To achieve the improvements shown here, in practice it will be necessary to etch the windowed structure described in § 4.2.1 with a high degree of accuracy. Additional calculations show that variations in the cavity thickness of only $\pm 200\text{\AA}$ (less than 1%) will reduce the maximum transmission change and contrast to less than 40% and 3dB respectively.

At present this accuracy cannot be provided purely by the epitaxial growth, so the only conceivable way to intentionally produce a high performance device is to etch controllably into the AlGaAs etch stop layer which usually forms part of the MQW *p-i-n* diode. The optical response of the cavity would need to be monitored during the process to stop at the optimum thickness.

5.4 LOW-FINESSE MQW REFLECTION MODULATORS

The major advantage offered by operating in reflection is that there is no need to remove the absorbing GaAs substrate, thus avoiding some difficult processing and also retaining the mechanical strength of the structure. Further benefits are that the contrast ratio is squared for the simple non-resonant case, or alternatively, the same contrast as for the transmission modulator can be achieved with a thinner MQW structure, thus reducing the bias voltage. A high reflectivity quarter-wave multilayer stack (MLS) can be integrated epitaxially [20] to form a back mirror within the basic MQW *p-i-n* diode. Here we examine two possible reflection modulators which use only a back reflector stack. In the first case the front surface is AR-coated to form a simple double-pass modulator. The second case is the uncoated structure, which leaves a low-finesse asymmetric cavity

5.4.1 THE AR-COATED REFLECTION MODULATOR ($R_f = 0.0001$, $R_b = 0.95$)

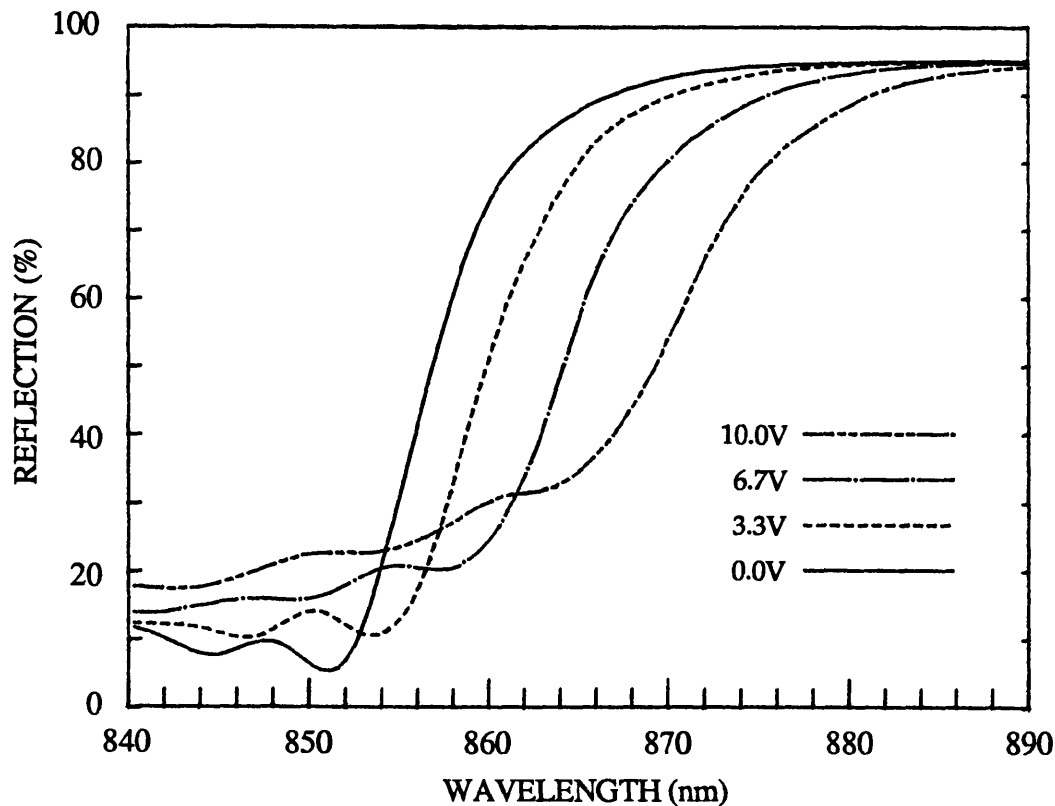


FIGURE 5.4.1.1: Calculated reflection spectra for a non-resonant MQW modulator with $R_f = 0.0001$ and $R_b = 0.95$. Device contains $62 \times 100\text{\AA}$ GaAs wells with 60\AA AlGaAs barriers.

A modulator of this type was first demonstrated by Boyd et al. in 1987 [21]. A maximum contrast ratio of $\approx 8:1$ (9.0dB) was observed for a bias of 14V at the wavelength of the unbiased e1-hh1 exciton peak, with the reflectivity increasing to $\approx 25\%$ for the biased state. The device in question had a very similar MQW structure to that used in our model, with only 3 more wells. At a bias of 9V a contrast ratio of $\approx 5.3:1$ (7.2dB) was measured, with $\approx 20\%$ on state reflection. This agrees quite well with the calculated spectra for 0V and 10V on the previous page in Fig. 5.4.1.1, where the reflectivities are 0.05 and 0.22 respectively. Notice that the on state for the device now tends towards 95% ($= R_b$), compared to 70% for the transmission modulator, whilst the extra absorption from the double pass reduces the off-state to 20-30%.

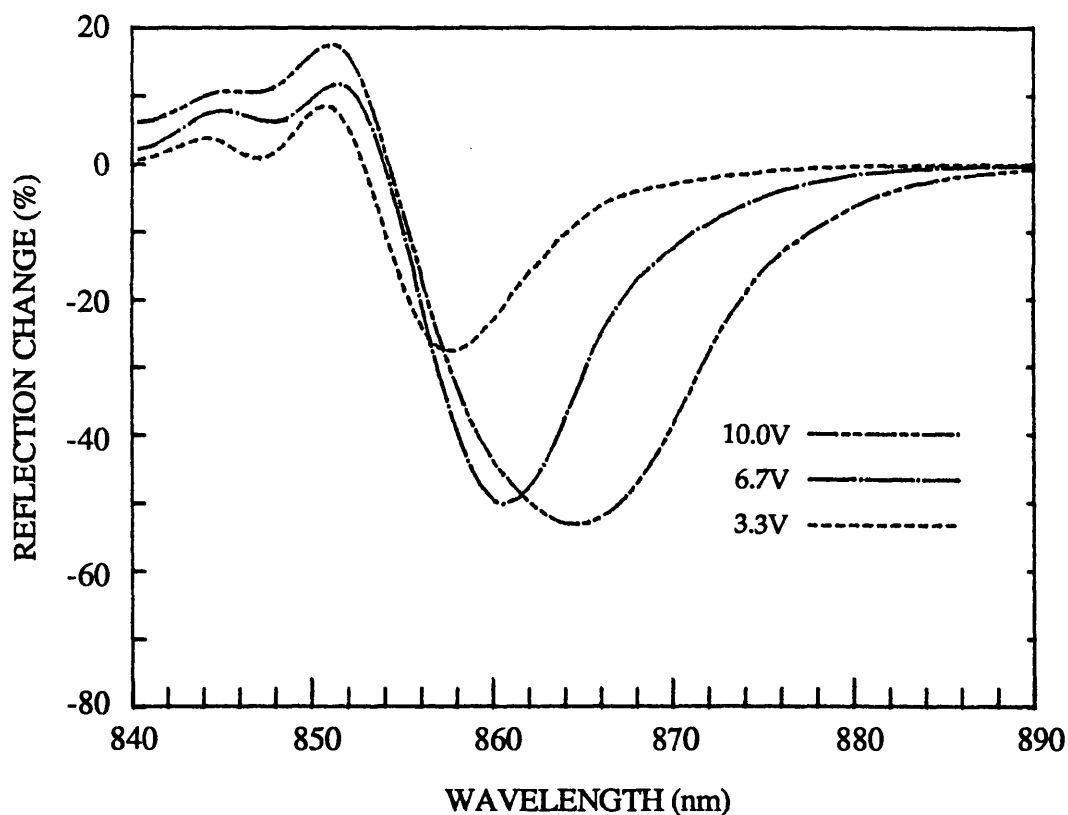


FIGURE 5.4.1.2:
Reflection change spectra for a non-resonant MQW modulator with $R_t = 0.0001$ and $R_b = 0.95$. Derived from Fig. 5.4.1.1.

Above, in Fig. 5.4.1.2, are the reflection change spectra. The maximum value of $\approx -53\%$ occurs at 10V, with a linewidth of over 10nm for a 40% change. We can also achieve a 50% reflection change at 6.7V, but with a smaller 40% linewidth of $\approx 5\text{nm}$.

From the contrast spectra, in Fig. 5.4.1.3 below, it can be seen that although the linewidth is largest for the 10V bias, just as for the reflection changes, the maximum contrast of 4.9dB occurs at 6.7V, with a 4dB linewidth of just under 5nm. At the highest bias the 3dB linewidth is almost 12nm.

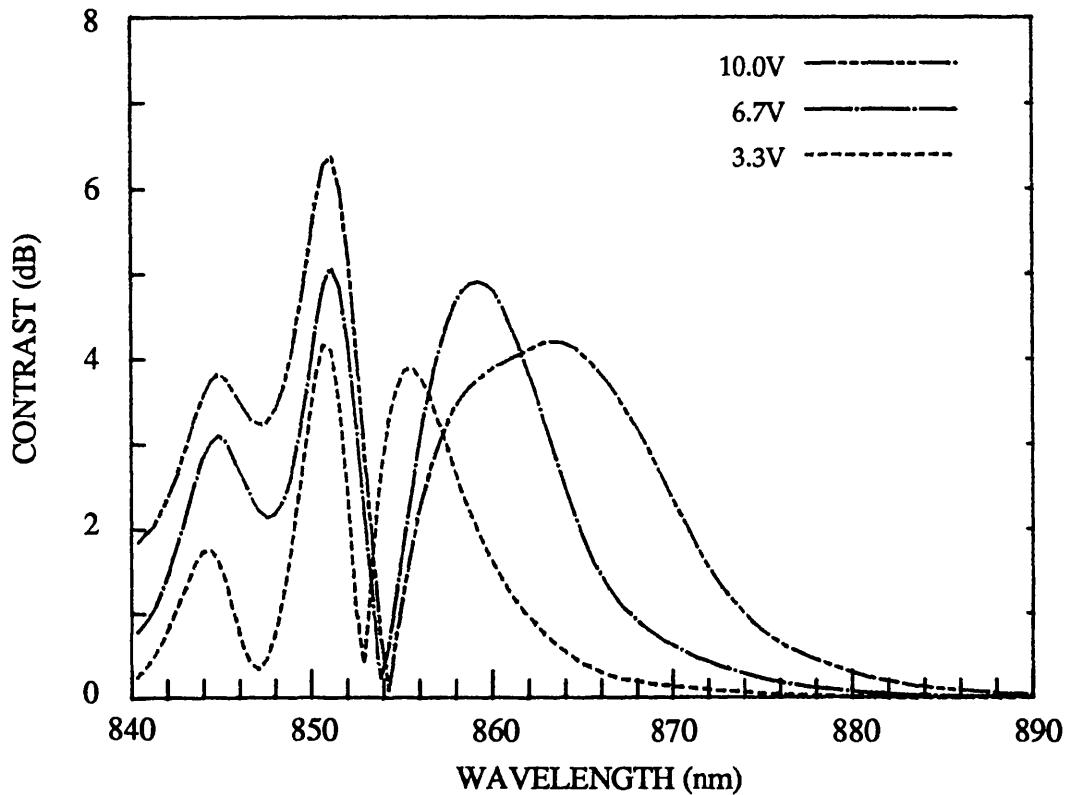


FIGURE 5.4.1.3:
Calculated reflection contrast spectra for a non-resonant MQW modulator with $R_f = 0.0001$ and $R_b = 0.95$. Derived from Fig. 5.4.1.1.

Despite the improvement in performance compared to the transmission modulators, the non-resonant reflection modulator considered here can only offer high contrast approaching 10dB at wavelengths which are undesirable because of the insertion loss. Higher contrast at the biased exciton wavelengths will only be achieved at the expense of thicker MQWs and larger bias voltages. Therefore, we shall now consider whether the modulation can be significantly improved by leaving the original resonance in the structure.

5.4.2 THE UNCOATED (ASYMMETRIC CAVITY) REFLECTION MODULATOR ($R_f = 0.30$, $R_b = 0.95$)

If the basic MQW reflection modulator is not AR-coated on the front surface, then we have an asymmetric FP cavity formed between the air: semiconductor interface at the front and the MLS at the back. The finesse of the cavity, given by Eq. 5.8, is ≈ 5 , which is only twice that of the uncoated transmission modulator. Thus it is unlikely that electro-refractive effects will play a major part in the modulation. However, we could perhaps expect some enhancement in performance, due to multiple pass electro-absorption, compared to the uncoated reflection modulator where there is only a double pass of the light through the MQWs.

There is a striking effect on the reflection spectra, as seen below in Fig. 5.4.2.1. The asymmetric cavity resonance is situated at $\approx 865\text{nm}$, just off the unbiased absorption edge. When biased to 10V the reflection falls to very low values at the centre of a broad resonance. The contrast is now very high and we also have broad-band large reflection changes.

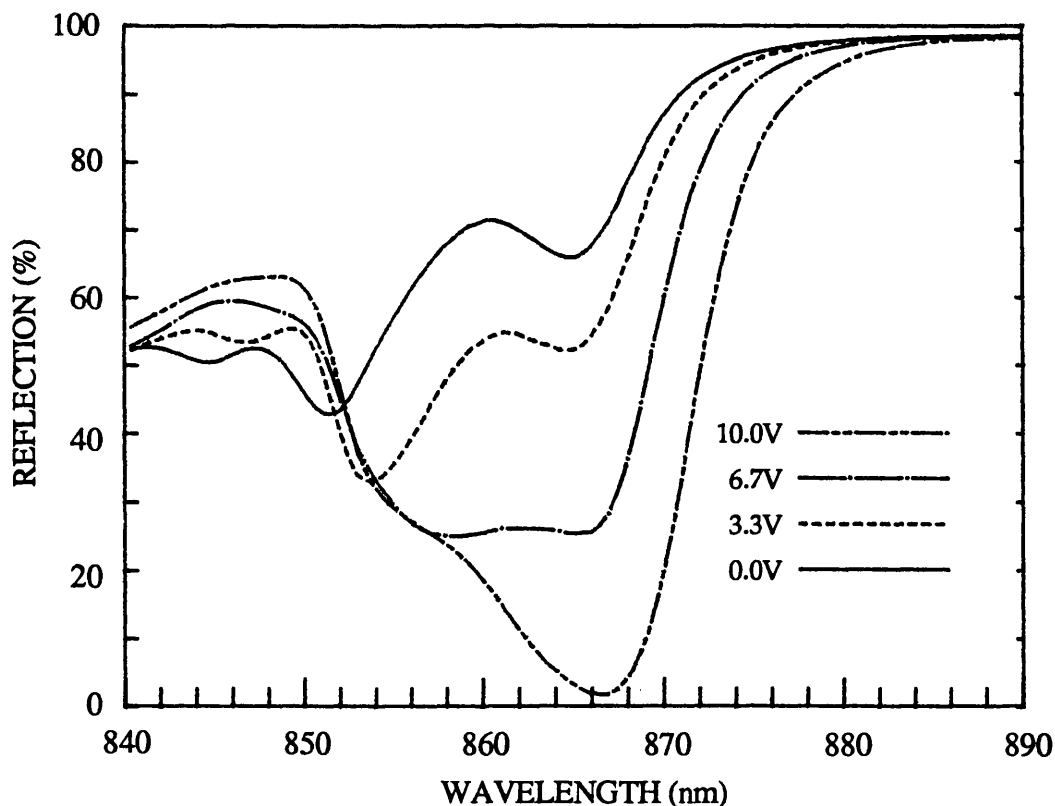


FIGURE 5.4.2.1:

Calculated reflection spectra for an MQW asymmetric FP cavity modulator with $R_f = 0.30$ and $R_b = 0.95$. Device contains $62 \times 100\text{\AA}$ GaAs wells with 60\AA AlGaAs barriers.

The device characteristic cannot simply be ascribed to multiple pass absorption, since the biased reflection is well below that at the unbiased heavy hole exciton (at $\approx 851\text{nm}$), at which we know the absorption coefficient to be significantly larger than that at the biased exciton. It is sufficient here to conclude that a subtle combination of electro-absorption and resonance is responsible for most of the incident light being retained by the cavity. For example, it is known that in the case of the high-finesse FP reflection modulator [8, 9], to be discussed in the next section, absorption at resonance raises the minimum reflection when the cavity is symmetric. The effect here appears to be the exact reverse of this. Absorption is induced at the resonance to "correct" for the asymmetry, and the reflection is lowered. A detailed explanation for the behaviour of this device is given in the next chapter.

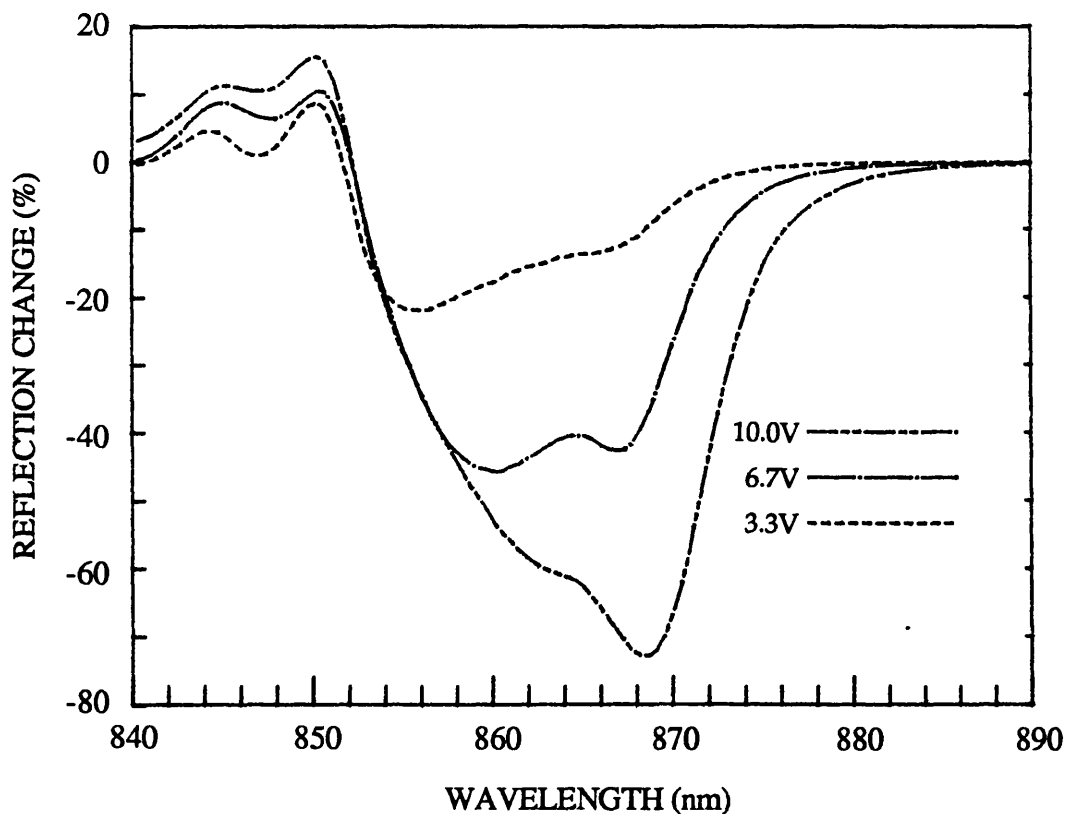


FIGURE 5.4.2.2:

Calculated reflection change spectra for an MQW asymmetric FP cavity modulator with $R_t = 0.30$ and $R_b = 0.95$. Derived from Fig. 5.4.2.1.

Above, in Fig 5.4.2.2, the reflection changes for this asymmetric cavity device are shown. At 10V there is a peak reflection change of $\approx -72\%$, which, incidentally, does not occur at the actual resonant wavelength,

where the biased reflectivity is a minimum and contrast highest, but at a slightly longer wavelength. This is due to a small electro-refractive shift ($< 2\text{nm}$) of the resonance, along with a broadening caused by electro-absorption. The modulation linewidth is more than 6nm for a reflection change of -0.60 . There is no trade-off between reflection change and linewidth when comparing with the previous modulators. For the same linewidth as the non-resonant transmission and reflection modulators, the change here is greater by 0.4 and 0.2 respectively. Insertion loss at this point is less than 1dB , although this would increase if the device were operated at the wavelength of maximum contrast.

Contrast spectra are shown in Fig. 5.4.2.3, with maximum values far higher than seen previously. At the biased resonance the contrast is $\approx 16\text{dB}$, which is an on:off ratio of almost $40:1$. 10dB contrast is achieved over a range of $\approx 4\text{nm}$.

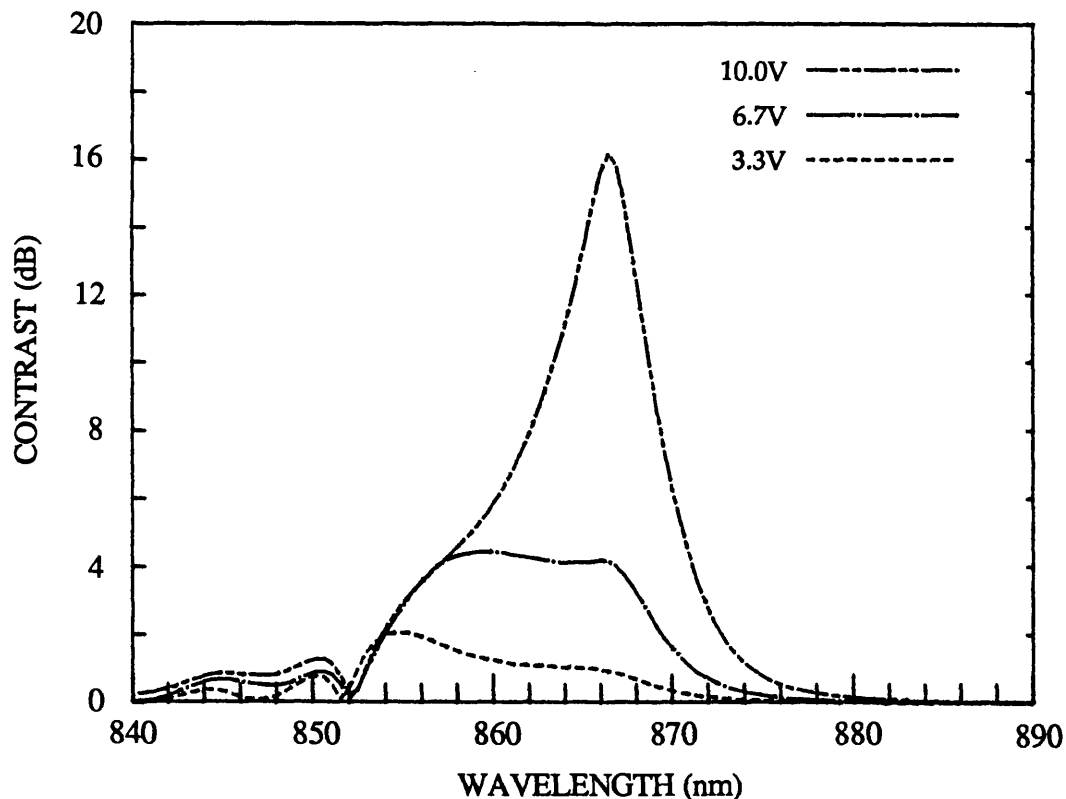


FIGURE 5.4.2.3:
Calculated reflection contrast spectra for an MQW asymmetric FP cavity modulator with $R_f = 0.30$ and $R_b = 0.95$. Derived from Fig. 5.4.2.1.

At both 6.7V and 10V the contrast linewidth for 4dB is greater than 10nm . Since the optimization of the cavity in this case was for the largest reflection change, it is possible that these contrast figures can even be

improved upon by moving the cavity resonance to a wavelength where the biased absorption is stronger.

In subsequent reference to this device we shall call it the AFPM (asymmetric Fabry-Perot cavity modulator).

5.5 HIGH-FINESSE MQW MODULATORS

The devices considered in this final modelling section are intended to utilise the electro-refractive effects in MQWs, avoiding, if possible, the absorptive effects. Unlike all the previous FP cavity devices considered they operate in a normally-off mode, with the reflection increasing at the operating wavelength as the resonance is phase-shifted to a longer wavelength. For convenience we shall generally refer to such devices as SFPMs (*symmetric Fabry-Perot cavity modulators*), even where the mirrors reflectivities are slightly mismatched, since they all exhibit characteristic narrow and deep resonances. MQW SFPMs have recently been investigated experimentally by Simes et al. [8] and Lee et al. [9] with contrast ratios of up to 8:1 being reported.

5.5.1 THE SYMMETRIC CAVITY MODULATOR ($R_f = 0.95$, $R_b = 0.95$)

A look at Eq. A17 in the Appendix shows that if the front and back mirror reflectivities are equal and there is also some background absorption, then the resonant reflection minimum for the FP cavity cannot reach zero. The maximum contrast is thus limited by absorptive effects. For a 10dB contrast ratio, with a maximum 3dB insertion loss (50% minimum on-state), the unbiased reflection minimum must be ≤ 0.05 . For this particular structure the maximum background absorption coefficient (from Eqs. 5.5, 5.6) is therefore $< 240 \text{ cm}^{-1}$. Similarly, Eq. A16 shows that the on-state, which is in the wing of the resonance when phase-shifted with bias, will be reduced by absorption, increasing the insertion loss. Because of this, the optimum wavelength for the SFPM is well away from the unbiased MQW absorption edge, where background absorption is as low as possible (few cm^{-1}) and electro-absorption is minimal. Hence the position of the cavity resonance out beyond 880nm in the reflection spectra of Fig. 5.5.1.1. (next page). Note that the wavelength range is now only 20nm for these figures, and the FWHM of the resonance is reduced to $\approx 1\text{nm}$. At the unbiased resonance the reflection is very close to zero, but as the bias is increased and the resonance shifts to longer wavelength, the reflection minimum rises. This is caused by an increase in the absorption. (The apparent increase in the resonant reflection for the 3.3V spectrum is due to noise in the absorption tail of the data file amplified by

the high finesse of the cavity). Working so far from the MQW absorption edge, the desired electro-refractive effects are significantly reduced, which means that, even at 10V, the resonance only shifts by its own linewidth. Thus the insertion loss will be sensitive to the position of the biased resonance.

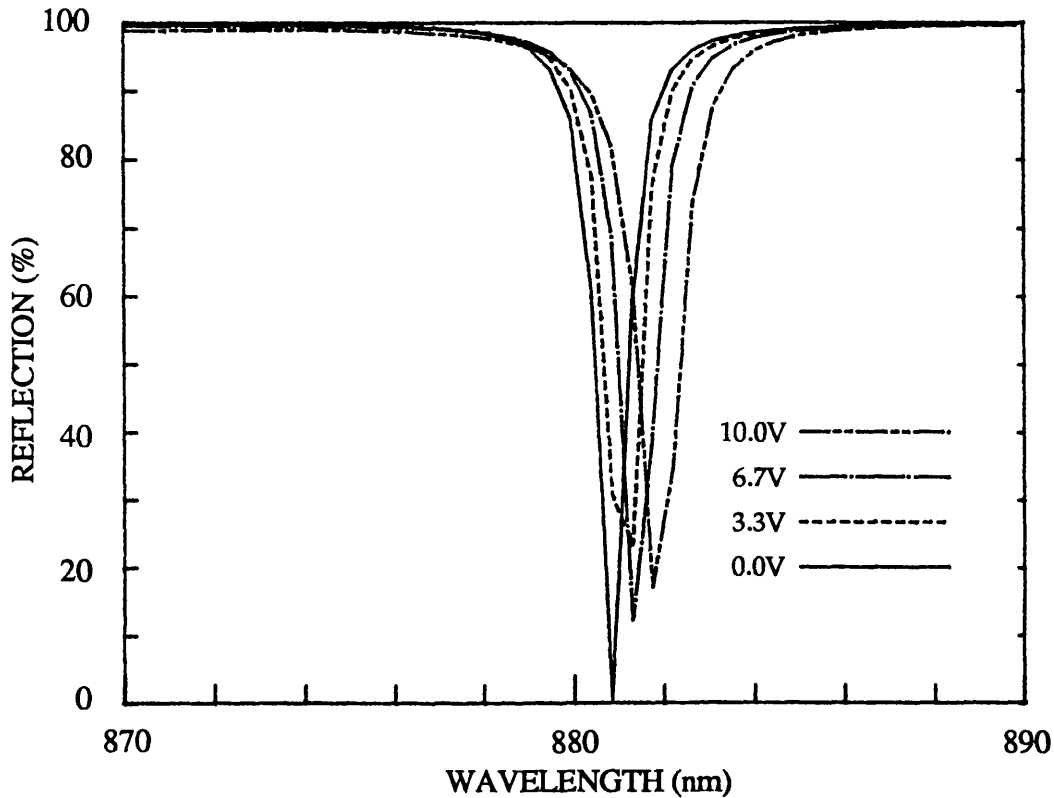


FIGURE 5.5.1.1:

Calculated reflection spectra for a high-finesse symmetric FP cavity MQW modulator with $R_t = 0.95$ and $R_b = 0.95$. Device contains $62 \times 100\text{\AA}$ GaAs wells with 60\AA AlGaAs barriers.

It is clear from Fig. 5.5.1.1 that the SFPM is capable of large modulation, with insertion loss of less than 1dB, provided that absorption at the unbiased resonance can be avoided. However, the most notable feature is the severe narrowing of the modulation linewidth. In Fig. 5.5.1.2 (next page) the reflection change spectra show that although the maximum change at 10V is more than 0.8, the linewidth is only 0.4nm for a change of 0.6. This is 16 times smaller than the corresponding linewidth for the AFPM in the previous section. The same problem occurs with the reflection contrast spectra, also in Fig. 5.5.1.2, where the maximum value is close to 30dB, but the linewidth even as low as 10dB is only 0.4nm – a factor of 6 smaller than that for the AFPM.

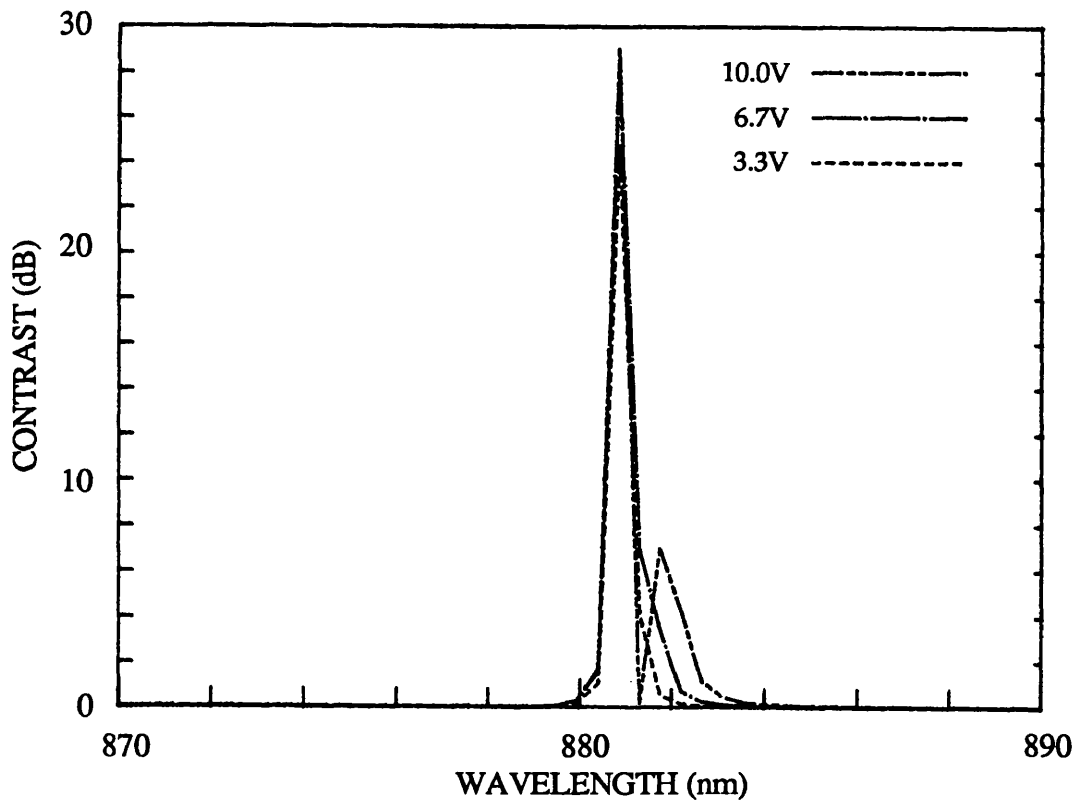
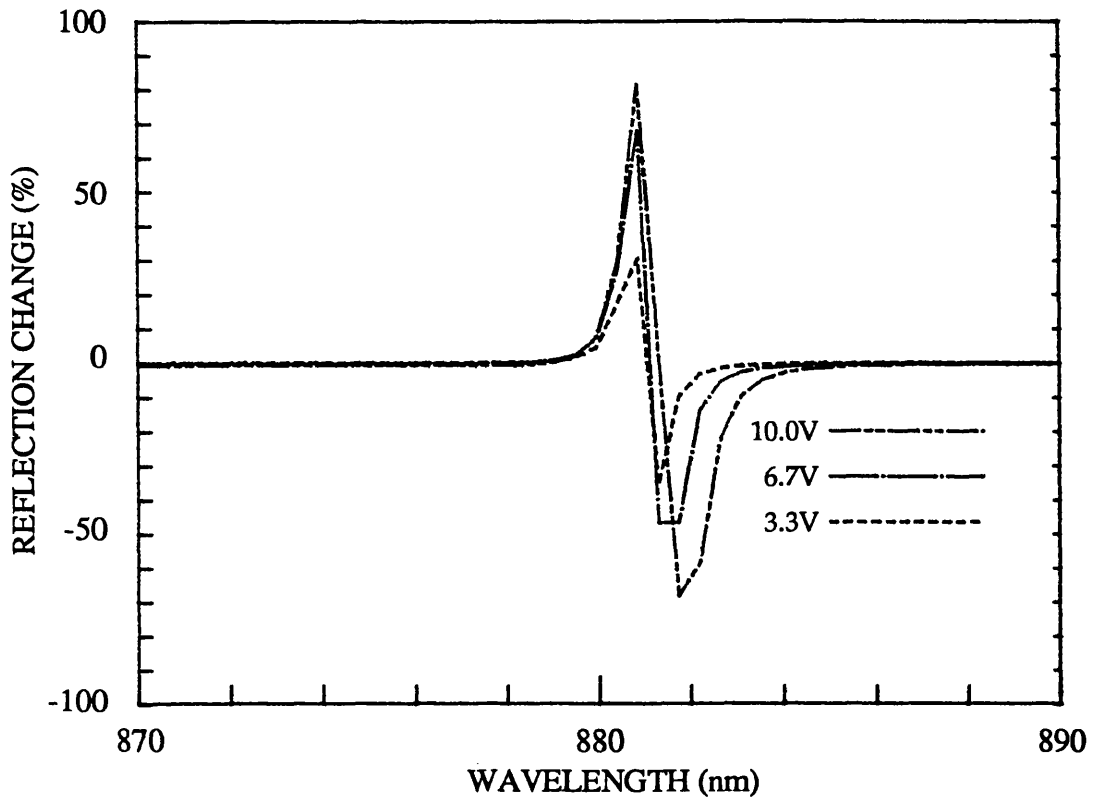


FIGURE 5.5.1.2:
 Calculated spectra of reflection change and contrast for a high-finesse symmetric FP cavity MQW modulator with $R_f = 0.95$ and $R_b = 0.95$. Derived from Fig. 5.5.1.1.

5.5.2 THE ABSORPTION-COMPENSATING CAVITY ($R_f = 0.90$, $R_b = 0.95$)

In order to compensate for background absorption, and achieve high contrast with the high-finesse SFPM operating closer to the MQW absorption edge, where the electro-refractive effects are stronger, a small amount of asymmetry must be introduced into the cavity mirrors. The front reflectivity is lowered relative to the back, so that with a small amount of absorption the effective back reflectivity is reduced to the same level as the front. The cavity is then effectively symmetric again and zero reflectivity at resonance can be obtained.

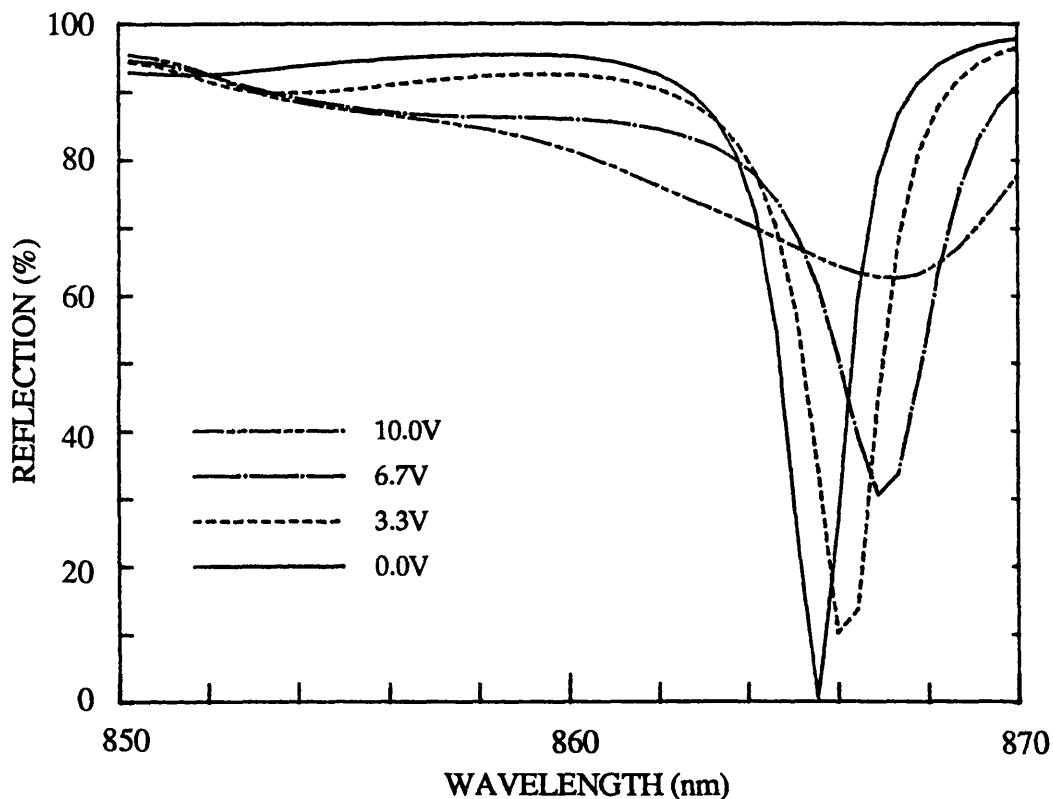


FIGURE 5.5.2.1:

Calculated reflection spectra for a high-finesse, absorption-compensating FP cavity MQW modulator with $R_f = 0.90$ and $R_b = 0.95$. Device contains $62 \times 100\text{\AA}$ GaAs wells with 60\AA AlGaAs barriers.

In this case we have reduced the front reflectivity to 0.90 and the critical absorption coefficient for zero reflection is now $\approx 440 \text{ cm}^{-1}$. Figure 5.5.2.1 shows the reflection spectra, again optimized for maximum reflection change. For a contrast of 10dB with 3dB insertion loss, the background absorption can now be in the range $927 \text{ cm}^{-1} > \alpha > 124 \text{ cm}^{-1}$. With the device operating much closer to the absorption edge, although absorption

is compensated for in the unbiased state, electro-absorptive effects start to increase the insertion loss. In fact, the electro-absorption and electro-refraction are competing against one another. Electro-refraction shifts the resonance to longer wavelengths, thus increasing reflection at the unbiased resonant wavelength, whereas electro-absorption reduces the cavity finesse, thereby broadening the resonance and pulling down the on-state reflection. This can be clearly seen in Fig. 5.5.2.1. The phase shift of the resonance is greater at a given bias than for the previous symmetric cavity, but the biased resonance is strongly broadened and the minimum level raised.

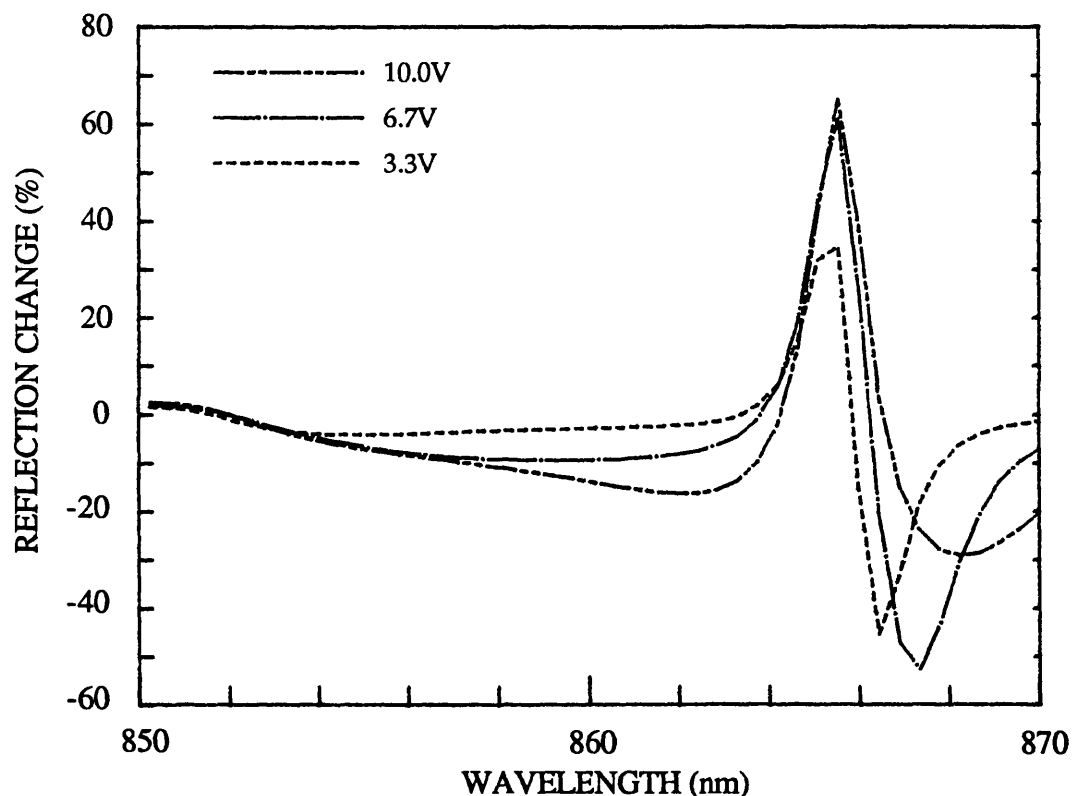


FIGURE 5.5.2.2:

Calculated reflection change spectra for a high-finesse, absorption-compensating FP cavity MQW modulator with $R_t = 0.90$ and $R_b = 0.95$. Derived from Fig. 5.5.2.1.

The reflection change spectra in Fig. 5.5.2.2 show reduced maximum values due to electro-absorptive effects. Hence the linewidth at a reflection change of 0.6 is only $\approx 0.25\text{nm}$ at 10V. It is unlikely that increasing the bias will further increase the reflection changes and contrast since it is the broadening of the resonance which prevents any increase of the on-state reflection beyond 6.7V. Contrast spectra, in Fig. 5.5.2.3 (over page), show the same characteristics as in the previous

section. Peak contrast is more than 20dB, but the linewidth even at 10dB is still rather narrow, being only $\approx 0.6\text{nm}$, despite the reduction in the finesse of the cavity which actually broadens the resonance linewidth at the half-maximum point.

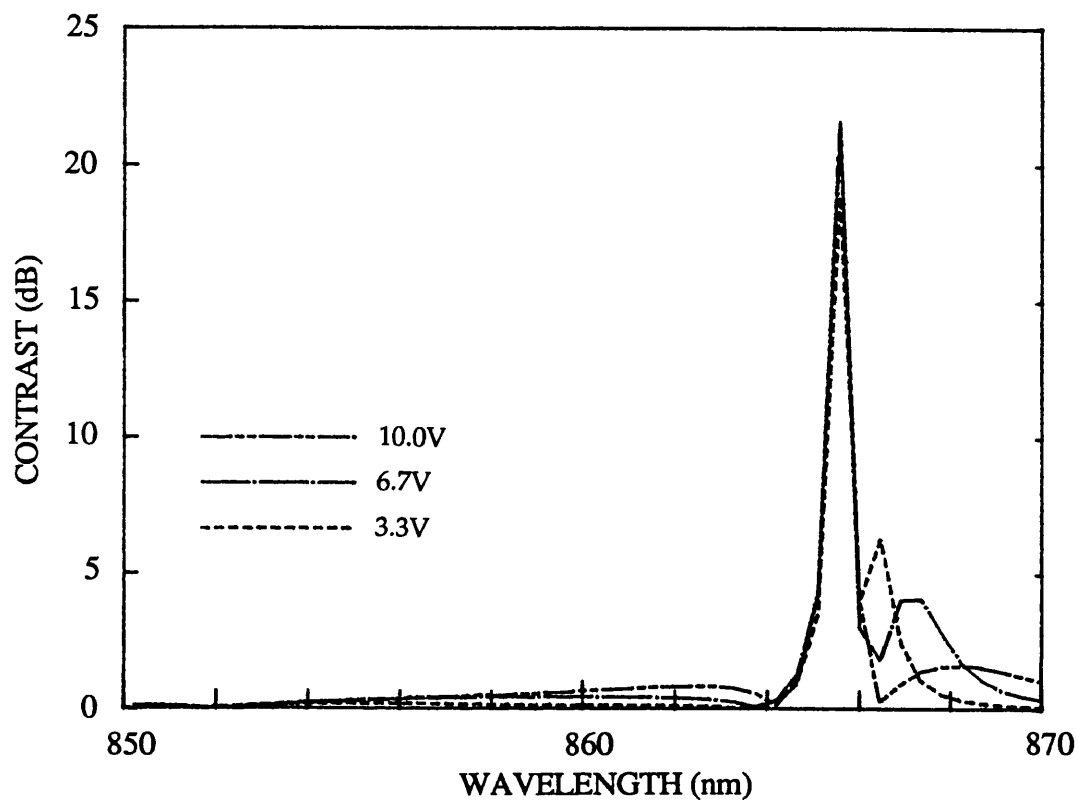


FIGURE 5.5.2.3:

Calculated contrast spectra for a high-finesse, absorption-compensating FP cavity MQW modulator with $R_f = 0.90$ and $R_p = 0.95$. Derived from Fig. 5.5.2.1.

5.6 SENSITIVITY OF FP CAVITY MODULATORS

The use of a resonant cavity to enhance optical modulation brings with it the undesirable side-effects of sensitivity of resonant wavelength to changes in the unbiased refractive index and cavity thickness. Aside from the fundamental dispersion of the refractive index close to the absorption edge and electro-refractive effects, the index will be dependent on the operating temperature of the device, since the band edge will shift with a coefficient of $\approx 3\text{\AA}/\text{K}$ [22, 23]. Assuming that the refractive index is known accurately at a specified operating wavelength, errors in the thickness of the cavity from growth will mean that the device operates at a non-optimum wavelength. Furthermore, variations in the grown thickness of the cavity over the area of a wafer will have the same effect.

Here we make a simple assessment of the tolerance of the AFPM and the absorption-compensating SFPM to fluctuations in temperature and cavity thickness.

If we consider the finesse of the FP cavity, from Eq. 5.8:

$$\mathcal{F} = \frac{\pi\sqrt{F}}{2}$$

The finesse is also defined as : $\frac{\text{Resonance separation}}{\text{Resonance FWHM}} = \frac{\pi}{2(\delta\phi)}$

where $\pm\delta\phi$ is the (half-max.) phase excursion away from the resonance.

Hence, using Eq. 5.3: $\delta\phi = \frac{1}{\sqrt{F}} = \frac{(1-R_\alpha)}{\sqrt{R_\alpha}}$ (5.9)

Clearly the phase shift of the cavity resonance by \pm half the resonance width ($\delta\phi$), relative to the input wavelength, will destroy the device performance. Eq. 5.9 thus gives us a limit which must not even be approached if the device is to operate at the desired wavelength in a stable manner. From Eq. 5.7, we can substitute into Eq. 5.9 to obtain a critical thickness fluctuation, δL_{crit} , for which the cavity reflection will rise from zero to half-maximum level, i.e.:

$$\delta L_{\text{crit}} = \frac{\lambda}{4\pi n} \left(\frac{1-R_\alpha}{\sqrt{R_\alpha}} \right) \quad \text{.....(5.10)}$$

There is also the corresponding critical refractive index change, δn_{crit} , given by:

$$\delta n_{\text{crit}} = \frac{\lambda}{4\pi L} \left(\frac{1 - R_{\alpha}}{\sqrt{R_{\alpha}}} \right) \quad \dots(5.11)$$

The variation of refractive index with temperature in MQW waveguides close to the absorption edge has been studied recently by Sonek & Chen [23], who found, for a temperature range 285-305K:

$$\frac{\partial n}{\partial T} \approx 7.5 \times 10^{-4} \quad \dots(5.12)$$

This gives a critical temperature variation:

$$\delta T_{\text{crit}} = \frac{1333\lambda}{4\pi L} \left(\frac{1 - R_{\alpha}}{\sqrt{R_{\alpha}}} \right) \quad \dots(5.13)$$

Assuming a resonant wavelength of 870nm, and a mean cavity index, n , of 3.37, the corresponding cavity thickness, L , for 20 half-wavelengths is 2.5816 μm . Below in Table 5.1, we have calculated δL_{crit} and δT_{crit} for two cases. The first is the absorption-compensating SFPM in the unbiased state, the second is the AFPM in the biased state. In both cases the resonant reflection is made as close as possible to zero by including in the term R_{α} (Eq. 5.6) the critical value of αd which reduces Eq. 5.5 to zero. (See § 6.2.1 for discussion). Thus we are considering the state which determines high contrast for the two devices.

TABLE 5.1:
Comparison of the sensitivity of FP cavity modulators to thickness and temperature.

Device	R_f	R_b	$\alpha d_{R=0}$	R_{α}	$\delta L_{\text{crit}} (\text{\AA})$	$\delta T_{\text{crit}} (\text{K})$
SFPM	0.90	0.95	0.027	0.90	± 22	± 3.8
AFPM	0.30	0.95	0.576	0.30	± 262	± 45.7

These conditions already look rather imposing, especially for the SFPM. The allowed growth tolerance is only about 0.1% of the cavity thickness¹ for the SFPM, and still only $\approx 1\%$ even for the AFPM. This accuracy in

¹ After this work was completed, a paper by Yan et al. [24] appeared in print. The authors arrive at very much the same conclusions that have been put forward here and in the previous section, concerning the tolerable background absorption and cavity thickness fluctuations for viable operation of SFPMs.

calibration and cross-wafer uniformity is at present not attainable. It is known, however, that small areas on a wafer have had the correct cavity thickness so as to be able to demonstrate the SFPM device [8,9], albeit with degraded performance due to background absorption. For the AFPM the usable areas should be somewhat larger.

The temperature limits again look problematic for the SFPM, but more encouraging here for the AFPM. Note that this calculation does not include the effect of temperature on the background absorption at the resonant wavelength, which for the SFPM will certainly increase the off-state reflection.

Now suppose we enforce the more stringent requirement that the phase shift is limited such that the off-state reflection does not rise above 0.05, in which case the device should still be capable of ≈ 10 dB contrast. Again assume that the condition $B=0$ (Eq. 5.5) is still satisfied. For small phase deviations, $\delta\phi$, around the resonance, Eq. 5.2 becomes:

$$R \approx \frac{F(\delta\phi)^2}{1 + F(\delta\phi)^2} \quad \dots(5.14)$$

Inserting $R \leq 0.05$ (for 10dB contrast) into Eq. 5.14 gives the result:

$$\delta\phi_{10dB} \leq \frac{1}{4.36\sqrt{F}} \quad \dots(5.15)$$

So, comparing Eqs. 5.9 & 5.15, to maintain the high performance of the modulator the permitted thickness and temperature variations are less than 1/4 of the limits in Table 5.1, which suggests that even if the operating temperature could be accurately controlled to ± 1 K or better, the yield of SFPM devices per wafer would be very uneconomic, with uniformity to better than 2 monolayers being required. The AFPM appears to be the only real prospect for a high-contrast, normal-incidence MQW modulator, with $\pm 60\text{\AA}$ thickness variation allowed and a temperature range of ± 10 K, but, even for this device, the engineering needed is quite daunting.

5.7 SUMMARY

The purpose of this chapter has been to consider the benefits to be had by deliberately incorporating FP resonance into a normal-incidence MQW modulator. The model used is simple but effective. The emphasis is on the effects of electro-absorption and electro-refraction occurring within the MQW active region when combined with a single cavity resonance close to the absorption edge, instead of attempting to model the complete spectral response of the multilayer structure, which requires knowledge of the refractive index dispersion and a transfer matrix approach.

The calculated performance figures for the range of transmission and reflection modulators investigated here are collected in Table 5.2 below.

TABLE 5.2:

The maximum calculated modulation for various types of GaAs MQW FP cavity modulators. The MQW structure is fixed at $62 \times 100\text{\AA}$ wells with 60\AA barriers. I.L. is the insertion loss. @ Δ and @C are the levels at which the linewidth is measured for T/R change and contrast respectively.

R_f	R_b	$\Delta_{\max}(T/R)$	$\Delta\lambda(\text{nm})$	@ Δ	I.L.(dB)	$C_{\max}(\text{dB})$	$\Delta\lambda(\text{nm})$	@C	Bias(V)
0.0001	0.30	-0.263(T)	6.0	-0.20	1.73	2.42	4.8	2	6.7
0.01	0.30	-0.293(T)	6.5	-0.20	1.35	2.51	5.0	2	6.7
0.30	0.30	-0.484(T)	4.6	-0.40	0.35	3.24	3.8	3	10.0
0.0001	0.95	-0.500(R)	5.4	-0.40	1.30	4.90	4.8	4	6.7
0.30	0.95	-0.727(R)	6.5	-0.60	0.97	11.0	4.2	10	10.0
0.30	0.95	-0.670(R)	6.5	-0.60	1.55	16.1	4.2	10	10.0
0.95	0.95	+0.811(R)	0.4	+0.60	0.86	29.0	0.7	10	10.0
0.90	0.95	+0.567(R)	0.5	+0.50	1.91	21.5	0.6	10	6.7

Modelled characteristics for low finesse transmission modulators reproduce previous experimental results well, and we have shown that by not AR coating the front surface of such devices, and with careful control of the cavity thickness, the maximum transmission change may be increased by a factor of ≈ 1.8 compared to the non-resonant device, with a significant improvement in the insertion loss.

For a more robust device, however, the reflection mode of operation is preferred, so that the opaque GaAs substrate need not be removed from the window area. We have assessed two types of reflection modulator here. The "obvious" high-finesse SFPM structure, as we have called it, certainly appears to be capable of contrast in excess of 20dB and maximum reflection changes between 0.60-0.80 for $\approx 10V$ bias. The modulation in this case is achieved by using the electro-refractive effect, which accompanies the enhance MQW electro-absorption, to induce a red-shift of a deep FP resonance away from the unbiased resonant wavelength. However, we have noted how sensitive the operation of this device is likely to be to background absorption (off-state), electro-absorption (on-state/insertion loss), cavity thickness inaccuracies (off-state) and thermal effects on the refractive index (off-state). For uniform operation of the SFPM, giving $\approx 10dB$ contrast with high yields per wafer, the cavity thickness fluctuations must be below $\approx 5\text{\AA}$ (< 2 monolayers, or $\approx 0.02\%$ of the total device thickness), with temperature stabilized to better than $\pm 1K$.

An interesting and novel alternative to the use of the electro-refractive effect within a high-finesse SFPM is to revert to the electro-absorptive effect in an asymmetric cavity – the so-called AFPM. The construction of this cavity is much simpler than for the SFPM, since the accurate matching (or mismatching) of front and back reflectivities to accommodate background absorption and minimize the off-state is not required. Because of the asymmetry in its mirror reflectivities, the AFPM operates in a normally-on mode, as opposed to the normally-off mode for the SFPM. Electro-absorption is then used to reduce the reflectivity at resonance to levels close to zero, thereby achieving high contrast. Without optimizing the calculations for highest contrast the AFPM appears to be capable of more than 15dB, with a 10dB linewidth which is six times that for the SFPM. Maximum reflection changes are also comparable with those for the SFPM, in this case with more than *sixteen* times the linewidth (6.4nm cf 0.4nm). The AFPM is intrinsically a low-finesse device, even more so in the biased state, and therefore should be less sensitive to the factors stated above which seriously mar the potential performance of the SFPM. We estimate a cavity thickness fluctuation tolerance of about $\pm 60\text{\AA}$, with a stable temperature range of $\approx \pm 10K$.

REFERENCES (Chapter 5)

- [1] T. Y. HSU, W. Y. WU and U. EFRON, "Amplitude and phase modulation in a 4 μ m-thick GaAs/AlGaAs multiple quantum well modulator", *Electron. Lett.* (1988), **24**, pp. 603-4.
- [2] S. TARUCHA, H. IWAMURA, T. SAKU and H. OKAMOTO, "Waveguide-type optical modulator of GaAs quantum well double heterostructures using electric field effect on exciton absorption", *Jpn. J. Appl. Phys.* (1985), **24**, pp. L442-4.
- [3] T. H. WOOD, C. A. BURRUS, R. S. TUCKER, J. S. WEINER, D. A. B. MILLER, D. S. CHEMLA, T.C. DAMEN, A. C. GOSSARD and W. WIEGMANN, "100ps waveguide multiple quantum well (MQW) optical modulator with 10:1 on/off ratio", *Electron. Lett.* (1985), **21**, pp. 693-4.
- [4] J. E. ZUCKER, T. L. HENDRIKSON and C. A. BURRUS, "Low-voltage phase modulation in GaAs/AlGaAs quantum well optical waveguides", *Electron. Lett.* (1988), **24**, pp. 112-3.
- [5] P. J. BRADLEY, M. WHITEHEAD, G. PARRY, P. MISTRY and J. S. ROBERTS, "Effect of device length and background doping on the relative magnitudes of phase and amplitude modulation in GaAs/AlGaAs PIN multiple quantum well waveguide optical modulators", *Appl. Opt.* (1989), **28**, pp. 1560-4. See also P. J. BRADLEY, Ph.D. Thesis, University of London 1989.
- [6] D. R. P. GUY, N. APSLEY, L. L. TAYLOR and S. J. BASS, "Theory of an electro-optic modulator based on quantum wells in a semiconductor étalon", *SPIE Proc.* (1987), **792** (Quantum Well and Superlattice Physics), pp. 189-96.
- [7] D. R. P. GUY and N. APSLEY, "Optical devices using III-V quantum wells and multilayers", *SPIE Proc.* (1987), **861** (Quantum Wells in and Superlattices in Optoelectronic Devices and Integrated Optics), pp. 27-32.
- [8] R. J. SIMES, R. H. YAN, R. S. GEELS, L. A. COLDREN, J. H. ENGLISH, A. C. GOSSARD and D. G. LISHAN, "Electrically tunable Fabry-Perot mirror using multiple quantum well index modulation", *Appl. Phys. Lett.* (1988), **53**, pp. 637-9.
- [9] Y. H. LEE, J. L. JEWELL, S. J. WALKER, C. W. TU, J. P. HARBISON and L. T. FLOREZ, "Electrodispersive multiple quantum well modulator", *Appl. Phys. Lett.* (1988), **53**, pp. 1684-6.
- [10] J. S. WEINER, D. A. B. MILLER and D. S. CHEMLA, "Quadratic electro-optic effect due to the quantum-confined Stark effect in quantum wells", *Appl. Phys. Lett.* (1987), **50**, pp. 842-4.
- [11] H. C. CASEY Jr, D. D. SELL and M. B. PANISH, "Refractive index of Al_xGa_{1-x}As between 1.2 and 1.8eV", *Appl. Phys. Lett.* (1974), **24**, pp. 63-5.

- [12] A. N. PIKHTIN and A. D. YASKOV, "Dispersion of the refractive index of semiconducting solid solutions with the sphalerite structure", *Sov. Phys. Semicond.* (1980), **14**, pp. 389-92.
- [13] M. GLICK, D. PAVUNA and F. K. REINHART, "Electro-optic effects and electroabsorption in a GaAs/AlGaAs multi-quantum-well heterostructure near the band gap", *Electron. Lett.* (1987), **23**, pp. 1235-7.
- [14] See for example H. A. McLEOD, "Thin film optical filters", Ch. 5 "Multilayer high-reflectance coatings", pp. 88-110, Adam Hilger 1970.
- [15] D. ATKINSON and M. WHITEHEAD, unpublished calculations and measurements.
- [16] T. H. WOOD, C. A. BURRUS, D. A. B. MILLER, D. S. CHEMLA, T. C. DAMEN, A. C. GOSSARD and W. WIEGMANN, "High speed optical modulation with GaAs/GaAlAs quantum in a *p-i-n* diode structure", *Appl. Phys. Lett.* (1984), **44**, pp. 16-18.
- [17] M. WHITEHEAD, P. STEVENS, A. RIVERS, G. PARRY, J. S. ROBERTS, P. MISTRY, M. PATE and G. HILL, "Effects of well width on the characteristics of GaAs/AlGaAs multiple quantum well electroabsorption modulators", *Appl. Phys. Lett.* (1988), **53**, pp. 956-8.
- [18] K. W. JELLEY and R. W. H. ENGELMANN, "An etch tunable antireflection coating for the controlled elimination of Fabry-Perot oscillations in the optical spectra of transverse modulator structures", *IEEE Photon. Technol. Lett.* (1989), **1**, pp.235-7.
- [19] R. B. BAILEY, R. SAHAI and C. LASTUFKA, "1 x 16 arrays of GaAs/ AlGaAs multiple quantum well optical modulators with 26:1 contrast", Post-deadline paper PD1, OSA Meeting "Quantum Wells for Optics and Optoelectronics", Salt Lake City, UT, U. S.A., Mar. 6-8th 1989.
- [20] J. P. VAN der ZIEL and M. ILEGEMS, "Multilayer GaAs-Al_{0.3}Ga_{0.7}As dielectric quarter wave stacks grown by molecular beam epitaxy", *Appl. Opt.* (1975), **14**, pp. 2627-30.
- [21] G. D. BOYD, D. A. B. MILLER, D. S. CHEMLA, S. L. McCALL, A. C. GOSSARD and J. H. ENGLISH, "Multiple quantum well reflection modulator", *Appl. Phys. Lett.* (1987), **50**, pp. 1119-21.
- [22] J. M. HALLEY, P. WHEATLEY, M. WHITEHEAD and J. E. MIDWINTER, "Thermal crosstalk in multi-quantum well optical logic arrays", Paper 3, IEE Colloquium "Multi-quantum well devices -Physics, engineering and applications", IEE, London WC2, England, 8th Dec. 1986.
- [23] G. J. SONEK and Y. J. CHEN, "Effect of temperature variations on optical waveguiding in GaAs multiple quantum wells", *IEEE J. Lightwave Technol.* (1989), **LT-7**, pp. 1130-35.

- [24] R. H. YAN, R. J. SIMES and L. A. COLDREN, "Analysis and design of surface-normal Fabry-Perot electro-optic modulators", *IEEE J. Quantum Electron.* (1989), QE-25, pp. 2272-79.

MQW ASYMMETRIC FABRY-PEROT CAVITY MODULATORS

6.1 Introduction

6.2 Theory of Operation of the AFPM

6.2.1 The Fabry-Perot Equations in the AFPM Limit

6.2.2 Absorption Limits for AFPM Operation

6.3 Modelling of AFPM Performance

6.3.1 Limits to Contrast and Operating Voltage

6.3.2 Sensitivity of Contrast to Operating Wavelength

6.4 Initial Demonstration of an AFPM

6.4.1 Device Construction

6.4.2 Experimental Results

6.4.3 Comparison with Modelled Spectra

6.5 Multilayer Stack Reflectors for an Integrated AFPM

6.5.1 Design of Multilayer Stack (MLS) Reflectors

6.5.2 The Integrated AFPM Structure

6.5.3 MLS Reflectors Grown by MOVPE

6.6 The Integrated AFPM

6.6.1 Design and Fabrication of the Integrated AFPM (CB145)

6.6.2 Reflection Modulation Measurements on the Integrated AFPM (CB145)

6.7 Summary

6.7.1 Measured AFPM Performance

6.7.2 Future Considerations for AFPM Design and Operation

6.1 INTRODUCTION

We saw in Chapter 5 that an optical modulator based on MQW electro-optic effects within a high-finesse symmetric Fabry-Perot (FP) cavity – the SFPM – should offer very high contrast operation (in excess of 20dB in reflection). The penalty paid for use of high-finesse cavities is the extremely narrow linewidth over which the devices work. Typically, 10dB contrast can be achieved over only $\approx 0.5\text{nm}$, with ΔR in the 60–80% range, depending on the actual mirror reflectivities chosen.

A further conclusion from the previous chapter is that there appears to be an alternative to the high-finesse device, which we refer to as an asymmetric FP cavity modulator (AFPM). Only one high reflector is employed in this case at the back surface – the front mirror is conveniently defined by the air:semiconductor interface with a reflectivity of ≈ 0.3 .

A comparison of the characteristics of the SFPM with those of the AFPM is summarized schematically in Figure 6.1.1 (over page), which emphasises the difference in optical bandwidth and operating characteristics – the SFPM being normally-off (unbiased), whereas the AFPM is normally-on. With the latter type of device we show that, by using resonant electro-absorption rather than electro-refraction, we can in principle achieve high on:off ratios at bias voltages below 5V, with low insertion loss ($<3\text{dB}$) and therefore large absolute reflectivity changes. According to our modelling, this type of device offers roughly the same maximum contrast as the high-finesse device, but with much broader optical bandwidth because of the low cavity finesse. With an optimized AFPM structure we predict that the 10dB contrast linewidth should be $\approx 8\text{nm}$ with reflection changes of 40-50% over the same range.

In this penultimate chapter we shall investigate the AFPM in detail both theoretically and experimentally. Firstly, we discuss the simple theoretical basis for the AFPM characteristics and the likely modulation limits of the device. Then we demonstrate the device concept experimentally with an adapted MQW transmission modulator, having an evaporated gold back reflector. A more viable AFPM requires the integration of a multilayer quarter-wave stack as the high reflectivity mirror. We conclude with the design and experimental demonstration of both the reflector stack and the fully integrated AFPM.

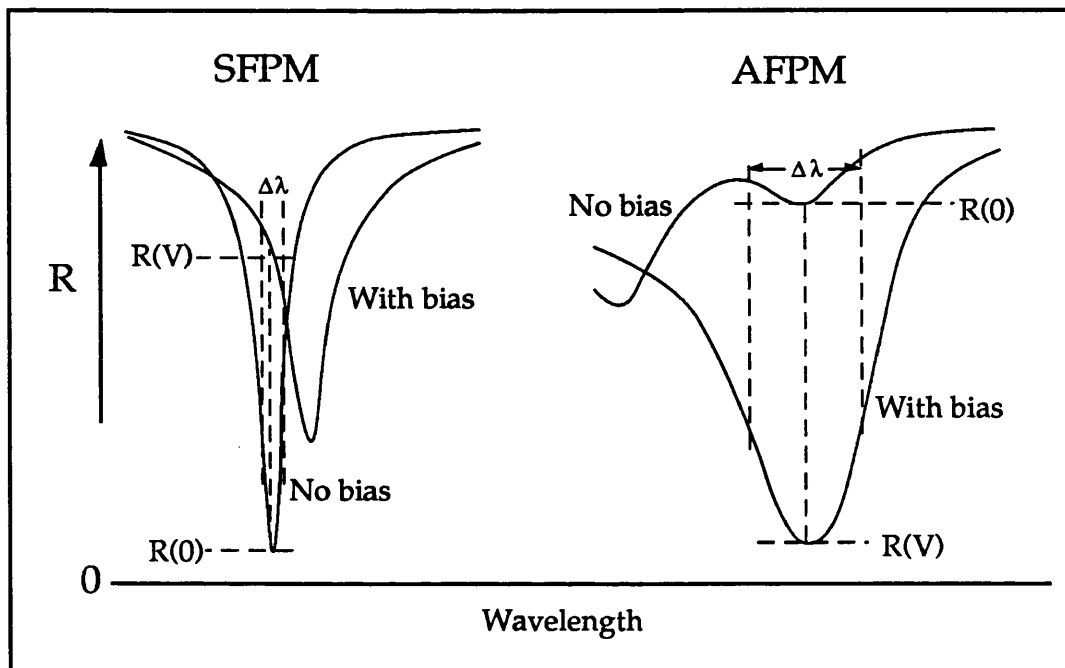


FIGURE 6.1.1:

A schematic of the biased and unbiased spectra for the high-finesse symmetric FP cavity modulator (SFPM) and the low-finesse asymmetric FP cavity modulator (AFPM). $\Delta\lambda$ is the linewidth for significant modulation – in this case reflection change.

6.2 THEORY OF OPERATION OF THE AFPM

6.2.1 THE FABRY-PEROT EQUATIONS IN THE AFPM LIMIT

The net reflection from an absorptive FP cavity is given in the Appendix as:

$$R = \frac{(B + F \sin^2 \phi)}{(1 + F \sin^2 \phi)} \quad \dots(6.1)$$

where the terms B and F are given by Eqs. 5.5 and 5.3 respectively.

On resonance the $\sin^2 \phi$ terms go to zero, so the reflection reduces simply to $R = B$, with B a function of the front and back reflectivities, R_f and R_b and internal transmission of the cavity, $\exp(-\alpha d)$, only, i.e.

$$B = \frac{R_f [1 - (R_\alpha / R_f)]^2}{(1 - R_\alpha)^2} \quad \dots(6.2)$$

$$\text{where } R_\alpha = \sqrt{R_f R_b} e^{-\alpha d} \quad \dots(6.3)$$

To obtain the highest contrast in reflection we must bring R as close to zero as possible using the resonant absorption in either the biased or unbiased state of the device. If the device operates in the bias absorbing mode, at a wavelength off the unbiased absorption edge, then the values we choose for the mirror reflectivities can still determine whether the high absorption state is the low reflection state or vice versa. In general the more unequal the two mirror reflectivities, the higher the net cavity reflection at resonance in the low absorption state.

By inspection we can see immediately from Eq. 6.2 that there is a solution which makes B, and thus the resonant reflection, equal to zero. This occurs when $R_\alpha = R_f$. Inserting this solution into Eq. 6.3 gives us the critical value for αd to achieve zero reflection.

$$\alpha d_{R=0} = \frac{1}{2} \ln(R_b / R_f) \quad \dots(6.4)$$

For the AFPM, as in § 5.4.2, we have $R_f = 0.30$, $R_b = 0.95$, so the critical αd value for this structure is ≈ 0.58 . This is the maximum *change* in αd needed to achieve zero reflection, since the minimum absorption possible

for what would be the device on-state is obviously zero. We have already seen in Chapters 3 & 4 that absorption changes of this order are achievable using GaAs-AlGaAs MQWs. For example, if we extrapolate from Table 4.1, a structure similar to CPM405, but with ≈ 70 quantum wells rather than 60, would provide the necessary $\Delta\alpha d$ factor.

If we now consider the insertion loss for the AFPM structure, which is determined by the on state reflection, by a straightforward manipulation of the standard FP equations (see Appendix) it is possible to express the reflection at resonance for a non-absorbing cavity as follows:

$$R_{\min}(\phi = 0, \alpha = 0) = \frac{(\sqrt{R_f} - \sqrt{R_b})^2}{(1 - \sqrt{R_f R_b})^2} \quad \dots(6.5)$$

Again putting in the relevant mirror reflectivities for the AFPM, we find that the maximum on-state reflection is ≈ 0.84 . Thus we can in principle get simultaneous high contrast (theoretically infinite) and low insertion loss, and therefore very large reflection changes. This explains the modelled results of § 5.4.2.

The essence of the AFPM characteristic can be understood if we think of the device as having voltage-tunable back mirror reflectivity, due to the effect of the applied electric field on the MQW absorption. In the unbiased state absorption is low, the back mirror reflectivity is much larger than that of the front, so complete destructive interference between light reflected from the front surface (without entering the cavity) and that reflected from the back cannot occur. When bias is applied, the absorption in the cavity increases, reducing the amplitude of the light passing through the cavity. Given the correct amount of attenuation we can achieve destructive interference and complete cancellation of the net intensity reflected from the cavity. Another way to think about it is that the absorption is used to make the asymmetric cavity equivalent to a symmetric one with no absorption, in which case the net reflection must fall to zero at resonance. Furthermore, the biased resonance will be broad, resembling that for a low finesse cavity with $R_f = 0.30$, $R_b \approx 0.30$.

Finally, as a parallel to the above, Wherrett [1] has previously carried out a theoretical optimization of Fabry-Perot cavities for high-contrast optical bistable switching, where the modulation mechanism is the rather different one of non-linear refraction close to the band edge of a semiconductor. He concluded that operating in reflection with an

asymmetric cavity (with mirrors close to the AFPM specification) is the most efficient means of compensating for unwanted background absorption and achieving high contrast or large reflection changes. This was confirmed experimentally by Miller et al. [2] in experiments on CdHgTe étalons coated on one side with gold.

6.2.2 ABSORPTION LIMITS FOR AFPM OPERATION

We have derived in Eq. 6.4 the condition for theoretically infinite contrast with an AFPM. More important for useful device operation than achieving $R=0$ is that high contrast should not be extremely sensitive to the amount of absorption which can be field-induced at the operating wavelength. The modulator should be able to work with a range of absorption to allow some tolerance in the design and fabrication.

In Figure 6.2.2.1 we have plotted Eq. 6.2 for $R_f=0.30$, $R_b=0.95$ and for αd in the range 0 to 1, in order to find the limits for which the AFPM will achieve a certain contrast. We have also included the corresponding curve for $R_f=0.30$, $R_b=0.85$ to illustrate the effect of variation in the back mirror reflectivity. For the two curves we see, as expected, a rapid fall towards zero at αd_{crit} – the minimum R is limited by being calculated at discrete points. The first point to note is that lowering R_b by 10% only changes αd_{crit} by a similar amount.

If we set a lower limit of 50% for the on state reflection of the AFPM (equivalent to a maximum insertion loss of 3dB), then we find that the standard AFPM will tolerate an unbiased αd of ≈ 0.08 . To put this into perspective, this represents an absorption coefficient of $\approx 1500\text{cm}^{-1}$ in an MQW structure such as CPM405 of Chapter 4, containing $\approx 60 \times 90\text{\AA}$ quantum wells. Thus we should be able to operate close to the MQW absorption edge and obtain strong modulation at low bias.

The main effect of R_b being reduced to 0.85 is seen in the upper limit on αd for 3dB insertion loss, which is reduced by a factor of 4 compared to the standard AFPM case. Even at the limit of zero absorption the resonant reflection is only 0.57. An AFPM device with lower than normal back reflectivity will have to be operated further away from the MQW absorption edge in order to reduce insertion loss, and thus will require higher bias voltages to shift the necessary amount of absorption into the operating wavelength. It is therefore important that the

reflectivity of the back mirror is made as high as possible to minimize insertion loss.

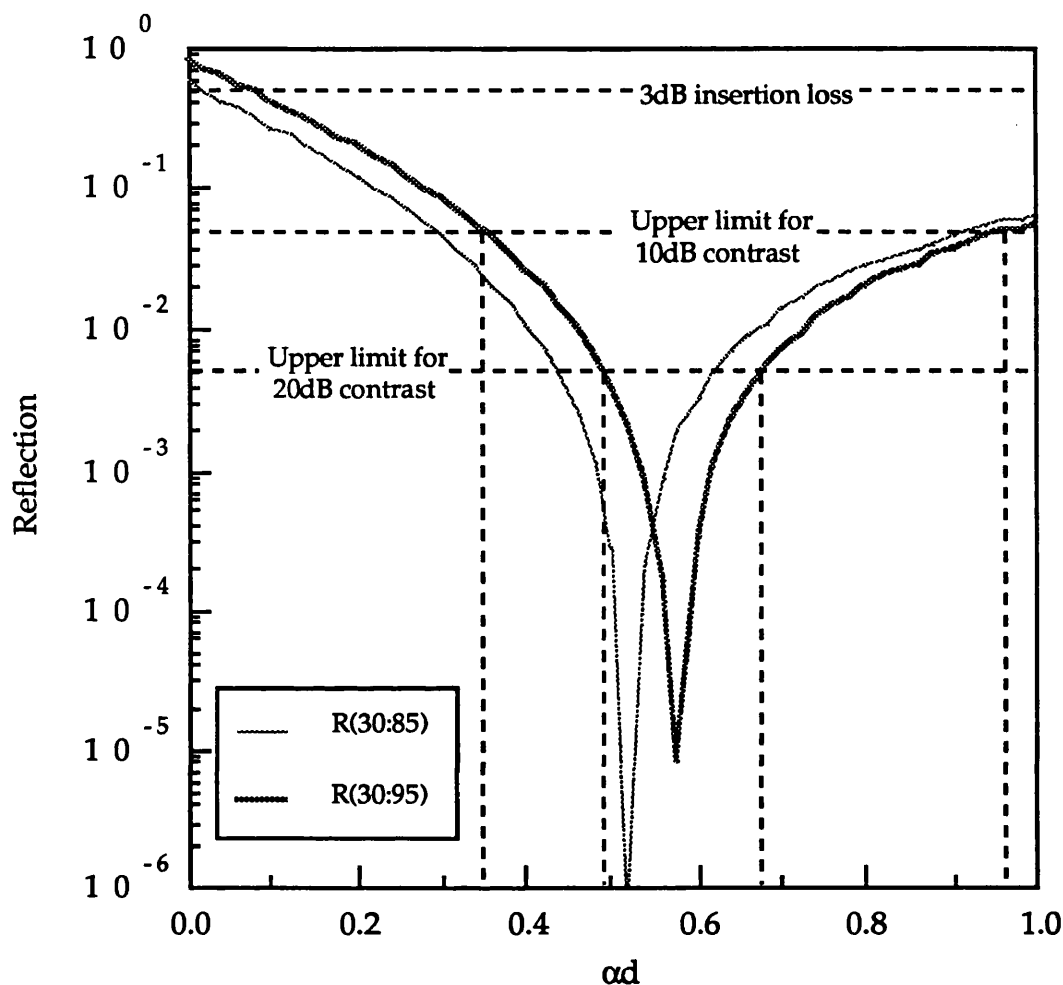


FIGURE 6.2.2.1:

Calculation of the limits for the absorption required to achieve 20dB or 10dB contrast for the standard AFPM ($R_f = 0.30$, $R_b = 0.95$) and an AFPM with lower back reflectivity (0.30, 0.85).

Having defined $R = 0.50$ as our minimum allowable on state we require biased reflectivities of 0.05 and 0.005 for contrasts of 10 and 20dB respectively. The dashed lines on Fig. 6.2.2.1 mark these boundaries. It is encouraging that to achieve *at least* 20dB contrast the biased αd can lie anywhere between 0.493 and 0.675, whilst 10dB contrast should be quite easily achieved with αd allowed to be in the rather wider range between 0.349 and 0.970. For the device with only 85% back reflectivity the operating ranges are almost exactly the same width – the lowering of the reflectivity simply shifts everything to lower αd by ≈ 0.06 .

We can also use Eqs. 6.2 & 6.4 to underline the problem caused by unwanted absorption in high-finesse FP modulators. As was shown in Chapter 5, with such devices the unbiased state is the off state because the cavity mirrors are equal, or nearly so. If we have exactly equal reflectivities at front and back, then any background absorption in the cavity will raise R above zero, reducing the on:off ratio. This forces us to use the device at wavelengths well away from the MQW absorption edge to the extent that (i) the advantage of using MQWs for their enhanced electro-refractive properties compared to a bulk semiconductor is likely to be lost, and (ii) the operating wavelength for quantum wells of $\approx 100\text{\AA}$ width will be around 890-900nm, and beyond the wavelength limit for (Al, Ga)As-based semiconductor laser sources.

To compensate for absorption in the cavity, and thus allow operation closer to the MQW absorption edge, a small amount of asymmetry can be introduced – the front reflectivity being made slightly lower than the back. For a device with $R_f = 0.90$, $R_b = 0.95$, Eq. 6.4 gives $\alpha d_{R=0} \approx 0.027$, which is equivalent to $\alpha \approx 500\text{cm}^{-1}$ for the CPM405 MQW structure quoted above.

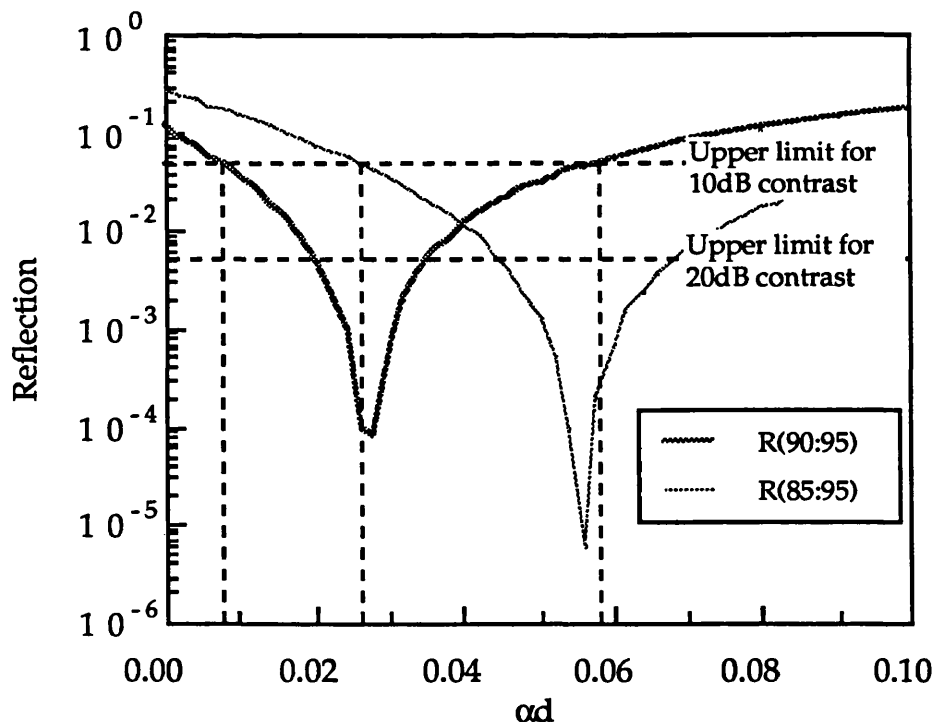


FIGURE 6.2.2.2:

Calculation of the absorption limits which permit high contrast (10dB) operation with a high-finesse quasi-symmetric FP modulator. Curves for two different cavities are displayed

With the same specification for on and off R levels as for the AFPM above, in Figure 6.2.2.2 we have plotted Eq. 6.2 for two "quasi"-SFPMs. Note that the αd range is only one tenth of that in Figure 6.2.2.1. Here we have only marked the range over which R remains $\leq 5\%$. This is the upper limit for the off state for 10dB contrast. The sensitivity of the high-finesse device to fluctuations in the mirror reflectivities and the level of background absorption is immediately apparent. By reducing R_f by only 5% the critical αd value is doubled, however the maximum αd range within which R remains $\leq 5\%$ is only $\approx 0.026-0.104$ (for the lower finesse structure). This is eight times smaller than the corresponding range for the standard AFPM. Furthermore, as we observe experimentally in § 6.5, it is quite difficult in practice to achieve the accuracy and uniformity of reflectivity from a multilayer mirror which Fig. 6.2.2.1 suggests is necessary to successfully fabricate high-finesse FP cavity modulators.

6.3 MODELLING OF AFPM PERFORMANCE

6.3.1 LIMITS TO CONTRAST AND OPERATING VOLTAGE (OPTIMIZED CAVITY)

In section 5.4.2, where we first considered the idea of the AFPM, the modelled performance was optimized for maximum reflection change. Consequently the maximum contrast calculated was $\approx 16\text{dB}$, which was limited by the amount of absorbing material used ($62 \times 100\text{\AA}$ wells) and the position of the FP cavity resonance relative to the MQW absorption edge. Here we shall look at the maximum contrast limits for 10V and 5V bias, and the minimum bias required to achieve a contrast of 10dB. We use the same model as for Chapter 5, simply adjusting the cavity thickness to place the resonance at the wavelength of optimum bias-absorbing effect in order to satisfy Eq. 6.4 as closely as possible. The maximum allowed insertion loss for these calculations is again 3dB.

In general, there will be a trade-off between bias, contrast and insertion loss. To reduce insertion loss we move the resonant wavelength further away from the MQW absorption edge. This requires a higher field to get the increased Stark shift necessary to put sufficient absorption at the resonance to achieve strong modulation. Also, the lower the insertion loss, the larger the increase in absorption needed to observe high contrast (see Fig. 6.2.2.1). However, at a fixed bias voltage, a higher field will permit fewer quantum wells, thus reducing the absorption which can be field-induced at the resonance. Furthermore, the shifted exciton will suffer a greater loss of oscillator strength the higher the field. The net result is a strong reduction in the maximum contrast at fixed bias as we move the cavity resonance away from the absorption edge.

If we allow the bias to increase to accommodate more quantum wells in order to compensate for the factors above which reduce the electro-absorption, then insertion loss will also increase as the αd value in the tail of the absorption edge becomes larger.

For the 10V bias limit we find that the maximum contrast is obtained with 75 wells at an average field of 83.3kV/cm , which equates to $\approx 10\text{V}$ across a total MQW structure of $\approx 1.2\mu\text{m}$. The modelled spectra are shown in Figs. 6.3.1.1-2 (over page). The well and barrier thicknesses used are the same as in Chapter 5, i.e. 100\AA and 60\AA respectively.

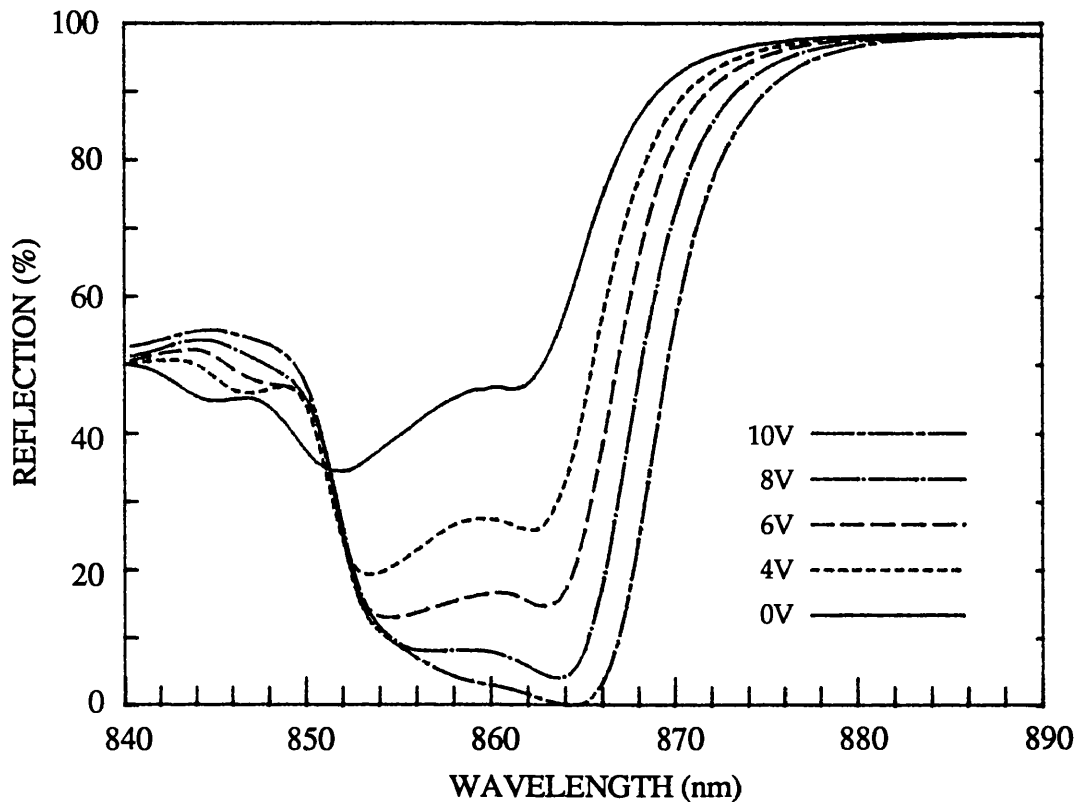


FIGURE 6.3.1.1:

Calculated reflection spectra optimized for maximum contrast at 10V bias for an MQW AFPM. Device contains $75 \times 100\text{\AA}$ wells with 60\AA AlGaAs barriers.

The zero bias spectrum in Fig. 6.3.1.1 shows light and heavy hole excitonic absorption features at ≈ 844 and 851nm respectively. The FP cavity resonance is at $\approx 861\text{nm}$. As bias is increased and the reflection falls towards zero, the contrast increases to a peak value of $\approx 37\text{dB}$, and there is a shift in the resonant wavelength of 3-4nm. This is dependent on the magnitude of the refractive index changes in this part of the spectrum and the position of the FP resonance relative to the index changes. It is possible for the index change to be positive, negative or even approximately zero at the wavelength of the unbiased resonance, depending on the field applied (see § 3.5). This will have some bearing on the insertion loss at the wavelength of maximum contrast. In Fig. 6.3.1.1 we see that the biased resonance shifts to a position where the unbiased reflection is $\approx 15\%$ higher than that at the unbiased resonance. Thus the electro-refractive effect is partly responsible for reflection changes as high as 72%, seen in Fig. 6.3.1.2.

The contrast spectra (over page) illustrate the non-linearity of the contrast with bias at the resonant wavelength. To achieve high yields of

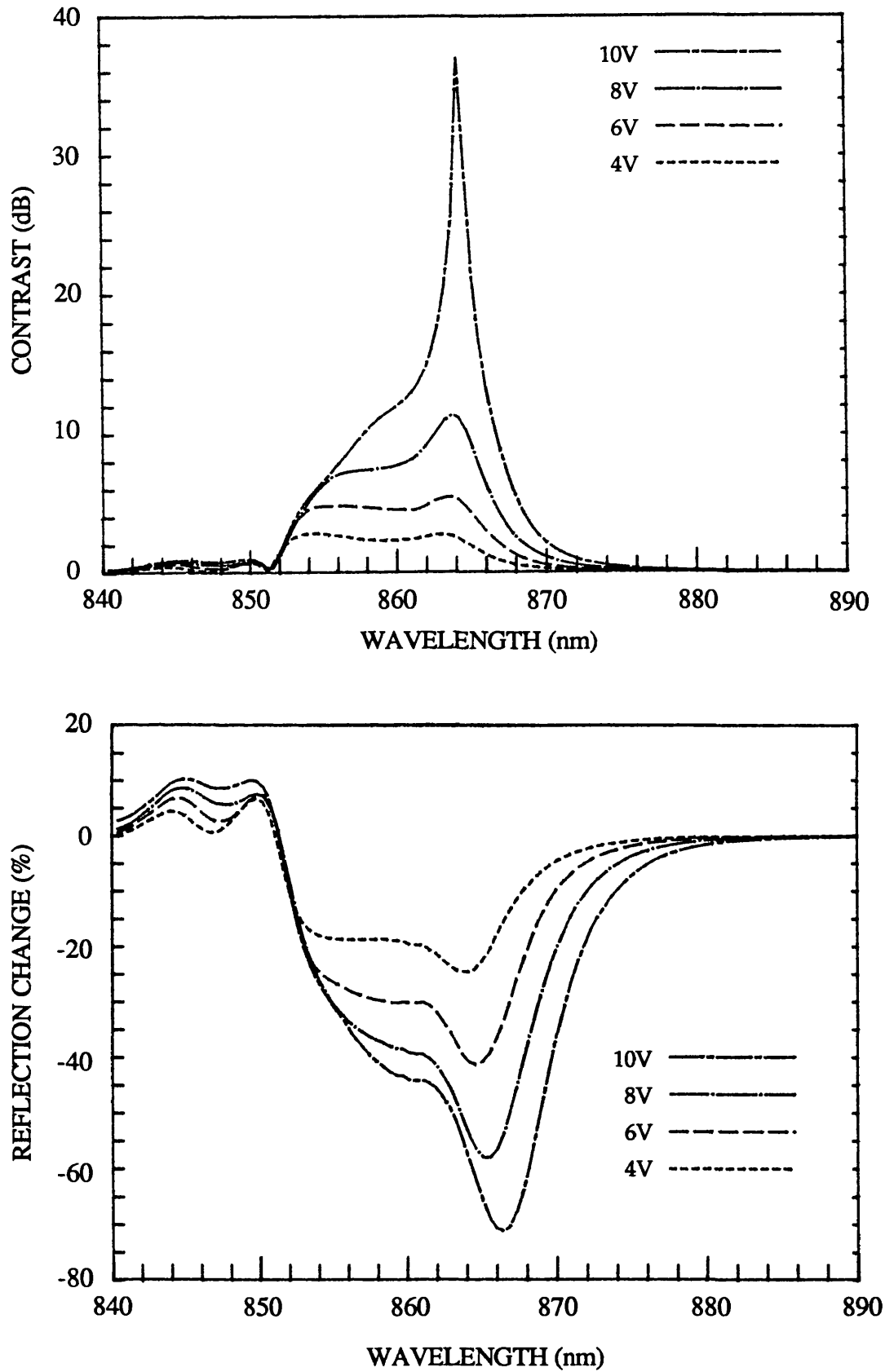


FIGURE 6.3.1.2:

Calculated contrast and reflection change spectra for MQW AFPM with optimized contrast at 10V bias.

devices offering 20-30dB contrast at a specified wavelength will be very difficult because of the narrowness of the peak ($\approx 2\text{nm}$ at 20dB), the position of which will be dependent on the cavity thickness and operating temperature. However, the linewidth for 10dB contrast is $\approx 9\text{nm}$ at the highest bias, so, depending on the application, this does give some tolerance of input wavelength drift relative to the modulator operating point.

Looking at the reflection changes, the linewidths are comparable with the results for the transmission modulators of Chapter 4, but for changes roughly twice as large. At 10V bias the reflection change is 50% over 6nm, whilst at 4V the maximum change is $\approx 40\%$. This is significantly better than the maximum change observed with the 47\AA well transmission modulator (§ 4.6), which required as much as 16V bias.

When the operating voltage limit is reduced to 5V we find that maximum contrast is achieved using only 47 wells at an applied field of $\approx 67\text{kV/cm}$. The modelled reflection spectra are shown below in Fig. 6.3.1.3, with the contrast and reflection changes over the page in Fig. 6.3.1.4.

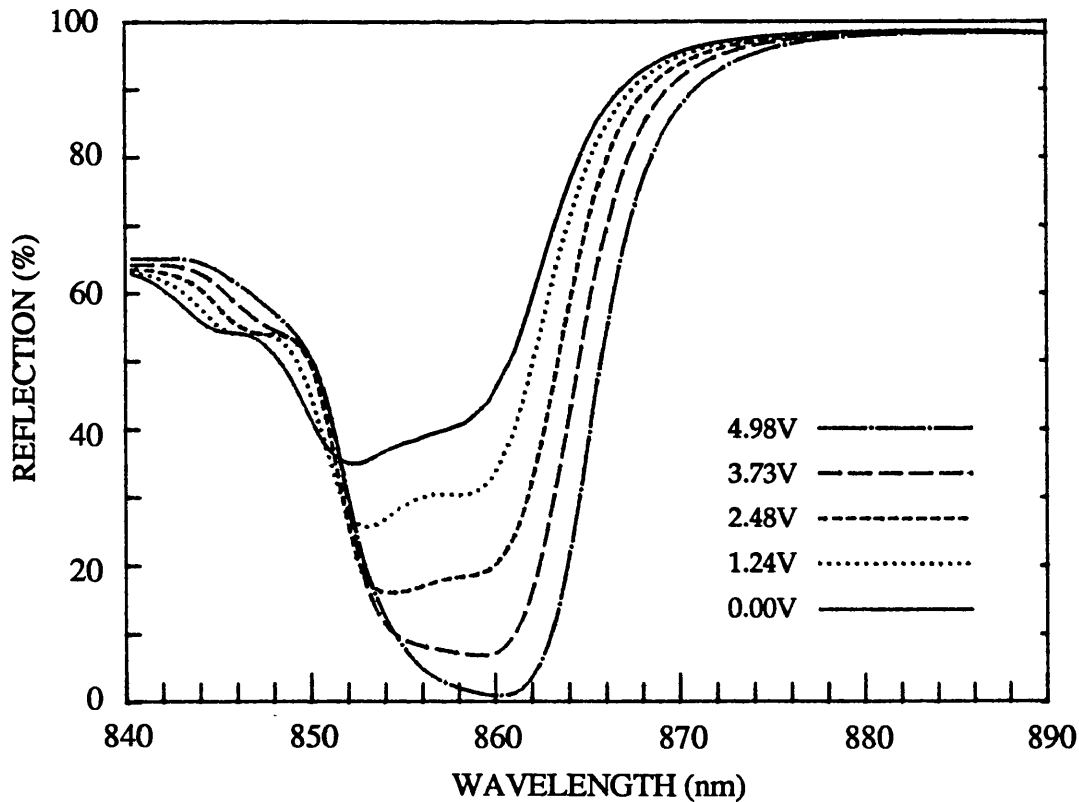


FIGURE 6.3.1.3:

Calculated reflection spectra optimized for maximum contrast at 5V bias for an MQW AFPM. Device contains $47 \times 100\text{\AA}$ wells with 60\AA AlGaAs barriers.

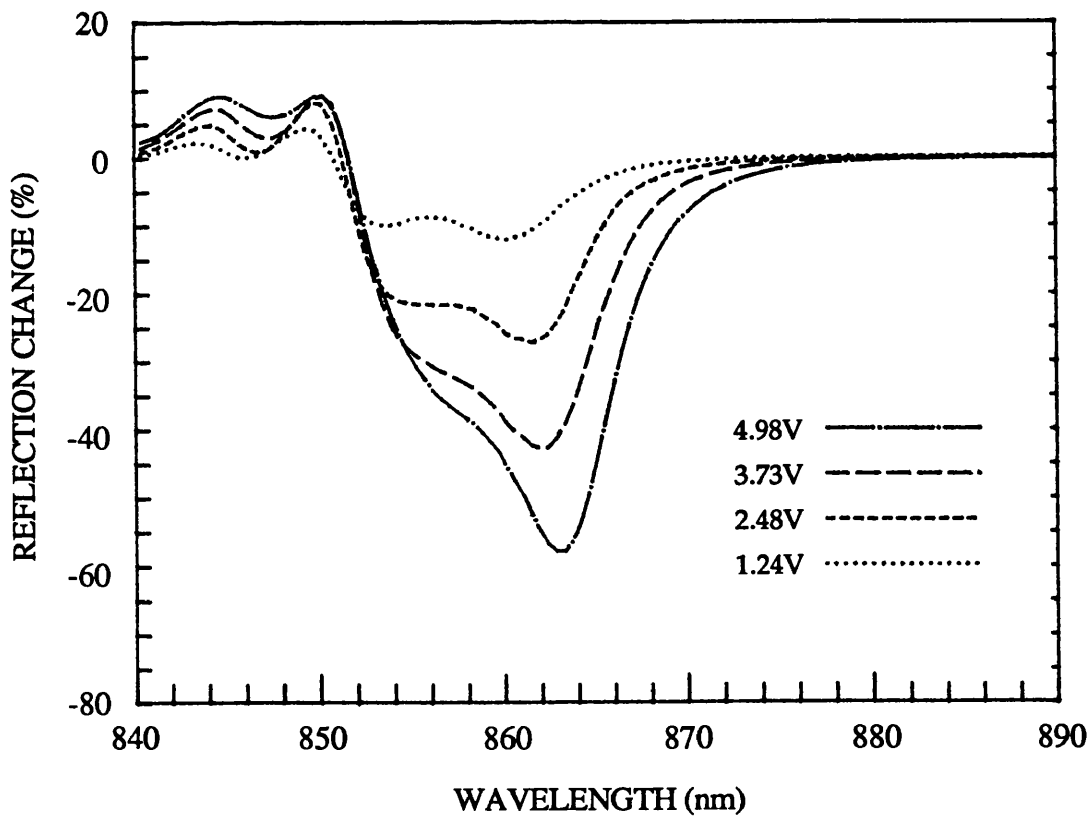
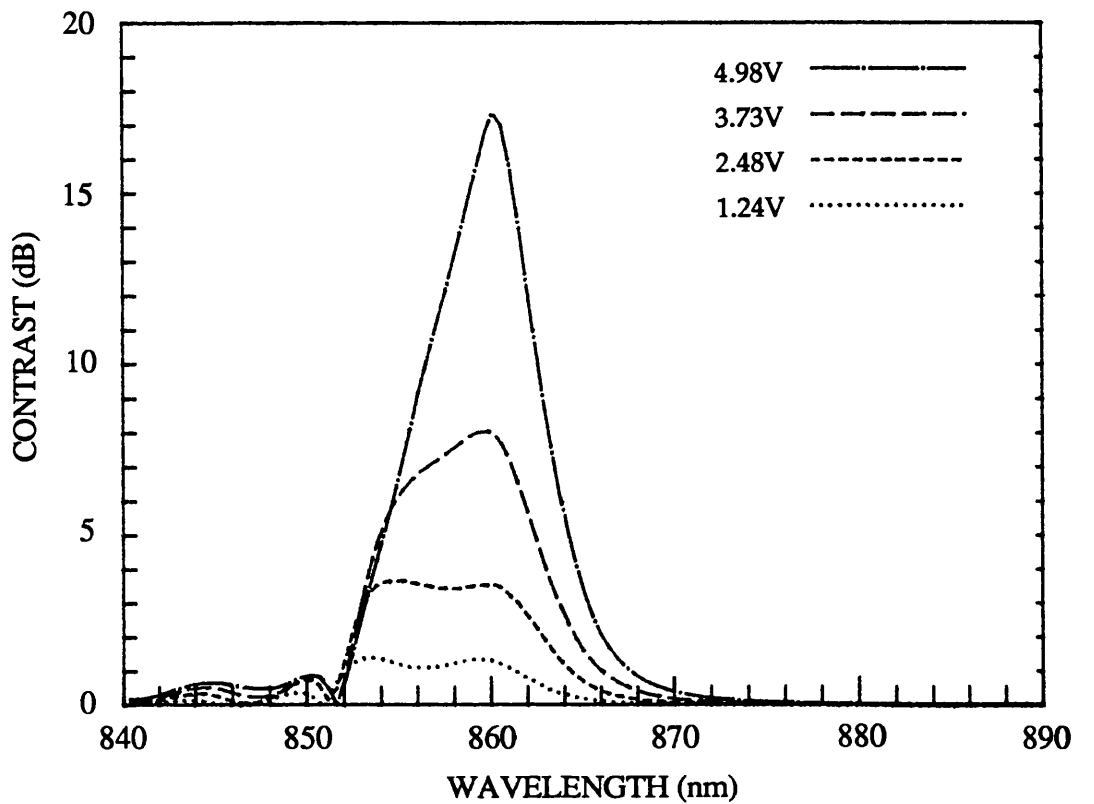


FIGURE 6.3.1.4:

Calculated contrast and reflection change spectra for MQW AFPM with optimized contrast at 5V bias.

The reduction of the amount of absorbing material means that the optimum operating wavelength is now closer to the MQW absorption peak and so the resonance and the heavy hole exciton are not clearly resolved in this case. There is an obvious narrowing of the region over which large changes in reflection occur, and maximum contrast is now down to $\approx 15\text{dB}$ at the 3dB insertion loss limit at $\approx 861\text{nm}$. However at 5V we can still achieve 10dB contrast over a 6nm range, and if, for example, 3dB is considered sufficient modulation, then the linewidth is more than 8nm at only $\approx 2.5\text{V}$, with insertion loss of no more than 4.5dB. Along with reflection changes in excess of 50%, these results indicate the potential for operation of the AFPM at voltages levels which are compatible with high-speed electronic circuitry.

Conscious of the need to operate at low bias voltages, the final set of modelled spectra are for a device where the bias voltage for 10dB contrast has been minimized. The MQW structure here contains only 31 wells, and thus requires only $\approx 3.3\text{V}$ to reach maximum contrast (Fig. 6.3.1.5). For 3dB modulation the bias falls to as little as 1.6V (Fig. 6.3.1.6).

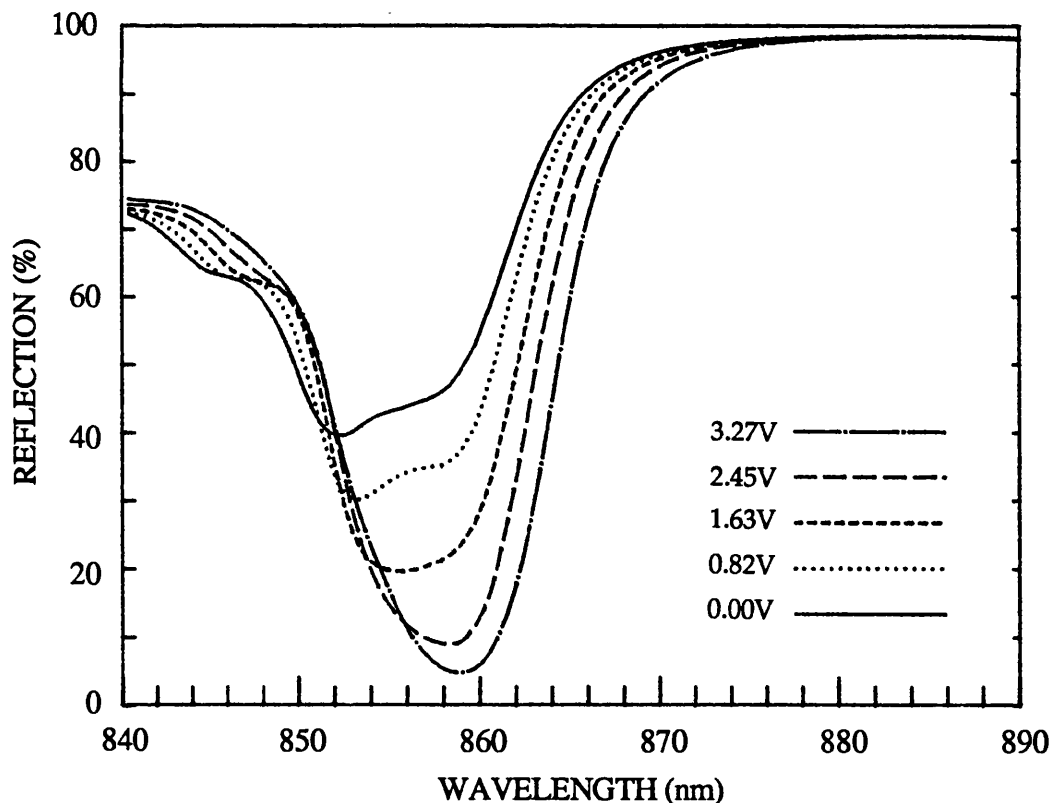


FIGURE 6.3.1.5:

Calculated MQW AFPM performance with $31 \times 100\text{\AA}$ wells (60\AA AlGaAs barriers). This structure offers 10dB contrast with minimum bias voltage.

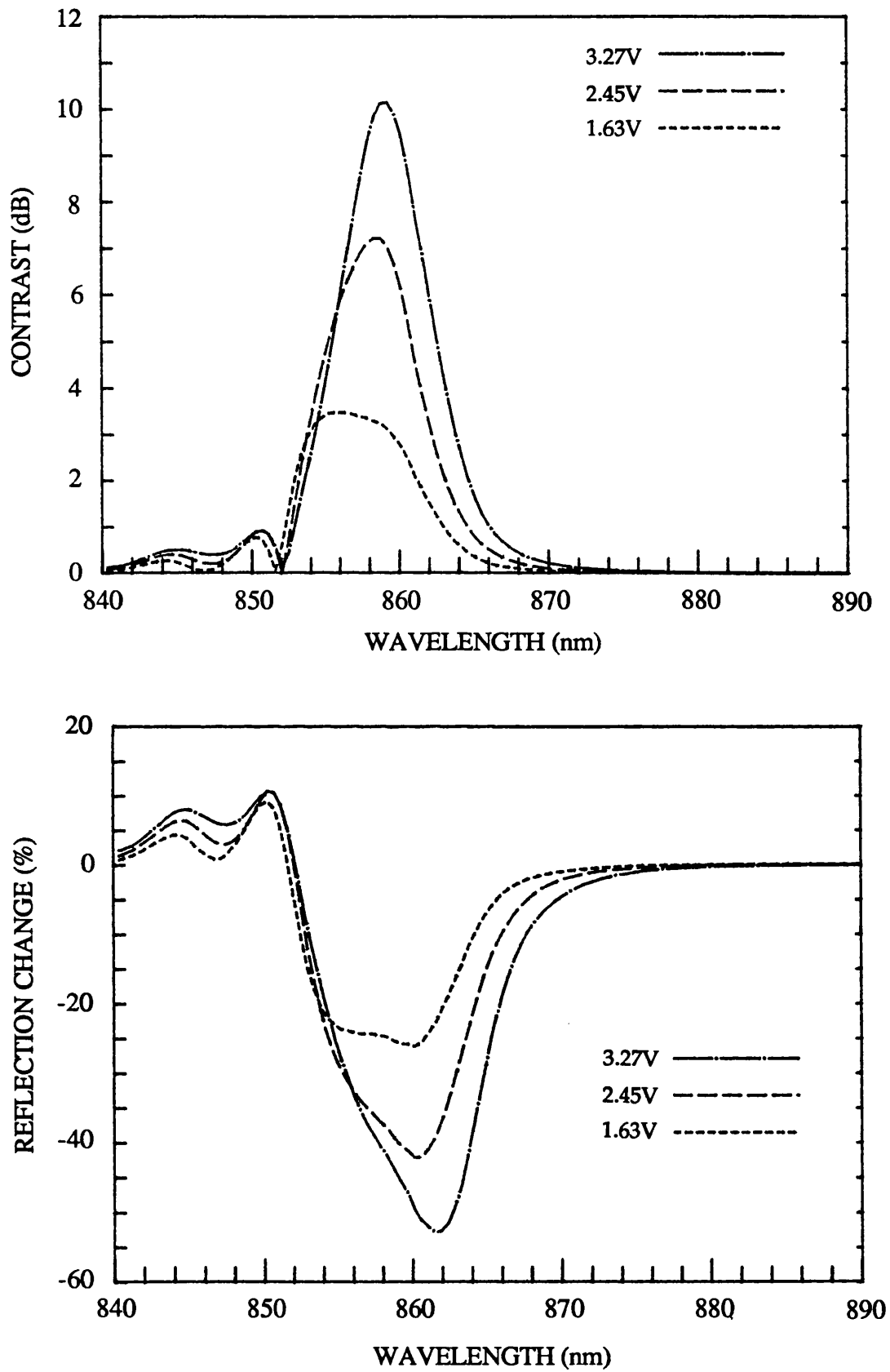


FIGURE 6.3.1.6:

Calculated contrast and reflection change spectra for the 10dB AFPM with minimized bias.

Obviously at the 10dB limit the contrast linewidth is very narrow, but 3dB is possible over $\approx 5\text{-}6\text{nm}$, with less than 4dB insertion loss. The decrease in absorber thickness appears to have a less dramatic effect on the reflection change than on the maximum contrast. Even with as little as 31 wells the change in reflection can exceed 50% (Fig. 6.3.1.6) and at $\approx 1.6\text{V}$ is as large as the maximum changes seen for most of the MQW transmission modulators at considerably higher bias (see Table 4.1).

It should be pointed out that this modelling is all for an insertion loss of 3dB, but this could be relaxed to reduce the operating voltage for a given contrast or increase the contrast for a given voltage, i.e. if we allowed 6dB loss, then we could operate with the resonance very close to the MQW absorption edge. There is also the possibility of using a d.c. bias voltage with an a.c. signal superimposed in order to avoid having to provide the full voltage swing necessary to obtain maximum contrast. In this case the insertion loss would obviously increase. How much depends on the non-linearity of the reflection with bias.

6.3.2 SENSITIVITY OF CONTRAST TO OPERATING WAVELENGTH

In the previous section we modelled spectra for an optimized cavity thickness. It is clear that the maximum contrast achievable with the AFPM at a given bias is dependent on the position of the cavity resonance with respect to the absorption edge. Therefore we show here how much the maximum contrast varies over a wide range of resonant wavelengths. The contrast curves in Figs 6.3.2.1-2 represent the *envelope* of maximum contrast with 3dB insertion loss at a fixed bias for devices whose resonant wavelengths span the given range. This is not a comprehensive optimization, but represents the sort of variation in performance one could expect from an epitaxially-grown AFPM cavity, where the absorbing structure is fixed but the cavity thickness varies by a few % over the wafer area. Again we have considered the 10V and 5V limits. It should be noted that the resonant wavelength referred to here is that for the unbiased state. In some cases the wavelength of maximum contrast is not exactly the same as the unbiased resonance, e.g. when small electro-refractive effects come into play. However the difference is generally only $\approx 1\text{nm}$.

For the 10V case, in Fig. 6.3.2.1, we find a good illustration of the effect which we described quantitatively in the previous section. There is a peak contrast of ≈ 35 dB which falls off sharply to either side. At longer wavelengths the reduction is due to the decrease in the biased absorption at resonance. Note also that the insertion loss decreases, so that it is possible to achieve 10 dB contrast with less than 2 dB insertion loss. At wavelengths shorter than the peak the biased absorption becomes so large that it is higher than the critical value for zero reflectivity (see Fig. 6.2.2.1) and so the contrast is reduced. As the cavity resonance shifts right into the absorption edge the device characteristics become quite complex. The general feature is that the insertion loss at the resonant wavelength climbs into the 6-13 dB range, and so we have to choose an operating wavelength which is further and further away from the resonance, again resulting in reduced contrast. It would appear that the contrast remains higher than 10 dB only over a wavelength range of ≈ 4 -5 nm (which corresponds to a change in the cavity thickness of $\approx 150 \text{ \AA}$). However this can be extended on the short wavelength side by reducing the bias voltage.

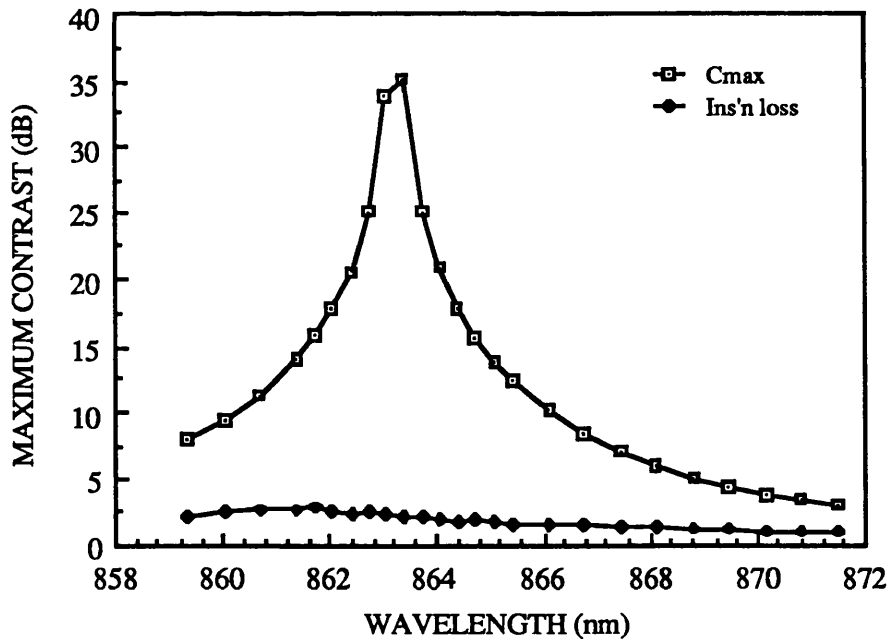


FIGURE 6.3.2.1:

Variation of maximum contrast and insertion loss as a function of resonant wavelength for 10V bias limit.

In the 5V bias limit we find obviously that the peak contrast is reduced and also that it is closer to the MQW absorption edge. This is a result of

the lower electric field for optimum bias absorbing effect, which reduces the shift of the absorption edge. However it still appears possible to achieve 10dB contrast over a range of resonant wavelengths similar to the 10V case, with insertion loss creeping over the 3dB level at the short wavelength end, although this can again probably be avoided by using lower bias.

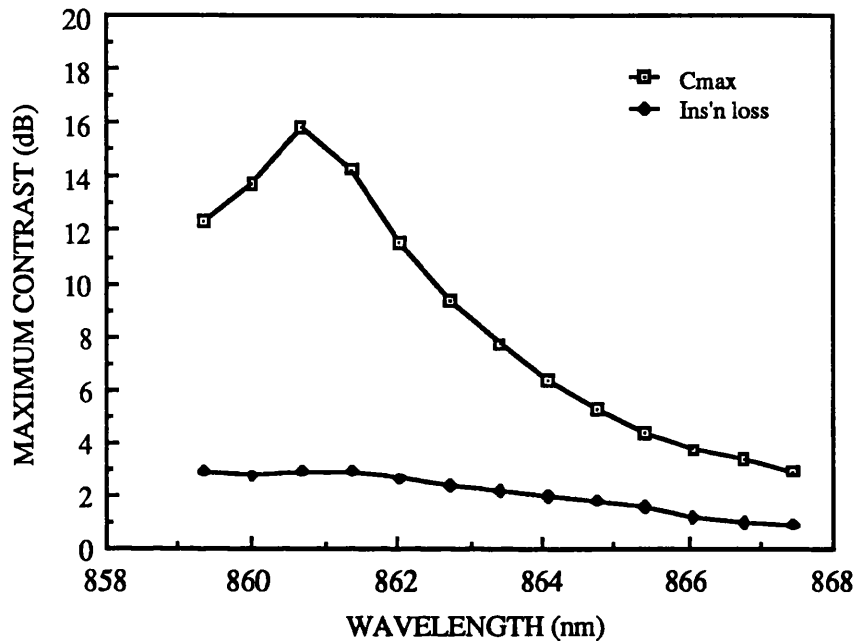


FIGURE 6.3.2.2:
Variation of maximum contrast and insertion loss with resonant wavelength for an MQW AFPM at the 5V bias limit. MQW e1-hh1 exciton peak is at ≈ 851 nm.

6.4 INITIAL DEMONSTRATION OF AN AFPM

6.4.1 DEVICE CONSTRUCTION

At the time the potential of the AFPM was realised we had not yet investigated the growth of multilayer stack (MLS) reflectors within the MQW p-i-n diode to the extent that we could be confident of the quality of the structure. Therefore, in order to demonstrate the principle of the AFPM and confirm our modelling a test device was improvised using a standard MQW transmission modulator, fabricated according to the method of § 4.2.2, with an evaporated gold film on the back surface to provide the high R_b required – the uncoated front surface of the device forming the other mirror. This structure is shown below.

The MQW p-i-n diode (MV370) contained 50 wells of $\approx 85\text{\AA}$ separated by barriers of $\approx 67\text{\AA}$, and was determined to be of high quality from the QCSE seen in photocurrent spectra (see § 2.5.9). It was estimated that, with $0.425\mu\text{m}$ of absorber and bias absorbing $\Delta\alpha$'s similar to the CPM405 device, according to Fig. 6.2.2.1 we should be able to reduce the biased reflection sufficiently to achieve just over 10dB contrast.

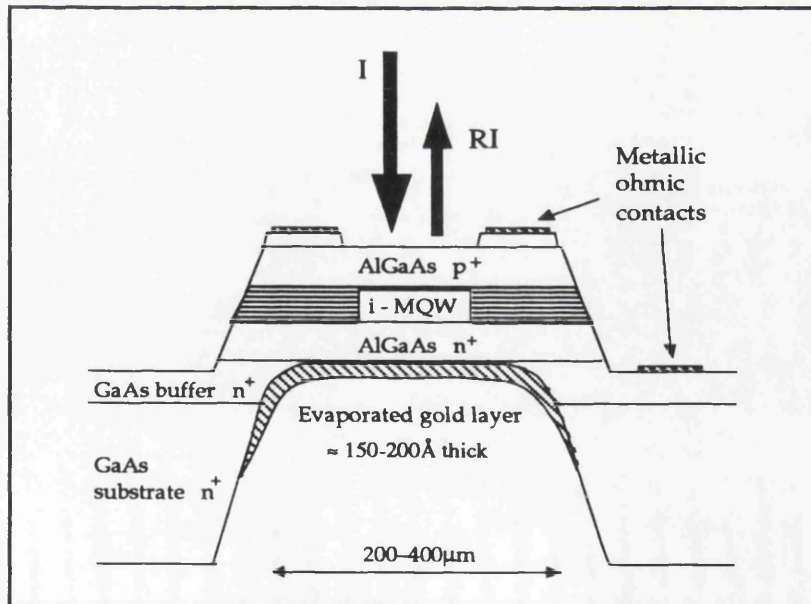


FIGURE 6.4.1: The first AFPM test structure.

This is in fact the same cavity structure as that used for the reflection modulator of § 4.8; only the MQW p-i-n is different. At the time that particular device was tested, however, the AFPM principle had not been

conceived and the "unwanted" FP resonances were in roughly the least favourable spectral position to enhance the modulation.

6.4.2 EXPERIMENTAL RESULTS

Using the experimental set-up described in Chapter 4, reflected intensity spectra from the test AFPM were recorded at room temperature for a range of bias voltages. The device was then replaced by a freshly-deposited gold mirror, which in the near-IR has a spectrally-flat reflectivity close to 100%, particularly around the 850nm region, and the reflected spectrum from this was recorded. The device spectra were then normalized to the gold spectrum to remove the effects of spectral variation in the intensity of the tungsten lamp source.

Viewing the image of the modulator with the IR camera, significant changes in the reflected intensity could be observed near 860nm when 7-8V were applied to the device. This is confirmed by the normalized reflection spectra shown in Fig. 6.4.2.1.

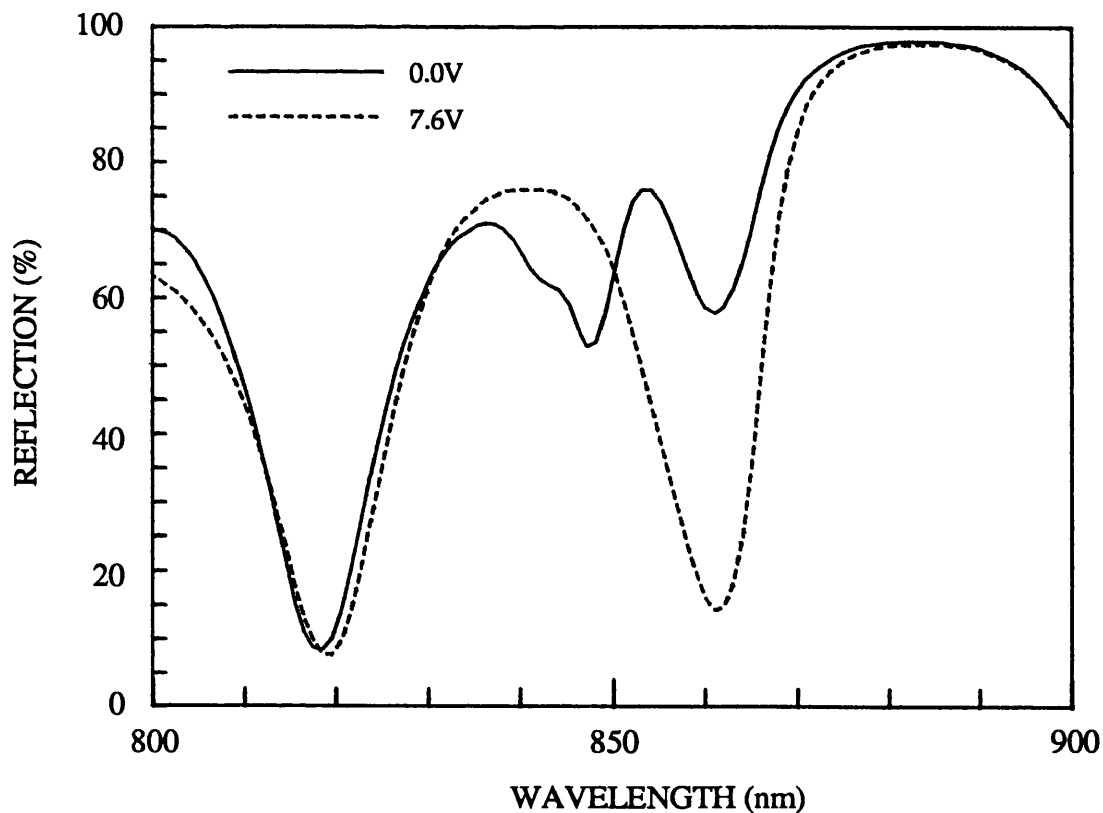


FIGURE 6.4.2.1:
Normalized reflection spectra for the MV370 AFPM at 0V and 7.6V.

In agreement with the calculated R vs αd curves in Fig. 6.2.2.1, we see a deep reflection resonance in the region where strong MQW absorption occurs ($\approx 820\text{nm}$). The same structure can be seen in the spectra for the reflection modulator of § 4.8. However, here we also have evidence for the asymmetric nature of the cavity in the rather shallower resonance just off the MQW absorption edge at $\approx 860\text{nm}$. As theoretically predicted, the reflection falls significantly when absorption is increased with applied bias at this resonant wavelength.

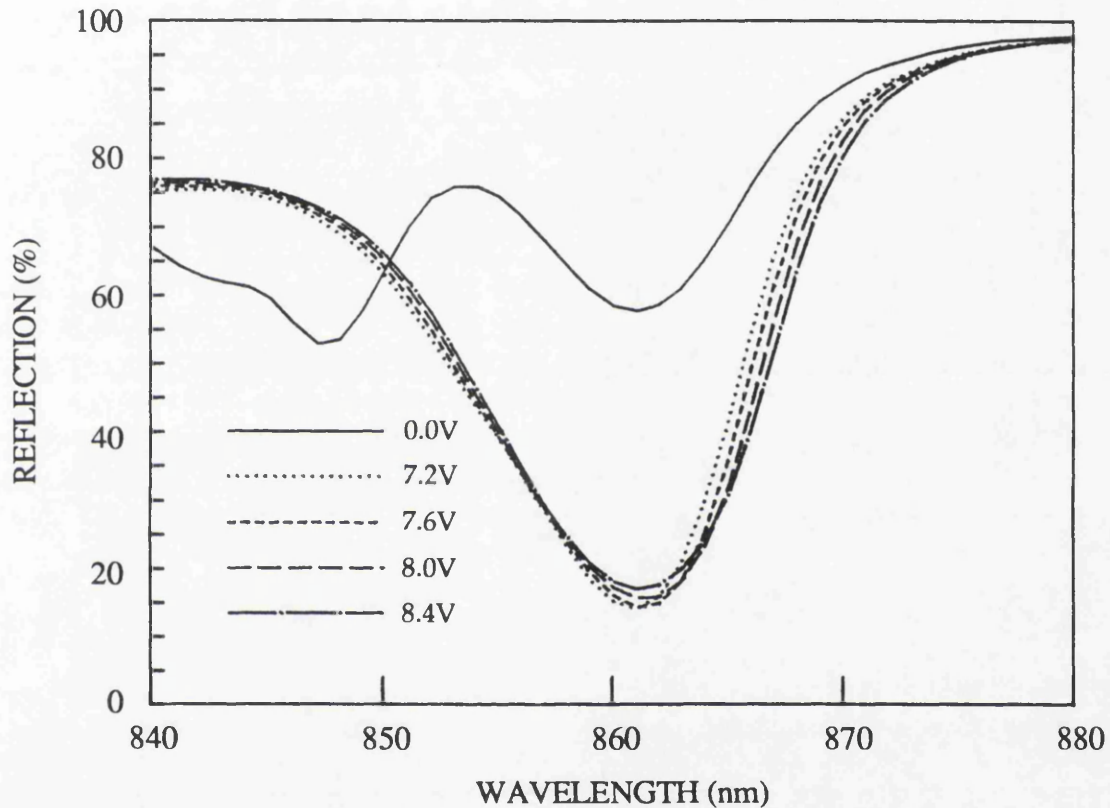


FIGURE 6.4.2.2:

Normalized reflection spectra for the MV370 AFPM at zero bias and a range of reverse bias voltages, showing the relative insensitivity of the modulation to bias voltage.

More detail of the reflection modulation is shown in Fig. 6.4.2.2, where we have plotted the unbiased spectrum along with the biased spectra in the range 7.2-8.4V. The modulation, at least in terms of reflection *change*, is quite insensitive to the voltage changes, again a feature predicted from Fig. 6.2.2.1.

The contrast and reflection change at the optimum bias of 7.6V are shown in Fig. 6.4.2.3. Maximum contrast appears to be $\approx 6\text{dB}$ (4:1) with an insertion loss of 2.5dB. Maximum reflection change is $\approx -43\%$. Aside from the fact that these figures are better than those for any of the

transmission modulators of Chapter 4, particularly when <8V bias is required, we note that the modulation linewidths are also as large, if not larger. For example, 4dB contrast is achieved over 6-7nm, and a reflection change of -40% or more over ≈ 5 nm.

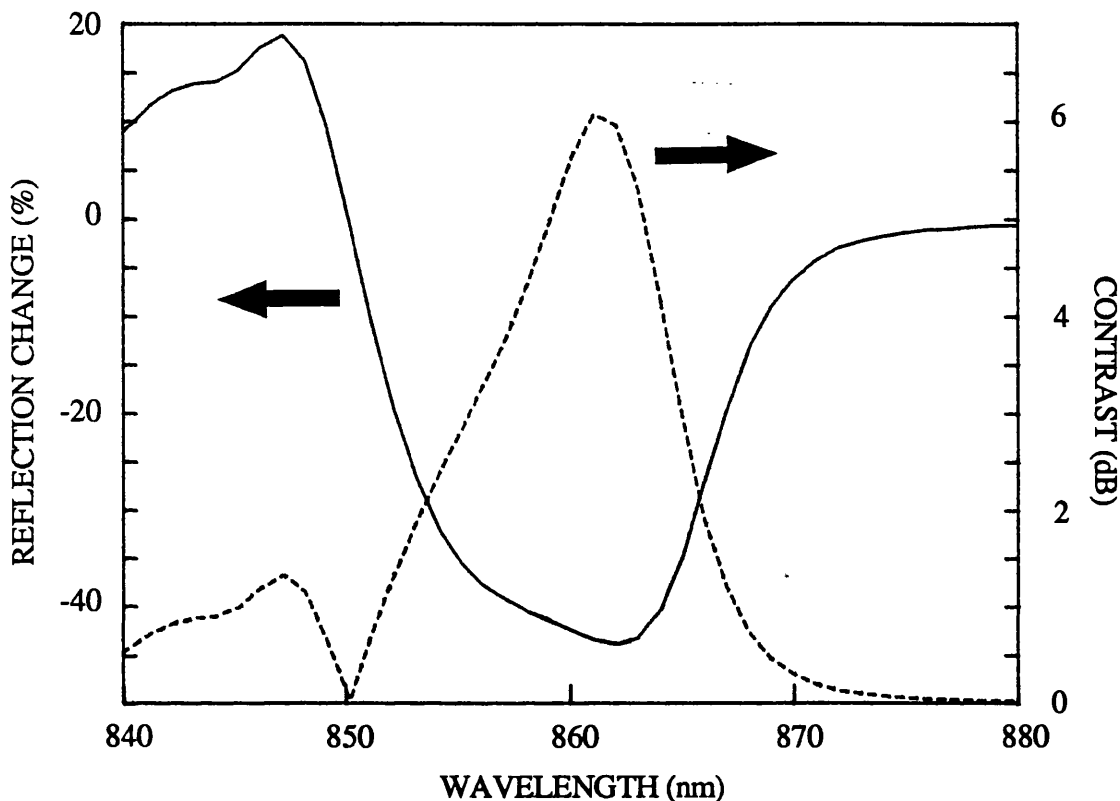


FIGURE 6.4.2.3: Reflection changes and reflection contrast for the MV370 AFPM at the optimum reverse bias of 7.6V.

6.4.3 COMPARISON WITH MODELLED SPECTRA

We have simulated biased and unbiased reflection spectra for the test AFPM using the FP cavity model of Chapter 5. Because the well width in the model is slightly larger than that of the MV370 MQW structure the e1-hh1 exciton peak absorption feature appears at a longer wavelength. To compensate for this, we have set the FP cavity resonance in the model at the same distance from the exciton as in the real device ($\lambda_{\text{res}} - \lambda_{\text{exc}} \approx 13.6$ nm), rather than at the same absolute wavelength. The number of wells in the model is also reduced compared to the real device, so that the total absorber thickness is roughly the same in both cases ($43 \times 100\text{\AA}$ cf $50 \times$

85Å), and the barrier thickness is increased to maintain the total MQW structure. In this way voltages and fields are equivalent in experiment and model.

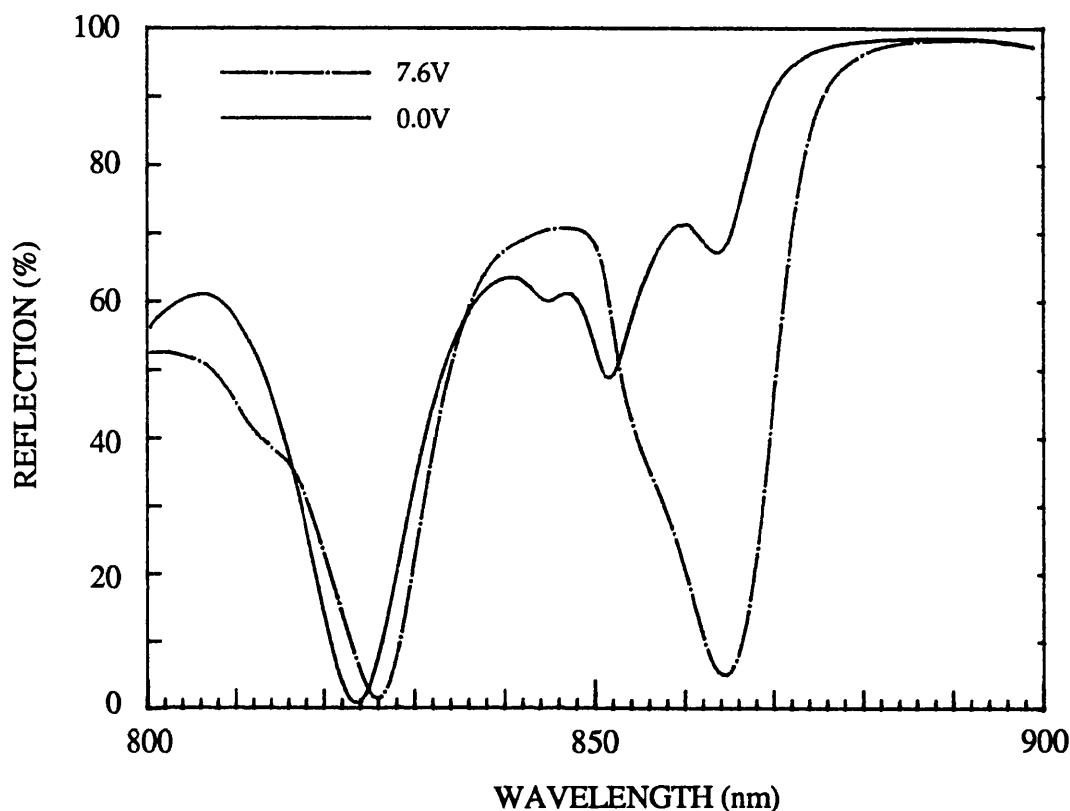


FIGURE 6.4.3.1:

Modelled reflection spectra, with and without bias, for an AFPM with a similar MQW structure to that of the MV370 device.

In comparing the modelled spectra displayed in Figs. 6.4.3.1-2 with those for the test AFPM very good qualitative agreement is seen in the spectral characteristics. Of the discrepancies, we first notice that the biased reflectivity minimum, for what is almost exactly the same bias, is lower for the model than for the real device. Because of the sensitivity of contrast to this low reflection state the modelled maximum on:off ratio is more than a factor of 3 larger (13:1 compared to 4:1).

This could possibly be ascribed to the difference in the well widths – the narrower wells in the real device requiring higher fields for a given Stark shift of the absorption edge. However, it was subsequently realised (see § 6.6) that a significant amount of background light was being detected, which was not incident on the modulator, but simply scattered into the detector. This is almost certainly the cause of the higher than predicted low reflection level, especially in view of the apparent measured

minimum level of $\approx 9\%$ at the resonance which lies completely within the unbiased MQW absorption spectrum (Fig. 6.4.2.1).

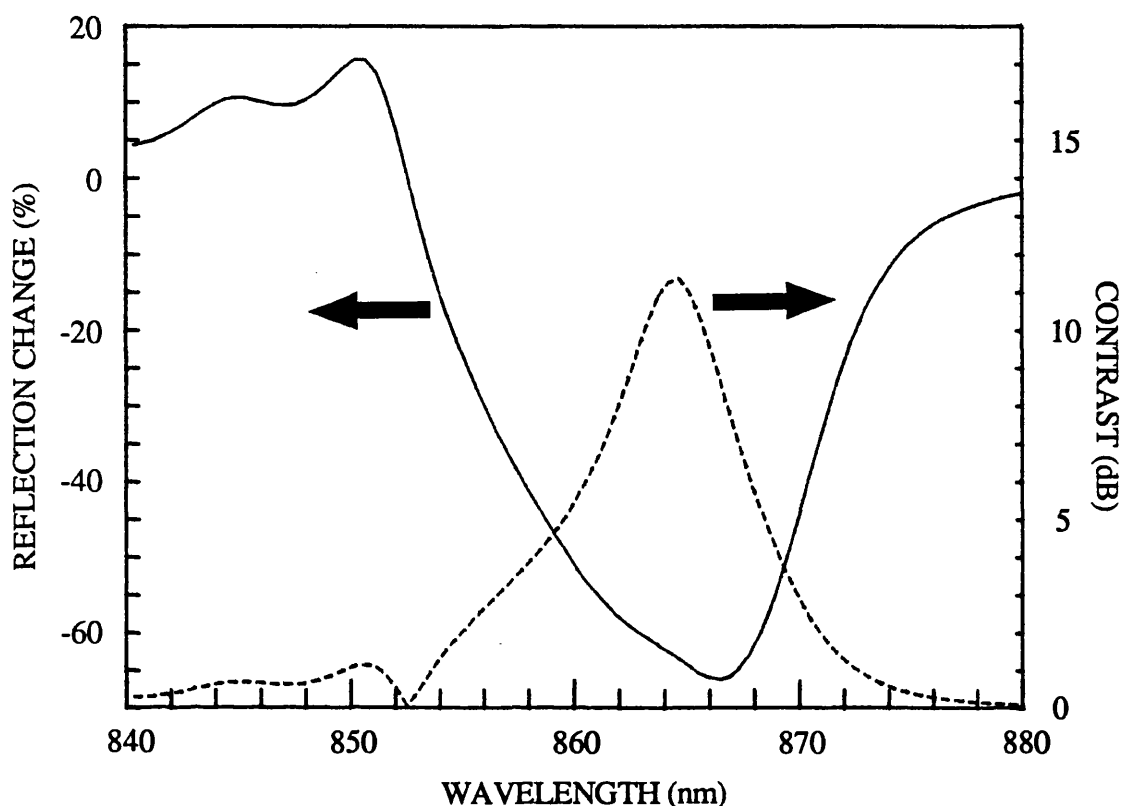


FIGURE 6.4.3.2:

Modelled spectral reflection changes and reflection contrast derived from Fig. 6.4.3.1.

At this wavelength the MQW absorption coefficient would typically be $\approx 10000\text{cm}^{-1}$, which for $50 \times 85\text{\AA}$ wells makes $\alpha d \approx 0.425$. From Fig. 6.2.2.1 the resonant R at this level of absorption should therefore be only $\approx 2\%$. Even allowing a 20% uncertainty in the value of α , this minimum R should be no higher than 5-6%. Thus the biased reflection at the operating wavelength of the real device is artificially high, resulting in the lower apparent contrast.

The second noticeable difference between the real and modelled data is the higher insertion loss in the experimental case, which reduces the maximum ΔR to $\approx -43\%$. One possible explanation for this is that the gold layer is not quite thick enough to constitute a bulk reflector. This would lead to a lowering of the back reflectivity and thus increased loss due to absorption at the resonant wavelength, as modelled in Fig. 6.2.2.1. It may also be the case that the absorption tail close to the edge is underestimated in our calculations from photocurrent spectra.

6.5 SEMICONDUCTOR MULTILAYER STACK REFLECTORS FOR AN INTEGRATED AFPM

6.5.1 DESIGN OF MULTILAYER STACK (MLS) REFLECTORS

The fabrication of high reflectivity mirrors consisting of multiple pairs of dielectric films of different refractive index is nowadays a standard industrial process, and the basic principles of MLS design can be found in a number of textbooks [3-5]. We shall briefly describe here the main features of such structures and the specific considerations in designing an epitaxial semiconductor high reflector.

The propagation of electromagnetic radiation, with a wavelength λ , through a homogeneous dielectric film of refractive index n , can be represented by a characteristic 2×2 matrix which relates the components of the electric (or magnetic) field in the input plane ($z=0$) to those at the output plane ($z=t$, t = layer thickness).

$$M = \begin{bmatrix} \cos \delta & \frac{i}{u} \sin \delta \\ i u \sin \delta & \cos \delta \end{bmatrix} \quad \dots(6.6)$$

where
$$\delta = \frac{2\pi}{\lambda} n t \cos \beta \quad \dots(6.7)$$

The angle, β , is the angle of propagation from the surface normal within the dielectric layer, and is related to the external angle of incidence, θ , by Snell's Law, where n_m is the index of the external (entrance) medium.

$$n_m \sin \theta = n \sin \beta \quad \dots(6.8)$$

The term u in the matrix elements of Eq. 6.6 is polarization dependent and takes the following form:

$$u = \begin{cases} \frac{n}{\cos \beta} & \text{parallel} \\ n \cos \beta & \text{perpendicular} \end{cases} \quad \dots(6.9)$$

"Parallel" and "perpendicular" refer to the directions of polarization with respect to the plane of incidence.

We can represent a complex multilayer structure by the product of the matrices for the individual layers, i.e.

$$M_{MLS} = M_1 M_2 M_3 M_4 \dots M_{l-1} M_l \dots (6.10)$$

$$M_{MLS} = \begin{bmatrix} m_{11} & m_{12} \\ m_{21} & m_{22} \end{bmatrix} \dots (6.11)$$

From the elements of this final matrix the amplitude and intensity reflection coefficients (r and R) are derived thus:

$$r = \frac{(m_{11} + m_{12} u_{out})u_{in} - (m_{21} + m_{22} u_{out})}{(m_{11} + m_{12} u_{out})u_{in} + (m_{21} + m_{22} u_{out})}, \quad R = |r|^2 \dots (6.12)$$

with u_{in} and u_{out} being the respective u values for the semi-infinite input and output media e.g. air *in* and GaAs substrate *out*.

The highest reflectance is achieved if the MLS is composed of N periods of the form AB , where A and B represent layers of refractive index n_A, n_B with optical thickness $n_A t_A, n_B t_B$ respectively, and where $n_A t_A, n_B t_B$ are both equal to one quarter of the incident wavelength, λ_0 . That is, for light at normal incidence there will be a first-order high reflectance band centred at λ_0 where:

$$n_A t_A + n_B t_B = \lambda_0 / 2 \dots (6.13)$$

The maximum value of the reflectivity at the centre wavelength is dependent on the ratio (n_A/n_B) and the number of layer pairs, N , according to:

$$R_{max} = \left[\frac{\left(\frac{n_m}{n_s}\right) - \left(\frac{n_A}{n_B}\right)^{2N}}{\left(\frac{n_m}{n_s}\right) + \left(\frac{n_A}{n_B}\right)^{2N}} \right]^2 \dots (6.14)$$

where n_m is the refractive index of the medium from which light is incident and n_s is the index of the exit medium, normally the substrate supporting the MLS. All expressions here are for the case of non-absorbing materials.

With the advent of precisely-controlled epitaxy there has been a considerable amount of investigation of semiconductor MLS structures [6,7], directed more recently towards device applications such as MQW FP étalon modulators [8-10] and surface emitting lasers [11]. The work has been mainly confined to the Ga(Al)As material system, which, besides being the most mature epitaxial technology, offers good lattice matching over the full range of the ternary alloy composition. To obtain the widest high reflection band and the highest reflectivity with fewest periods we require the largest possible index difference between the MLS components. The limit on this is the wavelength at which the higher index (smaller band-gap) semiconductor begins to absorb. Thus GaAs is ruled out because it absorbs strongly at wavelengths close to the required MLS centre wavelength ($\approx 860\text{nm}$). We therefore choose a ternary alloy with 0.1 Al mole fraction as the high index layer, which begins to absorb only below $\approx 800\text{nm}$ at room temperature, and AlAs as the low index layer. At a wavelength of 850nm the refractive indices of $\text{Al}_{0.1}\text{Ga}_{0.9}\text{As}$ and AlAs are ≈ 3.54 and 2.98 respectively [12, 13]. To determine the required number of periods for the MLS in our epitaxial AFPM structure, putting these numbers into Eq. 6.7 as n_A and n_B , with $n_m \approx 3.54$ (a weighted mean for MQW) and a substrate of GaAs ($n_s = 3.62$), we find that the peak reflectivity increases as follows:

<u>N (periods)</u>	<u>R_{max} (peak reflectivity)</u>
0	0.0001
2	0.116
4	0.365
6	0.609
8	0.780
10	0.883
12	0.940
14	0.969

As expected, the maximum reflectivity tends asymptotically towards 100%. The requirement for the AFPM is a minimum back reflectivity of $\approx 95\%$, which is achieved with 12-14 periods.

It is important for device applications not only to achieve a high peak reflectivity, but to be able to ensure that R_{max} occurs at the optimum wavelength relative to the MQW absorption spectrum. This would impose almost impossibly strict tolerance limits on the growth of MLS structures were it not for the fact that the high reflectivity band can be

made suitably broad by choosing materials with the maximum possible index difference. Unlike the maximum reflectivity, the bandwidth of the MLS is solely dependent on the index difference between the A and B layers, and is given by:

$$\left(\frac{\Delta\lambda}{\lambda_0}\right) = \frac{4}{\pi} \sin^{-1} \left[\frac{|n_B - n_A|}{n_B + n_A} \right] \quad \dots(6.15)$$

With the indices quoted above, at $\lambda_0 = 860\text{nm}$, the bandwidth is $\approx 95\text{nm}$. For the 12-period MLS this is the range over which the reflectivity is at least 91%.

Using Eqs. 6.6-6.12 we have modelled the reflectance spectrum at normal incidence of an MLS structure suitable for an integrated AFPM. The dispersion in refractive index of the various layers has been ignored. As long as the index mismatch is maintained over the 30nm or so over which modulation occurs due to the QCSE this should present no problems.

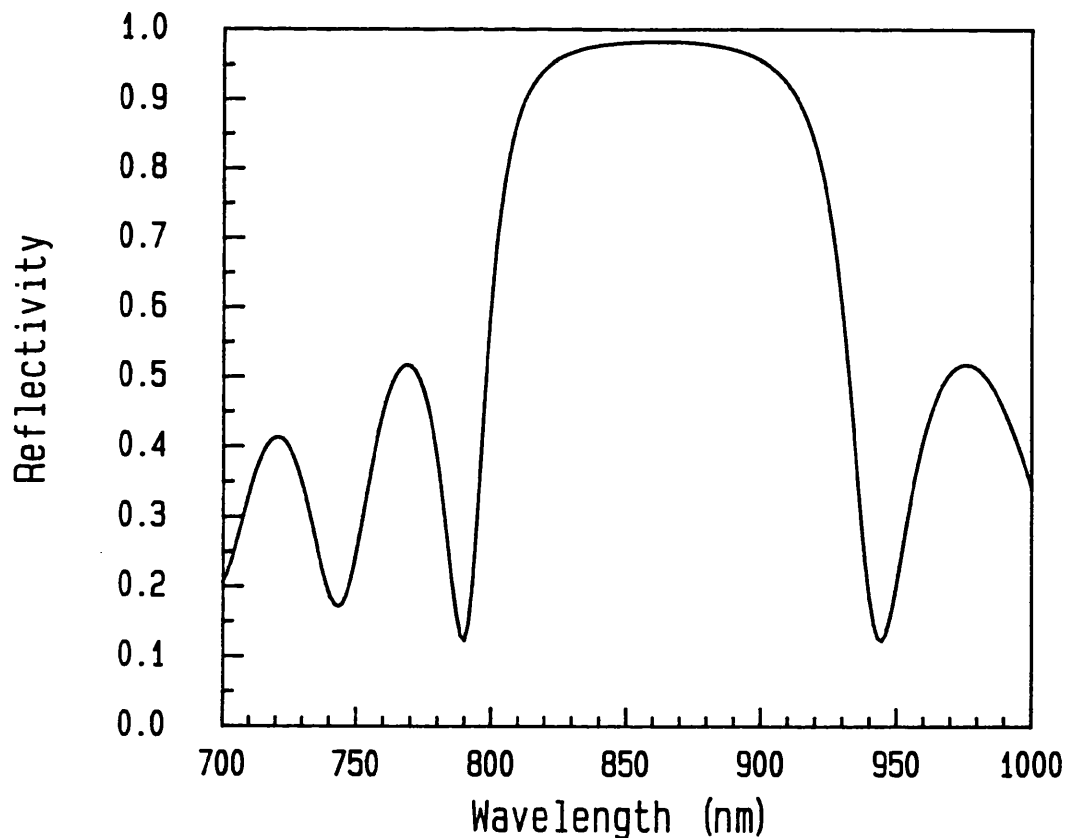


FIGURE 6.5.1:

The modelled reflectance spectrum of a 12-period MLS of $(606\text{\AA} \text{Al}_{0.10}\text{Ga}_{0.90}\text{As} + 721\text{\AA} \text{AlAs})$.

We have also neglected absorptive effects in the GaAs substrate, which should be effectively decoupled from the MLS with a sufficient number of periods. Figure 6.5.1 (previous page) shows the modelled reflectance spectrum of a structure containing 12 periods of (606Å Al_{0.10}Ga_{0.30}As + 721Å AlAs), with the AlGaAs uppermost, on a substrate of GaAs. Indices are as for the table of calculated MLS reflectivities. The correctness of this multiple matrix reflectance modelling has been verified by comparison with the work of another research group [14] and running a number of other test structures for which the spectra have already been published in the literature.

6.5.2 THE INTEGRATED AFPM STRUCTURE

Having modelled the reflective properties of the MLS we are now concerned with what happens when this structure is included as part of an epitaxial p-i-n diode containing quantum wells. Using the same program as for the MLS we have computed the reflectance spectrum of the integrated AFPM structure shown below in Fig. 6.5.2.1.

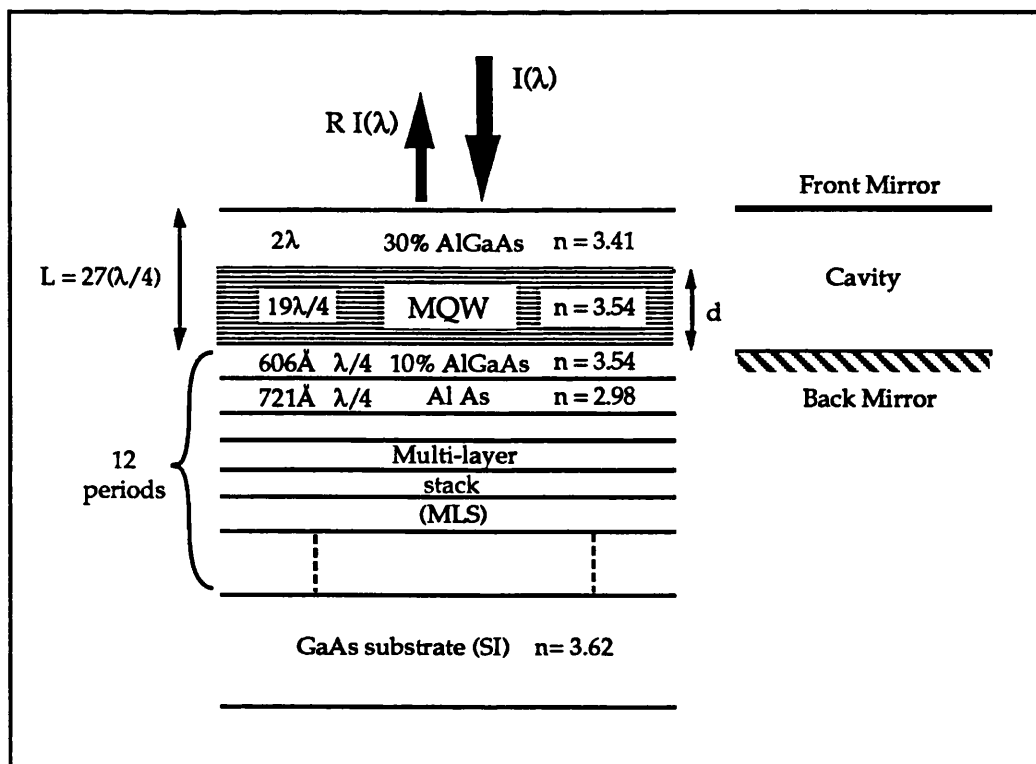


FIGURE 6.5.2.1:

The structure of the integrated MQW asymmetric FP modulator.

The presence of the overlayers of AlGaAs and MQW means that there are now two mirrors – the AlGaAs:air and the MLS:MQW interfaces, with a spacer layer filled with semiconductor. This constitutes the asymmetric FP cavity. We ignore reflections taking place at the MQW:AlGaAs interface because of the small refractive index mismatch.

A feature of this particular structure which should be noted is that the cavity thickness must be equal to an *odd* integral number of $\pi/2$ (or $\lambda/4$) in order to put the shallow asymmetric cavity resonance at the desired operating wavelength. Normally, with a symmetric FP étalon, to achieve a resonance at a chosen wavelength, the cavity is made an integral number of *half-wavelengths* thick. This is explained in more detail in Figure 6.5.2.2, where the phase shift of successive reflected rays from the AFPM is shown schematically. The rays have been drawn at off-normal incidence simply to show clearly the multiple beams, and the incident wavelength is equal to the centre wavelength of the MLS. The first component of the total reflected amplitude does not enter the cavity but undergoes a π phase shift on reflection from the air:semiconductor interface because of the lower index of the medium from which the wave is incident. The Fresnel formula gives $r_f = (n_1 - n_2)/(n_1 + n_2)$ for a wave travelling from medium 1 to 2 across a dielectric interface, thus r_f is negative with respect to the incident wave – equivalent to a π phase shift.

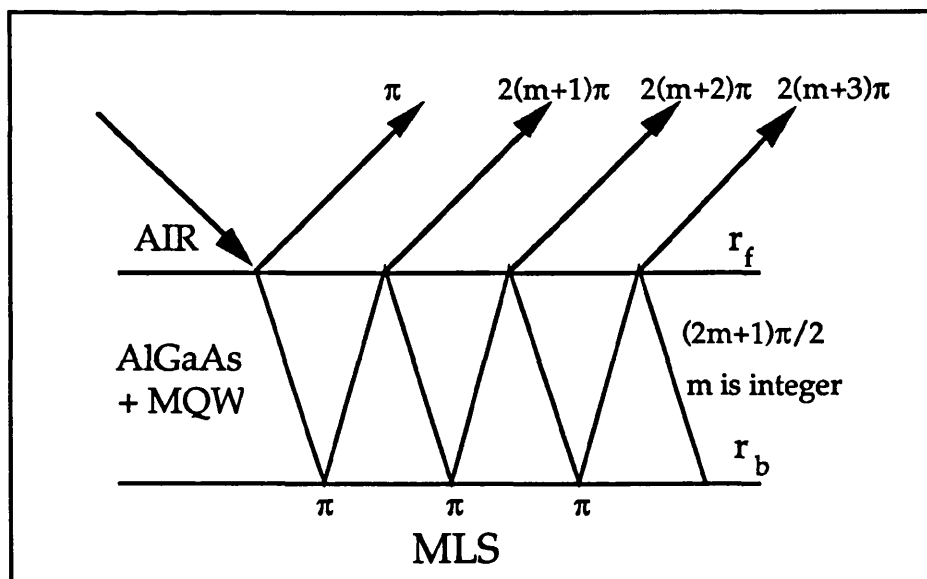


FIGURE 6.5.2.2:

Illustrating the phase relationship between the components of the total reflected amplitude from the integrated AFPM.

All subsequent rays make an integral number of round trips, plus π phase shift for each reflection from the MLS, which add up to $2(m + n)\pi$ relative to the incident wave (m and n are both integers with m determined by the cavity thickness and n being the order of the reflected component). The reflection back into the cavity from the front mirror causes no phase shift since light is incident from the higher index medium. Thus the first reflected ray is an odd multiple of π out of phase with the rays which pass through the cavity, and maximum destructive interference can occur at the MLS centre wavelength.

The effect of the cavity thickness on the shape of the high reflectance band and position of the resonances is illustrated by Figs. 6.5.2.3 and 6.5.2.4. In the first case we have modelled the multilayer structure of Fig. 6.5.2.1 with the cavity $27\lambda/4$ thick. Here, an FP resonance sits as required at the MLS centre wavelength (860nm), with extra resonances either side of this within the high reflectance band. The number of these will increase as the thickness of the cavity is increased, reducing the mode spacing. In the second case an extra quarter-wavelength has been added to the top AlGaAs layer, resulting in a shift of the FP resonances away from the MLS centre.

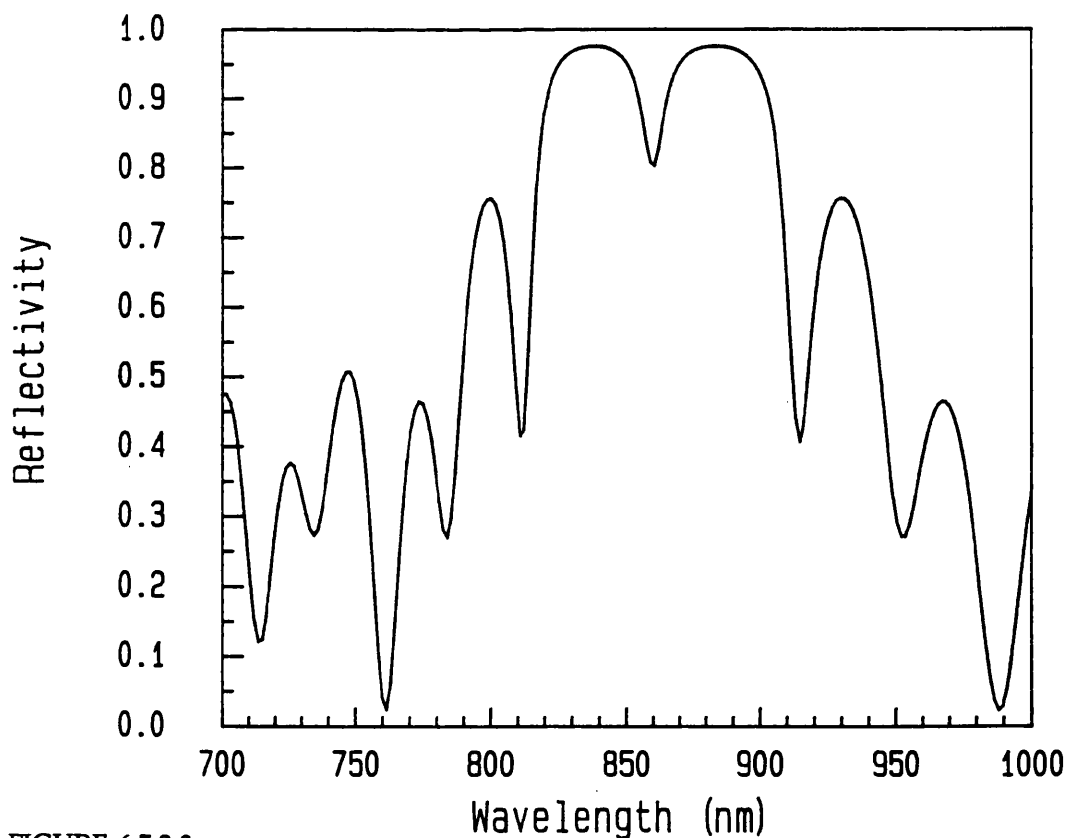


FIGURE 6.5.2.3:
The modelled reflectance spectrum of the "correct" AFPM structure.

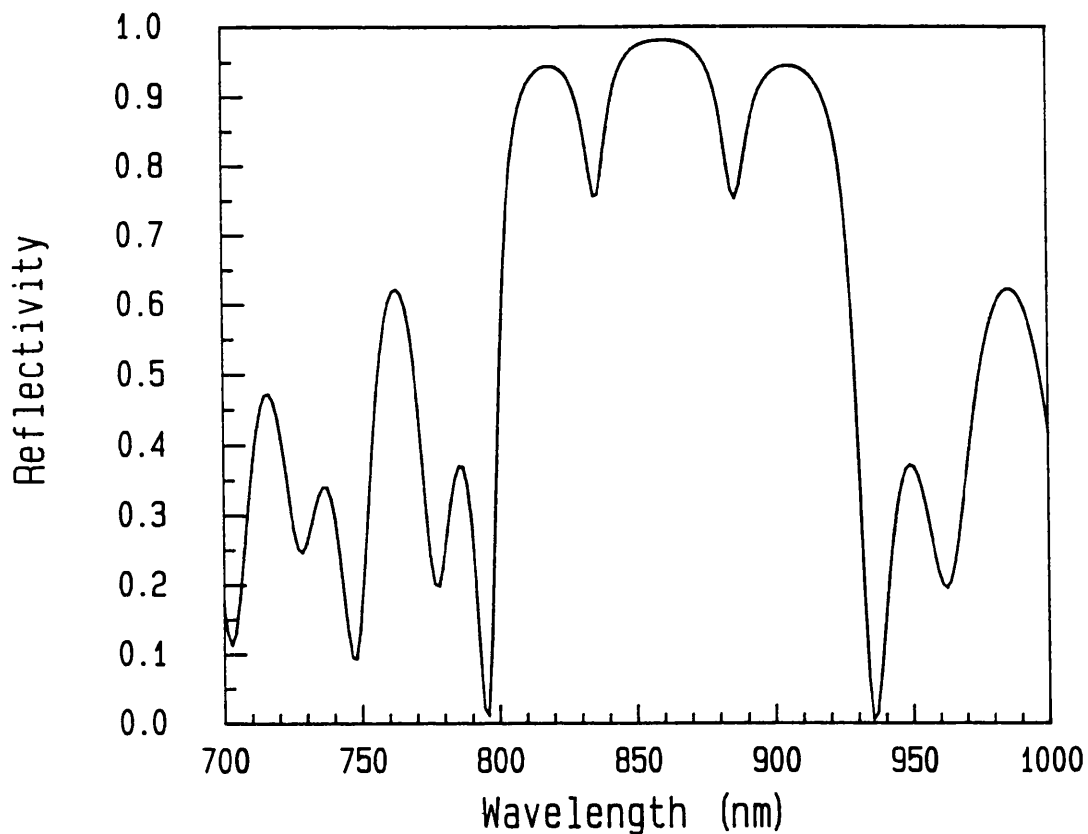


FIGURE 6.5.2.4:
The modelled reflectance spectrum of the "incorrect" AFPM structure.

The intention here has been to get some feel for the main features likely to be found in the reflectance spectra of structures containing MLS mirrors, so the effect of absorption has not been taken into account in modelling these spectra. However, as already mentioned, the MLS layers are chosen to be of an Al mole fraction such that very little absorption occurs at the MLS centre wavelength (also the AFPM operating wavelength), which in turn is required to be $\approx 10\text{nm}$ away from the unbiased absorption edge of the MQW structure. The presence of absorption at wavelengths below $\approx 850\text{nm}$ will merely dampen oscillations in the reflection spectrum, whilst the low initial absorption in the real device at wavelengths longer than this should allow valid comparison of real and modelled (unbiased) AFPM spectra.

6.5.3 MLS REFLECTORS GROWN BY MOVPE

Prior to attempting to grow the full epitaxial AFPM structure we wished to be certain of the quality of the built-in reflector stack. A number of MLS structures were grown in order to check that peak reflectivities in

excess of 95% were being achieved, and in the correct wavelength band. Note that if the layer thicknesses or the estimate of the layer refractive indices are only $\approx 4\%$ out, this means that the centre wavelength of the stack will be more than 30nm away from the desired position of $\approx 860\text{nm}$, so growth calibration must be reasonably accurate. Wafer scanning shown in Fig. 6.5.3 indicates the high quality which was eventually achieved. The structure was that of the modelled MLS in Fig. 6.5.1.

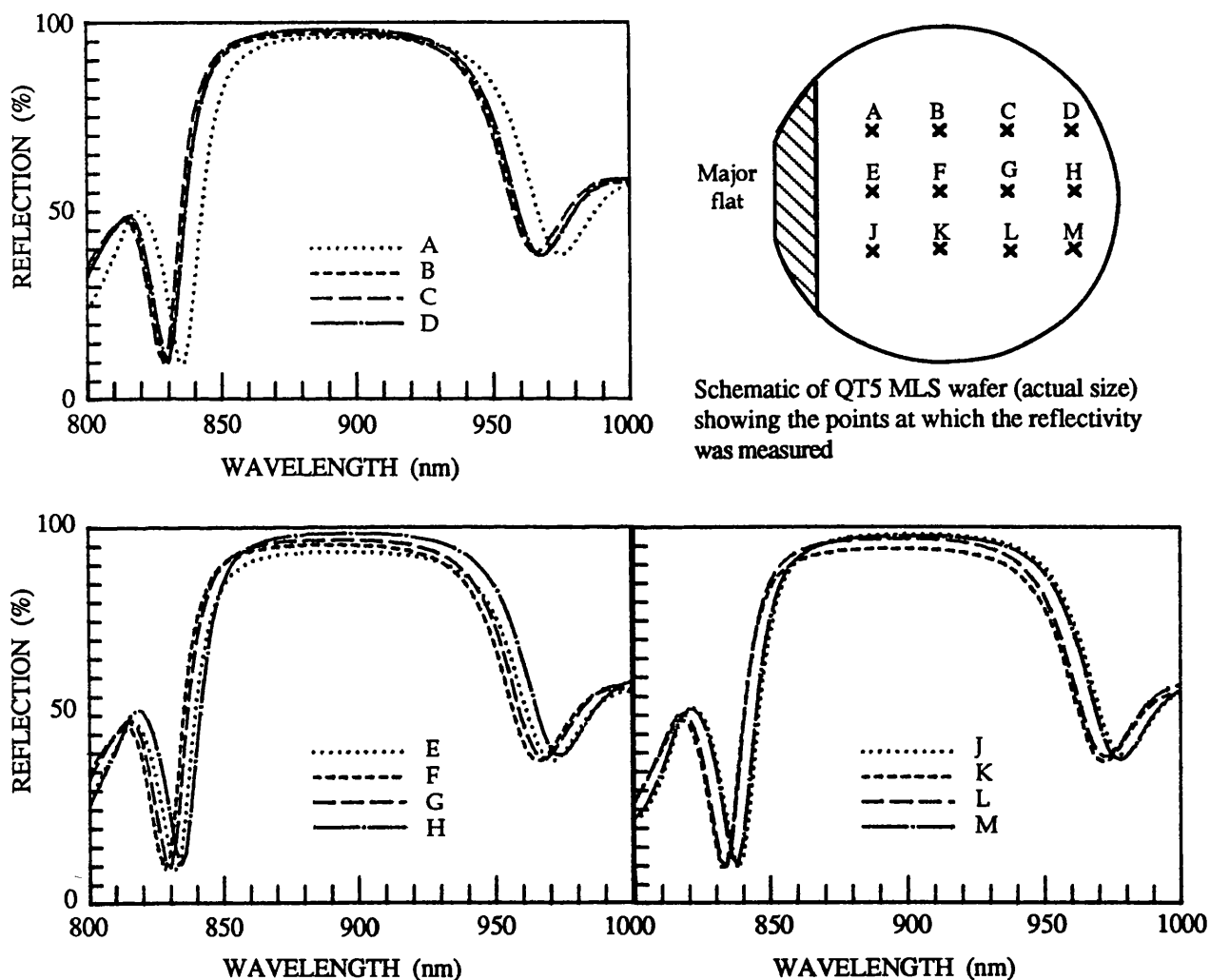


FIGURE 6.5.3:

Wafer mapping of the reflectance spectrum for a 12-period MLS structure (QT5) grown by MOVPE at Sheffield University by J. S. Roberts & C. Button.

Reflectivity of more than 90% is observed over a range of at least 80nm for the sampled area of 6cm^2 . The centre wavelength, λ_0 , varies by only $\approx 1\%$, and even though the average value is closer to 900nm, rather than 860nm, the reflectivity remains suitably high at what would be the

optimum operating wavelength of an AFPM with 100Å quantum wells. Measurements were carried out using the standard experimental set-up of § 4.2.2, with reflected intensity spectra normalized to Au layer freshly deposited on part of the wafer itself, shown in Fig. 6.5.3 as the shaded region.

6.6 THE INTEGRATED AFPM

6.6.1 DESIGN AND FABRICATION OF THE INTEGRATED AFPM (CB145)

The integrated structure which was finally grown, after optimization of the growth of the MLS mirror alone, was largely based on the modelled AFPM of § 6.5.2. Figure 6.6.1.1 shows the exact details.

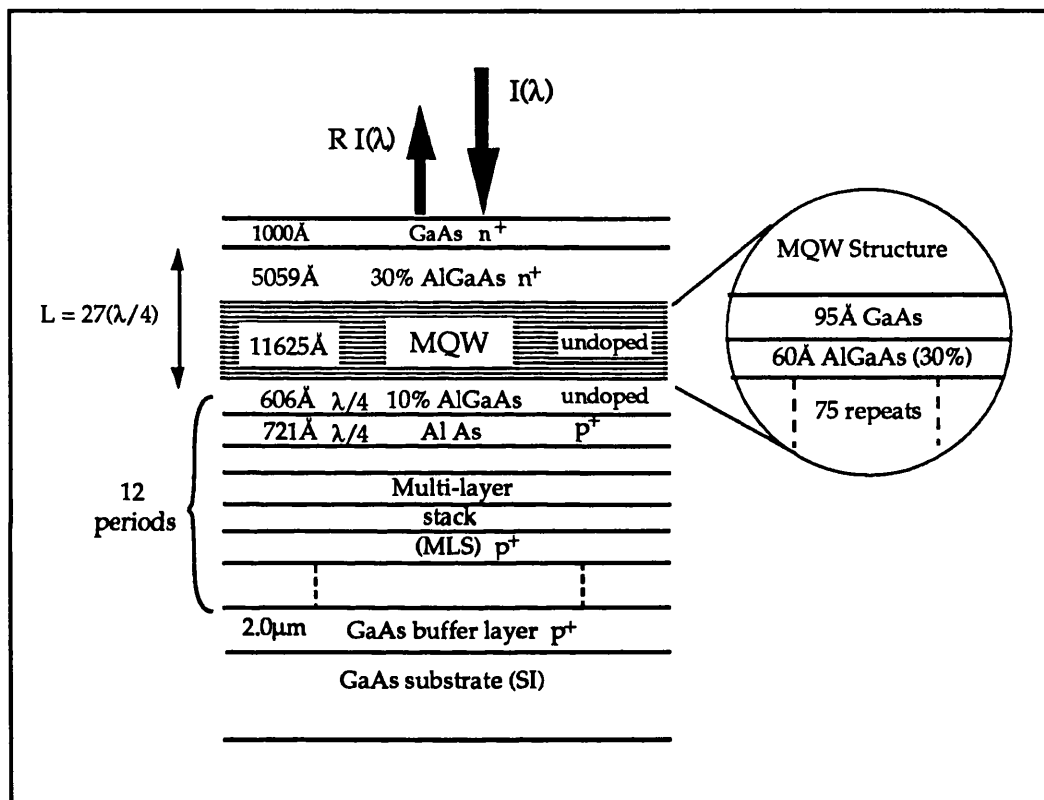


FIGURE 6.6.1.1: The as-grown integrated AFPM structure (Sample CB145).

In contrast to previous MQW diodes this structure had to be grown upside-down – as *n-i-p* rather than *p-i-n* – because of the high *p*-type background doping ($> 10^{17}$) in the MOVPE-grown AlAs. The MLS must be situated below the MQWs so that light can be modulated in reflection from the top surface. So, to avoid any extra *p-n* junctions due to different intrinsic doping types in the AlAs and $\text{Al}_{0.1}\text{Ga}_{0.9}\text{As}$, the MLS was doped *p*-type throughout, apart from the uppermost $\text{Al}_{0.1}\text{Ga}_{0.9}\text{As}$ layer, which was left undoped to act as a buffer region, preventing any diffusion of the *p*-type dopant into the undoped MQWs. The MLS was grown on top of a thick *p*⁺ GaAs buffer layer (accessed by mesa etching to allow ohmic

contacts to be made), the whole structure being on a semi-insulating GaAs substrate.

From the results of Chapter 4, $75 \times 95 \text{ \AA}$ quantum wells in the MQW region were regarded as being sufficient to easily attain the critical level of absorption at the operating wavelength. Together with $\text{Al}_{0.3}\text{Ga}_{0.7}\text{As}$ barriers of 60 \AA the whole MQW structure was designed to be 19 quarter-wavelengths at $\approx 860 \text{ nm}$ and a weighted mean refractive index of ≈ 3.53 . As in previous devices we have kept the barrier thickness to 60 \AA to reduce bias voltage, whilst maintaining the field necessary for the quantum-confined Stark shift. The diode is completed with a layer of n -doped $\text{Al}_{0.3}\text{Ga}_{0.7}\text{As} \approx 0.5 \mu\text{m}$ thick, which represents another 8 quarter-wavelengths, and, for contacting purposes, a highly n -doped GaAs layer of $\approx 0.1 \mu\text{m}$. This last layer was intended to be selectively etched away from the fabricated device window to avoid absorptive losses.

The (MQW + AlGaAs) cavity has been designed here to be equivalent to a total of $27\lambda/4$. However, the calibration of growth rates for the MOVPE system is accurate to only $\approx 5\%$. Furthermore, there is generally a variation in grown thickness across the surface of the wafer of $\approx 5\%$ caused by non-uniform gas flow in the MOVPE reactor. Therefore, getting the right cavity length for a required resonant wavelength would seem to be something of a lottery. In fact, all these inaccuracies actually work in our favour, at least for the demonstration of the device. 5% variation over the area of an epitaxial structure which is roughly $2\text{-}3 \mu\text{m}$ thick means $1000\text{-}1500 \text{ \AA}$ variation over the wafer. This is more or less equivalent to a π phase change, which is also the phase difference between adjacent FP resonances. Hence, some part of the wafer should offer the cavity thickness necessary to put the FP resonance at the desired wavelength.

To show the variation in the position of the FP resonance and find the most useful device areas on the as-grown wafer we have mapped the reflection spectrum at the points on the wafer marked in the inset of Figure 6.6.1.2 (over page). In the square centimetre labelled B the uniformity is quite good, with the effect of the $e1\text{-}hh1$ and $e1\text{-}lh1$ exciton absorption clearly visible between $\approx 842\text{-}850 \text{ nm}$, and the asymmetric cavity resonance at $\approx 860 \text{ nm}$. In area A the cavity resonance is still at a suitable wavelength to provide good AFPM characteristics, although the variation is more significant than in area B. This will affect the maximum contrast, the bias voltage at which it is achieved and the

insertion loss. In area C the resonance approaches the exciton absorption edge too closely for the material to be useful. However, this is an indication of the fact that there is indeed enough absorption in the MQW structure to strongly reduce the cavity reflectivity.

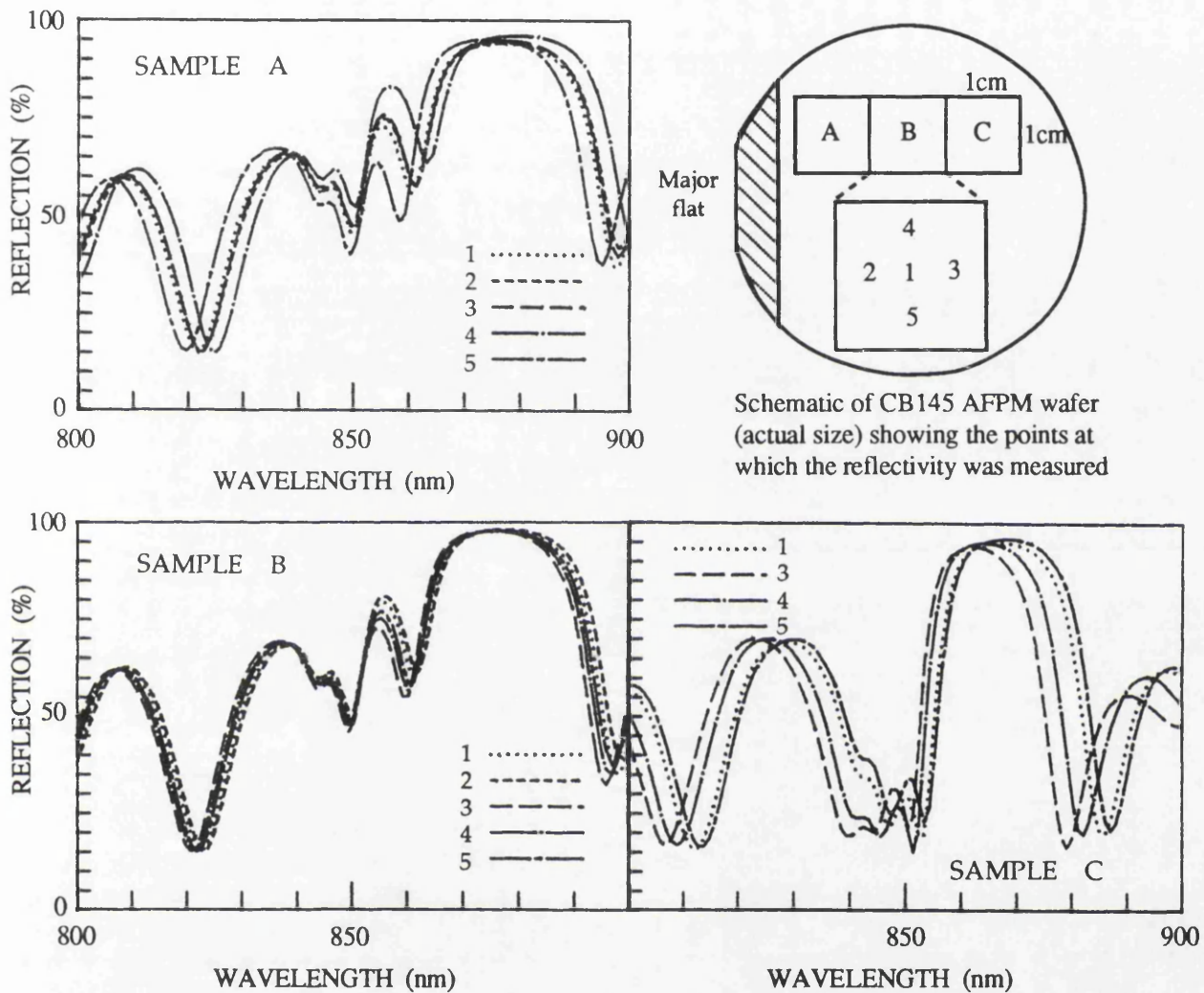


FIGURE 6.6.1.2:

Wafer mapping of AFPM structure CB145 showing the effect of the variation of the position of the cavity resonance relative to the MQW absorption edge. Data not corrected for background light.

Having identified the areas of the wafer where the FP resonance was at a suitable wavelength relative to the MQW absorption spectrum, a number of AFPMS were fabricated. The reflection modulator requires only the same processing steps as the basic MQW p-i-n photodiode (see Chapter 2), except that the depth of the mesa etch must be more accurately controlled to leave part of the p⁺ GaAs buffer layer exposed for contacting. Despite some uncertainty as to the effect of the multiple heterojunctions in the

reflector stack on the electrical properties, it was found that the AFPM diodes had generally very similar I-V characteristics to previous MQW diodes without integrated stacks.

6.6.2 REFLECTION MODULATION MEASUREMENTS ON THE INTEGRATED AFPM (CB145)

All measurements were again made using the experimental set-up of Figs. 2.3.4.1 & 4.2.2.1, and the normalization method described in § 6.4.2. It was discovered during these experiments that there was a component of the measured reflected signal which was not actually incident on the modulator itself, but backscattered from the metal barrel of the microscope objective used to focus light onto the device. The presence of a significant amount of scattered light was only suspected when we observed the image of the AFPM on the IR camera and the "measured" contrast seemed much too small ($\approx 3:1$ max.) for the change in appearance of the device. This was verified by preventing the light from the monochromator from entering the focussing lens, at which the detected signal fell to zero. Figure 6.6.2.1 shows the image of the AFPM in its on and off states at a wavelength around 862nm. To obtain a bright enough image the monochromator slits must be set wide open, thus the incident light is more broad band than would be the case for the actual measurement of reflection spectra. The lowest off state is obtained with 8-9V bias.

To remove the spurious reflected signal, with the monochromator set at the correct operating wavelength and the light focussed tightly into the modulator window, we removed the modulator from the focal plane of the microscope objective and replaced it with a piece of coarse black cloth, intended to act as a perfect absorber. The output of the lock-in amplifier, into which the reflected signal is fed, was then set to zero using the variable offset control. Any signal subsequently detected could then be solely ascribed to the AFPM device.



IMAGE OF UNBIASED AFPM

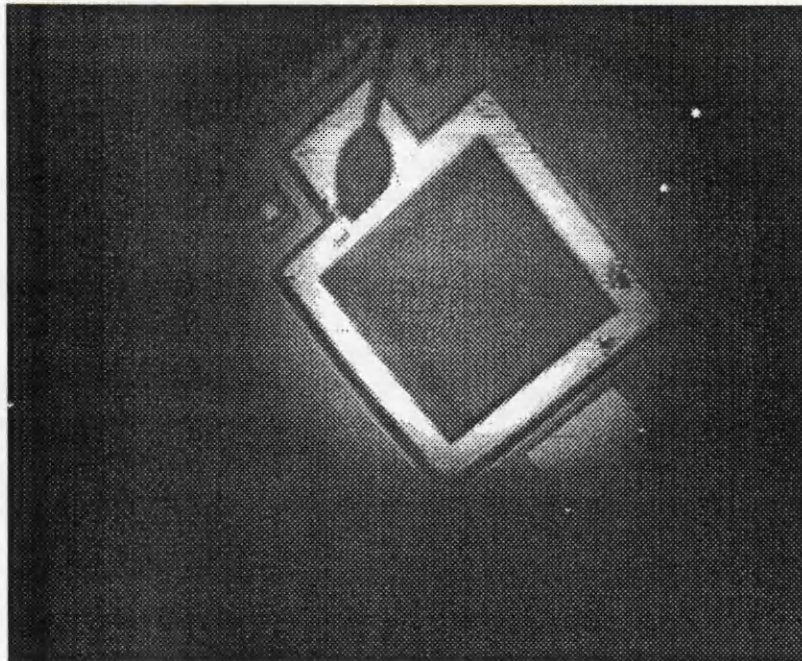


IMAGE OF BIASED AFPM (9V)

FIGURE 6.6.2.1:
Frame-grabbed images from an IR camera of the CB145 AFPM in its on and off states. The device window is $400\mu\text{m} \times 400\mu\text{m}$. (Frame-grab software courtesy of Mark Abbott, UCL.)

In Figs. 6.6.2.2-4 we have plotted the normalized reflection spectra of the CB145 AFPM for bias voltages between 0 and 12V, with particular attention to biases either side of the optimum 9V.

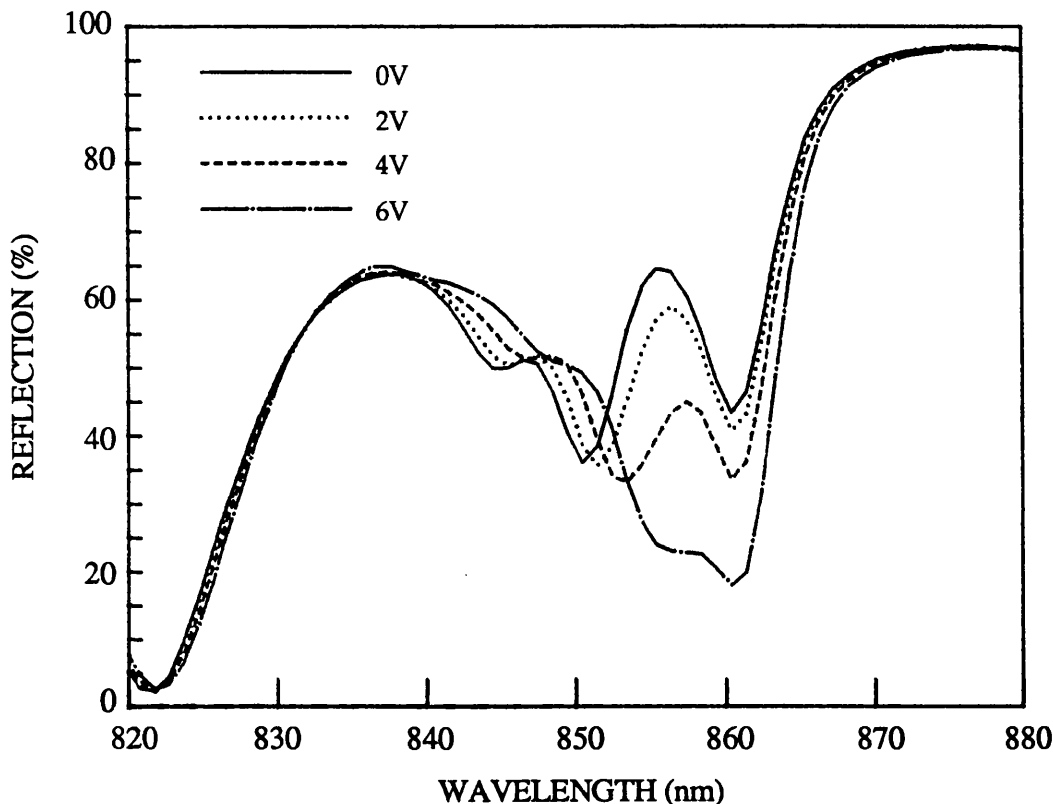


FIGURE 6.6.2.2:
Normalized reflection spectra for CB145 AFPM at bias voltages below the optimum.

Firstly there are a couple of spectral features which are worth noting. Close to 822nm there is an FP resonance which is made deep by the MQW absorption which remains strong at all biases. The level of this minimum – in the 2-3% range – is confirmation that the spectra are well calibrated. The R vs αd calculations in Fig. 6.2.2.1 indicate that R should remain ≤ 0.03 for αd in the wide range between 0.39 and 0.86. For this device $d \approx 0.71\mu\text{m}$, so the upper limit on α is $\approx 12,000\text{cm}^{-1}$. We have already found α to be in the region of $11\text{-}12000\text{cm}^{-1}$ in this part of the spectrum for comparable MQW structures studied in Chapter 3.

Looking at the FP resonance at the device operating point, it appears to be a little deeper than expected. The on state reflectivity is $\approx 44\%$ rather than the 60-70% we might expect with $\alpha \leq 1000\text{cm}^{-1}$ in the exciton absorption tail at $\approx 860\text{nm}$. The explanation for this is almost certainly absorption in the GaAs cap layer, which was not removed from the first

batch of devices, and which is likely to cause a loss in intensity of $\approx 10\%$ per pass. However, the contribution from this layer also reduces the amount of field-induced absorption required of the MQWs in order to bring the reflection down close to zero. With this GaAs layer removed, ignoring for the moment the effect on the resonant wavelength, it would therefore have been necessary to apply slightly more bias to the device to achieve the same off state.

As far as the bias response is concerned, little happens until we get up to $\approx 4\text{V}$ (equivalent to $\approx 33\text{kV}\cdot\text{cm}^{-1}$). The heavy-hole exciton can be seen shifting progressively towards the FP resonance, then, between 4-6V, there is a sharp increase in the reflection change as the exciton absorption becomes aligned with the resonance.

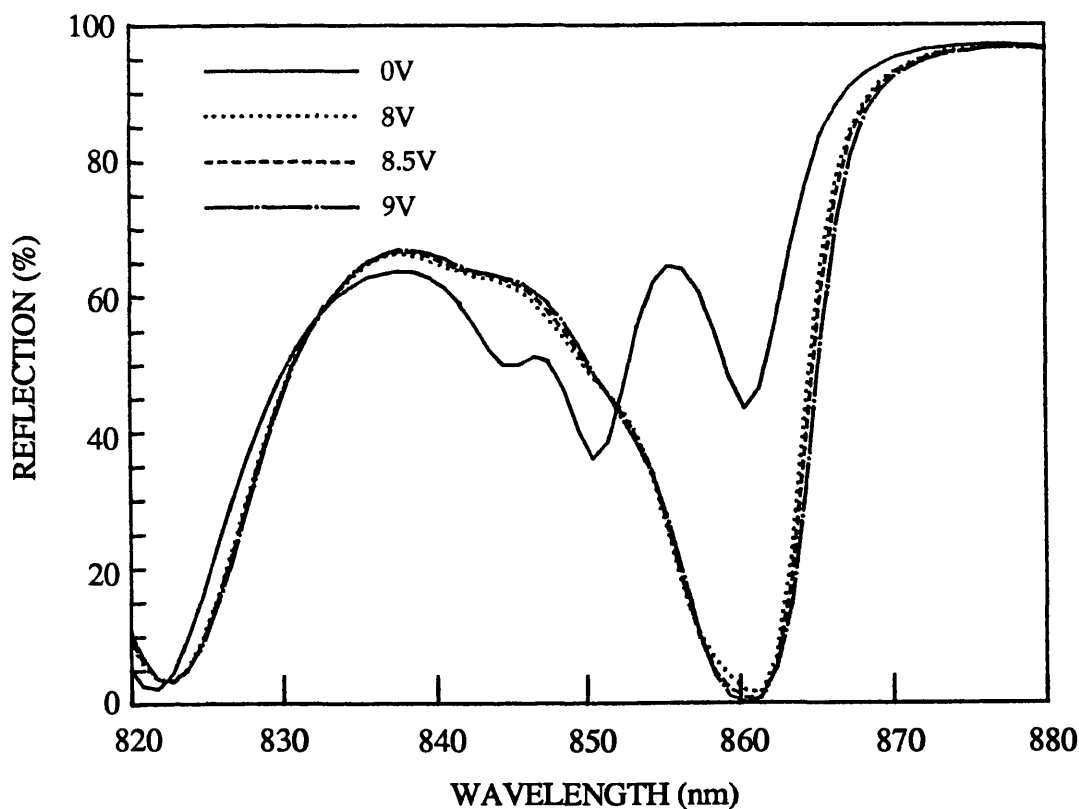


FIGURE 6.6.2.3:

Normalized reflection spectra for CB145 AFPM around the optimum bias point (9V).

There are further large changes up to 8V, but the whole spectrum then becomes almost independent of bias voltage up to $\approx 12\text{V}$, and the reflection minimum close to 860nm remains below $\approx 2\%$. In fact, at 9V the reflection falls below the lower limit of what we can accurately measure. The minimum recorded appears to be $\approx 0.1\%$, however, the background noise in the measurement system and accuracy limits of the

A-D converter mean that we can only be confident that the minimum is not more than $\approx 0.4\%$. Thus the maximum contrast ratio is at least 100:1 (20dB).

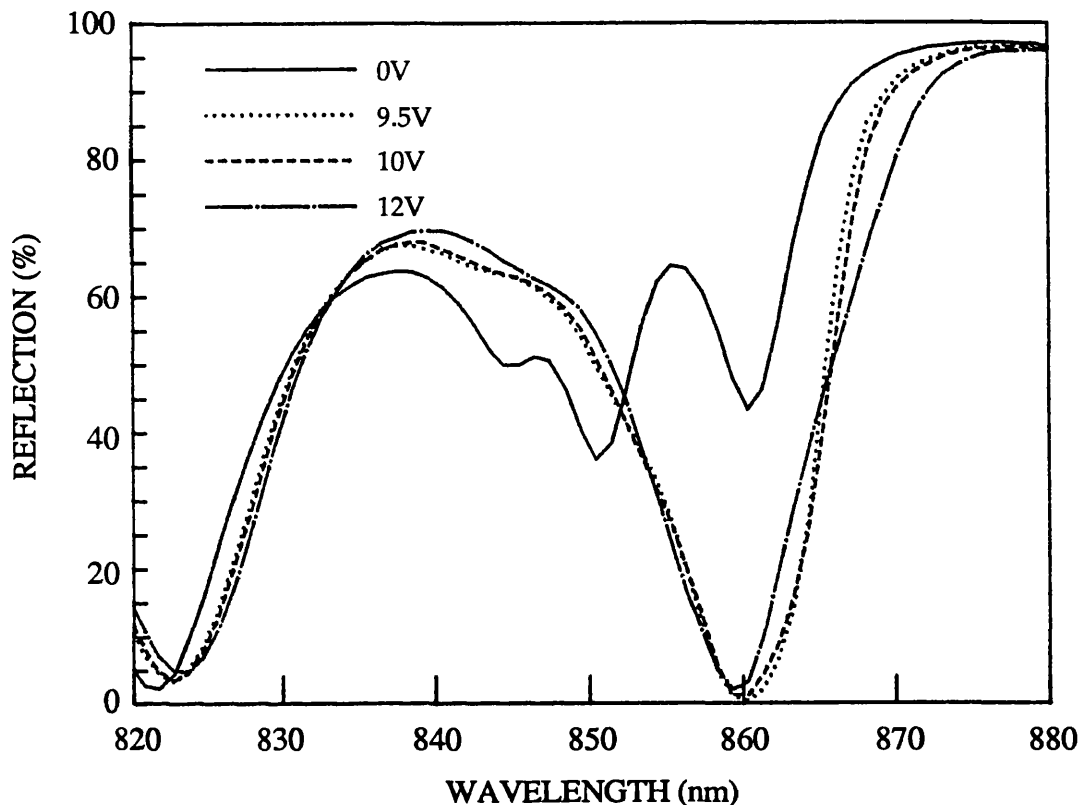


FIGURE 6.6.2.4:
Normalized reflection spectra for CB145 AFPM increasing the bias beyond the optimum.

The spectra above show a clear definition of the unbiased cavity resonance and the e1-hh1 exciton peak at the MQW absorption edge. In the modelled spectra of § 6.3, where the separation of the resonance and the exciton is roughly the same as here, the resonance is much less distinct. This can be simply ascribed to the improved quality of the more recent MQW structures, giving a sharper absorption edge. The modelled AFPM characteristics are based on electro-absorption spectra for the KLB461 sample (§ 3.4) where doping broadening effects were apparent.

The spectral changes in reflection are displayed in Fig. 6.6.2.5 (over page). The reason for the double minimum in ΔR for 8-10V bias is the broadened shape of the FP resonance under bias. At the optimum bias the cavity finesse has effectively decreased from ≈ 10 , for low absorption, to $\approx 2-3$ at high absorption. A maximum ΔR of $\approx -53\%$ is observed near

863nm, and importantly for device applications, $|\Delta R|$ is 40% or greater over at least 7nm between 8-10V. The experimental reflection changes are not as large as might have been expected for this type of structure, but this is due again to the increased insertion loss caused by the GaAs capping layer, which means that at the resonance we cannot possibly get any more than $\approx 44\%$ change.

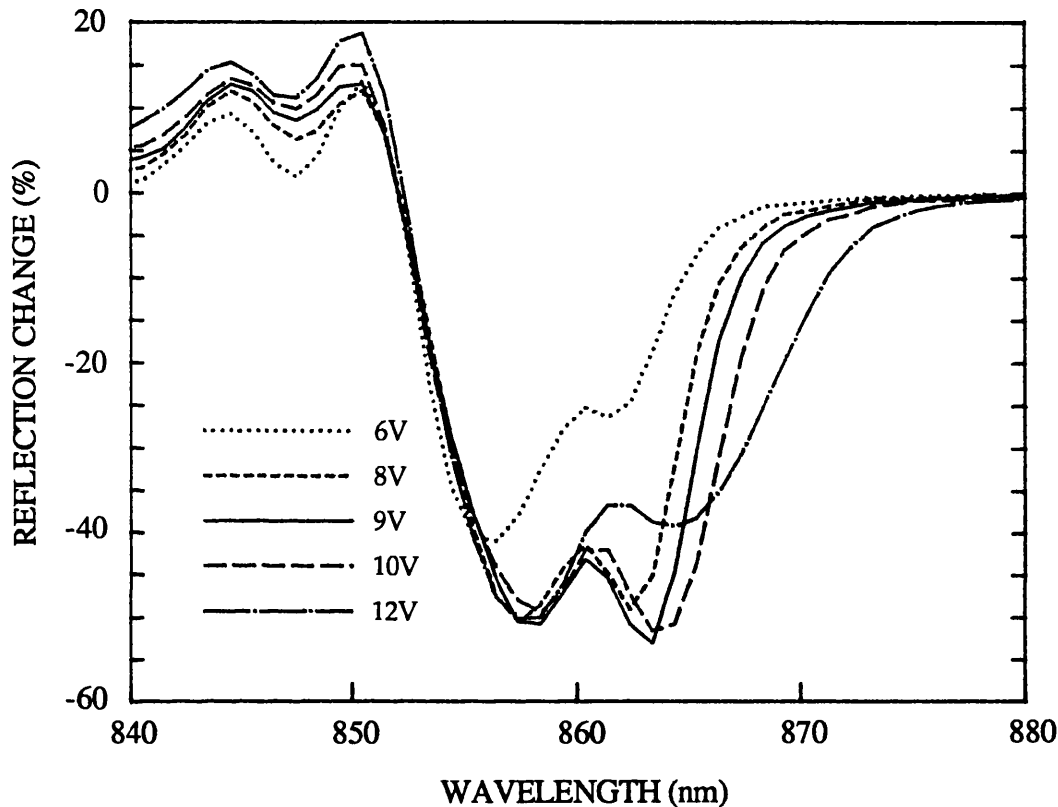


FIGURE 6.6.2.5:
Normalized reflection change spectra for CB145 AFPM.

With optimization and the removal of the GaAs cap layer, from the results of our earlier modelling (§ 5.4.2, § 6.3.1) it should be possible to increase $|\Delta R_{\max}|$ to more than 70% and achieve a ΔR of $\geq 50\%$ over 7-8nm.

The contrast spectra, which are plotted on the following page in Fig. 6.6.2.6, apparently show that the peak modulation at 9V is in excess of 26dB. As we have already said, we cannot be certain of the accuracy of the measurement at this particular point, but the peak is at worst up to the 20dB mark. The linewidth at such high contrast is, however, not much different from that expected for the high-finesse SFPM structures, being 1nm or less. This would pose problems in a real working environment with other devices in close proximity, where temperature fluctuations

could force the resonance peak to move, and worse, drift relative to the MQW absorption edge. If, however, such high contrast is not necessary and 10dB is sufficient, then the linewidth is rather better, being $\approx 4.3\text{nm}$ at the optimum bias of 9V, and at least 2.3nm in the range 8-12V.

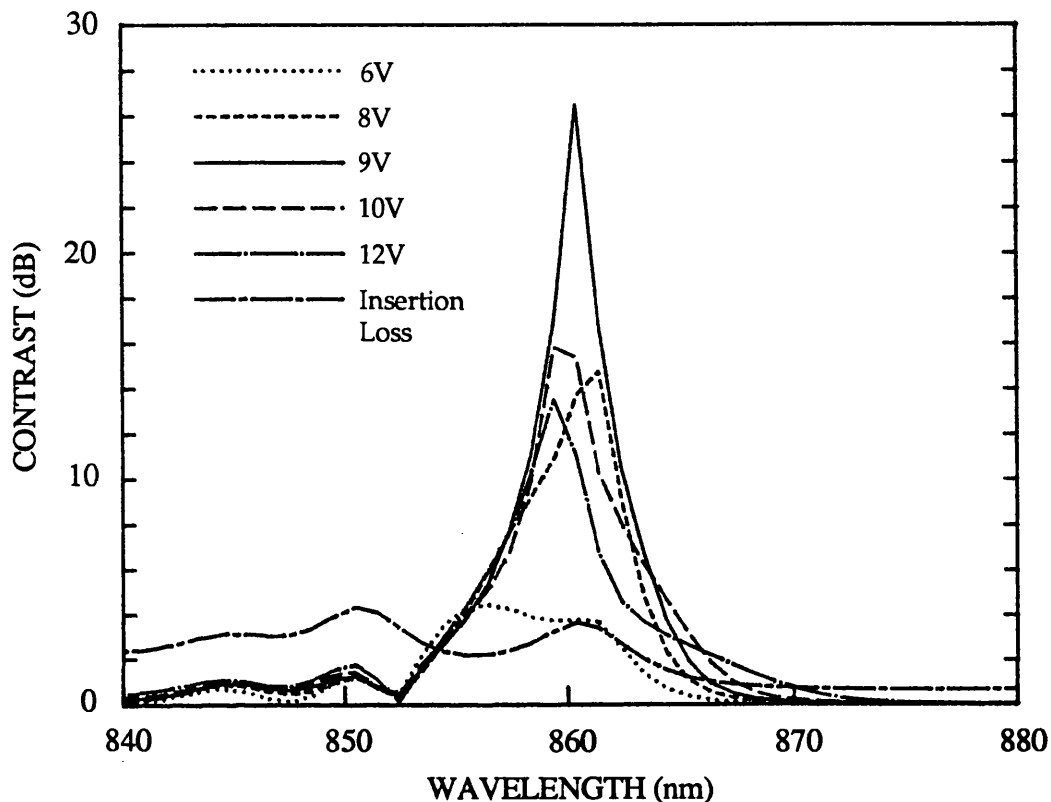


FIGURE 6.6.2.6:
Contrast spectra for CB145 AFPM. Also shown is the zero-bias insertion loss.

Confirming the estimates made in § 5.6, calculations of the effect of temperature changes on the shift of the MQW absorption edge, relative to the shift of the FP resonance due to thermally-induced refractive index changes, indicate that the operating temperature of the AFPM will need to be controlled to $\approx \pm 10^\circ\text{C}$ in order to achieve stable, high contrast modulation [15].

One further property of the AFPM structure which we have not emphasised up to now is the potential for high efficiency photodetection. At the biased resonant wavelength the reflection falls roughly to zero when there is sufficient absorber in the cavity. Incident light is at this point almost completely absorbed. The fraction transmitted into the GaAs substrate is roughly $(1 - R_{\text{MLS}})$, and so should be less than 5%. Thus we have the means of achieving the theoretical maximum responsivity

of ≈ 0.68 A/W (at ≈ 850 nm) with an MQW region only $\approx 1\mu\text{m}$ thick.

Photocurrent spectra in Fig. 6.6.2.7 show the expected increase in responsivity with bias due to the FP resonance at ≈ 860 nm, where the photocurrent is initially less than that at the e1-hh1 exciton because of the low absorption. The resonant photocurrent peak rises to ≈ 1.6 times the original exciton height (at ≈ 850 nm) despite the fact that there is a significant loss in absorption strength as the exciton is field-shifted.

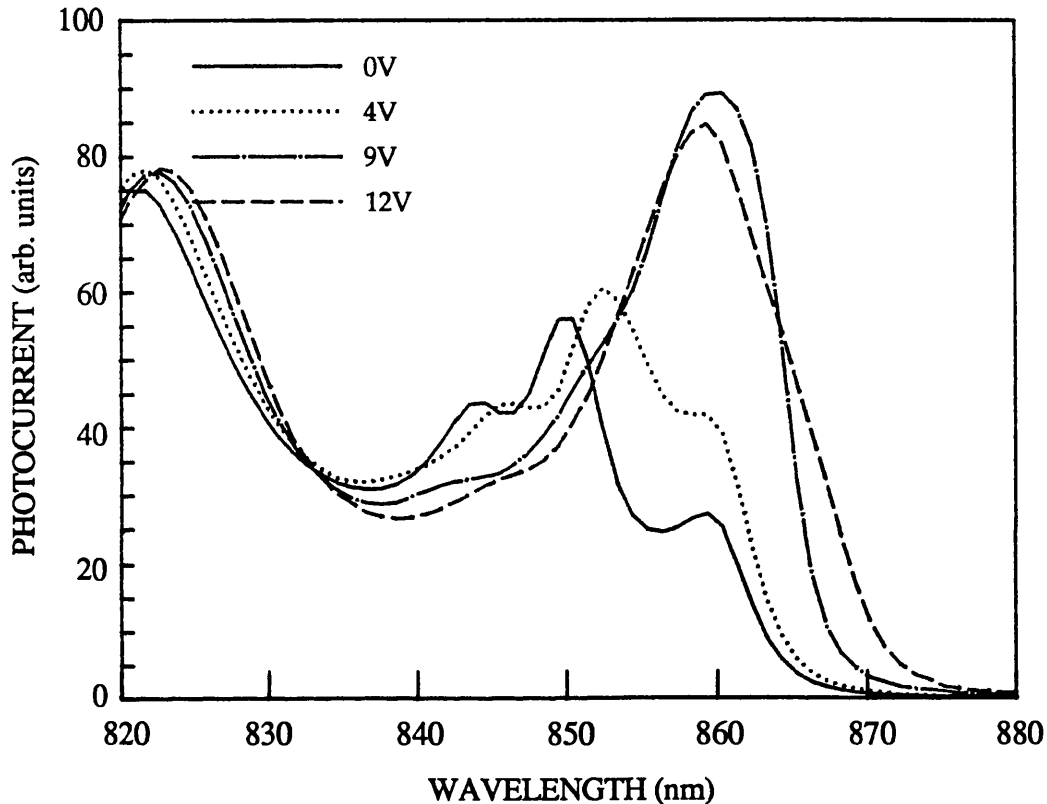


FIGURE 6.6.2.7:

Biased photocurrent spectra for CB145 AFPM. The actual responsivity has not been calibrated as yet.

This dual functionality is useful for example in an optical to electronic interface. The modulator could either operate in a "send" mode – impressing information onto a d.c. optical input, which is then reflected back to be detected in a separate part of the system, or in a "receive" mode – generating photocurrent at a fixed bias according to a modulated optical input. The principle has already been demonstrated with an MQW reflection modulator by Wood et al. [16].

The work which has been presented in this chapter can be found in alternative forms in a series of recent publications [17-19].

6.7 SUMMARY

6.7.1 MEASURED AFPM PERFORMANCE

In this final chapter we have designed and demonstrated a novel optical reflection modulator. The MQW asymmetric Fabry-Perot cavity modulator (AFPM for short) has been proven to be capable of contrast higher than 20dB (100:1) with less than 10V bias. At the 10 dB contrast level for the AFPM the modulation linewidth is significantly better than that for high-finesse symmetric cavity MQW modulators [9,10], which have not yet achieved this level of contrast. Previous MQW modulators operating at normal incidence in transmission have contained as much as 4 μ m of MQW material to achieve 10dB contrast [19], thus requiring high bias voltages and incurring very large insertion losses. A reflection modulator of a similar construction to the AFPM, but made non-resonant by the application of a front surface AR coating [20], has shown up to 9dB contrast. The insertion loss in this case was also high since the operating wavelength was at the unbiased e1-hh1 exciton peak. Table 6.1 is a comparison of the optimum performance of various types of MQW modulator with that of the AFPM.

Reference	Maximum Contrast (dB)	Insertion Loss (dB)	Bias (V)	Figure of merit (V^{-1})
Chapter 4	2.2	1.8	6	0.204
Chapter 4	3.4	3.2	12	0.088
Hsu et al. [20]	10.0	13.0	20	0.038
Boyd et al. [21]	8.7	5.7	18	0.085
Simes et al. [9]	9.0	5.8	25	0.062
Lee et al. [10]	7.0	2.9	15	0.161
AFPM	≥ 20	3.7	9	≥ 0.60

TABLE 6.1:

Performance of a number of normal incidence GaAs MQW modulators. The first three are transmission modulators, the last four are reflection modulators.

The first two devices are from our own measurements on MQW transmission modulators in Chapter 4 of this thesis. The data are for the 87Å well modulator at the optimum bias-absorbing and bias-transmitting wavelengths.

The figure of merit is defined as Contrast/(Insertion Loss x Voltage), which is somewhat arbitrary, but serves to underline just how much the use of the AFPM has improved the performance figures. Obviously this figure of merit does not show the wavelength sensitivity of the modulation. However, the AFPM has a larger linewidth than any of the other devices, at any of the contrast levels reached. At 3dB, for example, referring back to Fig. 6.6.2.6 we find that the AFPM linewidth is $\approx 10\text{nm}$.

The modulation is also very large in terms of reflection change, ΔR , rather than contrast. At 9-10V a ΔR of at least 40% over a 9-10nm range has been measured experimentally, with peak changes of more than 50%. Only the device demonstrated by Lee et al [10] has previously shown a ΔR of $\approx 40\%$. Modelling suggests that changes in reflection of more than 70% are attainable with the structure we have already tested.

Although we have made no high frequency measurements of the AFPM performance a very similar structure (i.e. MQW *p-i-n* diode incorporating a reflector stack) has been demonstrated by Boyd et al [22] operating at 5.5 GHz, a limit due only to the RC time constant. We note that the use of the asymmetric cavity, which reduces the amount of MQW material required to produce a given contrast, and hence narrows the intrinsic region of the diode, will lead to higher device capacitance when structures are optimized to operate with fewer wells at lower bias voltages.

6.7.2 FUTURE CONSIDERATIONS FOR AFPM DESIGN AND OPERATION

We have usually considered in our modelling in this chapter an AFPM with 95% reflectivity at the back surface. This is simply to get a reasonable picture of the expected device performance when the MLS mirror is not perfect i.e. real. However, it should be noted that the insertion loss for a given background absorption at the resonance can be reduced by making the back mirror reflectivity even closer to 100%. Adding in a few more periods to the MLS structure as we have grown it would do this. Twenty periods should suffice to push the reflectivity uniformly up to 98-99%.

The maximum reflection change would then increase, but on the other hand so would the critical amount of absorption needed to achieve a zero reflectivity. Thus more wells and more bias would be needed to operate at the same wavelength. The alternative would be to move the resonance closer to the MQW absorption edge, but this would tend to offset improvements in the insertion loss gained by increasing the back reflectivity.

The AFPM structures modelled and tested have been the simplest form of this device, with the front mirror simply defined by the GaAs:air interface. This gives a very reproducible front reflectivity of $\approx 30\%$. Since we know we can reliably achieve MLS reflectivities of $\approx 95\%$, this leaves us the cavity length as the only possible problem parameter to fix in order to make the device work well. It may be sensible from a fabrication point of view to keep the most simple structure, however, in the quest for ever lower operating voltages, there is the possibility of increasing the front reflectivity of the cavity, retaining the asymmetric character, but reducing the critical absorption for high contrast. If R_f were 0.5 rather than 0.3, with $R_b = 0.95$, the critical αd would fall from 0.58 to 0.32 (see Eq. 6.4). The drawback is that the insertion loss at resonance becomes more sensitive to the absorption present in the unbiased state. With $\alpha d = 0.08$ and $R_f = 0.3$ the on-state reflection is ≈ 0.48 , but this drops to ≈ 0.28 for $R_f = 0.5$ (see Appendix for relevant equations). To increase the front surface reflectivity is a seemingly simple matter of growing a few periods of another MLS. However, the calculation in § 6.5.1 of the MLS reflectivity as a function of the number of periods shows that there is a very rapid change in the reflectivity from ≈ 0.12 to 0.78 going from 2 to 8 periods. The control of the front mirror reflectivity to somewhere between 0.40 and 0.60 will therefore be quite difficult, and may well be best avoided.

The final comments concern the angular dependence of the modulation and the sensitivity to temperature.

We have only considered the case of light incident normal to the surface here. It is likely that applications such as optical interconnections will necessitate using the AFPM off-normal, in order to achieve spatial separation of the incident and reflected signals and avoid feedback into the optical source. There are two principle effects which come into play. Firstly, the effective cavity thickness increases as the incident angle increases relative to the normal, which shifts the position of the cavity resonance. The strong refraction towards the normal on entering the

semiconductor will compensate for this to some extent. Secondly, away from normal incidence the centre wavelength of the MLS reflector begins to shift relative to the input wavelength [4], which alters the phase change on reflection from the stack (the phase change is only π radians at the centre wavelength) and thus affects the position of the resonance. The peak reflectivity is also reduced at non-normal incidence and there is a polarization dependence. All of which will complicate the device response.

Temperature will affect the AFPD in two ways. The MQW absorption edge will shift with temperature by roughly 3\AA per degree [23]. At the same time the change in refractive index associated with the absorption shift will cause the resonant wavelength to change. It is unlikely that the two will move at the same rate. The contrast or reflection change is fairly sensitive to the position of the MQW absorption edge relative to the asymmetric cavity resonance. So the effect of temperature will probably be more marked for this type of device, where the absorption edge and the resonance shift relative to the input wavelength and also relative to each other, than for a non-resonant electro-absorptive modulator.

Finally, from our initial proposal and preliminary demonstration of the AFPD [17, 18] there has been interest from other research groups in the general asymmetric cavity concept. Very soon after we produced the first integrated structure [19], Yan et al at the University of California, Santa Barbara achieved substantially the same results with an MBE-grown device [24]. The idea has also been applied to the InGaAs-InP quantum well system [25] as a means of overcoming the intrinsically poorer electro-absorption properties (compared to GaAs-AlGaAs) for this material which is potentially important for the $1.55\ \mu\text{m}$ optical fibre low-loss window.

REFERENCES (Chapter 6)

- [1] B. S. WHERRETT, "Fabry-Perot bistable cavity optimization on reflection", *IEEE J. Quantum Electron.* (1984), QE-20, pp. 646-51.
- [2] A. MILLER, G. PARRY and R. DALEY, "Low-power nonlinear Fabry-Perot reflection in CdHgTe at 10 μ m", *IEEE J. Quantum Electron.* (1984), QE-20, pp. 710-15.
- [3] M. BORN and E. WOLF, "Principles of Optics" 6th Edition, Ch. 1.6 "Wave propagation in a stratified medium. Theory of dielectric films", pp. 51-70, Pergamon Press, 1980.
- [4] HANDBOOK OF OPTICS, Ed. W. G. Driscoll, Ch. 8, "Filters and coatings based on interference in thin films", pp. 42-63, McGraw Hill/Optical Society of America, 1978.
- [5] H. A. McLEOD, "Thin film optical filters", Ch. 5 "Multilayer high-reflectance coatings", pp. 88-110, Adam Hilger 1970.
- [6] J. P. VAN der ZIEL and M. ILEGEMS, "Multilayer GaAs-Al_{0.3}Ga_{0.7}As dielectric quarter wave stacks grown by molecular beam epitaxy", *Appl. Opt.* (1975), 14, pp. 2627-30.
- [7] R. L. THORNTON, R. D. BURNHAM and W. STREIFER, "High reflectivity GaAs-AlGaAs mirrors fabricated by metalorganic chemical vapour deposition", *Appl. Phys. Lett.* (1984), 45, pp. 1028-30.
- [8] D. R. P. GUY and N. APSLEY, "Optical devices using III-V quantum wells and multilayers", *Proc. SPIE (Technologies for optoelectronics, 1987)*, 861, pp. 27-32.
- [9] R. J. SIMES, R. H. YAN, R. S. GEELS, L. A. COLDREN, J. H. ENGLISH, A. C. GOSSARD and D. G. LISHAN, "Electrically tunable Fabry-Perot mirror using multiple quantum well index modulation", *Appl. Phys. Lett.* (1988), 53, pp. 637-9.
- [10] Y. H. LEE, J. L. JEWELL, S. J. WALKER, C. W. TU, J. P. HARBISON and L. T. FLOREZ, "Electrodispersive multiple quantum well modulator", *Appl. Phys. Lett.* (1988), 53, pp. 1684-6.
- [11] P. L. GOURLEY and T. J. DRUMMOND, "Visible room-temperature, surface-emitting laser using an epitaxial Fabry-Perot resonator with AlGaAs/AlAs quarter-wave high reflectors and AlGaAs/GaAs quantum wells", *Appl. Phys. Lett.* (1987), 50, pp. 1225-7.
- [12] H. C. CASEY Jr, D. D. SELL and M. B. PANISH, "Refractive index of Al_xGa_{1-x}As between 1.2 and 1.8eV", *Appl. Phys. Lett.* (1974), 24, pp. 63-5.
- [13] A. N. PIKHTIN and A. D. YAS'KOV, "Dispersion of the refractive index of semiconducting solid solutions with the sphalerite structure", *Sov. Phys. Semicond.* (1980), 14, pp. 389-92.

- [14] D. R. P. GUY, private communication.
- [15] P. J. STEVENS, Ph. D. Thesis, University of London 1990.
- [16] T. H. WOOD, E. C. CARR, B. L. KASPER, R. A. LINKE, C. A. BURRUS and K. L. WALKER, "Bidirectional fibre-optical transmission using a multiple-quantum-well (MQW) modulator/detector", *Electron. Lett.* (1986), **22**, pp. 528-9.
- [17] M. WHITEHEAD and G. PARRY, "High contrast reflection modulation at normal incidence in an asymmetric multiple quantum well Fabry-Perot structure", *Electron. Lett.* (1989), **25**, pp. 566-8.
- [18] M. WHITEHEAD, G. PARRY, A. RIVERS and J. S. ROBERTS, "Multiple quantum well asymmetric Fabry-Perot etalons for high-contrast, low insertion loss optical modulation", *OSA Proceedings on Photonic Switching*, J.E.Midwinter & H.S.Hinton, eds., (Optical Society of America, Washington, D.C., 1989), Vol. 3, pp.15-21.
- [19] M. WHITEHEAD, A. RIVERS, G. PARRY, J. S. ROBERTS and C. BUTTON, "Low-voltage multiple quantum well reflection modulator with on:off ratio>100:1", *Electron. Lett.* (1989), **25**, pp.984-5.
- [20] T. Y. HSU, W. Y. WU and U. EFRON, "Amplitude and phase modulation in a 4 μ m-thick GaAs/AlGaAs multiple quantum well modulator", *Electron. Lett.* (1988), **24**, pp. 603-4.
- [21] G. D. BOYD, D. A. B. MILLER, D. S. CHEMLA, S. L. McCALL, A. C. GOSSARD and J. H. ENGLISH, "Multiple quantum well reflection modulator", *Appl. Phys. Lett.* (1987), **50**, pp. 1119-21.
- [22] G. D. BOYD, J. E. BOWERS, C. E. SOCCOLICH, D. A. B. MILLER, D. S. CHEMLA, L. M. F. CHIROVSKY, A. C. GOSSARD and J. H. ENGLISH, "5.5 GHz multiple quantum well reflection modulator", *Electron. Lett.* (1989), **25**, pp. 558-60.
- [23] J. M. HALLEY, P. WHEATLEY, M. WHITEHEAD and J. E. MIDWINTER, "Thermal crosstalk in multi-quantum well optical logic arrays", Paper 3, IEE Colloquium "Multi-quantum well devices -Physics, engineering and applications", IEE, London WC2, England, 8th Dec. 1986.
- [24] R. H. YAN, R. J. SIMES and L. A. COLDREN, "Electroabsorptive Fabry-Perot reflection modulators with asymmetric mirrors", *IEEE Photon. Technol. Lett.* (1989), **1**, pp. 273-5.
- [25] A. K. TIPPING, G. PARRY and A. MOSELEY, "Modelling the optimum performance of InGaAs/InP based asymmetrical Fabry-Perot modulator devices", submitted to *Semiconductor Science and Technology*, October 1989.

CONCLUSIONS

As the conclusions from the work contained in this thesis have been summarised at the end of each chapter, we shall simply re-iterate the main points here.

In Chapter 2, using photocurrent spectroscopy, it was demonstrated that MQW *p-i-n* diodes of sufficient quality for optical modulation can be grown by MOVPE. In the course of this work, both MOVPE and MBE materials ultimately displayed the quality necessary to show near theoretical performance – at least for wells of $\approx 100\text{\AA}$.

Having considered the problems associated with low-finesse FP resonance in MQW transmission modulation spectra, we showed in Chapter 3 that absorption spectra may be deduced with reasonable accuracy from photocurrent spectra. Spectra derived in this way conform very closely to electro-absorption sum rules.

The performance of non-resonant MQW transmission modulators in terms of maximum contrast/transmission change is ultimately limited by the trade-off between absorption change, $\Delta\alpha$, and the proportion of absorbing (QW) material in the MQW structure. In Chapter 4 we have examined the effect of altering the well width. As well widths become narrower, $\Delta\alpha_{\text{max}}$ increases. However, we found in Chapter 2 that the isolating AlGaAs barriers cannot be reduced much below $\approx 60\text{\AA}$ before interwell coupling becomes strong. Thus the proportion of absorbing material falls as well width is reduced. As a result the product $\Delta\alpha_{\text{max}}d$, where d is the total QW thickness, remains reasonably constant. The principal effects of changing the well width are to increase the field required for maximum modulation and push the operating point to shorter wavelengths for narrow wells, and to switch the operating point from the biased to the unbiased e1-hh1 exciton peak for wide wells, whilst reducing the field for maximum modulation.

We concluded from the modelling of MQW FP cavity modulators, in Chapter 5, that high-finesse devices designed to utilise electro-refractive effects would be undesirable from an applications point of view, despite being capable, in theory, of more than 20dB contrast at $\approx 10\text{V}$. The problems with this type of device are a narrow optical bandwidth and a high sensitivity to temperature and cavity thickness variations due to epitaxial growth.

Further FP device modelling has enabled us to propose, and subsequently demonstrate, a better alternative to the high-finesse device. The asymmetric Fabry-Perot cavity modulator (AFPM) achieves very high contrast by using MQW electro-absorption to obtain complete destructive interference of light reflected from the device. Being an intrinsically low-finesse device, the AFPM can exhibit large absolute reflection changes over an optical bandwidth much larger than that of high finesse devices, and even non-resonant modulators. Its sensitivity to temperature and cavity thickness variations should also be significantly less than that of high-finesse devices. The AFPM is thus by far the best option for high-contrast, low-voltage modulation in a normal-incidence structure.

We have calculated in Chapter 5 that the AFPM operating voltage can be reduced to less than 5V for a contrast of 10dB, with 3dB insertion loss. It is likely that the voltage can be reduced further by using wider ($\approx 150\text{\AA}$) wells or coupled quantum wells, although with larger insertion losses.

Future work on the AFPM should focus on designs to meet specific applications since the contrast and reflection change must always be traded off against insertion loss and bias voltage. Consideration must also be given to the effect of temperature changes.

FABRY-PEROT CAVITY EQUATIONS

Here we derive the equations which govern the transmission and reflection of light at normal incidence in an absorptive Fabry-Perot cavity.

Consider a plane electromagnetic wave of amplitude E_0 at normal incidence on the Fabry-Perot cavity structure in Fig. A1. The cavity is bounded by the interfaces between the cavity medium, refractive index n_2 , and the external media with indices n_1 and n_3 . These interfaces constitute the cavity mirrors. The thickness of the cavity is L , and it contains an absorbing layer with *amplitude* absorption coefficient γ , and thickness d .

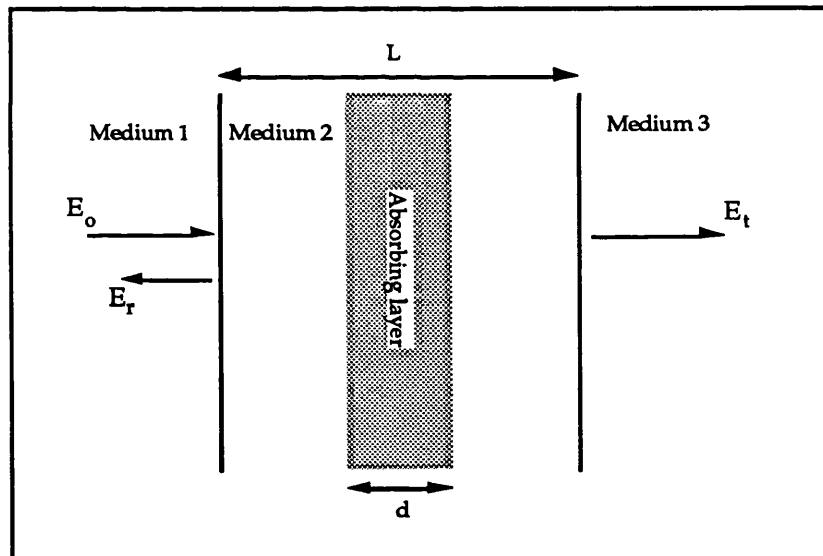


FIGURE A1:

The model Fabry-Perot cavity

On passing from medium 1 into the cavity, the incident wave suffers partial reflection with an *amplitude* reflection coefficient r_{12} , the corresponding transmission coefficient being t_{12} , with the subscript indicating the direction of propagation. These coefficients are determined by the refractive indices of the two media at the interface, according to the Fresnel equations, as shown on the following page.

$$r_{12} = \frac{n_1 - n_2}{n_1 + n_2} \quad r_{21} = \frac{n_2 - n_1}{n_1 + n_2} \quad t_{12} = \frac{2n_1}{n_1 + n_2} \quad t_{21} = \frac{2n_2}{n_1 + n_2}$$

With each traversal of the cavity the wave undergoes a phase shift $e^{i\delta}$, where $\delta = (2\pi n_2 L)/\lambda$, and an attenuation $e^{-\gamma d}$. Hence we may write the sum of the amplitudes of the transmitted waves as:

$$E_t = E_o t_{12} t_{23} e^{i\delta} e^{-\gamma d} + E_o t_{12} t_{23} r_{23} r_{21} e^{i3\delta} e^{-3\gamma d} + E_o t_{12} t_{23} (r_{23} r_{21})^2 e^{i5\delta} e^{-5\gamma d} + \dots$$

and that for the reflected waves:

$$E_r = E_o r_{12} + E_o t_{12} t_{21} r_{23} e^{i2\delta} e^{-2\gamma d} + E_o t_{12} t_{21} r_{23}^2 r_{21} e^{i4\delta} e^{-4\gamma d} + E_o t_{12} t_{21} r_{23}^3 r_{21}^2 e^{i6\delta} e^{-6\gamma d} + \dots$$

Taking the sum to infinity for the transmitted waves, we find that the amplitude transmission coefficient is:

$$t = \frac{E_t}{E_o} = \frac{t_{12} t_{23} e^{i\delta} e^{-\gamma d}}{1 - r_{23} r_{21} e^{i2\delta} e^{-2\gamma d}} \quad \dots(A1)$$

Similarly, for the amplitude reflection coefficient:

$$r = \frac{E_r}{E_o} = r_{12} + \frac{t_{12} t_{21} r_{23} e^{i2\delta} e^{-2\gamma d}}{1 - r_{21} r_{23} e^{i2\delta} e^{-2\gamma d}} \quad \dots(A2)$$

This expression is simplified further by making the substitutions $r_{21} = -r_{12}$ and $t_{12} t_{21} = 1 - r_{12}^2$, based on the Fresnel equations above, to give:

$$r = \frac{r_{12} + r_{23} e^{i2\delta} e^{-2\gamma d}}{1 - r_{21} r_{23} e^{i2\delta} e^{-2\gamma d}} \quad \dots(A3)$$

In experiments we can measure only the *intensity* transmission and reflection coefficients, the expressions for which are obtained by multiplying t and r by their respective complex conjugates, t^* and r^* . Thus we have:

$$T = tt^* = \frac{(1 - r_{12}^2)(1 - r_{23}^2) e^{-2\gamma d}}{1 + r_{21}^2 r_{23}^2 e^{-4\gamma d} - 2r_{21} r_{23} e^{-2\gamma d} \cos 2\delta} \quad \dots(A4)$$

and

$$R = rr^* = \frac{r_{12}^2 + r_{23}^2 e^{-4\gamma d} - 2r_{21}r_{23} e^{-2\gamma d} \cos 2\delta}{1 + r_{21}^2 r_{23}^2 e^{-4\gamma d} - 2r_{21}r_{23} e^{-2\gamma d} \cos 2\delta} \quad \dots(A5)$$

where we have used the following substitution for the normal situation where $n_1 = n_3$, air being the external medium at the front and back.

$$t_{12}^2 t_{23}^2 = t_{12} t_{21} \left(\frac{n_2}{n_1} \right) t_{23} t_{32} \left(\frac{n_3}{n_2} \right) = (1 - r_{12}^2)(1 - r_{23}^2)$$

The intensity reflection coefficients for the front and back surfaces of the cavity, R_f and R_b , are defined by $R_f = r_{12}^2 = r_{21}^2$ and $R_b = r_{23}^2$. Substituting also $\cos 2\delta = 1 - 2\sin^2 \delta$ and $\alpha = 2\gamma$, where α is the *intensity* absorption coefficient, Eqns A4 and A5 can be recast as follows:

$$T = \frac{(1 - R_f)(1 - R_b)e^{-\alpha d}}{(1 - \sqrt{R_f R_b} e^{-\alpha d})^2 + 4\sqrt{R_f R_b} e^{-\alpha d} \sin^2 \delta} \quad \dots(A6)$$

$$R = \frac{R_f + R_b e^{-2\alpha d} - 2\sqrt{R_f R_b} e^{-\alpha d} + 4\sqrt{R_f R_b} e^{-\alpha d} \sin^2 \delta}{(1 - \sqrt{R_f R_b} e^{-\alpha d})^2 + 4\sqrt{R_f R_b} e^{-\alpha d} \sin^2 \delta} \quad \dots(A7)$$

If we now make the following definitions:

$$R_\alpha = \sqrt{R_f R_b} e^{-\alpha d} \quad \dots(A8)$$

$$A = \frac{(1 - R_f)(1 - R_b)e^{-\alpha d}}{(1 - R_\alpha)^2} \quad \dots(A9)$$

$$F = \frac{4R_\alpha}{(1 - R_\alpha)^2} \quad \dots(A10)$$

$$B = \frac{R_f [1 - (R_\alpha / R_f)]^2}{(1 - R_\alpha)^2} \quad \dots(A11)$$

we can express the intensity transmission and reflection coefficients in a final, very simple form:

$$T = \frac{A}{1 + F \sin^2 \delta} \quad \dots(A12)$$

$$R = \frac{B + F \sin^2 \delta}{1 + F \sin^2 \delta} \quad \dots(A13)$$

It is often useful, as we have done in this thesis when presented with a spectrum containing Fabry-Perot oscillations, to look at the maxima and minima of those oscillations in order to derive information about the cavity absorption or its surface reflectivities. From Eq. A12, we can see by inspection that the limiting cases for transmission will occur when the

$\sin^2\delta$ term has its maximum and minimum values of 1 and 0 respectively. Maximum transmission occurs when $\delta = 0$ or $m\pi$, where m is an integer; minimum transmission when $\delta = m\pi/2$. Thus we have:

$$T_{\max}(\delta = 0, m\pi) = A = \frac{(1-R_f)(1-R_b)e^{-\alpha d}}{(1-\sqrt{R_f R_b}e^{-\alpha d})^2} \quad \dots(A14)$$

$$T_{\min}(\delta = m\pi/2) = \frac{A}{1+F} = \frac{(1-R_f)(1-R_b)e^{-\alpha d}}{(1+\sqrt{R_f R_b}e^{-\alpha d})^2} \quad \dots(A15)$$

Maximum reflection occurs at the point of minimum transmission and vice versa. The reflection equations at anti-resonance and resonance respectively are therefore:

$$\begin{aligned} R_{\max}(\delta = m\pi/2) &= \frac{B+F}{1+F} = \frac{R_f + R_b e^{-2\alpha d} + 2\sqrt{R_f R_b} e^{-\alpha d}}{(1 + \sqrt{R_f R_b} e^{-\alpha d})^2} \\ &= \frac{(\sqrt{R_f} + \sqrt{R_b} e^{-\alpha d})^2}{(1 + \sqrt{R_f R_b} e^{-\alpha d})^2} \quad \dots(A16) \end{aligned}$$

$$\begin{aligned} R_{\min}(\delta = 0, m\pi) &= B = \frac{R_f + R_b e^{-2\alpha d} - 2\sqrt{R_f R_b} e^{-\alpha d}}{(1 - \sqrt{R_f R_b} e^{-\alpha d})^2} \\ &= \frac{(\sqrt{R_f} - \sqrt{R_b} e^{-\alpha d})^2}{(1 - \sqrt{R_f R_b} e^{-\alpha d})^2} \quad \dots(A17) \end{aligned}$$

In the limit of zero absorption, for example at wavelengths $\approx 20\text{nm}$ off the MQW absorption edge which we observe experimentally, Eqns A14-17 reduce to their most simple form.

$$T_{\min}^{\max}(\alpha = 0) = \frac{(1-R_f)(1-R_b)}{(1 \mp \sqrt{R_f R_b})^2} \quad \dots(A18)$$

$$R_{\min}^{\max}(\alpha = 0) = \frac{(\sqrt{R_f} \pm \sqrt{R_b})^2}{(1 \pm \sqrt{R_f R_b})^2} \quad \dots(A19)$$

PUBLICATIONS

This is a list of published papers which have resulted directly from the content of this thesis, or to which I have contributed.

As primary author:

- [1] **"Quantum confined Stark shifts in MOVPE-grown GaAs-AlGaAs multiple quantum wells"**
M.Whitehead, G.Parry, J.S.Roberts, P.Mistry, P.Li Kam Wa and J.P.R.David,
Electronics Letters, Vol.23, No.20, pp.1048-50, 24th Sept. 1987.
- [2] **"Experimental confirmation of a sum rule for room-temperature electro-absorption in GaAs-AlGaAs multiple quantum well structures"**
M.Whitehead, G.Parry and K.Woodbridge,
Paper 129, 8th National Quantum Electronics Conference, University of St.Andrews, Scotland, 21-25th Sept. 1987.
- [3] **"Electric field effects in quantum well devices and their applications in digital optics"**
M.Whitehead, A.Rivers, G.Parry, J.S.Roberts, P.Mistry, P.Li Kam Wa and M.A.Pate,
Paper 8, IEE Colloquium "Optical techniques for information processing", IEE, Savoy Place, London WC2, England, 25th Nov. 1987.
- [4] **"Experimental confirmation of a sum rule for room-temperature electro-absorption in GaAs-AlGaAs multiple quantum well structures"**
M.Whitehead, G.Parry, K.Woodbridge, P.J.Dobson and G.Duggan,
Applied Physics Letters, Vol.52, No.5, pp.345-7, 1st Feb. 1988.
- [5] **"Modelling of field-induced optical modulation in GaAs-AlGaAs multiple quantum well Fabry-Pérot structures"**
M.Whitehead, G.Parry and P.Wheatley,
Paper 18, SIOE '88, UWIST, Cardiff, Wales, 28-29th Mar. 1988.
- [6] **"The effects of well width on the characteristics of GaAs/AlGaAs multiple quantum well modulators"**
M.Whitehead, P.Stevens, A.Rivers, G.Parry, J.S.Roberts, P.Mistry, M.A.Pate and G.Hill,
Applied Physics Letters, Vol.53, No.11, pp.956-8, 12th Sept. 1988.

- [7] **"An investigation of étalon effects in GaAs-AlGaAs multiple quantum well optical modulators"**
M.Whitehead, G.Parry and P.Wheatley,
IEE Proceedings Pt.J, (Optoelectronics), Vol.136, (Special Edition on Semiconductor & Integrated Optoelectronics), pp.52-58, February 1989.
- [8] **"High contrast reflection modulation at normal incidence in an asymmetric multiple quantum well Fabry-Perot structure"**
M.Whitehead and G.Parry,
Electronics Letters, Vol.25, No.9, 27th April 1989.
- [9] **"Multiple quantum well asymmetric Fabry-Perot etalons for high-contrast, low insertion loss optical modulation"**
M.Whitehead, G.Parry, A.Rivers and J.S.Roberts,
Postdeadline paper PD4 at IEEE/OSA Topical Meeting on Photonic Switching, Salt Lake City, Utah, USA, March 1-3 1989.
- [10] **"Multiple quantum well asymmetric Fabry-Perot etalons for high-contrast, low insertion loss optical modulation"**
M.Whitehead, G.Parry, A.Rivers and J.S.Roberts,
OSA Proceedings on Photonic Switching, J.E.Midwinter & H.S.Hinton, eds., (Optical Society of America, Washington, D.C., 1989), Vol. 3, pp.15-21.
- [11] **"Low-voltage multiple quantum well reflection modulator with on:off ratio > 100:1"**
M.Whitehead, A.Rivers, G.Parry, J.S.Roberts and C.Button,
Electronics Letters, Vol.25, No.15, pp.984-5, 20th July 1989.
- [12] **"Modelling the limits of low voltage operation for the GaAs multiple quantum well asymmetric Fabry-Perot cavity modulator"**
M. Whitehead and G. Parry,
To be presented at IEE Colloquium "Modelling of optoelectronic devices", IEE, Savoy Place, London WC2, England, 12th Feb. 1990.

As a contributor:

- [1] **"Thermal crosstalk in multi-quantum well optical logic arrays"**
J.M.Halley, P.Wheatley, M.Whitehead and J.E.Midwinter,
Paper 3, IEE Colloquium "Multi-quantum well devices -Physics, engineering and applications", IEE, Savoy Place, London WC2, England, 8th Dec. 1986.

- [2] **"A novel non-resonant opto-electronic logic gate using a GaAs-AlGaAs multi-quantum well electro-absorption modulator"**
P.Wheatley, P.J.Bradley, M.Whitehead, J.E.Midwinter, G.Parry, P.Mistry, M.A.Pate and J.S.Roberts,
Paper 6, ibid.
- [3] **"Novel nonresonant optoelectronic logic device"**
P.Wheatley, P.J.Bradley, M.Whitehead, J.E.Midwinter, G.Parry, P.Mistry, M.A.Pate and J.S.Roberts,
Electronics Letters, Vol.23, No.2, pp. 92-3, 15th Jan. 1987.
- [4] **"Hard-limiting optoelectronic logic devices"**
P.Wheatley, M.Whitehead, P.J.Bradley, G.Parry, J.E.Midwinter, P.Mistry, M.A.Pate and J.S.Roberts,
IEEE/OSA Topical Meeting on Photonic Switching, Incline Village, Lake Tahoe, Nevada, U.S.A., Mar. 1987. (Subsequently published in "Photonic Switching", Springer Series in Electronics and Photonics, No.25, Eds. T.Gustafson and P.W.Smith, Springer-Verlag 1988.)
- [5] **"Three-terminal non-inverting optoelectronic logic device"**
P.Wheatley, M.Whitehead, J.E.Midwinter, P.Mistry, M.A.Pate and J.S.Roberts,
Optics Letters, Vol.12, No.10, pp.784-6, Oct. 1987.
- [6] **"The design and optimisation of phase modulators in GaAs/AlGaAs multiple quantum well material"**
P.J.Bradley, M.Whitehead and G.Parry,
Paper 19, SIOE '88, UWIST, Cardiff, Wales, 28-29th Mar. 1988.
- [7] **"MOVPE-grown p-i-n diodes for electro-optic modulators and photodiodes with enhanced electron ionization coefficients"**
J.S.Roberts, J.P.R.David, P.Mistry, R.B.Franks, M.Whitehead and G.Parry,
Paper P9-2, 4th International Conference on MOVPE, Tokyo, Japan, May 16-20th 1988.
(Subsequently published in J. Crystal Growth (1988), 93, pp. 877-884.)
- [8] **"Computer modelling of the electric field-dependent absorption spectrum of multiple quantum well material"**
P.J.Stevens, M.Whitehead, G.Parry and K.Woodbridge,
IEEE J. Quantum Electron., Vol. QE-24, pp.2007-16, Oct.1988.

- [9] **"Limits to the performance of transverse and waveguide MQW electro-absorption and electro-refraction modulators"**
P.J.Stevens, M.Whitehead, P.J.Bradley, A.W.Rivers, G.Parry, J.S.Roberts, P.Mistry, M.A.Pate and G.Hill,
Poster presentation (Technical Digest pp. 33-36) at 14th European Conference on Optical Communications (ECOC '88), Brighton, England, 11-15th Sept. 1988.
- [10] **"Effect of device length and background doping on the relative magnitudes of phase and amplitude modulation in GaAs-AlGaAs multiple quantum well waveguide modulators"**
P.J.Bradley, M.Whitehead, G.Parry, P.Mistry and J.S.Roberts,
Applied Optics, Vol.28, No.8, pp.1560-4, 15th April 1989.
- [11] **"GaAs/AlGaAs multiple quantum well optical modulator using a multilayer reflector stack grown on Si substrate"**
P.Barnes, P.Zouganeli, A.Rivers, M.Whitehead, G.Parry, K.Woodbridge and C.Roberts,
Electronics Letters, Vol.25, No.15, pp.984-5, 20th July 1989.
- [12] **"Digital optoelectronic devices and systems"**
G.Parry, M.Whitehead and J.E.Midwinter,
Chapter 13 in "GaAs technology and its impact on circuits and systems", IEE Circuits and Systems Series 1, published by Peter Peregrinus Ltd., UK, 1989.

PATENT:

A UK patent application (No. 8904185.9), entitled "Fabry-Perot Modulator" was filed on 23rd Feb. 1989. This covers the AFPM and some variants on the basic form described here.